NEW EXPERIMENTAL APPROACHES TO THE POPULATION BALANCE EQUATION: *EULERIAN AND LAGRANGIAN VIEWPOINTS*

A DISSERTATION

SUBMITTED TO THE FACULTY OF THE GRADUATE SCHOOL

OF THE UNIVERSITY OF MINNESOTA

BY

GREGORY WALTER SITTON

IN PARTIAL FULFILLMENT OF THE REQUIREMENTS

FOR THE DEGREE OF

DOCTOR OF PHILOSOPHY

FRIEDRICH SRIENC, ADVISOR

JUNE 2009

Acknowlegments

To my friends for support and humor, Friedrich for guidance, lab members for insight and conversation, family both blood and in-laws for sanity, my parents for a shoulder to lean on, and my dear wife for all the above and more: without you none of this would have been possible.

I would also like to thank my funding sources:

- The National Science Foundation for partially supporting this work through a SBIR grant to R8Scan Corp.
- The University of Minnesota for an Innovation Grant
- Systec Corporation for supplying Teflon AF capillaries used in construction of the Teflon Flow cell

Abstract

Cell-to-cell variability in an asynchronous population of cells can be generally related to genetic differences, to different positions in the cell cycle, to the exposure of a heterogeneous environment, or to stochastic variations due to the low number of molecules in individual cells. To experimentally measure this cell to cell variability in response to different extra-cellular environments, one must measure the cells' phenotype using either an Eulerian or Lagrangian reference frame. In the Eulerian reference frame one measures the state of an entire cell population at discrete time points. In order to extract the single-cell dynamics from a time series of such measurements it is necessary to solve an inverse problem that extracts single cell behavior from the population data. This requires assumptions about cell behavior that may not be accurate in all cases. In contrast, in the Lagrangian reference frame one tracks individual cells over time and the dynamic properties of cells directly result from the observations. The properties of the entire cell population are then obtained as the sum of contributions of the individual components.

Experimental data generated with the Eulerian viewpoint is primarily generated using flow cytometry. This instrument yields the cellular property distribution as a snapshot in time and cells are discarded after the measurement. Automated flow cytometry was developed to obtain high frequency snapshots of the cellular property distribution over time. This technique was used in this thesis to both quantitatively and qualitatively describe the cell cycle dynamics of CHO cells, transient gene expression in CHO cells, and to develop a fed-batch control strategy for CHO cells.

To evaluate the single cell variability using the Lagrangian reference frame we have developed a novel flow cytometry instrument that is able to track individual, suspended cells in time. Individual cells can be repeatedly measured as they grow and express different proteins or as they respond to specific external stimuli of the growth environment. The measurement approach takes advantage of the Segre Silberberg effect that applies when dilute particles are subjected to Poiseuille flow in a capillary. Under such conditions particles of a given size and shape self-organize on the same streamline and keep their relative position in an oscillatory flow regime. We

demonstrate that tens and perhaps hundreds of suspended cells can be tracked over hours with this device.

With the developed instrument we have followed the Gfp expression modulated by variation in growth temperature as well as the induction kinetics of Gfp in individual yeast and CHO cells over extended periods of time. The data indicate a large variability of the kinetic response of individual cells that is not apparent if the Eulerian reference frame is used with conventional flow cytometry. Thus, the instrument permits evaluation of suspended cell populations at a level of detail that can not be achieved by existing instrumentation. The developed approach will be useful in the study of individual cell behavior and helpful in the rapid development of new drugs.

Table of Contents

List of Tables

List of Figures

Chapter 7 Cell Population Laboratory for Engineers

Chapter 8 Single Cell Tracking Cytometer: Theory

Chapter 9 Mammalian Cell Single Cell Tracking Data

Chapter 10 Yeast Gfp Expression: Response to Temperature Fluctuations

Chapter 11 Flow Cytometry without Alignment of Collection Optics

Chapter 12 Future Applications

Chapter 14 Appendices

1 Introduction

In both medicine and biotechnology, understanding how the phenotype of cells in a culture changes over time is of fundamental importance. Phenotypes of cells can be quantitatively described as a vector where each element of the vector represents the amount of a chemical component of the cells. This vector is referred to as the state of the cells **n**(**x**, t). To describe how the state of the cells change over time across an entire population of cells the population balance model was derived (Fredrickson, et al. 1967). The root assumption of the population balance model is that a culture is a complex distribution of cells which act independently of each other but dependently on their environment. The population balance model is essentially a mass balance on cells. Therefore, the rate of change of cell number must be accounted for by cellular flux within the state space, also known as cellular growth, cell division, and the partitioning of the internal composition of the cell during division. In mathematical terms, with a steady-state extra-cellular environment this is expressed as:

$$\frac{\partial n(x,t)}{\partial t} + \nabla \bullet [r(x,t) * n(x,t)] = \int_{x}^{\infty} (2 * \Gamma(y,t) * P(x,y,t) * n(y,t)) dy - \Gamma(x,t) * n(x,t) \tag{1.1}$$

where **n**(**x**, t) is the cell number distribution function, **r**(**x**, t) represents the single cell growth rate function, **Γ**(**x**, t) is the division rate function, and **P**(**x**, **y**, t) represents the probability of partitioning a cell of state **y** into a cell of state **x** (for example, a cell state can be defined as each stage of cell cycle). In this equation **x** and **y** represent differing internal cell states and t represents time. This equation represents the fact that the way the cellular distribution changes (left hand side of the equation, first term) is solely due

to cellular flux in state **x** (left hand side of the equation, second term) or because cells rearrange the distribution through daughter cell birth (right hand side of the equation, first term of the integrand) or mother cell division (right hand side of the equation, second term of the integrand). It is important to note that rate functions are deterministic while the division rate and partitioning functions are probabilistic.

Since the functions of $\mathbf{\Gamma}(\mathbf{x}, t)$, $\mathbf{P}(\mathbf{x}, \mathbf{y}, t)$, and $\mathbf{r}(\mathbf{x}, t)$ are unknown for a vast majority of cell systems, a major problem in implementing the population balance model is the experimental measurement of these functions. This is due to the root assumption of the population balance model that the behavior of the culture is comprised of the behavior of single, independent cells. Therefore, one must either devise an experiment to track an individual cell through time, or solve the inverse population balance equation to extract the single cell behavior from the histogram of a cellular property. These types of approaches are analogous to the fluid mechanic problem of converting Eulerian observations to Lagrangian information (Ramkrishna 2000). In the Eulerian reference frame one measures the state of an entire cell population at discrete time points. In order to extract the single-cell dynamics from a time series of such measurements it is necessary to solve an inverse problem which in most cases is a non-trivial task. In contrast, in the Lagrangian reference frame one tracks individual cells over time and the dynamic properties of cells directly result from the observations. The properties of the entire cell population are then obtained as the sum of contributions of the individual components.

Experimental data generated with the Eulerian viewpoint is primarily generated using flow cytometry. This instrument yields the cellular property distribution as a

snapshot in time and cells are discarded after the measurement. Automated flow cytometry was developed to obtain high frequency snapshots of the cellular property distribution over time (Kacmar, et al. 2004b). Automated flow cytometry rapidly draws a sample from a large population of cells, stains the cells, injects the sample into the flow cytometer, and then acquires the cellular property distribution. The differences in the histograms between each time point can then be compared, and quantitative and qualitative assessments can be made about how the culture has changed its properties. This technique was used in this thesis to both quantitatively and qualitatively describe the cell cycle dynamics of CHO cells, transient gene expression in CHO cells, and to develop a fed-batch control strategy for CHO cells. To extract the population balance functions an inverse problem must be solved (i.e. given n(**x**, t) solve for **Γ**(**x**, t), **P**(**x**, **y**, t), and **r**(**x**, t)). The major limitation of solving the inverse problem is that it can only be accomplished under certain steady-state conditions in the cell culture (Collins and Richmond 1962). Therefore, the inverse technique is not typically applicable to transient situations (Hatzis, et al. 1995). Furthermore, when one attempts to apply an inverse method, one a priori chooses a subset of state variables that can be measured and then attempts to measure their effect on the rate function. However, this approach begs the question if the selected state variables cause the change in the measured phenotype, or if they are merely correlated (Koch 1999).

Currently, experimental data generated with the Lagrangian viewpoint is restricted to either fluorescently tagging sub-populations of cells or taking time-lapse photography of individual cells. Once sub-populations of cells are fluorescently tagged, a cytometer or microscope can then be used to sample from the larger population of

suspended cells and examine how the tagged sub-population changes over time. The major limiting factors of fluorescently tagging sub-populations of cells to obtain single-cell tracking are both philosophical and technical. Philosophically, one does not obtain true single cell tracking when tagging sub-population of cells. Instead one simply treats all the tagged sub-population as an individual cell. Furthermore, from a technical standpoint, most dyes only maintain their fluorescence for a few days, and fluorescent dyes also occupy one of the potential fluorescence channels that could be used to measure a state variable.

Therefore, a method that can measure single cells without a fluorescent tag would be the ideal method to experimentally determine the population balance functions for suspended cultures. Currently, there are two major classes of cell measuring devices that can accomplish this, laser scanning cytometers and imaging cytometers (microscopy). Laser scanning and imaging cytometers (microscopy) attach relatively few cells to a surface, and then analyze the cells in place over time (Elfwing, et al. 2004 ; Shapiro and Perlmutter 2006). Thus, laser scanning and imaging cytometers are capable of measuring the rate function $\mathbf{r}(\mathbf{x},t)$, the division rate $\mathbf{\Gamma}(\mathbf{x},t)$ and the partitioning function $\mathbf{P}(\mathbf{x},\mathbf{y},t)$. However, since relatively few cells are analyzed these measurement techniques introduce statistical uncertainty (Tarnok 2006). Also, since the substrate a cell is attached to plays a significant role in both mammalian (Georges and Janmey 2005 ; Mitchell, et al. 2005) and yeast (Johanson, et al. 2006) cell physiology these instruments introduce an additional variable, the substrate composition into the cellular physiology. Therefore, laser scanning and imaging

cytometers enable single cell tracking for a few attached cells, while traditional flow cytometers measure many cells only once.

A significant aspect of this thesis describes the development of an instrument capable of tracking single suspended cells through time. The developed instrumentation combines the positive features of both traditional flow cytometers and laser scanning and imaging cytometers. Specifically, the proposed device will enable single cell tracking of large numbers of cells in suspension. Therefore, the rate, partitioning, and division functions of the population balance equation will be quickly and easily measured for cells in a uniform, well controlled environment in highly quantitative terms.

1.1 Thesis Organization

Chapter 2 provides background information to fully understand this thesis. It provides a detailed description of the workings of a flow cytometer to accompany all chapters. Appendix I contains all materials and methods. Appendix II describes the evolution of the experimental platform developed to obtain single cell tracking of suspended cells. The remainder of the thesis can be divided into two major sections: an Eulerian viewpoint (Chapters 4-7) and a Lagrangian viewpoint (Chapters 8-10). Data obtained under the Eulerian viewpoint was acquired using a modified automated flow cytometer. The rationale behind the modification is supplied in Chapter 3. This system was applied to monitor the cell cycle kinetics of CHO cells (Chapter 4), transient gene expression in CHO cells (Chapter 5), fed batch addition to CHO cells (Chapter 6), and application to an undergraduate ChE unit ops course (Chapter 7). Lagrangian viewpoint chapters primarily describe the theory of the developed instrument (Chapter 8) and its

use to acquire single cell data from mammalian cells (Chapter 9) and yeast cells (Chapter 10). More potential applications of the single cell tracking cytometer and future improvements to the base system are described in the future applications section in Chapter 12.

2 Flow Cytometry Background

2.1 Introduction

Flow cytometry is a useful technique for analyzing cell cultures at the single cell level. Through single cell analysis, important subpopulations of a culture can be detected rather than simply measuring a population averaged property. A flow cytometer can measure light scattering properties of cells including forward scatter (FSC) and side scatter (SSC). Finally, a flow cytometer has several fluorescence filters that allow measurement of many cellular properties and components provided the proper fluorescent stains or fluorescent markers are utilized.

A flow cytometer forces cells to pass through the path of a laser one cell at a time. This is achieved through use of a narrow flow cell. As long as the cell size is smaller than the narrowest part of the orifice in the flow cell and the cells are at sufficiently low concentration, the flow characteristics will align the cells to pass through the laser one at a time. The interaction between the cell and the laser is measured and recorded for each cell. A full set of interactions includes the FSC, SSC, and fluorescence emitted. Furthermore the fluorescence emitted is passed through a series of filters such that a different range of wavelengths can be isolated from each filter. Consequently it is possible to analyze both the intensity of fluorescence as well as restricting the measurement to a certain range. Green and red fluorescence, for example, are distinguished by this process. (Shapiro 1985)

By carefully selecting fluorescent dyes, it is possible to stain intracellular parts and to determine many cellular properties. Therefore a wide variety of cell

characteristics can be measured simply by analysis in a flow cytometer. These characteristics include both intrinsic and extrinsic cell properties. Determining the properties of interest in a culture requires that precise measurements be acquired at the single cell level. In order to properly understand the meaning of the measurement, it is important to understand how the flow cytometer itself operates. A summary of the components of the flow cytometer follows.

2.2 Fluidics

The goal of the fluidics is to generate a stream of cells passing through a laser beam. This laser is focused orthogonally to a small interrogation point intersecting the middle of a narrow sample stream. As discussed earlier, the laser interacts with a single cell by passing the cells through a narrow flow cell. At present, there are two methods commonly used to achieve single-file flow through the flow cell: sheath and capillary.

2.3 Sheath Cytometer

In the flow cell of a sheath cytometer, the sample is injected into the center of the flow of sheath fluid. The flow cell subsequently narrows resulting in an increased average velocity. By the conservation of mass, as the velocity increases for a given patch of fluid, the cross-sectional area of this patch must decrease. Thus, cells in the sample stream are hydrodynamically focused to a much narrower stream. The laser therefore can be focused on this sample stream and all cells in the sample will only cross at a specific point. Through this mechanism, the cytometer can analyze cells in the range of thousands of cells per second.

2.4 Capillary Cytometer

A capillary cytometer eliminates the need for sheath fluid. In this type of cytometer, the sample is simply aspirated into a glass capillary using a highly accurate piston pump driven by a micro-stepper motor. In the EasyCyte model made by Guava Technologies, the capillary has a constant inner diameter of 100 μm. This narrow capillary forces cells into single file flow, and at the midpoint of the capillary, the laser interrogates the single-file flow of cells and signals are generated as described in the next section. A significant advantage of this type of cytometer is that the exact sample volume that enters the capillary is the sample that is measured. This is in direct contrast to a sheath cytometer, where sample is injected into an unknown volume of sheath fluid. As a result, the capillary cytometer can measure concentrations of samples directly. However, to prevent overlapping of cells as they are interrogated by the laser, the capillary cytometer is limited to a maximum concentration of cells in the original sample of $5x10^5$ cells/mL.

2.5 Light Scattering

Light scattering occurs during the interrogation of a cell with the laser. As the light approaches the cell, it is diffracted, reflected, and refracted. These redirected photons are detected by the PMTs and the diode as previously described. In general, FSC and SSC are the main parameters of consideration although it is possible to place detectors in other positions.

Cells are not point particles, but instead the cell consists of many components. Theoretically, it is possible to break a cell into a sum of its components, an infinite number of point particle dipoles. These dipoles are excited by the laser and reradiate

with the majority of the reradiation at small angles from the axis of the laser termed forward scatter (FSC). FSC is the dominant parameter as destructive interference does not occur in the forward direction. The interference, caused by the many dipoles radiating light in similar directions with different path lengths, decreases the intensity of the right and other angle scattering. By detecting the total FSC signal, the researcher in essence is summing the collective effect of all of the dipoles present in a single cell. (Hiemenz and Rajagopalan 1997). The total FSC therefore is demonstrative of the cell size.

Sizing by light scattering is not a new idea. Mullaney, *et al.* used a photometer to determine cell size in much the same way that a flow cytometer does today. (Mullaney, et al. 1969) Determining the exact cell size though from light scattering is difficult. While FSC is correlated to cell size, the exact correlation can vary from cytometer to cytometer and according to other cellular properties. In order to get a true correlation with cell size, a calibration must be performed. This calibration involves measuring the FSC of standardized beads of similar size and refractive index to the cells of interest. Furthermore, it has been shown that the correlation is valid only over detection angles between 0.5 and 1.5 degrees. (Watson 1991) The sum of dipoles argument is the essence of light scattering theory called Mie theory. Mie theory is a decent approximation for cells in the flow cytometer, but Mie theory assumes the particles of interest are spheres. (Hiemenz and Rajagopalan 1997) Unfortunately, cells, especially budding yeasts such as *S. cerevisiae*, are not always spherical so the theory remains an approximation.

Although it is a weaker signal due to destructive interference, SSC is still of interest to record. Side scatter is important as it represents the internal composition, or granularity, of a cell. Should a dipole be completely excited, it will radiate at a right angle to the direction of excitation. Consequently any internal structure will produce scattered light at right angles to be detected as SSC. Normal operation of a flow cytometer tends to produce a linear correlation between the FSC and SSC. This makes physical sense as larger cells tend to have either more internal structures or larger internal structures to direct light to right angles. However, this is not to say that all cells have the same correlation between FSC and SSC. While all cells tend to have this linear correlation, the exact slope is in fact different. Bivariate plots of FSC versus SSC are key manners in which to detect contamination in a sample at substantially lower concentrations than possible through visual microscopy.

2.6 Fluorescence Measurement

In contrast to scattered light, fluorescence occurs directly from absorbed light that is reemitted. Natural fluorescence can be detected in all cells as each cell has a basal level of autofluorescence. Therefore the baseline for detection in cells is nonlinear, as larger cells tend to have slightly higher levels of autofluorescence. (Doan, et al. 2003) In addition, some cells have naturally occurring proteins that fluoresce. Genes encoding fluorescent proteins can be added to plasmids as with any other gene of sufficiently small size. Therefore, any cell could potentially be transformed with a plasmid leading to cells with higher fluorescence. The other methods that make a cell fluorescent are to introduce a fluorescent dye or a fluorescent analog of a natural compound.

One example of a naturally occurring fluorescent protein, green fluorescent protein, or Gfp, is prevalent in biological research. Gfp is not simply a fluorescent indicator. The utility of Gfp as a real time reporter in addition to indication of successful incorporation of a gene has been demonstrated previously. (Albano, et al. 1998 ; De Wulf, et al. 2000 ; Li, et al. 2000 ; Poppenborg, et al. 1997) Wild-type Gfp, which absorbs the maximum amount of light at 395 nm and emits at 508 nm, was isolated from a jellyfish, *Aequorea victoria*. (Heim and Tsien 1996) It is of importance to note that the emitted photons in general are higher wavelengths than the absorbed light due to Stokes' shift. Only emitted photons can be measured. Detection schemes in the flow cytometer are directed based on the possible emission spectra so fluorescence filters subdivide the range of wavelengths higher than the laser wavelength.

Gfp and other naturally occurring homologues have been mutated such that the absorption and emission spectra are shifted towards more convenient wavelengths. For example, the 488 nm argon laser is commonplace so an absorption maximum closer to this wavelength is ideal such that the emission intensity will increase. The Gfp mutant S65T and other Gfp mutants have already been adjusted in this manner. (Heim and Tsien 1996)(Anderson, et al. 1996 ; Cormack, et al. 1996) The high level of single cell variability in protein content requires utilization of a logarithmic scale.

Although Gfp can be utilized as a reporter protein, it is also of interest to consider a cell's total protein or to determine other cellular components. To perform these measurements requires cell staining with a fluorochrome. Many procedures have been developed to determine a wide variety of cellular properties utilizing

fluorochromes. All of the DNA staining mentioned earlier can also be performed in a flow cytometer. The fluorescent DNA stains, including propidium iodide (PI), are more accurately detected by the fluorescence PMTs than by other methods such as visual microscopy. In addition to being a DNA stain, PI is also considered a vitality stain as it can only bind to the DNA of cells that have compromised membranes. The utility of flow cytometer and PI is demonstrated by realizing that manually determined viability, which varies from researcher to researcher, is less precise than the viability determined by a flow cytometer. ((Al-Rubeai and Emery 1993)

2.7 Optics

The quality of any cytometer is defined by the instrument sensitivity, and the instrument precision. The precision of a cytometer is typically defined by the CV of a distribution of standard beads, and is primarily affected by the variation of laser intensity across the hydrodynamically focused sample core. The sensitivity of the device is a function of the signal to noise ratio defined by the ratio of the amount light collected from the sample to the amount of light collected from the excitation beam and other noise. In traditional systems, there are two ways to increase the signal to noise ratio. The first relies on minimizing the scattered light from the excitation source by using square cuvettes or using round cuvettes with apertures and pinholes that restrict light collection to only the core. The second way is to increase the amount of light collected from the core. This value is defined by the numerical aperture (NA) of the collection optics. Since there is an inverse relation ship between NA and depth of focus (which increases the difficulty of alignment), a NA of 0.65 is typically the maximum

used in cytometry. Thus, an ideal cytometer would have high precision and a high signal to noise ratio.

In both capillary and sheath cytometers, the laser crosses the middle of the flow cell, and light the forward scatter is measured at low angles from the laser's path. In general, FSC is measured by collecting light diffracted by the cells at an angle between 0.5-10^{o} from the laser's path. For this reason, FSC is also known as forward angle light scattering, or FALS. A diode or PMT is used to detect and convert the light scattering to an electronic signal. SSC is determined by measuring the light refracted and reflected by cells 90^{o} from the laser's path. For this reason, SSC is also known as right angle light scattering, or RALS. Far less light is scattered to this position than to the forward angle position. A diode is therefore insufficient for data collection purposes, and a photomultiplier tube (PMT), which internally amplifies the signal, is used for SSC. A PMT is present for each of the fluorescence signals as well.

These filters act in different ways. There is typically a short pass filter, a long pass filter, and several band pass filters. A short pass filter prevents all light with wavelengths longer than a specific value pass through the filter; the long pass filter prevents all light with wavelengths shorter than a specific value pass through the filter. Meanwhile band pass filters only allow light within a specific range of wavelengths to pass through the filter. In this way, it is possible to only measure the intensity of blue light emitted, for example, and to separate this measurement from the intensity of red light emitted.

2.8 Electronics and Data Collection

The scattered and emitted light must be converted to an electronic signal such that the data can be stored on a computer. This electronic signal is created when light falls on the detector. The light generates a current in both the diode and the PMTs. When a cell is not present in the interrogation point, the scatter and emitted fluorescence will return to a basal level, and the current should stop flowing. Therefore, there should be an initial increase as the cell enters the interrogation point, a maximum when the cell is in the interrogation point, and a terminal decrease as the cell leaves the interrogation point. This behavior is best described by the waveform of the voltage pulse created during this interaction. Figure 2-1 depicts this event.

The creation of a pulse also leads to three different possible ways to analyze the measurement. It is simple to evaluate only the maximum of the pulse. It is also of interest to integrate the pulse and to consider the pulse width. While all methods are acceptable, it is important to recognize the distinction between them. Simply evaluating the height limits the analysis to the effect of the entire cell being present within the laser's path. Meanwhile, the integral takes into account the entire measurement. The width demonstrates the length of time the cell was interrogated. When measurement of a perfect sphere is considered, these measurements should converge to depict the same trend as the measurement should become a perfect Gaussian curve. Orientation will affect these measurements though if a non-spherical, rotating object is considered.

Regardless of which quantification method is used, the pulse value must be assigned by an analog-to-digital converter to a channel. The allocation of these channels can also be adjusted. By adjusting the gain or voltage applied to the PMT and

diodes, the measurements can be shifted along the channel axis. Consequently, cytometric measurements are relative unless standard calibrations are performed. Another adjustment that can be made is through the amplification of the signal. For example, operation in a linear mode of amplification allocates 1024 channels evenly across a 10 volt range. Meanwhile, operating in a logarithmic mode allocates 256 channels for each decade of voltage. While 2.5 volts should correspond to channel number 256 in linear mode, channel number 256 should correspond to 0.1 volts in logarithmic mode. The logarithmic mode is therefore quite useful when there is a wide distribution in the measurements to be acquired as shown in Figure 2-2. One example of its utility lies in measurement of protein content, as there is a large variation in the protein content from cell to cell.

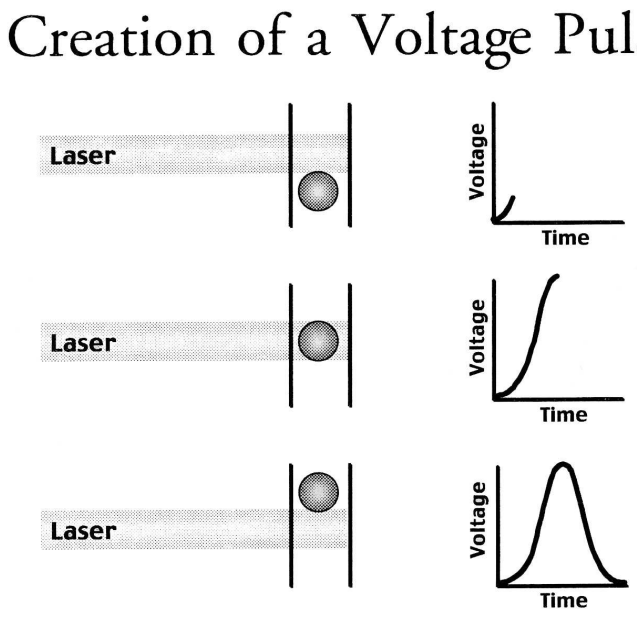

Figure 2-1: Creation of a voltage pulse in a flow cytometer. Waveform of a voltage pulse created due to a cell passing through the laser's interrogation point. Reproduced from BD FACS Training Manual (2001).

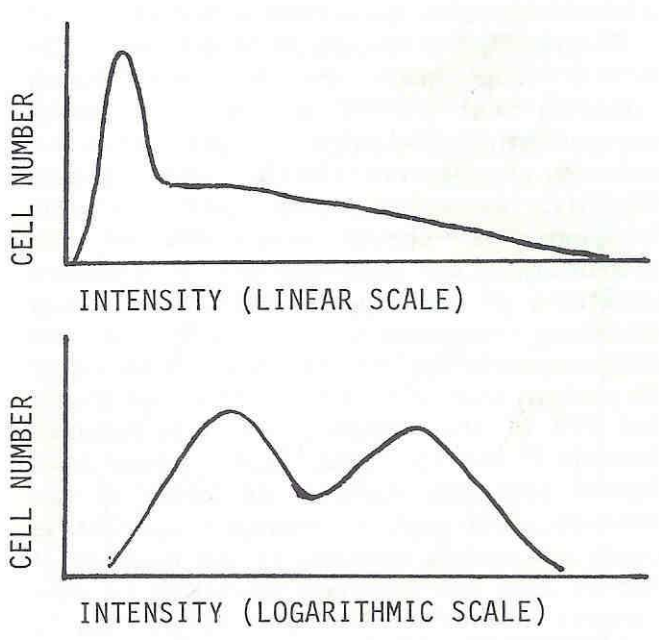

Figure 2-2: The difference between linear amplification and logarithmic amplification. Reproduced from Shapiro 1985. While the logarithmic amplification shows two distinct peaks, the linear amplification blurs the second peak such that the peak seems to not even be present.

3 Automated Staining Unit Characterization and Improvement

3.1 Introduction

To acquire a high frequency snapshot of the state of a population of cells automated flow cytometry was developed. The device utilizes a microchamber allowing on-line dilutions, cell fixation, cell staining, cell washing, and eventually cell number concentration. (Abu-Absi, et al. 2003 ; Zhao R, et al. 1999a) The system is comprised of a computer with a data acquisition card that controls a series of pumps, valves, and a flow cytometer (Figure 3-1). Iteratively, the computer will automatically sample from a bioreactor, pump the sample to a microchamber, stain the sample with desired reagents, allow the reagents to incubate, and then inject the sample into the flow cytometer for analysis. The data is then acquired and saved, and the cycle begins anew.

To complete a staining protocol, the same tubing is used for cell samples, staining solutions, and wash solutions. Thus, as the device steps through a staining protocol previous solutions and cell samples in the tubing must be replaced with new solution. Originally, this was accounted for with a plug flow assumption (Abu-Absi, et al. 2003 ; Zhao R, et al. 1999a) where no dispersion between fresh solution and the existing solutions occurs. In reality, the flow is not plug-flow, but instead is laminar flow and dispersion occurs. To overcome dispersion, excess quantities of cell samples or staining solutions were pumped through the device to overturn existing solutions in the tubing 3-10 times. This is only feasible when staining solutions or cell samples are both abundant and inexpensive. Thus, initially this device was primarily used for experiments measuring time courses of intrinsic cellular properties (FSC, SSC, Gfp fluorescence(Abu-Absi, et al. 2003 ; Gilbert, et al. submitted ; Kacmar, et al. 2004a ;

Kacmar, et al. 2006 ; Kacmar and Srienc 2005 ; Kacmar, et al. 2006 ; Sitton, et al. 2006 ; Sitton and Srienc 2008a ; Sitton and Srienc 2008b)) where sample was abundant, and for extrinsic properties using only inexpensive dyes (propidium iodide, BODIPY). If a dye is expensive or sample is limited, then minimal amounts of stain or sample must be used. In this case, dispersion must be accounted for and the automated cytometer redesigned to account for the dispersion. To accomplish this, a model was developed, the model was verified, and the lessons were applied to a redesigned microchamber.

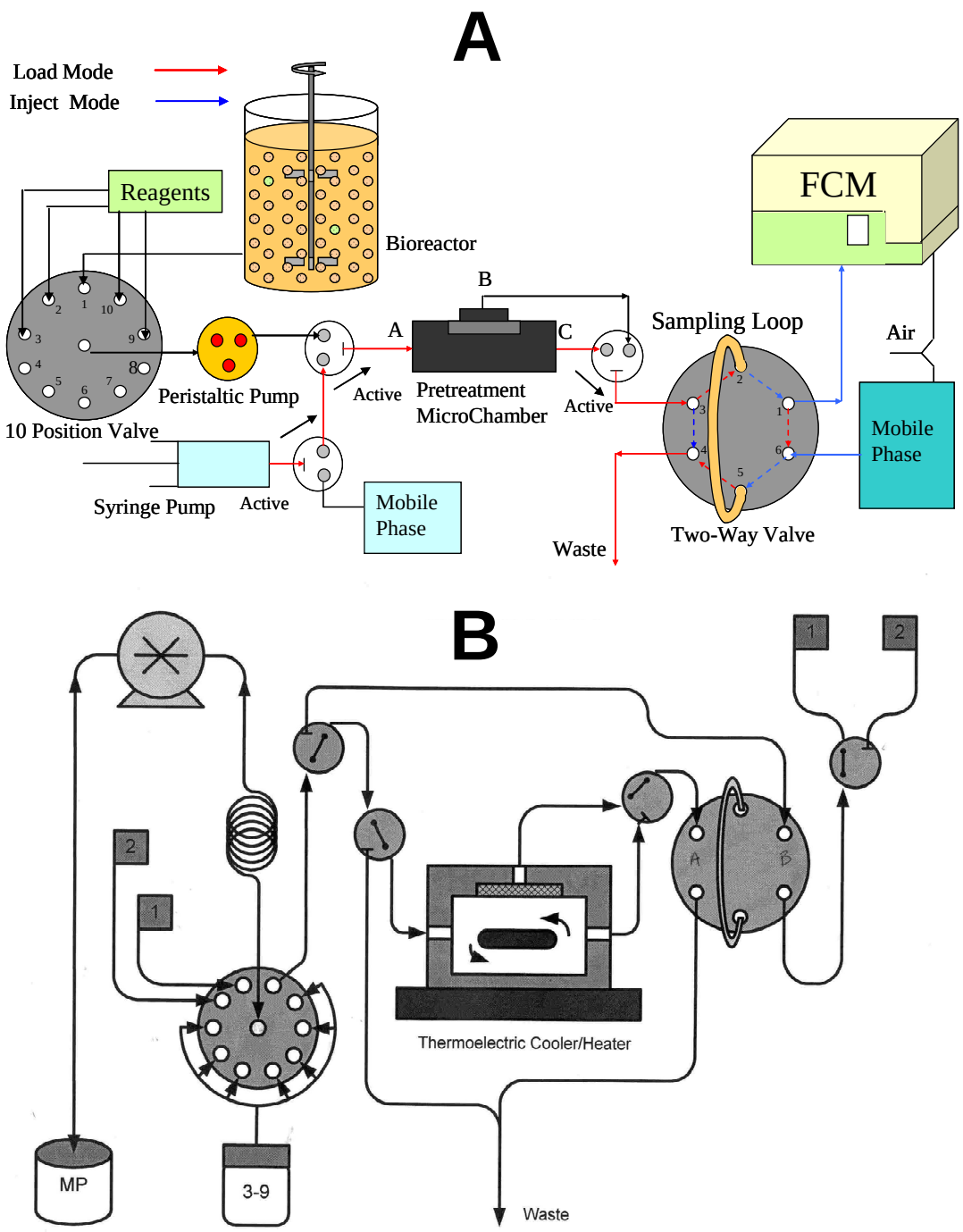

Figure 3-1: Flow schematics of the automated staining units. **(A)** The original automated staining unit and **(B)** the commercialized version manufactured by MSP Corp.

3.2 Dispersion Modeling

The first step to redesigning the automated flow cytometry system was to develop an appropriate model for dispersion of solutes in a laminar flow reactor. These equations have been described in numerous Chemical Engineering textbooks describing reactor engineering. (The discussion below uses Fogler's Elements of Chemical Reaction Engineering, 3rd edition). The equation for dispersion in a plug-flow reactor is:

$$\frac{\partial c}{\partial t} = D_a \frac{\partial^2 c}{\partial z^2} - U \frac{\partial c}{\partial z} \tag{2.1}$$

where c is the concentration of the species, D_a is the dispersion coefficient, z is the axial distance, and U is the mean velocity of the fluid. The dispersion coefficient is a measure of both convective and molecular diffusion. Convective diffusion can be caused by laminar flow, re-circulation due to sharp turns in the tubing, as well secondary flows induced by the curvature of the tubing.

In ideal laminar flow the dispersion coefficient, D_a can be estimated using the Aris-Taylor dispersion coefficient:

$$D_a = D_{AB} + \frac{U^2 R^2}{48 D_{AB}} \tag{2.2}$$

where R is the radius of the tubing, and D_{AB} is the is the molecular diffusion coefficient of species A in species B. Typical values of molecular diffusion coefficients for small molecules in water were estimated to be ~ 10^{-9} m^2 s^{-1}.

However, it is important to note that due to changes in the geometry of the tubing in the automated cytometer ideal laminar flow is not exhibited. Furthermore, if

the concentration of particulates in the loaded samples increases significantly, then effects such as particle-particle interaction and wall effects become significant and the Einstein-Stokes relation is no longer valid. However, for estimation purposes, these idealized equations can be used.

Using MATLAB, Equation (2.1) can be solved for c(x,t). Since the flow rate is constant during operation of the FCP, the time variable can be interchanged with the volume of fluid pumped through the device, thus c(x,Q) is calculated. The initial geometry of the system consists of a length L of tubing of radius R. An initial plug of sample with concentration of one is loaded into the length L_{draw} of tubing. From L_{draw} to L, fluid of concentration zero as shown in Figure 3-2.

The Dankwerts boundary conditions are used:

At z=0:

$$-\frac{D_a}{U}\frac{\partial c}{\partial z}+c=0 \tag{2.3}$$

and at z=L:

$$\frac{\partial c}{\partial z}=0 \tag{2.4}$$

With this model, we can then vary pump velocity and load distance and measure the resulting concentrations along the length of the tubing as a function of the volume pumped as shown in Figure 3-3 and Figure 3-4. From these plots, three observations have relevance to future designs of the automated cytometer:

1. Due to laminar flow and other convective forces, a fraction of the particulates precedes the plug-flow calculation (V=417 μL) of the volume. (Figure 3-4).

2. Higher load volumes lead to peak values at the tubing exit approaching the initial sample concentration. (Figure 3-4).
3. Higher flow rates result in lower dispersion and a peak concentration at the tubing exit approaching the initial sample concentration. (Figure 3-4).

a. Model Verification

To verify the model, 1 mL of suspended fixed yeast cells at a given concentration were loaded into the capacity loop (Figure 3-1B). Next, this plug of cells was pumped out the device through the pathway bypassing the microchamber. Fractions at the outlet were collected two ways: continuous pumping or pulsed pumping for 200 uL of sample at 1 mL/min. Cell counts from each collected fraction were obtained using a coulter counter and normalized to the concentration of the initial solution. As Figure 3-5 shows, the two methods yield virtually identical results. Therefore, since the pulsed pumping yields less experimental error and is physically easier to manipulate, the pulsed pumping technique was used throughout the rest of the experiments.

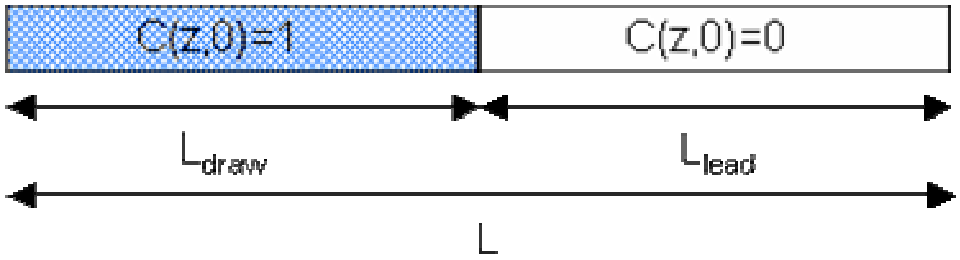

Figure 3-2: Geometry and initial conditions of the modeled laminar flow reactor. An initial plug of a tracer solution (concentration arbitrarily set to 1) is loaded into a capillary of length L over the length L_{draw}. The tracer is then pumped through the capillary displacing a solution of concentration zero over length L_{lead}.

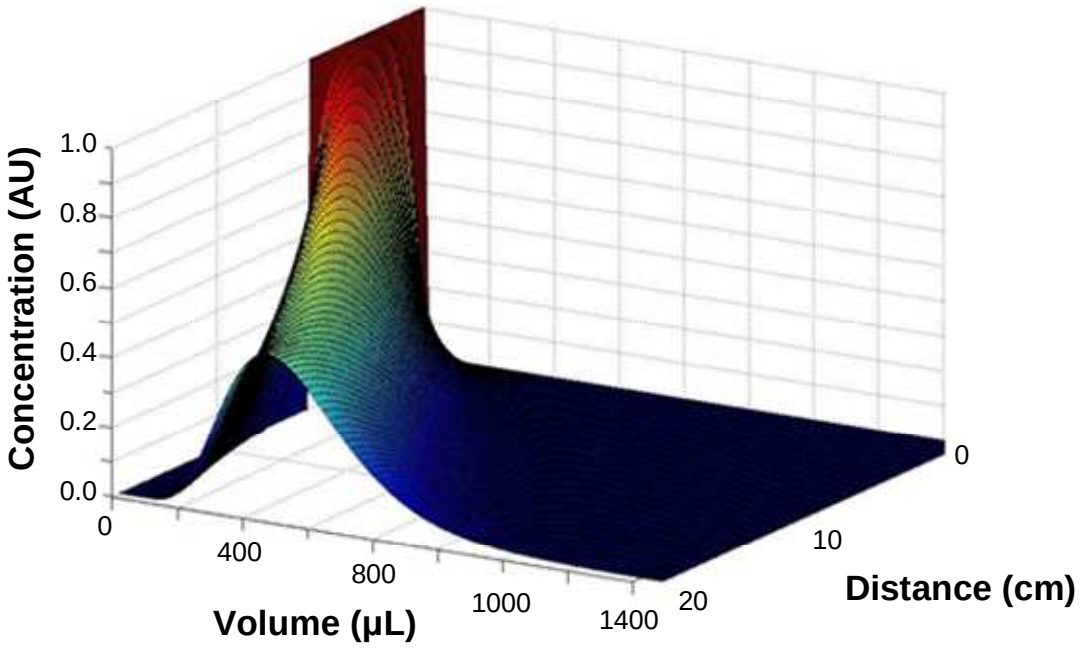

Figure 3-3: Tracer concentration in the tube as a function time. The concentration of tracer is a function of volume pumped through the FCP and distance (L) for a load volume of 250 uL and a pumping rate of 1 mL/min. At volume zero, the figure corresponds to the initial conditions specified in Figure 3-2.

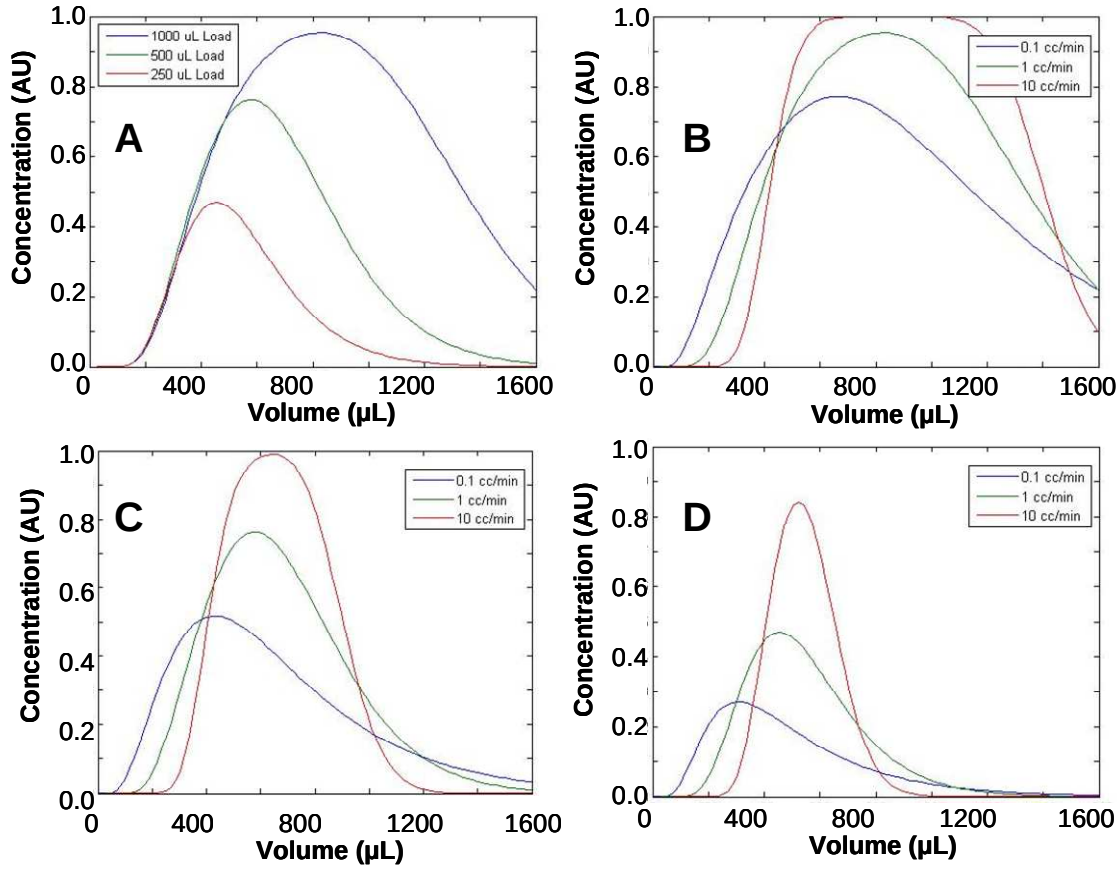

Figure 3-4: Predicted concentration profiles at the end of the simulated tube. For **(A)** increasing load volumes, **(B)** increasing flow rates at a load volume of 1 mL, **(C)** increasing flow rates at a load volume of 0.5 mL, and **(D)** increasing flow rates at a load volume of 0.25 mL.

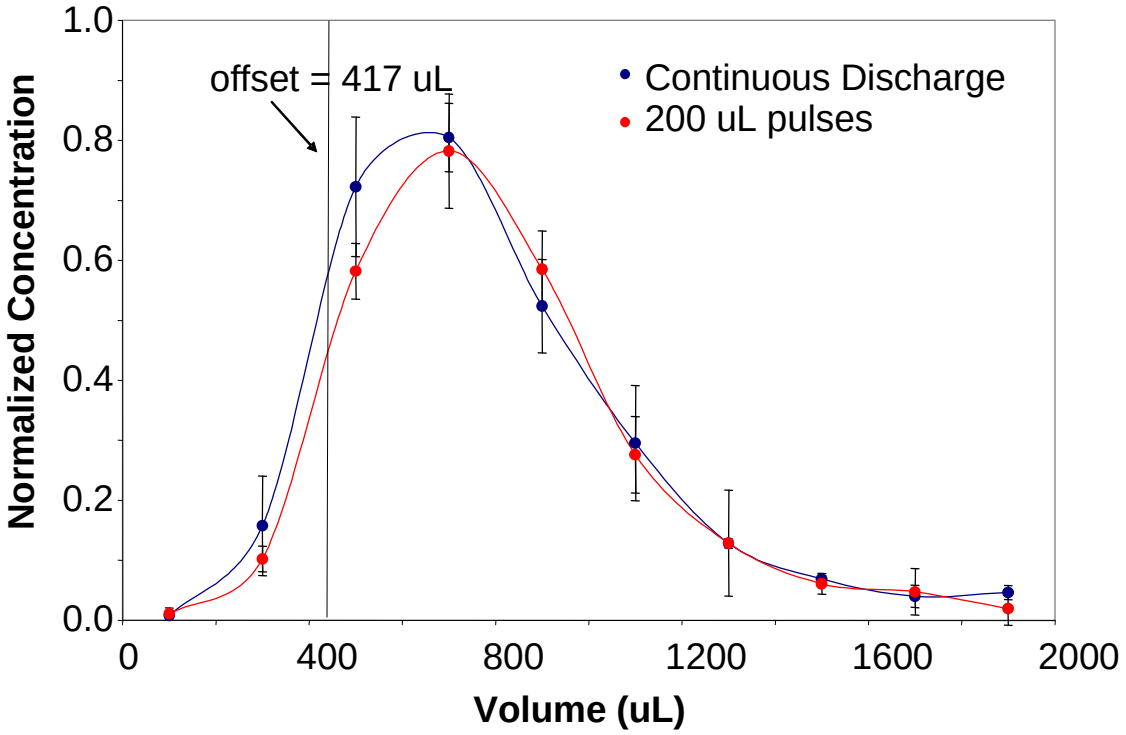

Figure 3-5: Fraction collection using continuous versus pulsed pumping. 500 uL of sample was drawn into the capacity loop of the commercialized system and discharged at 1 mL/min. 200 µL samples were taken with the pump running continually or in pulses. The offset indicates the amount of fluid between the initial load of tracer and the point of sample collection.

To characterize the dispersion of particulates as a function of load volume, 1000 μL, 500 μL, and 250 μL were drawn into the capacity loop. These samples were then discharged through the automated cytometer as indicated in Figure 3-1 at a flow rate of 1 mL/min Figure 3-6. To characterize the dispersion of particulates as a function of flow rate 500 μL of sample was drawn into the capacity loop and discharged at 0.1, 1, and 10 mL/min as indicated in Figure 3-7. Samples were collected every 200 μL as shown in Figure 3-5. Thus, the experimentally measured dispersion curves (Figure 3-6 and Figure 3-7) are virtually identical to the curves produced by the simulations, and the conclusions formed from the simulations are valid.

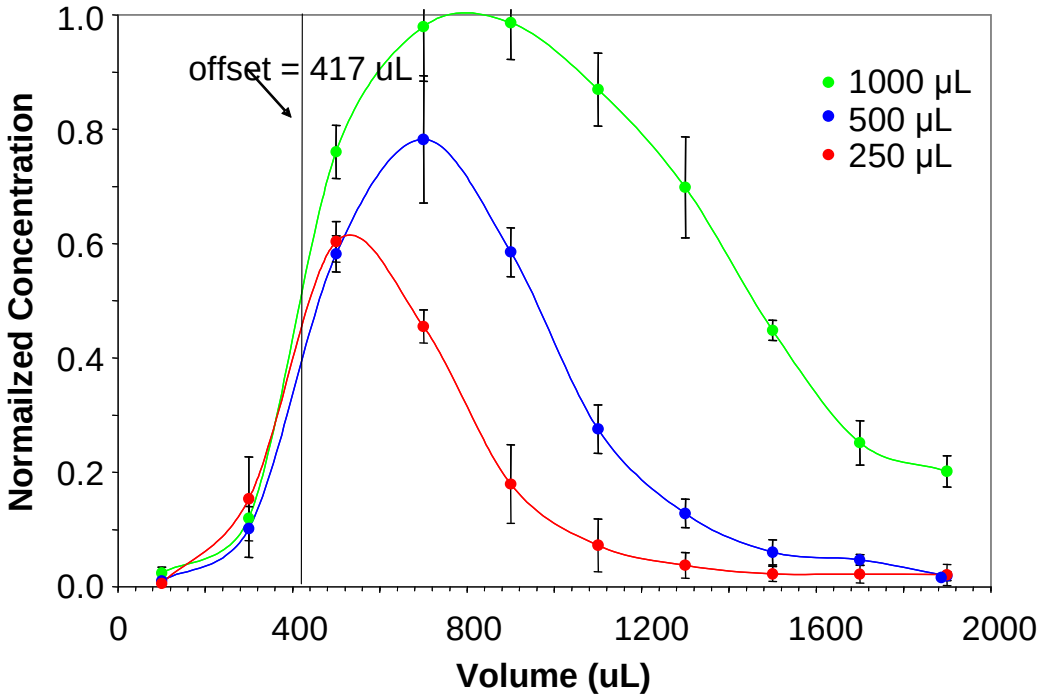

Figure 3-6: Dispersion pattern as a function of load volume. Concentrations are normalized to the concentration of the original sample.

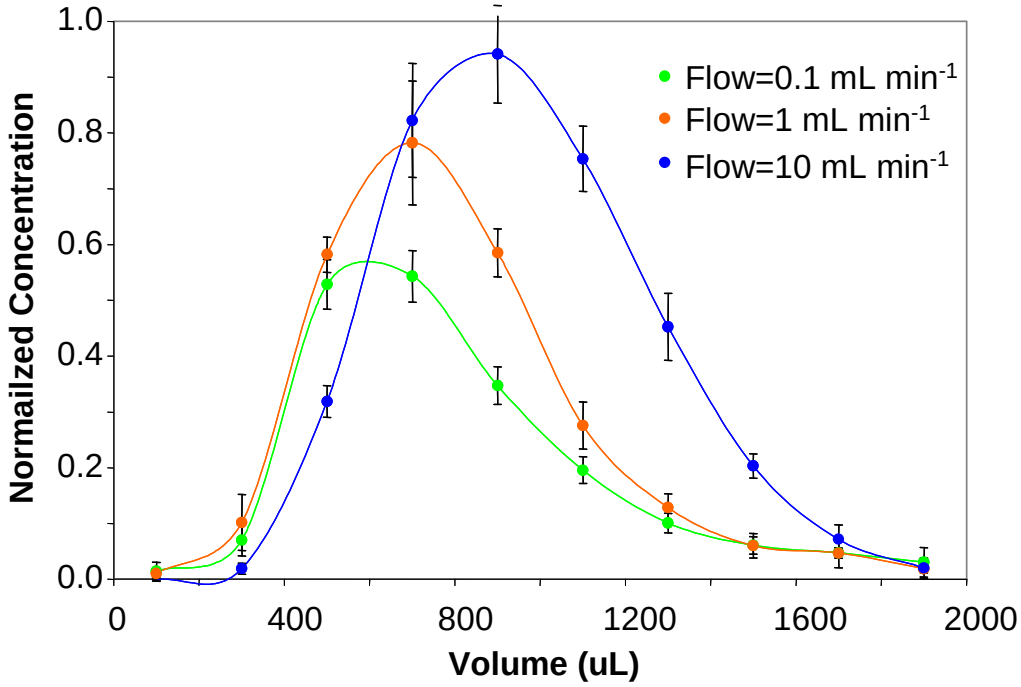

Figure 3-7: Dispersion pattern as a function of flow rate. Concentrations are normalized to the concentration of the original sample.

3.3 Microchamber Modeling Coupled to Laminar Flow Tubes

To stain cells, stain must be delivered to the microchamber. To accomplish this, first the fresh dye must overturn existing solution in the tubing prior to the microchamber. CSTR kinetics apply in the microchamber. To model this process, the laminar flow model described in previous models was coupled to a simple CSTR model with no reaction:

$$\left(c_{in}(t) - c_{out}(t)\right) = \tau \frac{dc_{out}}{dt} \tag{2.5}$$

where C represents the concentration of a non-reacting species, and τ is the volume of the CSTR divided by the flow rate. The solution to Equation (2.3) at the end of the tube (L_{lead}) yields the function $C_{in}(t)$. Next, Equation (2.5) is solved for C_{out}:

$$c_{out}(t) = e^{-t/\tau} \int_0^t \frac{c_{in}(t^*)}{\tau} e^{t^*/\tau} dt^* \tag{2.6}$$

Equation (2.6) can then be integrated and the concentration in the microchamber calculated as a function of time.

This model was used to simulate realistic conditions where the volume of a small plug of stain is delivered to the microchamber to attain a maximum concentration in the microchamber of 0.2% of the initial plug concentration. These values correspond to the use of Vybrant dye, a cell permeable DNA stain. The Vybrant dye is used as an example stain throughout the rest of this chapter. An absolute best case system was assumed where the tubing length from the leading edge of the plug to the microchamber was only 20 cm. The rest of model parameters are shown in Table 3-1.

Using these parameters, the functions $C_{in}(t)$ and $C_{out}(t)$ were calculated and shown in Figure 3-8A, B respectively.

Therefore, in the idealized system for the example given, a bare minimum of ~5 uL of Vybrant dye is required to bring the microchamber to a concentration approaching the manufacturer's specifications. This would lead to a cost of $3.12 per sample. Assuming a sampling rate of once every 30 minutes, this will cost ~$150 per day of automated staining at the absolute best case scenario. Any deviations from the best case scenario will lead to a geometric increase in the cost per sample. For example, using a more realistic 40 cm of tubing between the plug and the microchamber requires ~20 uL of dye per sample, increasing the cost per sample to $12.50 and the cost per day to $600.

Table 3-1: Model Parameters for the laminar flow reactor coupled to the microchamber.

Variable	Value	Units
Flow Rate	10*	mL/min
Volume of Dye	5**	uL
Length of Tube	20	cm
Temperature	300	K
Diffusion Coefficient	10^{-9}	$m^2 s^{-1}$
Tubing Diameter	0.0762	cm
Viscosity	1	cp
CSTR Volume	150	uL
τ	0.9	s

*Set to maximum value based on previous laminar flow simulations
** Value was adjusted to attain a desired maximum microchamber concentration

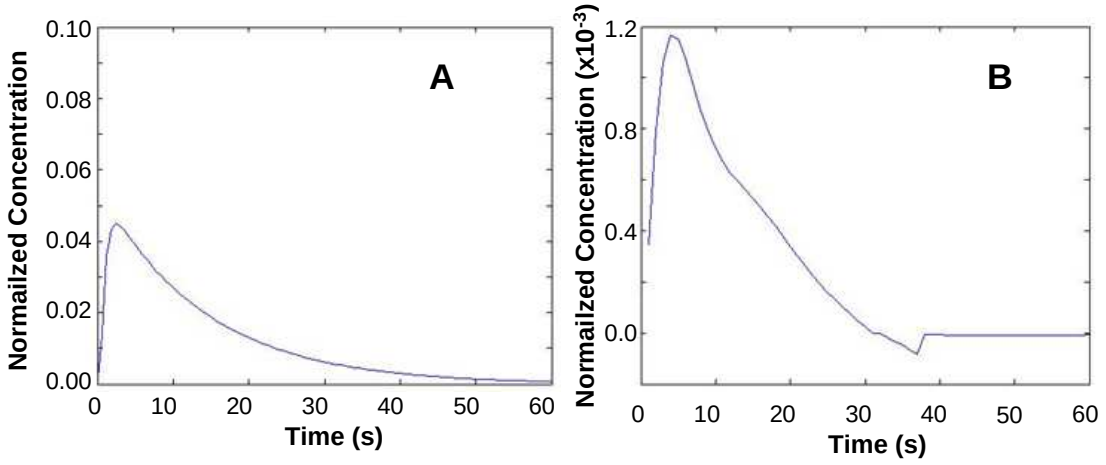

Figure 3-8: Predicted CSTR concentration when coupled to a laminar flow reactor. **(A)** $C_{in}(t)$ for the parameters given in table 3-1. **(B)** $C_{CSTR}(t)$ for the parameters given in table 3. (negative values reflect errors in the approximation of $C_{in}(t)$).

3.4 Automated System Redesigned

To use the Vybrant dye efficiently the dispersion of the dye must be minimized. There are four ways to lower the dispersion of a sample: shorter tubing lengths, plug flows, higher flow velocities, and lower temperatures. The diffusion due to laminar flow is the dominant term. Therefore, lowering the temperature of the tubing to effectively lower the diffusion coefficient will not lead to a significant decrease in the dispersion coefficient. It is not practical to increase the flow rate of the pump beyond the modeled 10 mL/min. Inducing an oscillatory flow is one method to attain plug flows in the system. However, this requires a complex system of pumps that has the potential to fail often and lead to variability in sample staining. Therefore, the one remaining option is to minimize the tubing lengths.

It is possible to achieve an effective tubing length of zero, if a syringe filled with dye is directly attached to the microchamber with no intervening tubing Figure 3-9. . In this situation, the dispersion due to the parabolic velocity profile and other diffusion effects would be effectively zero. Therefore, it would open up the possibility of using only 0.3 uL of Vybrant dye per sample, for a cost of $0.19 per sample and a total operating cost of $9 per day. This would be a 17 fold improvement over the best case scenario of using a plug of dye. Furthermore, this improvement would be applicable to other staining procedures using other more expensive dyes (BODIPY, Antibody staining, etc).

Implementing this requires an additional port on the microchamber. A dedicated syringe pump would be used to precisely add small amounts (on the order of 0.1 uL) to the cells in the microchamber. To demonstrate the accuracy of stain addition, fixed

yeast cells were loaded into the microchamber. Next, varying volumes of a concentrated PI solution were added to the cells and the mean red fluorescence of the population was measured. As Figure 3-10 shows, the cells become saturated with PI stain.

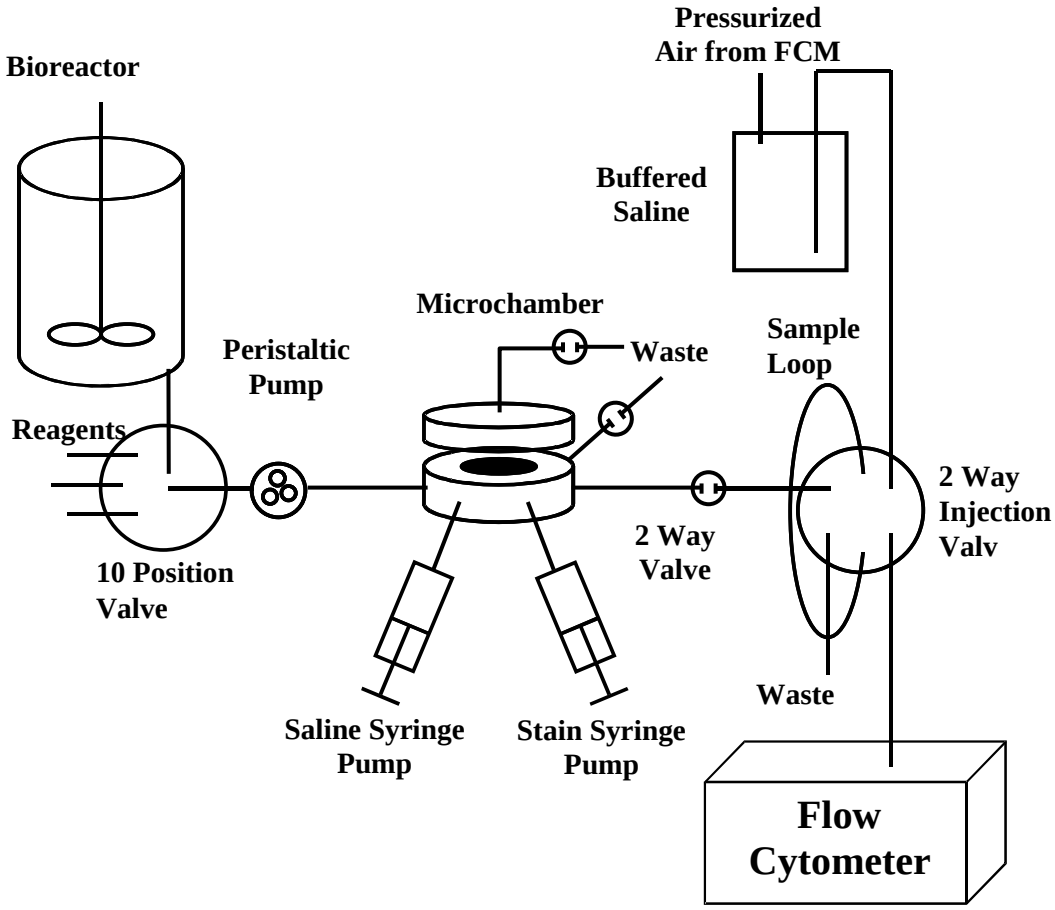

Figure 3-9: Schematic of the modified microchamber. A direct injection syringe port, a direct saline syringe pump port, and a port leading directly to waste were added to the microchamber.

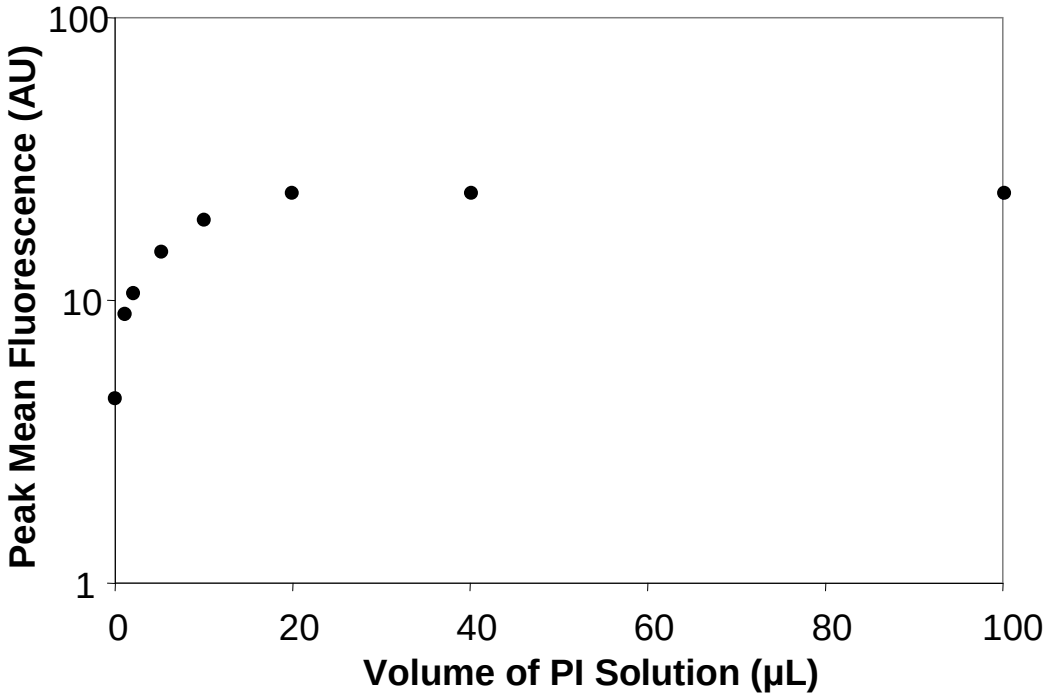

Figure 3-10: Stain syringe pump validation. Average red fluorescence measured by a Guava flow cytometer of PI stained ethanol fixed D603 yeast cells as a function of the volume of the staining solution added to the microchamber throught eh direct injection port. The PI solution was 500 µg/mL.

4 Growth Dynamics of Mammalian Cells Monitored with Automated Cell Cycle Staining and Flow Cytometry[1]

4.1 Chapter Summary

To accurately observe high frequency events during transient cell cycle kinetics we have implemented a single step 15 minute DNA staining protocol using automated flow cytometry. This protocol was used to sample and to analyze a Chinese Hamster Ovary (CHO) cell culture for the DNA distribution, viable cell concentration, apoptotic cell concentration, and light scattering properties every 25 minutes over 4.5 days in response to a nutrient deprivation and a nutrient upshift. After the nutrient deprivation and exposure to fresh growth medium two populations of cells started proliferating at different times likely corresponding to cells leaving the G0 and G1 cell cycle phases. After a nutrient upshift in late exponential growth, a cell cycle arrest occurred at the G1/S and G2/M boundary. The resulting cell cycle and proliferation kinetics followed damped oscillations that directly reveal the average time cells spend in each cell cycle phase. The observed detailed dynamics of the cell cycle progression is made possible through the high frequency sampling enabled by automated flow cytometry. The approach should be useful in studying cell cycle perturbations in response to different environmental conditions resulting from exposure to specific nutrients or to drugs.

4.2 Introduction

Determination of the cell cycle distribution is one of the most basic and most widely used applications of flow cytometry in basic biological research and in

[1] This chapter has been published in Cytometry A 2008 Jun; 73(6) pgs 538-45.

diagnostic applications. It traditionally involves cell fixation and permeabilization and cell staining with nucleic acid specific dyes, often after enzymatic removal of RNA. Variations of this methodology have been well documented in many reports, review articles and textbooks (Darzynkiewicz, et al. 2004). The cell preparation and staining steps typically involve several manual operations, and their careful execution determines the reproducibility and the quality of the cell cycle distribution that can be obtained. However, in many cases a large fraction of cells may be lost during fixation and staining steps which introduces the additional problem that the remaining cells may not be representative of the entire sample.

Traditional cell cycle staining protocols use either cell membrane permeable or impermeable dyes. Staining protocols using membrane permeable dyes are typically simple and short involving only addition of the dye to the cells. However, membrane permeable dyes often are more expensive in comparison to membrane impermeable dyes (Vybrant, DRAQ5 (Smith, et al. 1999)) or limited to a UV excitation source (Hoechst, DAPI). In contrast, membrane impermeable dyes such as PI or Acridine Orange are inexpensive and can be excited by common 488 nm light sources. Cell cycle staining protocols using membrane impermeable dyes are usually long, multistep procedures.

Time dependent changes in the cell cycle distribution of a growing cell population reflect transient growth conditions. The perturbations can be caused by changing nutritional conditions or by exposure to inhibitory substances. Transient growth conditions are also characteristic of synchronized cultures. The accuracy of the experimentally measured cell cycle kinetics is fundamentally limited by the sampling

frequency from the culture. This fundamental limitation stems from the Nyquist-Shannon sampling theorem (Jerri 1977) which states that, at best, one can only make accurate statements about a process that occur at a frequency half the sampling frequency. Thus, to observe the cell cycle kinetics with maximum detail, one must sample as frequently as experimentally feasible.

Since flow cytometry has traditionally been an offline technique, samples have to be manually taken and then subjected to the staining operations. Thus, frequent sampling involves significant labor. Also, if cell staining is performed manually, the chance for error can be significant. To overcome these problems, we have previously developed automated flow cytometry (Abu-Absi, et al. 2003 ; Zhao R, et al. 1999b) that can automatically sample and stain cells online. Its utility has been demonstrated in initial examples involving the monitoring of microbial (Kacmar, et al. 2004b ; Kacmar, et al. 2006) and mammalian cell cultures (Kacmar and Srienc 2005 ; Sitton, et al. 2006)

We demonstrate here that this approach can also be applied for automated cell cycle staining that affords the detailed evaluation of the cell cycle kinetics of growing cultures based on frequent sampling. To implement an online cell cycle stain, we first shortened the length of a traditional PI staining protocol to a single 15 minute step. This modified protocol was then implemented with the automated flow cytometry device and used to monitor the cell cycle kinetics of a CHO culture using 10 min sampling intervals over 4.5 days. During that time, the culture was subjected to recovery from nutrient deprivation and a nutrient upshift. The observed kinetics directly reveal the cell cycle and proliferation kinetics of the culture during both transient and balanced growth. Knowledge of the kinetics can be useful for instance in

elucidating the effects of nutrients and drugs on the underlying mechanisms governing cell cycle progression.

4.3 Results

4.3.1 Staining Procedure Development

Digitonin was previously shown to permeabilize the membrane to PI and RNase (Pestov, et al. 1999). Unlike organic solvents, digitonin does not reduce the activity of RNase, and completely permeabilizes CHO cells to RNase and PI in under a minute (data not shown). Thus, digitonin can be combined in a single solution with PI and RNase yielding the basis for a true one step staining procedure (Tao, et al. 2004). The total length of the staining protocol is then reduced to the time required to completely digest the RNA. To determine the minimum length of the RNA digestion step, 10^6 CHO cells were exposed at room temperature to 1 mL of a saturated digitonin, 30 μg/mL PI, and 80 μg/mL RNase solution. PI and RNase concentrations were similar to previously published protocols (Crissman and Steinkamp 1982 ; Pestov, et al. 1999). This preparation was then incubated at room temperature and periodically sampled and analyzed with a flow cytometer. As shown in Figure 4-1, the RNA was completely digested by nine minutes as shown by the mean and CV of the G1 peak approaching a constant value as seen in similar protocol optimization studies (Crissman, et al. 1976). This time can be likely further shortened by raising the temperature or increasing the RNase concentration. As seen in Figure 4-2A, the stained cells produce a DNA distribution where the fraction of cells in each phase of the cell cycle is readily identified.

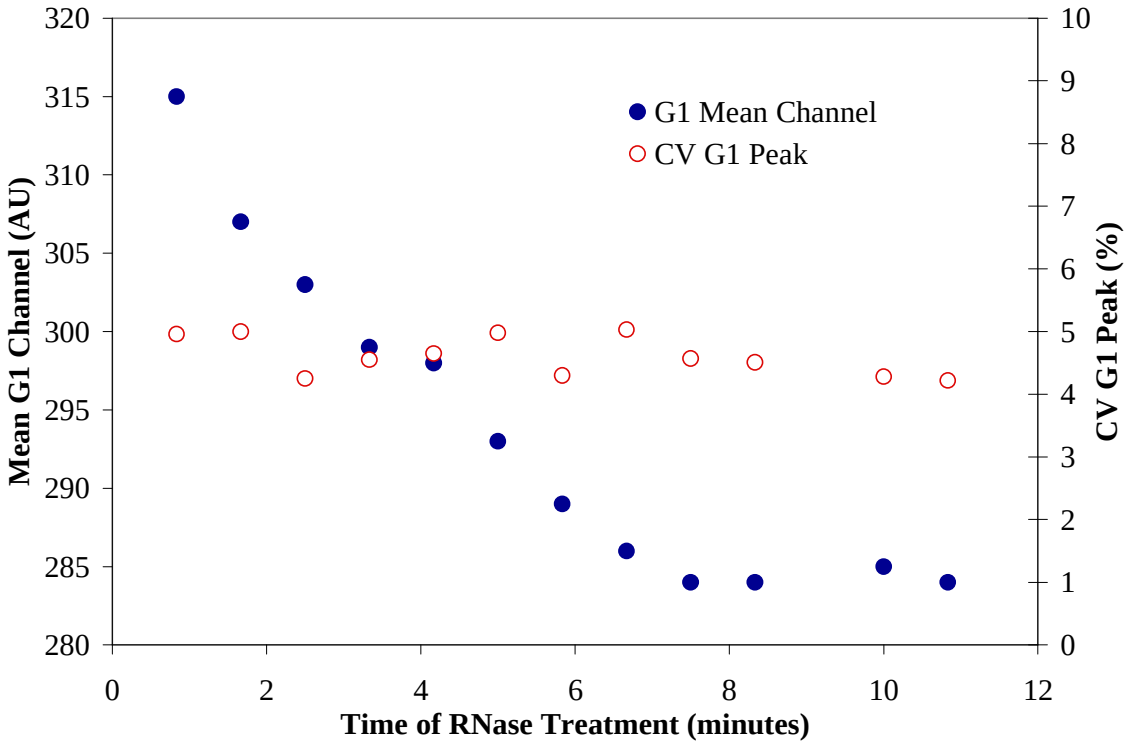

Figure 4-1: Kinetics of the RNase digestion. The online staining treatment used 80 ug/mL of RNase at room temperature. The reaction appears to go to completion at 9 minutes, which is a similar result shown in literature. (Crissman and Steinkamp 1982)

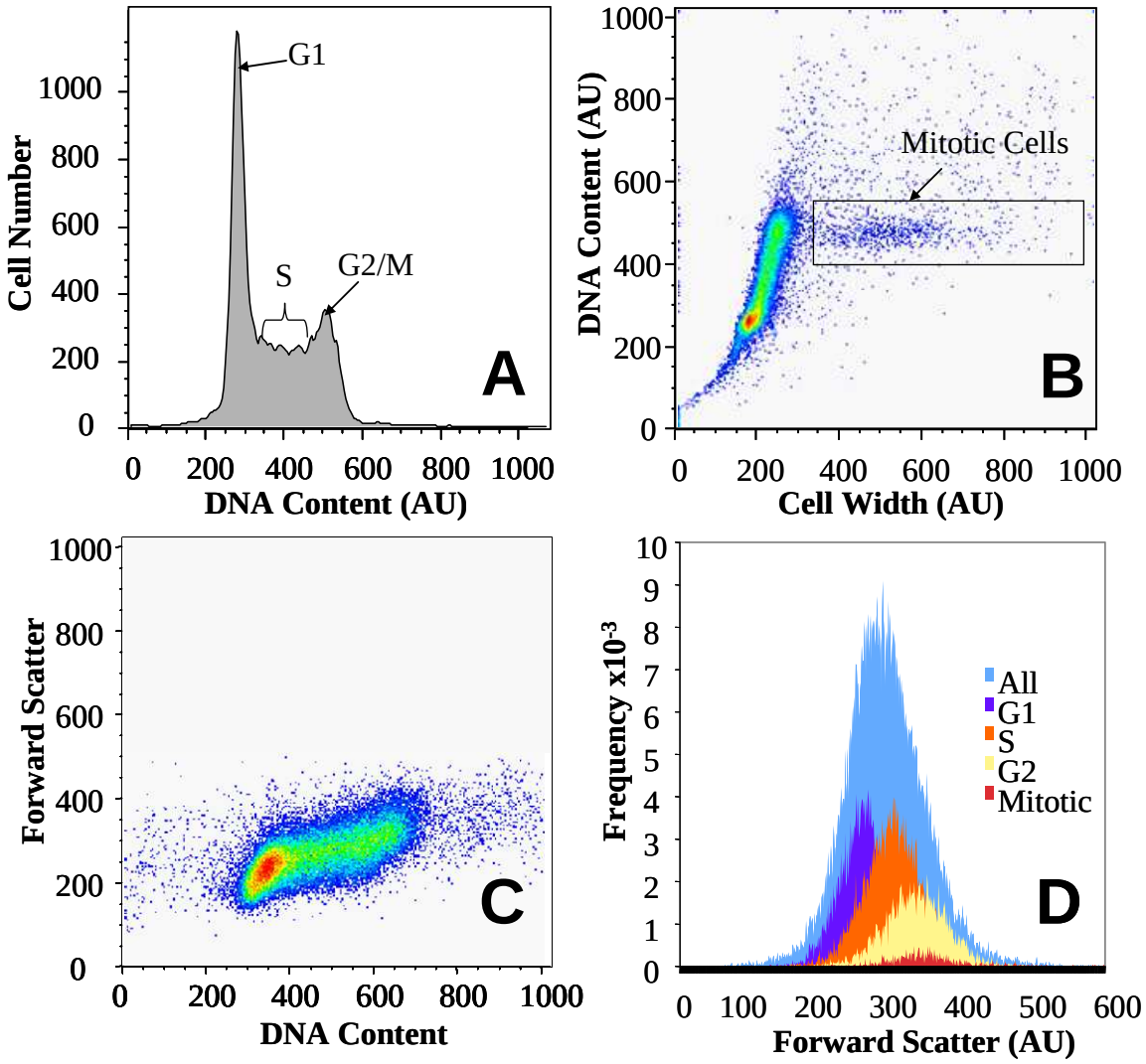

Figure 4-2: Online DNA stain distribution and FSC data. Histogram showing an example online cell cycle distribution **(A)**, cytogram depicting the isolation of mitotic cells **(B)**, the forward scatter versus DNA content cytogram **(C)**, and the histogram of the forward scatter distributions of individual cell cycle phases at an example time point during the culture **(D)**. Mitotic cells are defined as having twice the cell width and two copies of DNA as compared to a G1 cell.

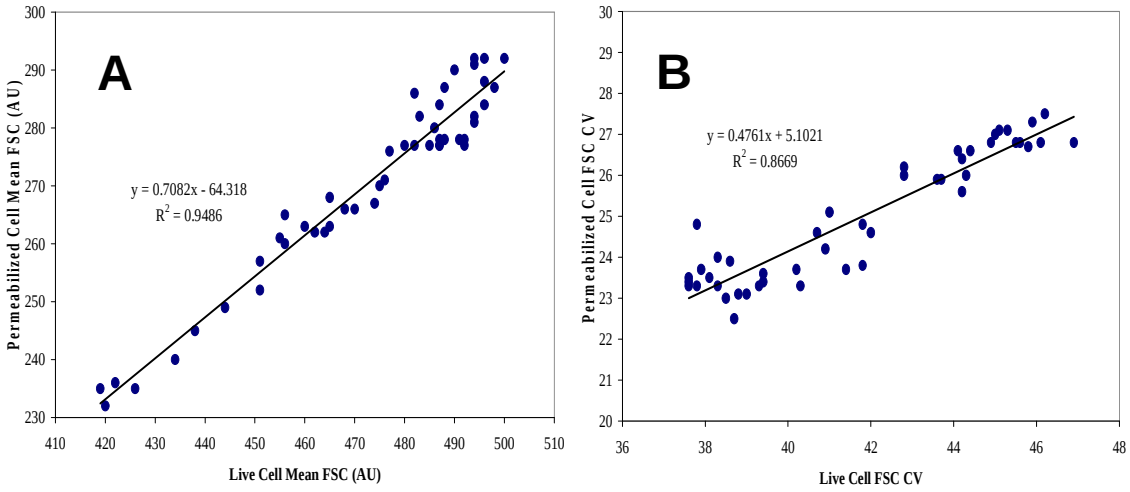

Figure 4-3: Relationship of light scatter between live and fixed CHO cells. Mean **(A)** and CV **(B)** of the viable, FSC distribution before the cell cycle staining protocol versus the mean of the FSC distribution after treatment (N=45 samples). The linear relationships indicate that cell morphology is maintained by the cell cycle staining protocol.

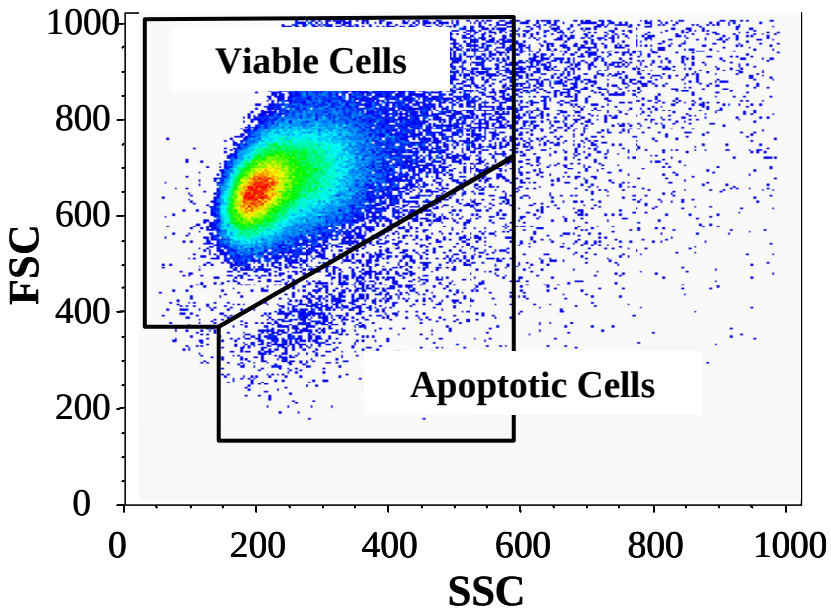

Figure 4-4: Identification of dead CHO cells. FSC versus SSC dot plot for a sample point during bioreactor operation. Apoptotic cells are defined as having decreased FSC and increased SSC as previously described.

4.3.2 Mitotic Cell Identification

Unlike organic solvents, digitonin does not induce aggregation of cells at room temperature. Thus, single cell morphology is preserved throughout the permeabilization and staining steps as shown in Figure 4-3A and Figure 4-3B, where the FSC mean and CV of the permeabilized versus viable populations are shown to be correlated for 45 samples of CHO cells at differing FSC values. Mitotic cells can be identified through their characteristic cellular DNA distribution that can be detected by comparing the width of the stained DNA signal versus the area of the signal as shown in Figure 4-2B. This type of analysis is especially applicable to suspension adapted CHO-S cells acquired with a low event rate. Microscopic examinations of CHO-S cells show that less than 0.5% of the cells are in clumps of three or more cells. Thus, the observed doublets reflect the mitotic population. A similar approach of differentiating mitotic cells based on morphology has been used for yeast (Block, et al. 1990 ; Frykman and Srienc 2001 ; Zilmer, et al. 1995) and mammalian cells (Boschman, et al. 1991 ; Kromenaker and Srienc 1991 ; Kromenaker and Srienc 1994a ; Kromenaker and Srienc 1994b ; Nusse, et al. 1990 ; Zilmer, et al. 1995). From these data, the fraction of cells in each cell cycle phase can be readily identified, as well as a measure of the cell size (FSC) as a function of cell cycle position (Figure 4-2C-D).

4.3.3 Batch Set-Up and Monitoring

The online cell cycle staining protocol was tested on a CHO culture that was grown in a bioreactor initially containing 1-L of fresh medium, and inoculated at time zero with a culture in late exponential phase. The bioreactor was then monitored by

alternately taking two samples from the bioreactor with the automated flow cytometer. The first sample was stained online for the cell cycle dynamics of the culture using the staining protocol as described. The second sample was directly acquired by the cytometer without any staining yielding data on the total cell concentration, the viable and non-viable cell fractions, and cell size evaluated based on light scattering properties. As a general feature of cell death through either necrosis or apoptosis cells change their morphology by decreasing in size and changing their internal structure. These morphological changes are detectable by measuring the change in light scatter using flow cytometry (Vermes, et al. 2000). Thus, non-viable cells can be differentiated from viable cells based on their differing forward (FSC) and side (SSC) light scattering characteristics (Vermes, et al. 2000) (Figure 4-1). This strategy for differentiating between viable and non-viable cells has been applied across many different mammalian cell lines (Darzynkiewicz, et al. 1992 ; Darzynkiewicz, et al. 1999 ; Fraker, et al. 1995) including CHO cells (Fieder, et al. 2005). It is assumed in well controlled batch cultures like these that apoptotic cells are the primary components of the non-viable cells (al-Rubeai and Singh 1998 ; Franek 1995).

Each respective sample was taken and analyzed every 25 minutes with eight minutes between the cell cycle staining and live cell analysis.

Over the course of the culture, offline samples were taken every 8-15 hours, and fixed with ice-cold 70% ethanol. At the conclusion of the online experiment the offline samples were manually stained with PI and analyzed on the cytometer as described in standard protocols (Crissman and Steinkamp 1982). As shown in Figure 4-5, there is excellent agreement between the offline and online samples.

4.4 Recovery from Nutrient Deprivation

Since the inoculation culture was in late exponential phase, the culture started growing with a large fraction of cells in G1 with a viable fraction of 96 % (Figure 4-6A,D). The cells initially appeared starved due to nutrient deprivation, since the initial mean cell size in each phase of the cell cycle was lower than the mean cell size during subsequent exponential growth (Figure 4-6C). During the first six hours, until arrow (a), the cells adjusted to the fresh medium by increasing their mean cell size across all phases of the cell cycle (Figure 4-6C). During this time, cells that were already committed to division completed the cell cycle as seen by an increase in the G1 fraction, a corresponding decrease in the S and G2 fractions, and an increase in the cell concentration (Figure 4-6A-B). From hours 0-6, the culture proliferated with a doubling time of 21 hours as shown in Figure 8. Once the cells were sufficiently recovered a large fraction of G1 cells entered S phase as seen by a decrease in the G1 fraction and a corresponding increase in the S fraction (arrow (a), Figure 4-6A-B). During this time, the entire culture ceased proliferating as shown in Figure 4-8, hours 6-15, indicating little to no cells were in the G2/M phase of the cell cycle as confirmed by Figure 4-6A.

Thus, the culture was partially synchronized. A partially synchronized cell population contains homogeneous cell cohorts that behave like a single cell. The cell cycle progression of these cohorts causes individual cell cycle fractions to oscillate. For instance, a cell cycle fraction will start increasing from a minimum value when a homogeneous cell cohort arrives and its front starts entering the specific cell cycle phase. The cell cycle fraction then reaches a maximum value when the entire cohort is in the cell cycle phase and this value starts decreasing again when the front of the cohort

starts exiting the specific cell cycle phase. Thus, the time between the occurrences of the minimum and the maximum cell cycle fraction indicates the average time it takes for a cohort to traverse the cell cycle phase. Thus, by observing when the subsequent minima and maxima of the G1, S, G2, and M fractions occurred due to the synchronized cohort, one can directly measure the lengths of the individual cell cycle phases in a culture of many cells.

For instance, the time from the S phase fraction minimum (hour 6, arrow (a)) to the S phase fraction maximum (hour 12, arrow (b)) indicates that it took six hours for the cohort to complete S phase. Alternately, the time between the G2 minimum (hour 12, arrow (b)) and the G2 maximum (hour 15, arrow (c)) indicate that it took three hours to complete the G2 phase. At this time (hour 15, arrow (c)), the M phase maximum appears to occur at the same time as the G2 maximum. This occurs because the sampling rate from the process is insufficient to properly differentiate the M phase in relation to the other cell cycle phases. The mitotic fraction correlates with the changes in the specific growth rate as shown in Figure 4-6C as previously described (Abu-Absi and Srienc 2002).

At hour 15 (arrow (c)), the cell concentration started to increase indicating that the synchronized cells have completed their passage through the cell cycle. At this time, the onset of apoptosis appears to occur as seen by an increase in the absolute apoptotic cell concentration (Figure 4-6D, arrow (c)). From hour 15 to 19 (arrows (c-d)), the fraction of cells in G1 phase begin to increase until hour 19 when the fraction of cells in G1 begin to decrease; indicating that the cells that have just reentered G1 at hour 15 (arrow (c)) have completed G1 and entered S phase. This implies that for these

cells, the length of G1 phase is 4 hours. Thus, the total length of the cell cycle and the expected average doubling time of the culture is 13 hours. However, immediately after the G1 peak maximum, the measured doubling time of the entire culture increased to 46 hours until balanced growth was reached at hour 34 (Figure 4-6A, arrow (e); Figure 4-8). The discrepancy between the synchronized cohort's average cycle time and the observed doubling time of the entire culture is likely explained by a fraction of cells that are not participating in the cell cycle and remain in the G0 phase of the cell cycle.

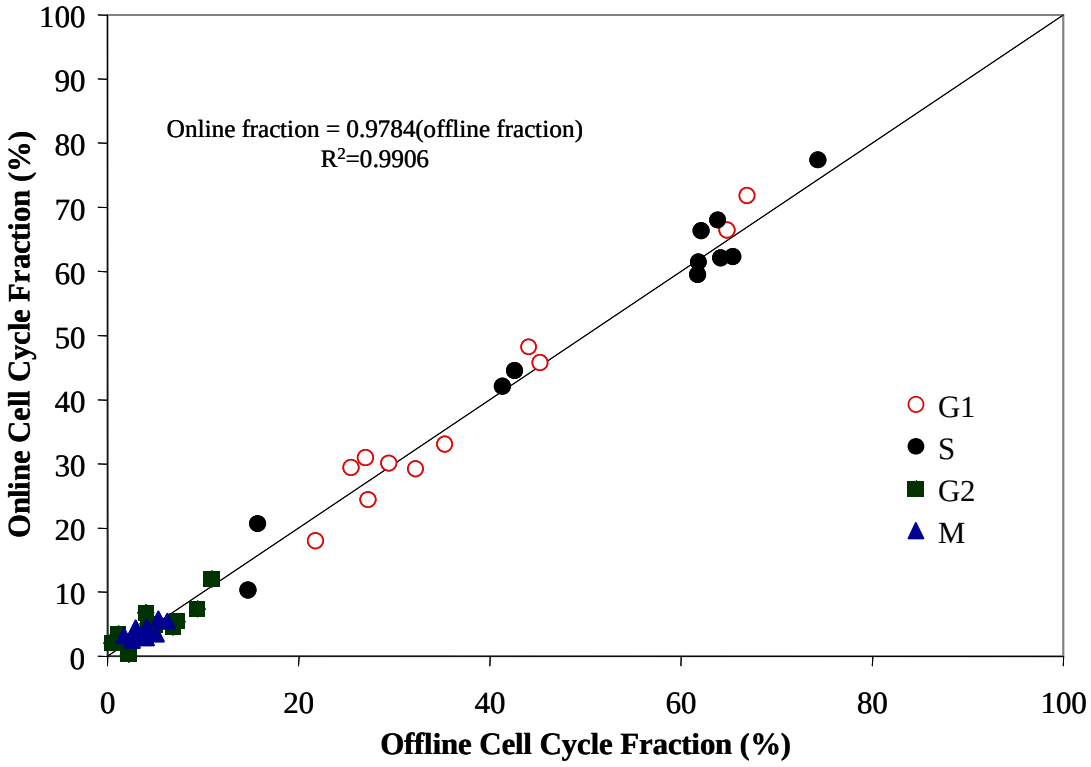

Figure 4-5: Correlation between online and offline cell cycle fractions. Cell cycle fractions were assessed with the developed cell cycle staining technique (N=11). Fractions were computed using Multicycle.

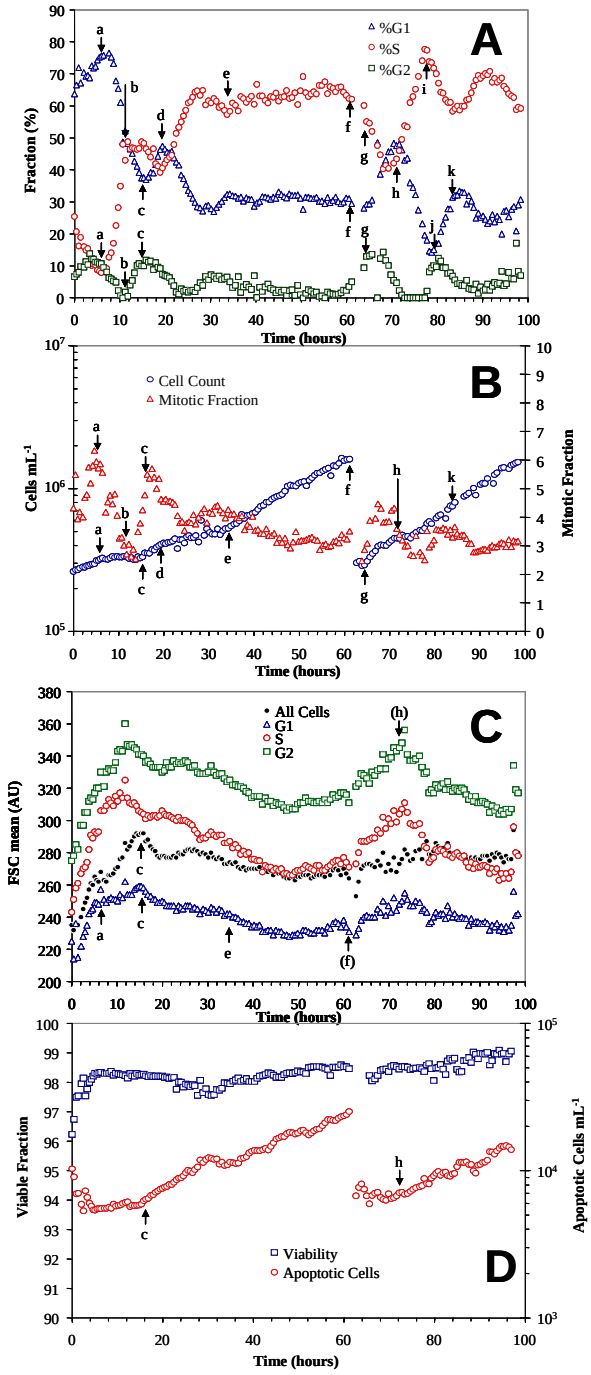

Figure 4-6: Time series cell cycle fraction and growth kinetics. **(A)** Cell cycle fractions as a function of time using the automated staining apparatus and developed staining protocol. **(B)** Cell number concentration as a function of time. The culture was passaged at hour 61. The mitotic fraction as determined in Figure 7 as a function of time is also shown. **(C)** Mean cell size as a function of time for each cell cycle fraction. Arrows correpsond to events described in the results section. **(D)** The viable cell fraction and the apoptotic cell concentration as a function of time.

4.5 Balanced Growth

The oscillations induced by the recovery from nutrient deprivation are damped, and the culture reaches balanced growth at hour 34 (arrow (e)) characterized by time independent forward scatter and DNA distributions. During the balanced growth phase, the culture proliferated at a doubling time of 14 hours (Figure 4-8), which is near the expected proliferation rate as determined by the minima and maxima of the cell cycle fractions. Balanced growth continued until the fed-batch addition at hour 62, arrow (f). By measuring the dividing population of cells during balanced growth, the single cell growth rates can be extracted from the distribution data using the integrated version of the population balance equation (Collins and Richmond 1962 ; Srienc 1999). The single cell rates of growth are a measure of how quickly a single cell is increasing its size as a function of its current state. In this study, the single cell rate of growth is calculated using the forward scatter distribution of each phase of the cell cycle in conjunction with the equations previously described (Kromenaker and Srienc 1991 ; Kromenaker and Srienc 1994a ; Kromenaker and Srienc 1994b). The mitotic population is assumed to be the dividing population. It is also assumed that the cells divide symmetrically. The resulting rates of growth are shown in Figure 4-7. These curves are qualitatively similar to previous results for the single cell rates of production of antibodies in hybridomas cells (Kromenaker and Srienc 1991 ; Kromenaker and Srienc 1994a ; Kromenaker and Srienc 1994b).

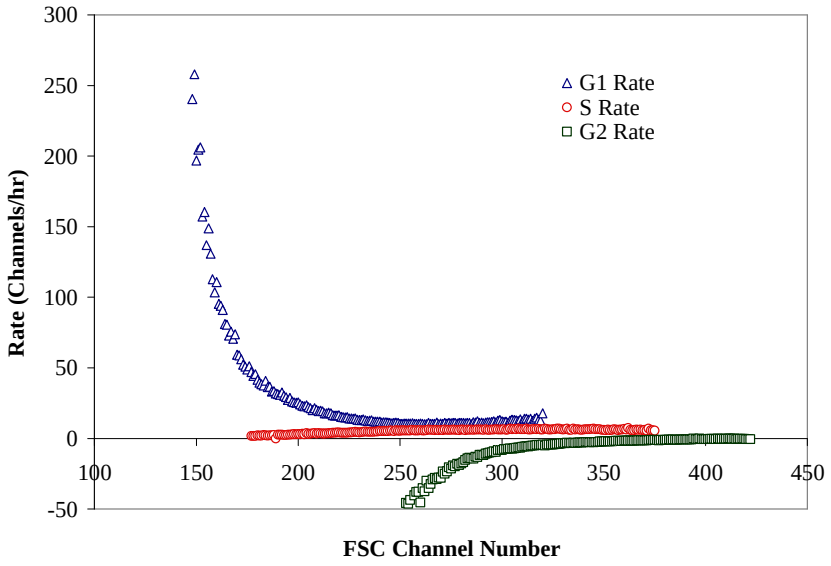

Figure 4-7: Single cell rates of growth in terms of forward scatter units. Data is calculated using the Collins-Richmond approach (Collins and Richmond 1962) using the mitotic fraction as the dividing population and the assumption of symmetric division. The data is qualitatively similar to data obtained by the same method for antibody production rates for each phase of the cell cycle (Kromenaker and Srienc 1991; Kromenaker and Srienc 1994b).

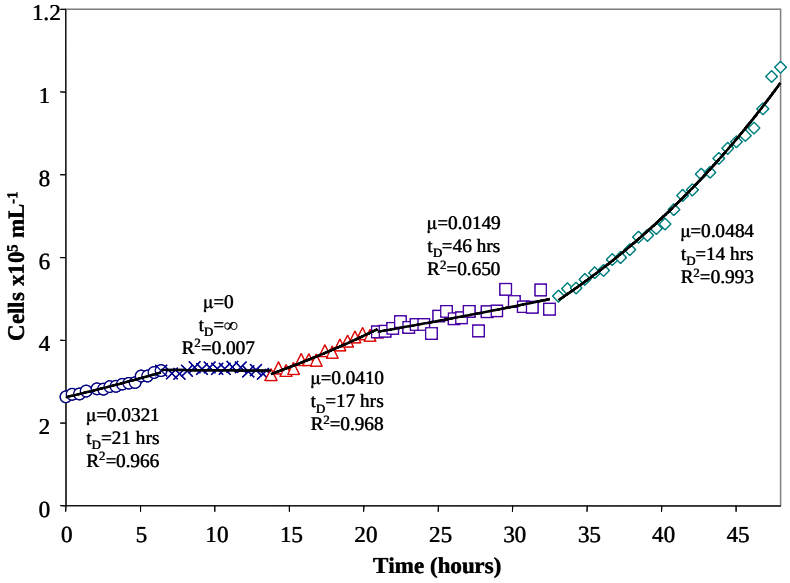

Figure 4-8: Proliferation rates of the culture during recovery from nutrient deprivation. The growth curve is broken into segments defined by the discontinuities. Proliferation rate μ, doubling time t_D, and the R^2 values for each segment are given.

4.6 Nutrient Upshift

At hour 62 (arrow (f)) the culture was diluted in a 1:10 ratio with fresh pre-warmed medium. Subsequently, for two hours, the culture was temporarily arrested as the cell number did not increase (Figure 4-6, arrows (f-g)). The arrest appears to have occurred both at the G1/S restriction point and the G2/M control point. The G1/S arrest is evidenced by a decrease in the S phase fraction while the G1 fraction remained constant. The G2/M arrest is evidenced by an increase in the G2 fraction and the cell number ceasing to increase. When the arrest ended after two hours, cell proliferation resumed at a temporarily decreased doubling time of 8 hours. The temporarily increased proliferation rate initiated a partial synchrony of the culture. Similar to previous arguments, the average time cells spend in individual cell cycle phases are directly revealed by tracking of the subsequent oscillation amplitudes of the G1, S, G2, and M fractions.

The time between subsequent S phase minimum (hour 71, arrow (h)) and maximum (hour 77, arrow (i)) indicates that it took six hours for the partially synchronized cells to complete S phase. Alternately, the time between the G2 phase minimum (hour 77, arrow (i)) and the G2 maximum (hour 80, arrow (j)) indicates that it took three hours to complete G2/M phase. At hour 80, arrow (j), the fraction of cells in G1 phase began to increase until hour 84, arrow (k) when the fraction of cells in G1 begins to decrease. Thus, the length of G1 phase is 4 hours and, the total length of the cell cycle and the expected average doubling time of the culture is 13 hours, as observed during the recovery from nutrient deprivation. During the course of the synchrony

induced by the nutrient upshift, it appears that the onset of apoptosis is correlated with the maximum in the G1 fraction at hour 71, arrow (h).

4.7 Discussion

The use of digitonin as a permeabilization reagent offers many advantages over traditional organic solvents. First, using digitonin in traditional PI staining protocols reduces the protocol to a single step (Tao, et al. 2004) which eliminates the risk of losing a large fraction of cells during separate washing, fixation, and staining steps. This guarantees that the remaining sample is representative of the entire sample. Second, as this study shows, digitonin can reduce the total staining protocol to less than 10 minutes which is important in a high frequency, real time analysis. Fourth, the general strategy of using digitonin to rapidly permeablize cells can potentially be applied to other stains or fluorescently labeled antibodies to quantify intracellular targets (Lazarus, et al. 1998 ; Schmid, et al. 2000a ; Schmid, et al. 2000b).

The developed staining protocol offers a unique way to study the cell cycle kinetics of a culture. Traditionally, individual growth perturbed cells are analyzed with time-lapsed video microscopy (Boonstra 2007) or representative samples of a culture are analyzed with flow cytometry (Murray and Hunt 1993). While time lapse video microscopy tracks individual cells over time at a very high frequency, the number of cells examined is relatively low. On the other hand, flow cytometry analyzes large numbers of cells such that infrequent events can be observed. However, since cytometry is traditionally an offline technique, the cell cycle distribution is infrequently measured leading to an incomplete picture of the time course data. Using automated flow cytometry and the developed staining protocol, the cell cycle distribution of large

numbers of cells can then be frequently determined and the kinetics can be used to help determine the mechanisms underlying cell cycle progression.

The automated flow cytometry approach yields useful kinetic information during transient and balanced growth situations. During transient growth, the relative minima and maxima of the oscillations of the G1, S, and G2 fractions directly reveal the average time cells spent in each cell cycle phases. Using this analysis, our experiments indicated that the expected doubling time is 13 hours. However, this value corresponds to a faster proliferation rate than indicated by the measured cell concentration increase (Figure 8). This is likely due to cells that have exited from the cell cycle and are temporarily in the G0 state of the cell cycle and not participating in proliferation (Boonstra 2003 ; Boonstra and Moes 2005 ; Boonstra 2007). Use of staining protocols that can separate G0 from G1 cells using stains such as acridine orange (Darzynkiewicz, et al. 1980a ; Darzynkiewicz, et al. 1980b), fluorescent antibodies such as Ki-67 (Gerdes, et al. 1983), or staining for specific cyclins (Darzynkiewicz, et al. 1996) would be useful in fully elucidating the G0 and G1 kinetics.

The observed cell cycle oscillations after the nutrient upshift and the recovery from nutrient deprivation are both caused by a temporary cell cycle arrest. After the nutrient upshift, the cell cycle was arrested at both the G1/S and G2/M boundary. This is likely due to the increased nutrient concentration increasing the cell size threshold for both the G1/S and G2/M checkpoints (Jorgensen and Tyers 2004). This is seen in Figure 4-6C arrow (h) where the mean cell size for each cell fraction increases after the nutrient addition. A similar effect is seen during the recovery from nutrient deprivation.

There appears to be differences in how the two cultures coordinated cell death with the cell cycle. During the recovery from nutrient deprivation an increase in the apoptotic cell concentration, termed the onset of apoptosis, is correlated with the beginning of cell proliferation (Figure 4-6D arrows (c) and (h)). During the nutrient upshift, the onset of apoptosis is correlated with cells transitioning from G1 to S. Across either treatment, the onset of apoptosis is correlated with an increase in the mean cell size of the population. These events highlight the advantage of using automated flow cytometry to analyze large numbers of cells frequently, as the increase in the apoptotic cell concentration represents only 2% of the newborn cells.

During balanced growth conditions, automated flow cytometry in conjunction with the Collins-Richmond approach (Collins and Richmond 1962) can be used to determine single cell rates of generation or destruction of some aspect of cell physiology (Srienc 1999). In this study, the single cell rate of growth was calculated using the forward scatter distribution of each phase of the cell cycle in conjunction with the equations in (Kromenaker and Srienc 1991 ; Kromenaker and Srienc 1994a ; Kromenaker and Srienc 1994b). Forward scatter was forced to be a conserved quantity by assuming symmetric division of the mitotic population. While it is unclear that forward scatter is a conserved quantity during cell division, the described approach can be applied to many other conserved, fluorescently labeled aspects of cell physiology such as total protein or cyclin content.

4.8 Conclusion

The high frequency assessment of the cell cycle kinetics should be useful in studying cell cycle perturbations in response to different environmental conditions

resulting from exposure to specific nutrients or to drugs. Knowledge of the kinetics can be useful for instance in elucidating the effects of nutrients and drugs on the underlying mechanisms governing cell cycle progression. This can then be practically applied to optimize medium and for investigating how culture variability affects culture productivity.

5 Transient Gene Expression in CHO Cells Monitored with Automated Flow Cytometry[2]

5.1 Chapter Summary

Transient gene expression is frequently used in industry to rapidly generate usable quantities of a protein from cultured cells. In gene therapy applications it is used to express a therapeutic protein *in vivo*. A quantitative assessment of the expression kinetics is important because it enables optimization and control of culture conditions for higher productivity. Previous experimental studies show a characteristic peak in average protein expression per cell after transfection followed by an exponential decrease of the expressed protein. Here, we show that the exponential decrease in single cell expression of enhanced Green Fluorescent Protein (eGfp) occurs in discrete steps. We attribute this to the absence of plasmid replication and to symmetric partitioning of plasmid and eGfp between dividing cells. This is reflected in the total eGfp in the bioreactor, which increased at a constant rate throughout the experiment. Additionally, the data provide a detailed time course of cell physiology during recovery from electroporation. The time course of cell physiology precisely indicates when the culture shifts growth phases. Furthermore, the data indicate two unique stationary phases. One type of stationary phase occurs when proliferation ceases while cells decrease their cell size, maintain granularity, and mean eGfp content decreases. The second type occurs when proliferation ceases while cells increase their cell size, increase granularity, and surprisingly maintain eGfp content. The collected data

[2] This chapter has been published in Cytotechnology. 2006 Sep 52(1):13-24.

demonstrate the utility of automated flow cytometry for unique bioreactor monitoring and control capabilities in accordance with the US Food and Drug Administration's Process Analytical Technology initiative.

5.2 Introduction

A significant problem in mammalian cell culture is the direct assessment of the concentration and composition of the biomass. It is well recognized that considerable single-cell variability exists in a cell culture and that this heterogeneity affects culture performance. Such culture variability is also likely to a large extent responsible for variations that are observed in the final product obtained. Therefore, new and improved measuring methods, able to detect the single-cell variability, could considerably enhance the monitoring and control of manufacturing processes ultimately resulting in better quality products. The Food and Drug Administration has recently recognized the practical value of this approach by establishing the Process Analytical Technology (PAT) initiative aiming at more reliable products on the basis of better control and understanding of biological-pharmaceutical manufacturing processes.

The monitoring and control of a cell cultivation process is generally limited by the data that can be collected. Typically, measured online culture process variables only characterize bulk properties (i.e. OD, OUR, DO_2, pH, etc) while offline measurements such as cell counts, viability, etc are assessed relatively infrequently. Furthermore, most of these measurements cannot determine the inherently heterogeneous nature of a culture. Culture heterogeneity is caused by factors such as the cell cycle, incomplete mixing, genetic variation, and stochastic events. Therefore, it is of considerable interest to detect this heterogeneity, to monitor it online, and

ultimately to control it with appropriate process conditions. To accomplish this, we developed an automated flow cytometry system (Abu-Absi, et al. 2003) that has already been shown to be useful for a variety of applications including monitoring of microbial (Kacmar, et al. 2004b) and mammalian cell cultures (Kacmar and Srienc 2005). Automated flow cytometry can provide online cell number and viability, with the ability to discriminate sub-populations even if they are present as a small fraction of the total cell population. It represents a general methodology that can provide information on virtually any characteristics of the sub-populations for which a flow cytometry stain exists.

Cell heterogeneity is expected to significantly affect the transient gene expression characteristics of a culture. However, it has been little studied likely due to the limited methods that are available. Reported transient gene expression studies focus on either the population averaged properties of the culture over time, or on the optimization of bulk culture variables (Derouazi, et al. 2004). Few studies address the issue of culture heterogeneity during transient gene expression ((Keith, et al. 2000). In addition to the inherent sources of heterogeneity in a culture undergoing transient gene expression, there is also heterogeneity induced by the specific transfection procedure. There are several protocols used to transfect mammalian cells; of these electroporation is a common non-viral technique (Cegovnik and Novakovic 2004). The efficiency and the effects of electroporation are expected to greatly depend on the initial physiological state of the cells. Here, we use automated flow cytometry to compare and to contrast the physiological response after electroporation of a culture in stationary phase to a culture in exponential phase. The results offer a detailed insight into the population

dynamics during transient gene expression. Furthermore, it is a further demonstration of automated flow cytometry as a tool to obtain detailed population data that directly comply with the goals of the PAT initiative.

5.3 Process Model

5.3.1 Cell Proliferation Model

Apoptosis, proliferation, and the transition of non-fluorescent to fluorescent cells due to plasmid expression can preferentially affect the fluorescent and non-fluorescent sub-populations of the viable cell population. Equations (4.1) and (4.2) describe these dynamics:

$$\frac{dF}{dt} = (\mu_F - k_{d,F})F + k_T N = \mu_F^* F + k_T N \tag{4.1}$$

$$\frac{dF}{dt} = (\mu_N - k_{d,N})F - k_T N = \mu_F^* F - k_T N \tag{4.2}$$

where F is the fluorescent cell number, N is the non-fluorescent cell number, μ_F and μ_N are the proliferation rates of the fluorescent and non-fluorescent sub-populations respectively, $k_{d,F}$ and $k_{d,N}$ are the cell death rates of the fluorescent and non-fluorescent sub-populations respectively, and k_T is the transition rate between the fluorescent and non-fluorescent cells. The terms (μ_F - $k_{d,F}$) *and* (μ_N - $k_{d,N}$) can be combined to yield an effective growth rate μ_F^* and μ_N^* respectively.

5.3.2 eGfp Production Model

The average single-cell eGfp content is obtained by taking the first moment of the distribution of eGfp content of transfected cells:

$$\bar{x} = \int_{TT}^{\infty} xf(x)\,dx \tag{4.3}$$

where $\bar{x}$ is the average single cell eGfp content, the transfection threshold (TT) is the level of green fluorescence slightly above the auto-fluorescence of non-transfected CHO cells, x is the eGfp content, and f(x) is the distribution of eGfp content. Since eGfp is an intracellular protein, multiplication of the fluorescent cell number in the bioreactor with the average single cell fluorescence results in the total eGfp content in the culture at each time point:

$$X(t) = \bar{x}(t)\,N(t) = \bar{x}(t)\,N_0 \exp(\mu t) \tag{4.4}$$

where X(t) is the total eGfp content, N(t) is the fluorescent cell number, N_0 is the initial transfected cell number, and μ is the growth rate of the culture.

As observed in this study, the total eGfp content increases linearly (Figure 5-5). It is assumed that the rate of increase of the total eGfp content is proportional to the initial plasmid copy number in the initially transfected population. Therefore, the rate of eGfp production is subsequently proportional to the initial number of transfected cells:

$$X(t) = k_1 P_0 t = k N_0 t \tag{4.5}$$

where k and k_1 are proportionality constants, P_0 is the initial plasmid copy number, and N_0 the initially transfected cell number.

Substituting Equation (4.5) into Equation(4.4), solving for $\bar{x}(t)$ and taking the natural log of both sides yields:

$$\ln\left(\bar{x}(t)\right) = \ln(k) + \ln(t) - \mu t \tag{4.6}$$

which describes the time course of the mean single cell eGfp content during the expression experiment.

5.4 Results

5.4.1 Proliferation Characteristics

The detailed single-cell data from frequent sampling reveal significant differences depending on culture history and culture conditions. The transient gene expression characteristics of a culture started from an exponential inoculum (culture E) was compared to a culture started from an inoculum in stationary growth phase for at least 12 hours (culture S). Each inoculum was divided into six 45 mL aliquots and centrifuged. The resulting cell pellets were independently re-suspended in medium containing plasmid, and at time zero, each of the aliquots was electroporated as described in the methods section. The fraction of viable cells of the cultures immediately before electroporation was 95% and 92% for cultures E and S respectively. The electroporated aliquots were then recombined, and used to inoculate a bioreactor that was monitored by automated flow cytometry.

With automated flow cytometry, the time course of apoptotic cells can be differentiated from viable cells based on their differing forward (FSC) and side (SSC) light scattering characteristics (Figure 5-1) (Fraker, et al. 1995). The frequent sampling provided by automated flow cytometry yields a detailed time course of the total cell count and the population fractions of apoptotic and viable cell populations (Figure 5-2A, B, C). Due to the high sampling frequency, the interconnected dynamics of the viable and apoptotic sub-populations can be precisely determined. On the basis of these

data one can clearly differentiate between different growth phases of the culture. Lag phase is defined by an initially decreasing or constant total cell count (arrow a Figure 5-2-A2). Lag phase ends when the culture transitions to the proliferation phase, distinguished by an increase in the viable cell number (arrow a Figure 5-2-A2). Proliferation ends when the culture transitions to stationary phase, distinguished by a constant viable cell number (arrows b, c Figure 5-2-A1, 2-A2). Subsequently, stationary phase ends when the culture transitions to the death phase distinguished by a decrease in the viable cell number (arrow d, Figure 5-2-B1).

The culture electroporated in an exponentially proliferating state (culture E) initially showed a lag phase, as evidenced by decreases in the total and viable cell counts and by an increase in the apoptotic cell count resulting in a decrease in the viable cell fraction until approximately 18 hours (arrow a, Figure 5-2-A, 2-B, 2-C, 2-D). At this time, the culture started proliferating, and continued increasing in cell number until stationary phase was reached at hour 125 (arrow b, Figure 5-2-A, 2-B, 2-C, 2-D). Interestingly, in culture E, the onset of apoptosis, as indicated by a significant increase in apoptotic cells, preceded the transition to stationary phase by approximately 15 hours (Figure 5-2-C). The onset of apoptosis was likely induced by a nutrient depletion event.

In contrast, the culture electroporated in a stationary state (culture S) initially proliferated as evidenced by increases in the total and viable cell counts, as well as a decrease in the apoptotic cell count resulting in an increase of the viable cell fraction (Figure 5-2-A, 2-B, 2-D). The end of this initial proliferation was reached at 12 hours and is marked by arrow (c). At this time point, apoptotic cells began appearing, and increased at a constant rate for the duration of the culture (arrow c, Figure 5-2-C). It is

interesting to observe two distinct proliferation periods in the total and viable cell counts, with each proliferation phase occurring at a constant rate. The initial proliferation period ends at 12 hours (arrow c) and is followed by a slow growth phase that ends at 38 hours (arrow d). Towards the end of the second proliferation period, proliferation is evidently balanced by cell death as reflected in the constant fraction of viable cells that is reached during that time. At hour 38, proliferation ceased and the culture entered death phase (arrow d, Figure 5-2-A, 2-C). Table 5-1 summarizes the properties of the cultures at the transitions between each growth phase.

Table 5-1: Growth characteristics of cultures E and S during TGE. Transitions between growth phases, initial and final cell counts, and initial and final viabilities, as indicated in Figure 2. Culture E was inoculated with an electroporated exponentially growing culture, while culture S was inoculated with an electroporated stationary phase culture.

Parameter	Culture E	Culture S
Initial Viable Cell Concentration (cells mL^{-1})	$2x10^4$	$8x10^4$
Initial Viability (%)	66	65
Lag phase exit (hrs)	18	0
Proliferation Rates (hr^{-1}) (before/after fed batch addition)	0.0387 / 0.0496	0.0453 / n/a
Peak Viability (%)	99	81
Steady State Apoptotic Cell Concentration (cells mL^{-1})	$1x10^4$	n/a
Onset of Apoptosis (hrs)	110	12
Stationary Phase Time (hrs)	125	n/a
Onset of Death Phase (hrs)	n/a	38
Final Cell Concentration (cells mL^{-1})	$2x10^6$	$6x10^4$
Final Viability (%)	97	48

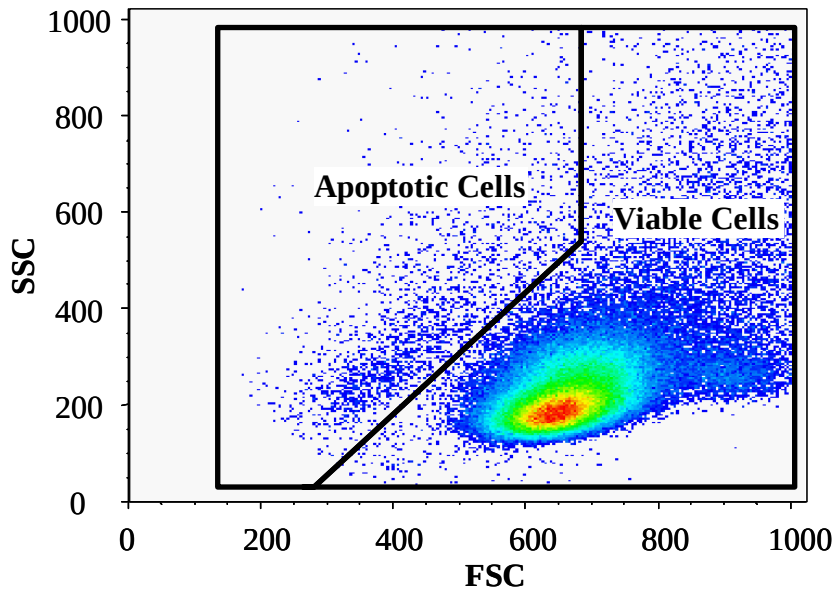

Figure 5-1: Identification of the non viable cell population. FSC versus SSC comparison for a sample point during bioreactor operation. Apoptotic Cells are defined as having decreased FSC and increased SSC as previously described (Schwartz and Osborne, 1995).

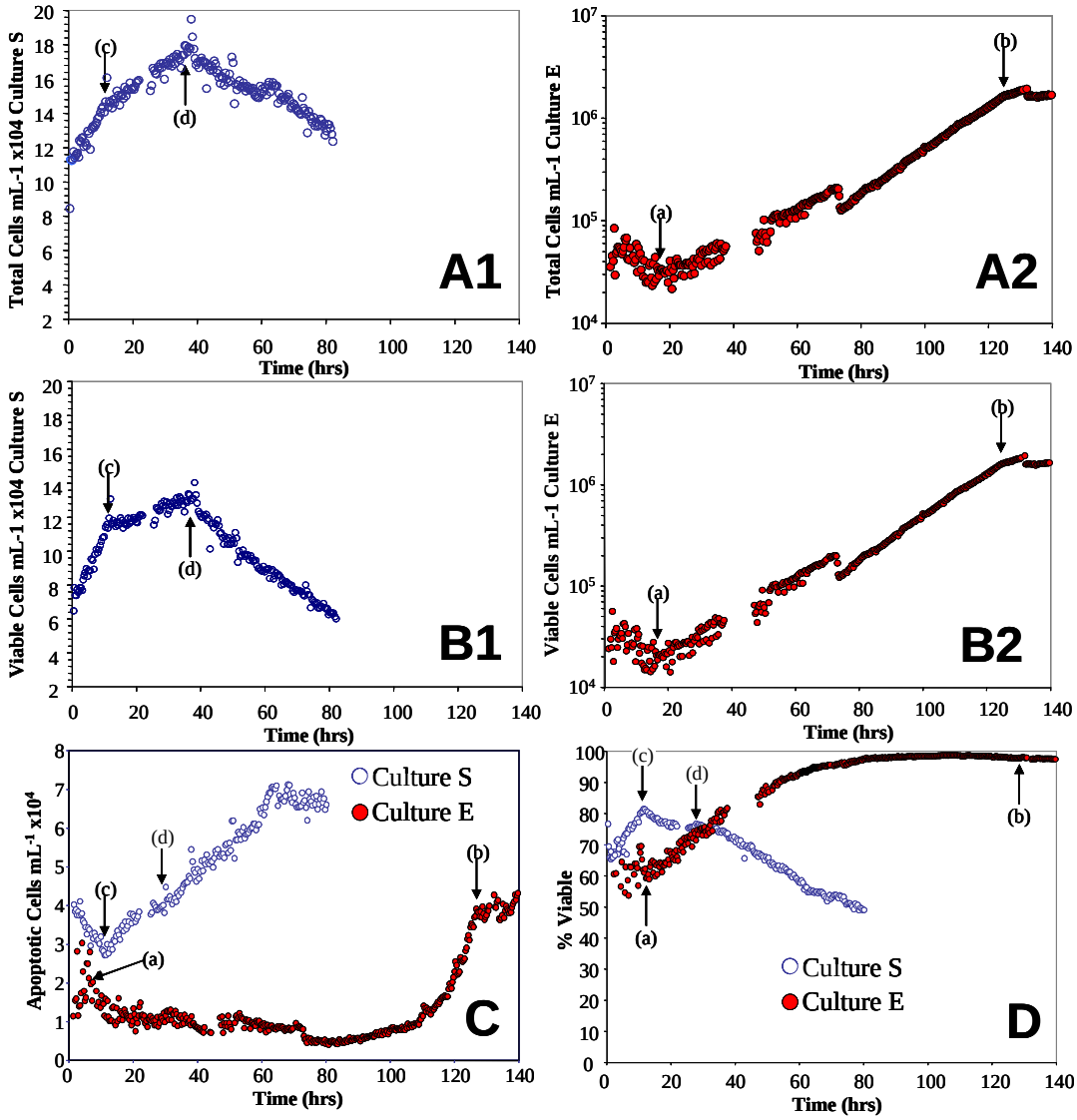

Figure 5-2: CHO culture growth, viability, and death curves. Culture E (●) and Culture S (○). **(A)** Samples were counted every 20 minutes using the automated flow cytometry setup as previously described (Kacmar and Srienc 2005). The high frequency sampling of total cell number enables determination of distinct growth phases: arrow a indicates the end of lag phase, arrow b indicates onset of stationary phase, arrow c indicates onset of cell death coupled with growth, and arrow d indicates death phase. **(B)** Viable Cell concentration as determined by light scattering properties. **(C)** Apoptotic cell concentration as determined by the light scattering properties. **(D)** The fraction of viable cells.

5.4.2 Transfection Efficiency

After electroporation, cells can only express eGfp if they received plasmid DNA. The viable cells that eventually become fluorescent must have received plasmid DNA during electroporation and are able to express, with a certain delay, the obtained genes. Therefore, the peak of the fraction of fluorescent cells within the viable cell population can be considered an indirect measure of the transfection efficiency. Culture E has a very high transfection efficiency of 60% (arrow b, Figure 3A). For culture S, the transfection efficiency was only 20% (arrow d, Figure 5-3A).

Discontinuities in the slope of the time-course of the fluorescent fraction indicate changes in the rates of apoptosis, proliferation, and plasmid expression between the fluorescent and non-fluorescent sub-populations. For culture E, three discontinuities are apparent (arrows a, b, c, Figure 5-3A). The discontinuity marked by arrow a, Figure 5-3A corresponds to the transition of an increasing fluorescent cell concentration to a constant fluorescent cell concentration (arrow a, Figure 5-3D). However, while the fluorescent cell concentration is constant, the non-fluorescent cell concentration continues to decrease until cell proliferation starts (arrow b, Figure 5-3A, D). Therefore, it appears that apoptosis was preferentially initiated in the non-fluorescent sub-population. Culture S exhibited a similar initial pattern of a rapid increase followed by a slower increase in the time-course of the fluorescent fraction (arrows d, e, Figure 5-3A). In contrast, the cell concentrations of the fluorescent and non-fluorescent sub-populations of culture S exhibited different kinetics for the initial gene expression (arrows d, e Figure 5-3C). There was a rapid increase in the fluorescent cell

concentration of culture S until arrow d when a slower rate of increase was observed. For culture S, it is important to note that the non-fluorescent population did not preferentially undergo apoptosis. Therefore, this data indicate that two separate processes, the preferential plasmid uptake (i.e. differing k_T values) and preferential apoptosis induced by the transfection procedure (i.e. differing effective growth rates, μ_F^* and μ_N^*), determine the peak transfection efficiency.

After the peak transfection efficiency of cultures E and S is reached (arrows b, e, Figure 5-3A) the fluorescent fraction remains constant. For culture S, one can observe that different effective growth rates (μ_F^* and μ_N^*) are equal after the peak fluorescent fraction is reached. Furthermore, the μ_F^* and μ_N^* values are equal despite differing viable cell proliferation and apoptosis rates (Figure 5-2-B, C). Therefore, this indicates that after hour 25, apoptosis and proliferation was not preferentially initiated in either the fluorescent or the non-fluorescent cells (Figure 5-3C, D). For culture E, the fluorescent fraction began to decrease after the fed-batch addition (arrow c, Figure 5-3A). This is due to the non-fluorescent population increasing in number at a statistically significant 14% faster rate than the fluorescent population (Figure 5-3D). This trend has two explanations: differing proliferation rates of the fluorescent (μ_F^*) and non-fluorescent sub-populations (μ_N^*) or transitions from a fluorescent to a non-fluorescent cell (negative k_T values). Most likely, cell proliferation has sufficiently diluted eGfp and plasmid to below the detection threshold thus generating a negative k_T value.

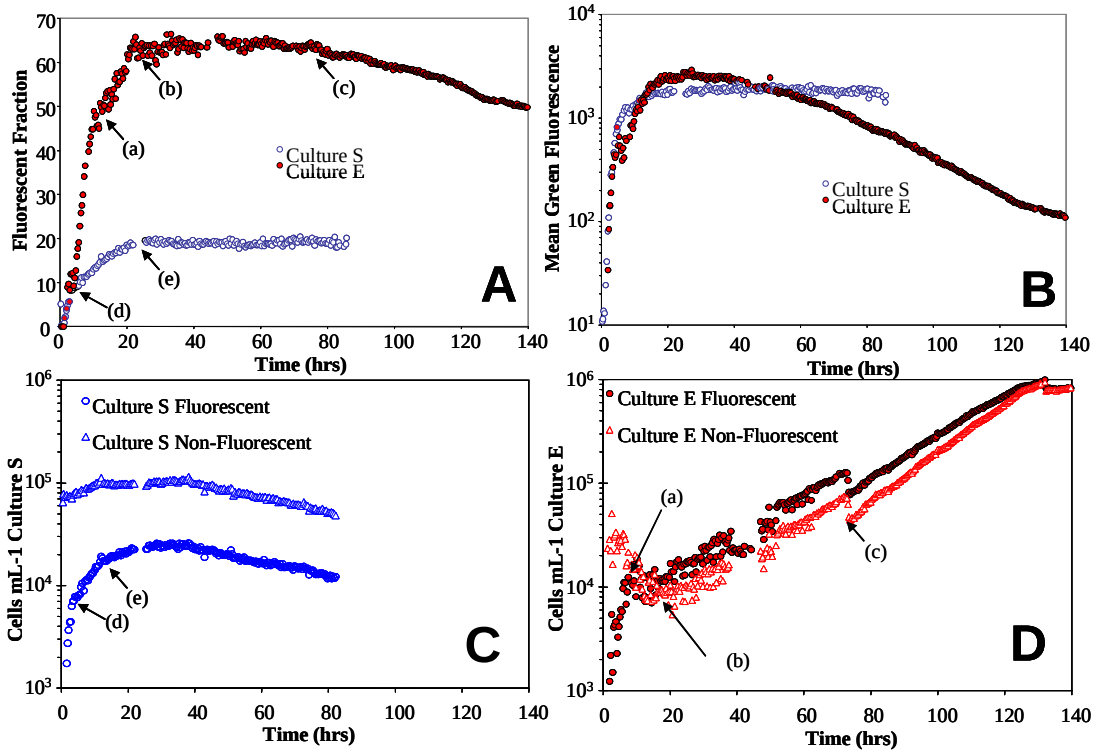

Figure 5-3: Time course of eGfp expression. **(A)** Time course of the fluorescent fraction. Culture E (●) and Culture S (○). For Culture E, the fluorescent fraction dropped due to the different growth rates of fluorescent and non-fluorescent cells. **(B)** Time course of the mean single-cell fluorescence of the fluorescent population. Culture E (●) and Culture S (○). **(C)** Growth curves for culture S fluorescent fraction (○), and culture S non-fluorescent fraction (Δ). **(D)** Growth curves for culture E fluorescent fraction (●), culture E non-fluorescent fraction (▲). For culture E, after the fed-batch addition, the fluorescent cells grew a statistically significant 14% slower than the non-fluorescent cells. Before the fed-batch addition there was not a statistically significant difference in the growth rates.

5.4.3 eGfp Expression and Partitioning During Cell Division

The physiological state of the cells prior to electroporation had a significant effect on the eGfp expression. The peak single cell eGfp expression of culture E was two times higher than culture S (Figure 5-3B). However, after reaching a peak value, the mean single cell fluorescence of culture E decreased exponentially, while in culture S, the mean single cell fluorescence remained constant. This indicates that the production and degradation of eGfp are balanced in the non-proliferating culture S. Furthermore, as seen in culture E, dilution effects due to cell proliferation can perturb the balance between synthesis and degradation of eGfp. This appears to be the case since culture E proliferated, and the non-replicating plasmid and expressed eGfp were partitioned between daughter cells. The partitioning therefore leads to an exponential decrease in the mean single cell fluorescence of culture E. In contrast, culture S did not proliferate and thus partitioning did not occur. Therefore, a constant mean single cell fluorescence of the fluorescent fraction was observed.

Examining the time-course of histograms representing single-cell green fluorescence of culture E, reveals an interesting effect caused most likely by the partitioning of plasmid and eGfp (Figure 5-4). In this graph one can clearly recognize five sub-populations with different, discrete levels of eGfp content. Initially, cells are charged with a large amount of plasmid and subsequently express eGfp at the highest discrete level of eGfp content. As cell division occurs, eGfp and plasmid is partitioned between daughter cells and the next discrete level of eGfp content appears. This process continues until a cell dilutes its plasmid and eGfp content to the lowest discrete

sub-population, and is then termed non-fluorescent. Therefore, each discrete level of eGfp content corresponds to a generation of cells.

5.4.4 Total eGfp Production

Multiplication of the fluorescent cell number concentration in the bioreactor with the average single cell fluorescence results in the total eGfp content in the culture at each time point. Total eGfp production in culture E increases linearly with time until 15 hours before stationary phase is reached at hour 110 (Figure 5-5). The linear rate of eGfp accumulation in the culture may indicate that proliferating cells are able to maintain the initial plasmid copy number. Since the plasmids are not replicated their total number presumably remains constant resulting in a constant rate of eGfp expression. This would indicate that plasmids are not significantly degraded during cell proliferation. Past 110 hr cultivation time, the onset of apoptosis occurs (arrow (b) Figure 5-2-C, arrow (a) Figure 5-5)). Subsequently, as transfected cells undergo apoptosis, plasmid and eGfp are lost from the viable cell population. Therefore, apoptosis artificially decreases the rate of total eGfp production, and makes it appear that plasmid has been exhausted. A similar effect is seen in culture S, since the slope of the total production lines change at hours 12 and 32, which corresponds to the onset of apoptosis (arrow (c) Figure 5-2C) and the termination of proliferation (arrow d Figure 5-2B).

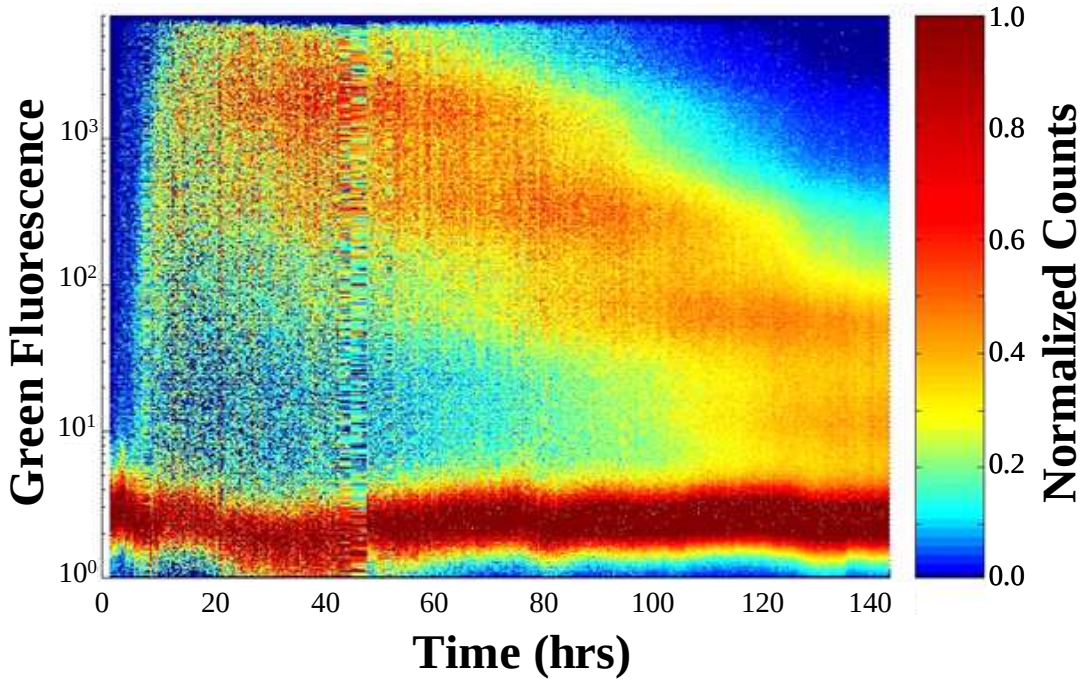

Figure 5-4: Time course of single cell distribution of eGfp fluorescence for the exponentially growing culture. The histogram is normalized to the maximum value of the distribution. Note the distinct, discrete subpopulations that evolve after peak fluorescence is reached.

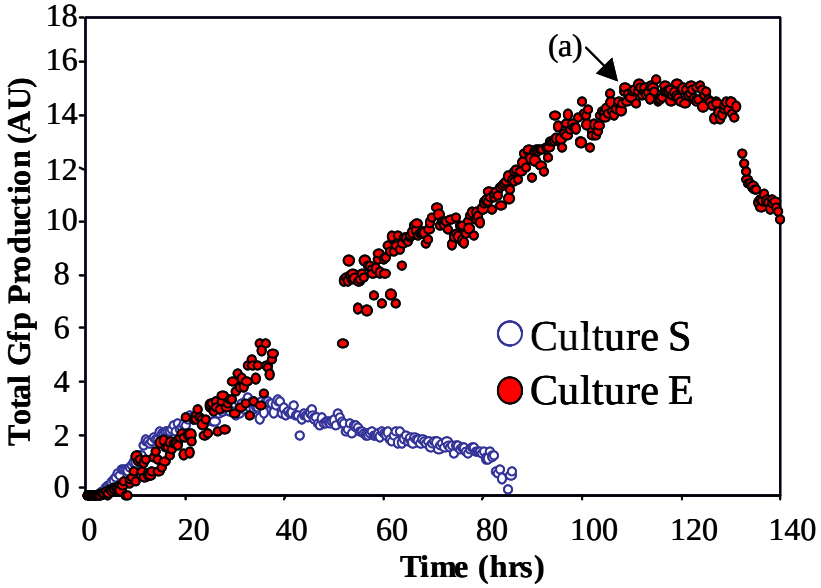

Figure 5-5: Total eGfp production for Culture E (●) and Culture S (○). Total eGfp production is defined by multiplying the total fluorescent cell number in the bioreactor by the average single cell fluorescence at each time point.

5.4.5 Cell Size and Intracellular Structure

Further insight into the state of the culture is given by the light scattering measurements. The small angle light scattering of a cell (FSC) correlates with cell diameter. Since electroporation opens holes in the cell membrane, cell mass is lost to the supernatant. After electroporation, the cellular membrane reseals and these cells are detected as the viable fraction. Before proliferation begins, cells in early G1 must increase their mass. Therefore, cultures E and S increase their mean cell size immediately before proliferation is initiated. The initial increases in cell size of cultures E and S occurs linearly. For culture E, at hour 18, cell proliferation began and there was a corresponding decrease in cell size (Figure 5-6A, 7). The increase in FSC at hour 10 for culture E corresponds to the increase in the SSC at the same time point (Figure 5-6C). Since SSC correlates with the density of internal cellular structures, this indicates that cell growth also significantly affects the internal cell structure.

The next two peaks in cell size of culture E occur with a period of 18 hours. These regular peaks can be likely explained by a partial synchrony in the culture, since the doubling time during this period was approximately 18 hours. At hour 72, the fed batch addition to culture E caused a change in the osmolality of the culture. Thus, the mean FSC increased, and then returned over 10 hours to the previous level (Figure 6A, arrow). The increase in the cell size of culture E at hour 72 is mirrored by a decrease in SSC (Figure 5-6C, arrow).

For culture S, two time periods can be distinguished on the basis of observed changes in cell size. The first time period is the immediate recovery from electroporation that occurs during hours 0-12. The second time period occurs from 12-

80 hours when FSC increases linearly. (Figure 5-6). This corresponds with a linear increase in the SSC of culture S (Figure 5-6C). Surprisingly, despite increases in the cell size and the internal complexity of cells the cell number does not increase and also, the single cell eGfp content remains constant. This is in direct contrast to culture E, where an increase in cell size and cell granularity preceded the beginning of cell proliferation.

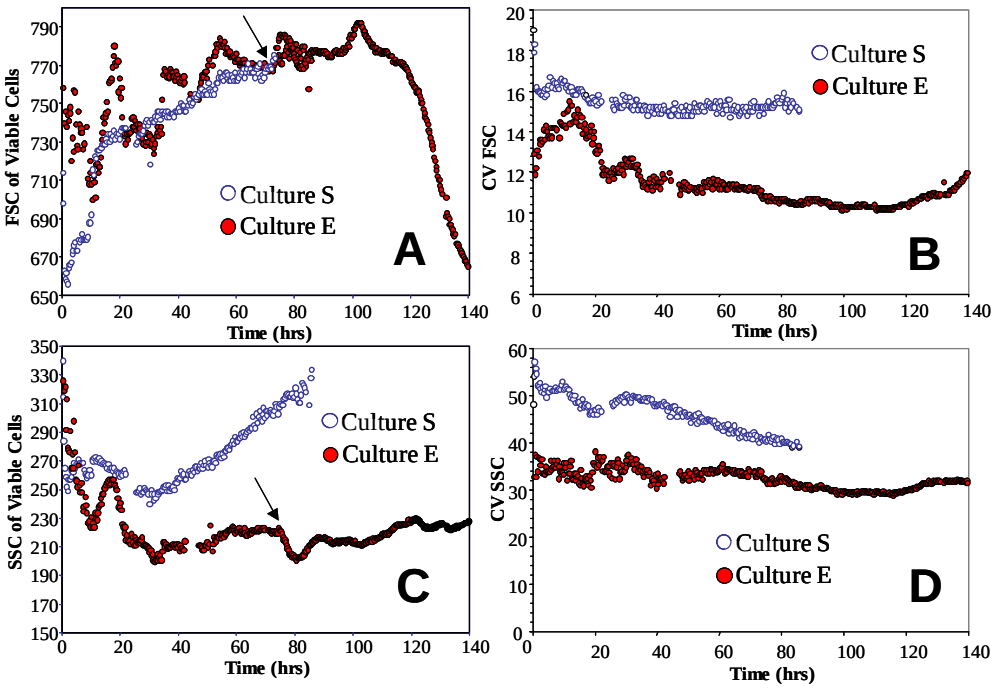

Figure 5-6: Time course of Cell Size and Cell Granularity. Culture E (●) and Culture S (○). **(A)** Average single cell size. Arrow indicates time of fed-batch addition to exponentially growing culture. **(B)** CV of cell size. **(C)** SSC versus time. Arrow indicates time of fed-batch addition to exponentially growing culture. **(D)** Time course of CV of SSC.

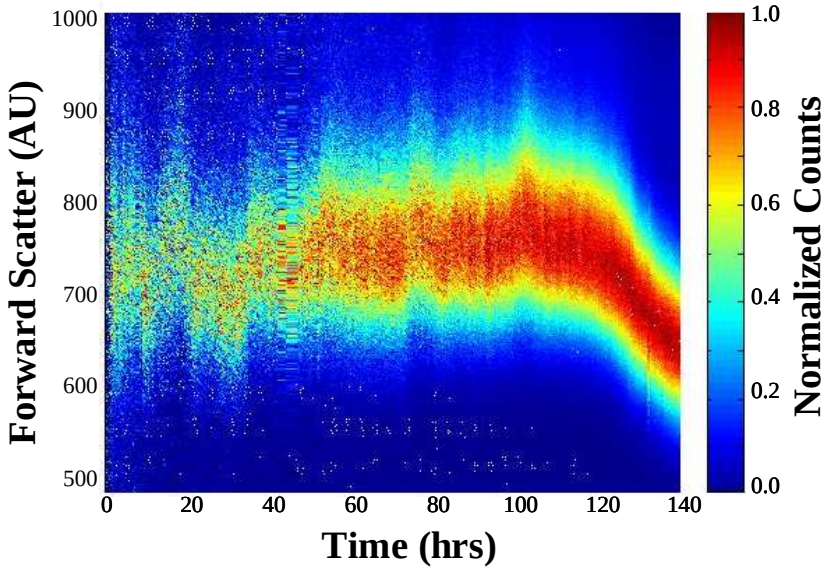

Figure 5-7: Time course of the cell size distribution. Time course histogram of the forward scatter for culture E. The histogram is normalized to the maximum value of the distribution.

5.5 Discussion

The detailed observation of the population dynamics of transient gene expression yields several interesting observations. The data clearly shows that (i) preferential plasmid uptake and preferential cell death between transfected and non-transfected populations determine the transfection efficiency; (ii) subsequent generations of proliferating transfected cells have distinctly different protein contents resulting in discrete subpopulations representing each cell generation; (iii) total eGfp production increases linearly with time; (iv) two fundamentally different stationary and death phases can be reached. One type of stationary phase occurs when proliferation ceases while cells decrease their cell size, maintain granularity, and mean eGfp content decreases (Culture E, hour 120+). The second type of stationary phase occurs when proliferation ceases while cells increase their cell size, increase granularity, and mean eGfp content is constant (Culture S).

The transfection process is affected by two separate processes including preferential cell death and preferential plasmid uptake. These two processes are dependent on both the physiological state of the cells prior to transfection and the parameters of the transfection procedure. Previous work has shown that cell size (Valic, et al. 2003), cell cycle position (Golzio, et al. 2002), and membrane tension (Barrau, 2004) are physiological variables that affect the transfection efficiency for electroporation. Also, the voltage gradient, pulse duration, and pulse shape are transfection parameters that affect the transfection efficiency for electroporation (Valic, et al. 2003). However, each of these studies only examines the peak transfection efficiency, and not the separate processes of preferential cell death and plasmid uptake

that the culture underwent to attain the peak transfection efficiency. This is an important observation since two separate processes influence the transfection efficiency, and thus identical transfection efficiencies can be obtained for differing final physiological states of the culture. Therefore, variations in culture performance and final product quality would be observed.

The observation of a linear increase in total eGfp content coupled with the observation of discrete levels of single cell protein content indicate that cell proliferation is irrelevant to the production rate of the desired product. This is because it is likely that plasmid is conserved between subsequent generations of cells. Therefore, at all times, a constant level of plasmid is being transcribed, and thus a constant amount of desired product is produced. Similar linear production rates of desired protein in a non-replicating plasmid system are seen for different transfection techniques (Derouazi, et al. 2004). Therefore, to attain maximum production, either the onset of apoptosis should be avoided or the proliferation of the culture should be arrested. Furthermore, the observation of a linear increase in total eGfp content yields a quantitative description of the average single cell eGfp content as described by equation six. Equation six accurately predicts the time course of the single cell protein content as shown for culture E in Figure 3C. However, equation six does not describe the average single cell eGfp content observed for culture S. It is likely that different culture physiology between cultures E and S are responsible for the different observed expression kinetics. These differences are highlighted by the two different stationary phases that were observed.

The observation of two distinct stationary phases provide qualitative evidence supporting the hypothesis that cell size increase and cell proliferation are two independent processes in mammalian cell culture (Conlon and Raff 2003).

5.6 Conclusions

The automated flow cytometry system provides a unique capability to study the time course of cell phenotype in unprecedented detail. New variables like cell counts, cell size, cell granularity, protein expression, as well as virtually any phenotype that has a cytometry stain can now be examined on-line. This opens up new and unique capabilities to understand cell physiology and to implement new and unique process control strategies. The described approach yields valuable insight into how cultures respond to specific treatments that are relevant to industrial processes and operations.

6 Mammalian Cell Culture Scale-Up and Fed-Batch Control Using Automated Flow Cytometry[3]

6.1 Chapter Summary

Detailed knowledge of mammalian cell culture proliferation kinetics is important to determine fed-batch strategies for industrial bioreactor operations. In particular, predicting the end of exponential proliferation in batch culture is a critical process parameter during culture scale-up. Using automated flow cytometry we show that an increase in the non-viable sub-population in CHO cell culture can predict the onset of stationary phase by approximately 40 hours. This enables a completely automated culture scale-up process as well as a reliable and reproducible control of fed-batch additions during culture expansion. It is shown that the automated scale-up results in a significantly higher total cell count in the reactor than manual scale up initiated in stationary growth phase. During individual, subsequent culture expansions, a significant variation in the proliferation rate was observed despite control of bulk culture parameters. Thus, automated flow cytometry is critical to uncovering useful process parameters that enable new control strategies. Such improved process supervision derived from knowledge-based data analysis is central to the FDA's Process Analytical Technology (PAT) initiative and is expected to result in better and higher quality products.

[3] This Chapter has been published in J Biotechnol. 2008 Jun 1; 135(2):174-80.

6.2 Introduction

Mammalian cell culture scale-up and maintenance is a critical component of the antibody production process in industry as well as in a laboratory setting for strain characterization and small scale protein production. Mammalian cell cultures are typically initiated with a frozen ampule of a recombinant cell line, typically Chinese Hamster Ovary (CHO) cells. The frozen cells are then thawed in growth medium where they proliferate. Prior to stationary phase, the culture is diluted into a larger volume of fresh medium in a larger bioreactor. This process is typically referred to as passaging the culture. In industrial scale-up operations, several passages are repeated until the culture arrives at the final production vessel, that may have a volume of 10,000 L or more. Once the culture reaches the final production vessel, fed-batch or intermittent harvest fed-batch processes are undertaken to extend the cultivation time of the cells and improve recombinant protein production (Chu and Robinson 2001).

Throughout the scale-up processes, the state of the culture is typically assessed using an unstructured viewpoint. In this approach, the biomass of a culture is assumed to be homogeneous and is mathematically grouped into a single term. The assumption of a homogenous biomass is clearly not true, since cultures are inherently heterogeneous due to factors such as the cell cycle, incomplete mixing, genetic variation, and stochastic events. Thus, it is likely that a greater understanding of culture heterogeneity can yield novel critical process parameters and control strategies to improve the yield and decrease the variability of the cell culture process. The FDA has recently recognized the practical value of this approach in the Process Analytical Technology (PAT) initiative aiming at more reliable products on the basis of better

control and understanding of the biological-pharmaceutical manufacturing process (Clementschitsch and Bayer 2006 ; DePalma 2004 ; Gnoth, et al. 2007 ; Kourti 2006).

Experimentally, flow cytometry is primarily used to measure culture heterogeneity over time. However, flow cytometry has traditionally been an offline technique. Thus, unless significant labor is expended for sampling from the process of interest, the culture heterogeneity can only be infrequently assessed. Also, if cell staining is performed manually, operator to operator error in the staining protocols is expected. To overcome these problems, we have previously developed automated flow cytometry (Abu-Absi, et al. 2003 ; Zhao R, et al. 1999b) that can assess the culture heterogeneity online. Its versatile utility has been demonstrated in initial examples involving the monitoring of microbial (Kacmar, et al. 2004b ; Kacmar, et al. 2006) and mammalian cell cultures ((Kacmar and Srienc 2005 ; Sitton, et al. 2006)). The full range of possible applications has not been exhausted as automated flow cytometry can in principle provide online data relating to any single-cell property for which a flow cytometry stain exists.

Thus, automated flow cytometry enables a unique way to examine how culture heterogeneity changes over time. From this data, novel control strategies and new critical process parameters can be determined. For example, in this study, we show how automated flow cytometry can be applied to closely monitor the cell death kinetics, and then use this information to predict the approach of stationary phase. Thus, this data can be used to support a novel cell culture fed-batch addition and passaging strategy.

6.3 Results

6.3.1 Fed-Batch Control Algorithm

Detailed monitoring of the growth and death kinetics of a culture can be used to predict the approach of stationary phase. As observed in previous studies (DiStefano, et al. 1996 ; Sitton, et al. 2006 ; Zanghi, et al. 1999) for different cell lines and medium compositions, the onset of cell death occurs in exponential phase and forewarns the approach of stationary phase. Therefore, the onset of cell death can be used to trigger fed-batch additions during the exponential growth phase. In this study, the fed-batch addition was initiated when the non-viable cell concentration exceeded four times the average of the non-viable cell concentration prior to the onset of cell death. Four times the averaged non-viable cell concentration was arbitrarily chosen to provide a large safety margin against possible errors in the sampling and analysis that would inadvertently trigger a fed-batch addition at the wrong time. While such event did not happen in our experiments we anticipate that a smaller safety margin could lead to a finer control of the process.

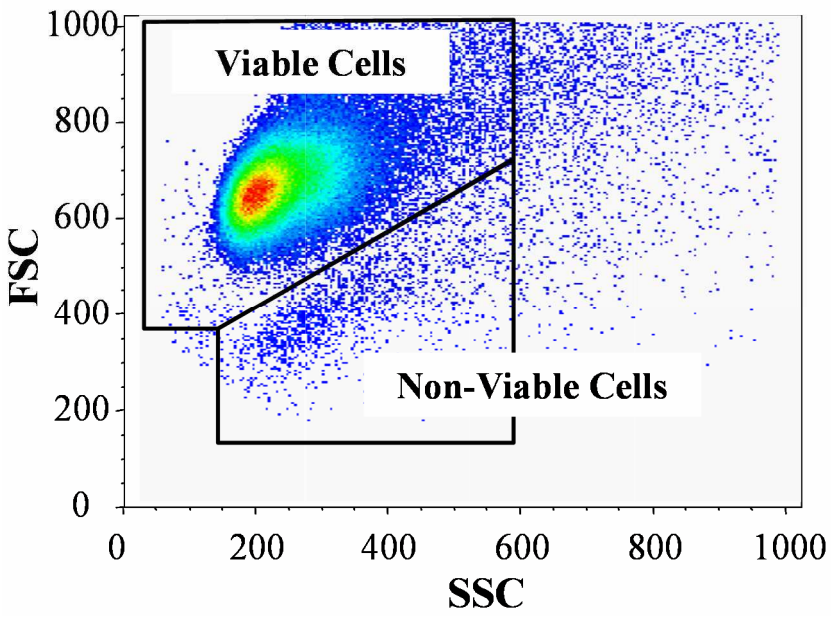

Figure 6-1: Identification of the non-viable population. FSC versus SSC dot plot for a sample point during bioreactor operation. Non-viable cells are defined as having decreased FSC and increased SSC as previously described (Fraker, et al. 1995).

6.3.2 Fed-Batch Cell Proliferation and Death Kinetics

To demonstrate the fed-batch addition strategy, two bioreactors were monitored in parallel by the automated flow cytometry system. Data on the viable cell concentration, non-viable cell concentration, and viable fraction were obtained every 25 minutes from each reactor. As a general feature of cell death through either necrosis or apoptosis cells change their morphology by decreasing in size and changing their internal structure. These morphological changes are detectable by measuring the change in light scatter using flow cytometry (Vermes, et al. 2000). Thus, non-viable cells can be differentiated from viable cells based on their differing forward (FSC) and side (SSC) light scattering characteristics (Vermes, et al. 2000) (Figure 1). This strategy for differentiating between viable and non-viable cells has been applied across many different mammalian cell lines (Darzynkiewicz, et al. 1992 ; Darzynkiewicz, et al. 1999 ; Fraker, et al. 1995) including CHO cells (Fieder, et al. 2005).

The two monitored bioreactors, A and B, were exposed to different fed-batch control algorithms. The fed-batch addition to bioreactor A was triggered by the control algorithm described in the previous section. The fed-batch addition to bioreactor B was triggered by the cell concentration ceasing to increase for 30 hours. Thus, culture B was in stationary phase when the fed-batch addition occurred. Both bioreactors were inoculated using equal amounts of inoculum from the same culture. The cells began to proliferate in exponential growth phase with a doubling time of 17 hours (Figure 2B). For the first 30 hours, the non-viable cell concentration remained relatively constant. Since the viable cell concentration is increasing while the non-viable cell concentration

remains constant, the non-viable fraction decreases (Figure 2D). The small differences in the two bioreactors are likely due to settling effects and other physiological changes induced during the 30 minute inoculation procedure.

At hour 54, both cultures entered the onset of cell death, likely due to a nutrient depletion event (Figure 2A). At the onset of cell death, the viable fraction of the culture reaches a maximum while the non-viable fraction reaches a minimum as shown in the inset of Figure 2C-D. For bioreactor A, the increase in the non-viable cell concentration continued until the fed-batch addition was initiated (arrow (a), Figure 2). From the onset of cell death to the fed-batch addition, the non-viable cell fraction increased by only 0.6% while the non-viable cell concentration increased by a factor of four.

After the fed-batch addition, the diluted cell culture appears to be partially synchronized. The synchrony is evidenced by changes in the growth rate of the culture as seen by changes in the rate of increase in the cell number (arrows (e), Figure 2B). These changes occurred with a period of 5 hours, and continued until the peak viable cell concentration was reached at hour 94 (arrow (c), Figure 2B).

The exponential increase in viable cell concentration in bioreactor B continued until stationary phase was reached at hour 90 (arrow (d), Figure 2B). The onset of cell death was detected 36 hours before stationary phase was reached. Bioreactor B reached stationary phase 11 hours earlier than bioreactor A due to the fed-batch addition to bioreactor A. Once the viable cell count in bioreactor B decreased for 30 hours, a fed-batch addition was triggered (arrow (b), Figure 2). After the fed-batch addition to bioreactor B, the viable cell number remained constant for 15 hours, until its decrease resumed (arrow (b), Figure 2B).

Thus, the proliferation kinetics of bioreactors A and B show that the onset of cell death precedes the transition to stationary phase, and that this information can be used to trigger actions to obtain a desired result. In this manuscript, if the desired result is to obtain a higher titer by maximizing the final integral viable cell count then the fed-batch addition should be triggered in stationary phase. On the other hand, if the objective is to maximize the total number of cells in the reactor, then as Figure 3 shows, the fed-batch addition should occur during exponential phase. Maximizing the total number of cells in the reactor is vital during a scale-up process.

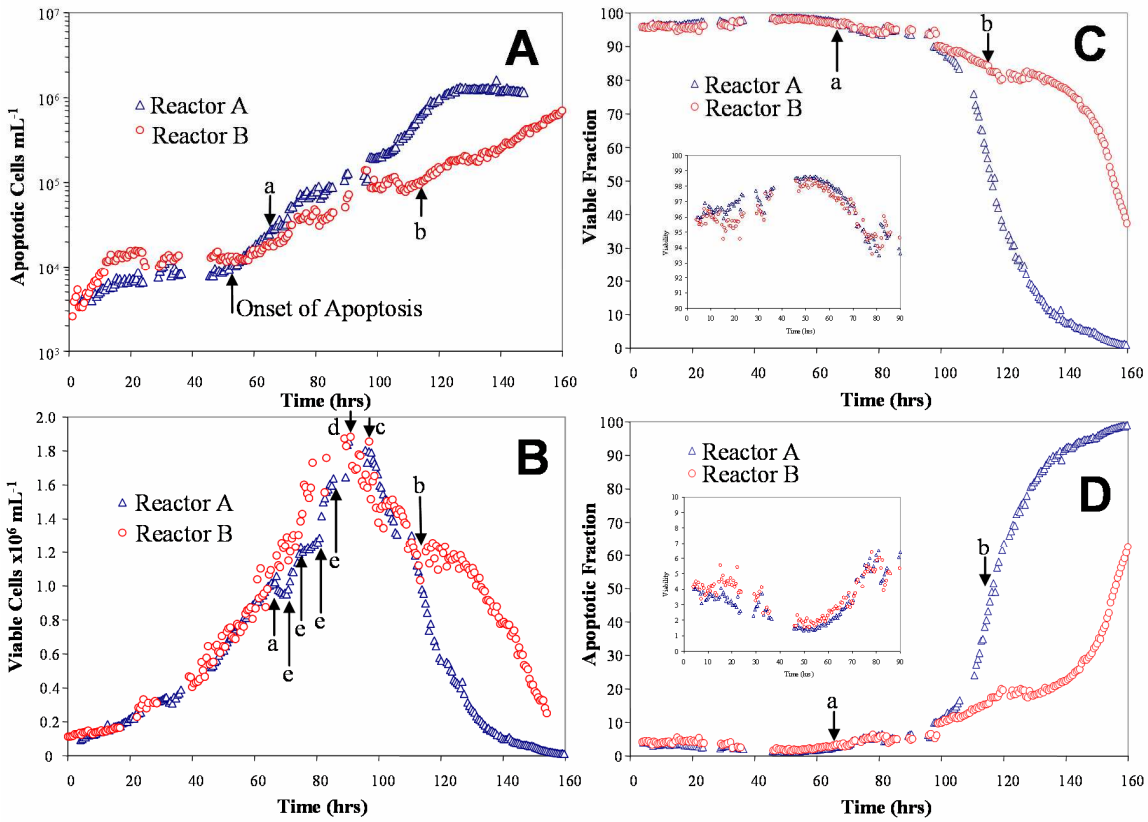

Figure 6-2: Growth and death kinetics of the cultures. Time courses of the non-viable cell concentration **(A)**, the viable cell concentration **(B)**, the viable fraction of cells **(C)**, and the non-viable fraction **(D)** as determined by the differing light scattering properties illustrated in Figure 1. The two bioreactors, A and B, were batched with an initial volume of 650 mL of medium and each reactor was inoculated at time zero with 150 mL of inoculum from the same 300 mL inoculum culture. The inoculum culture was grown in a spinner flask and harvested in exponential proliferation phase at a concentration of $5x10^5$ cells mL^{-1}. The inset of Figures C and D are zoomed into the period around the onset of cell death to denote that the viability reaches a maximum and the non-viable fraction reaches a minimum. Arrows (a) and (b) indicate fed-batch additions for bioreactor A and B respectively according to the respective control algorithms. Arrows (c) and (d) indicate the time the cultures entered stationary phase. Arrows (e) indicates when changes in the growth rate occurred due to a partial synchrony in the culture induced by the fed-batch addition.

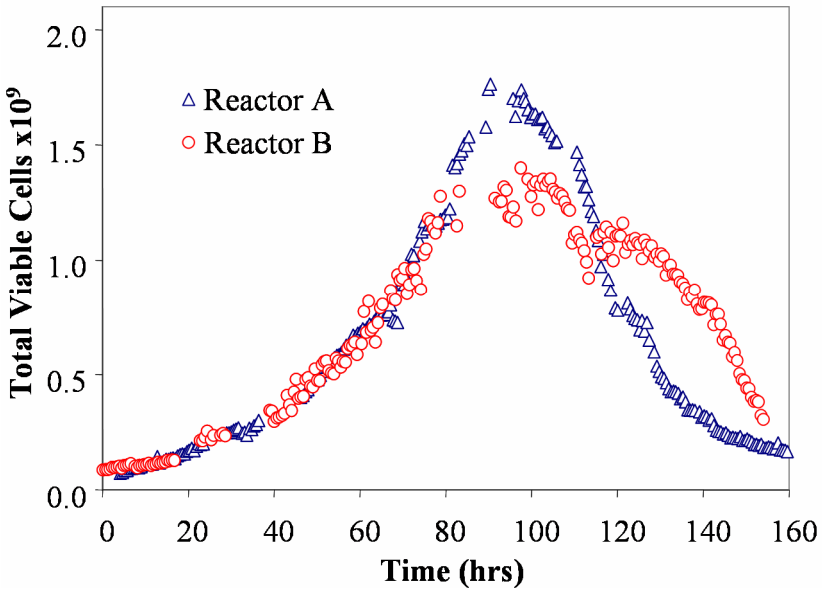

Figure 6-3: Time course of the total number of viable cells in the bioreactors. The total number of viable cells in the reactor is defined as the volume multiplied by the cell concentration. Bioreactor A attained a higher total cell number due to the feeding before the onset of stationary phase, which resulted in a larger volume of viable cells in bioreactor A.

6.3.3 Automated Culture Scale-Up

To automate the passaging of cells based on the predicted transition from exponential proliferation to stationary phase, a 1-L bioreactor was sampled by the automated flow cytometry system every 30 minutes and four simulated passages were triggered by the predicted transition to stationary phase. This corresponds to a culture scale-up from 1 L to 10,000 L. Passages were triggered once the onset of cell death occurred, and the non-viable cell concentration exceeded four times the initial reference concentration.

6.3.4 Scale-Up Growth Kinetics

After inoculation, the culture started growing exponentially and maintained a constant non-viable cell concentration until the onset of cell death at hour 30 (Figure 4A). After the onset of cell death, the non-viable cell concentration increased exponentially until the non-viable cell concentration reached the trigger-point at hour 72, arrow (a). At this point, the culture was passaged by removing 90% of the culture from the bioreactor and replacing it with fresh medium. After the passage, the culture experienced changes in the growth rate at hours 93 and 104 (Figure 4A arrows (e,f)). These discontinuities in the growth rate occurred despite control of the bulk culture parameters of pH, dissolved oxygen, and agitation. Such variation in the growth rate has been observed also in previous fed-batch experiments monitored by this system (Sitton et al. 2006). After the first passage, the non-viable cell concentration stopped increasing exponentially for 23 hours and remained at a constant level until the onset of

cell death occurred at hour 95. then it increased again until the trigger-point was reached and the next passage was induced at hour 150 (arrow (b)).

After the second passage, the culture again experienced discontinuities in the growth rate at hours 185 and 255 (Figure 4A arrows (g,h)). The non-viable cell concentration followed a trend similar to the first two cultures, where the non-viable cell concentration remained constant for the first 30 hours. Then, the onset of cell death occurred and the non-viable cell concentration increased exponentially until the trigger point was reached at hour 267 (arrow (c)). The culture was then passaged for a third time. After the passage, the culture maintained exponential proliferation with no apparent variation in the specific growth rate. The non-viable cell concentration followed a similar trend as in the previous batches, except the onset of cell death occurred in 18 hours. After the trigger point was reached for the fourth and final time (arrow (d)), the culture was passaged into the final vessel and allowed to reach stationary phase. The viability remained nearly constant throughout the scale-up of the culture with the exception of brief periods of decreased viability localized around the passaging event (Figure 4B, arrows (a-d)). When the culture reached stationary phase the viability decreased at a constant rate.

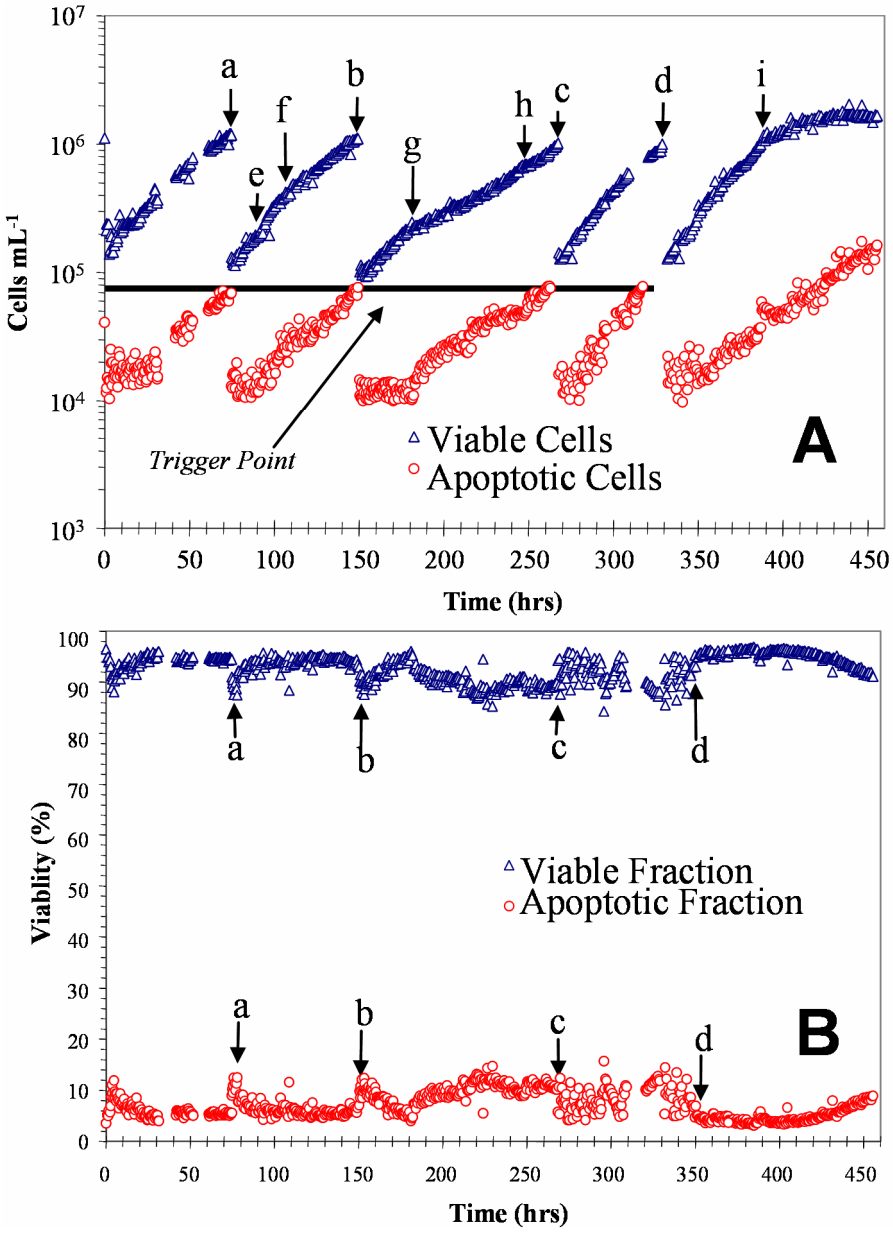

Figure 6-4: Cell growth and death kinetics of the passaged culture. **(A)** Depicts the live cell concentration and the non-viable cell concentration as a function of time. Arrows (a-d) indicate passages, while arrows (e,i) indicate changes in the growth kinetics within a passage. **(B)** Indicates the viable and dead cell fractions as a function of time. Initially, the 1-L bioreactor was batched with 900 mL of medium and inoculated with 100 mL of spinner flask culture at 10^6 cells mL^{-1}.

6.3.5 Cellular Light Scattering Dynamics during Scale-Up

The cell size as reflected by the light scattering signals changes throughout the scale-up process. For instance, immediately after inoculation, after the first passage, and after the second passage the mean cell size of the viable population decreased significantly (Figure 5A arrows (a,b)). However, subsequent passages do not yield such decreases in the cell size (Figure 5A arrows (c,d)). It is likely that these rapid changes in the FSC are due to osmotic effects when the culture is diluted.

The discontinuities in the proliferation rate of the culture (Figure 4A, arrows (e,f,g,h)) appear to be correlated with changes in the mean cell size. For instance, at hour 93 when the mean cell size started to increase significantly (Figure 5A, arrow (e)) the corresponding doubling time decreased (Figure 4A, arrow (e)). Also, when the doubling time increased (Figure 4A, arrow (g)) the cells began to increase their cell size (Figure 5A arrow (g)). These changes appear to affect all of the cells in the distribution evenly, since the CV of the FSC distribution remains constant throughout changes in the mean FSC (Figure 5B).

During culture passaging, the mean SSC of the viable population follows the same basic trend of a rapid increase followed by a return to a constant mean SSC value (Figure 5A arrows (a, b, c, d)). Also, once stationary phase is reached, both the mean and the CV of SSC begins to increase (Figure 5A,B arrow (i)).

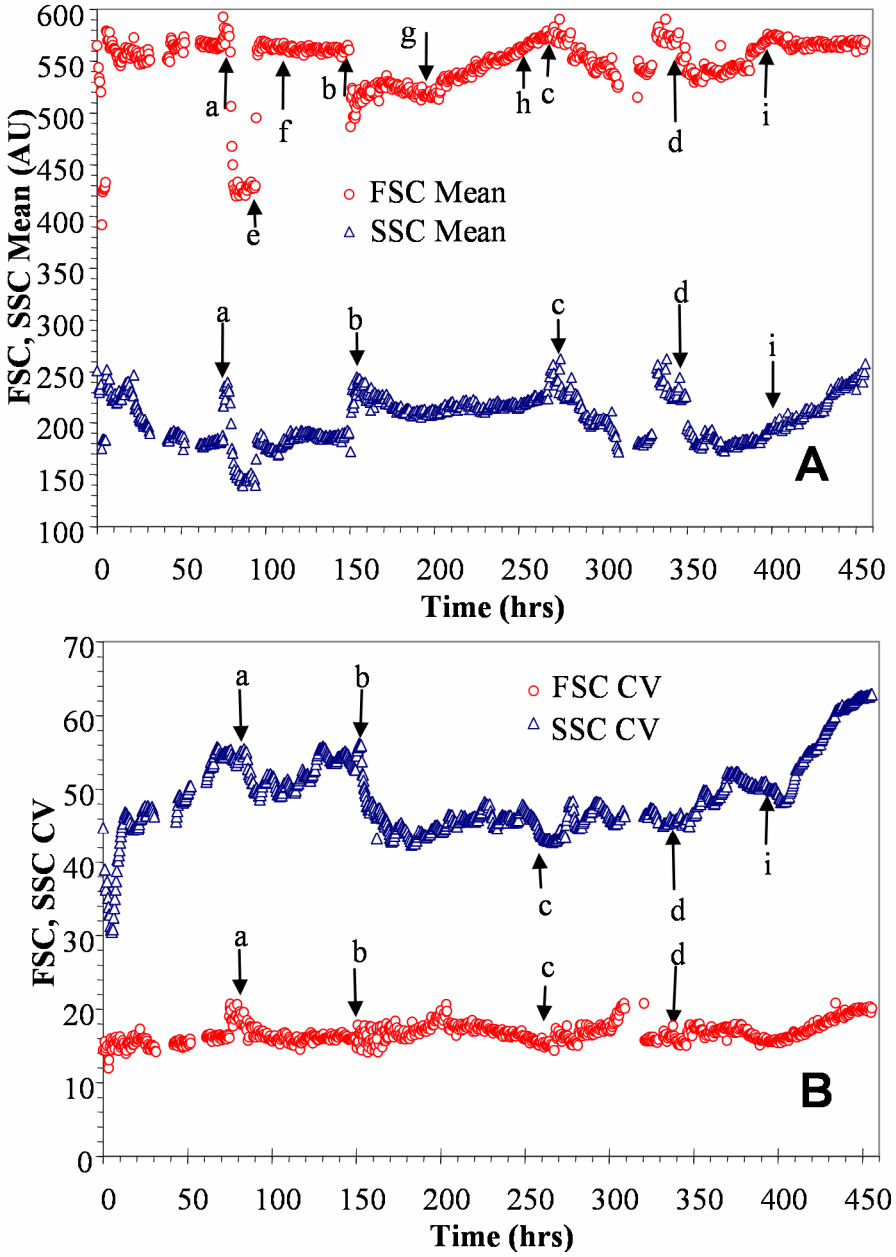

Figure 6-5: Light scattering means and CVs of the culture during the simulated scale up. Arrows (a-d) indicate passages, while arrows (e-i) indicate changes in the growth kinetics within a passage.

6.4 Discussion

The goal of a culture scale up process is to maximize the total number of viable cells in the minimal amount of time (Schoenherr, et al. 2000). This can be accomplished using the developed passaging strategy which maintains the culture in exponential proliferation and prevents entry into stationary/death phase. The same strategy can also be used to ensure that fed-batch additions occur during the appropriate proliferation phase. Central to this strategy is the ability of automated flow cytometry to accurately and frequently assess the cell proliferation and death kinetics. This enables the end of exponential phase to be predicted and action to be taken. Previous attempts at predicting the end of exponential proliferation have not been successful due to limitations in the techniques used to count cells (Grammatikos, et al. 1999). These limitations stem from two fundamental issues, the frequency of the sampling and the sensitivity of the measurement.

When discrete samples are taken from a continuous process, effectively digitizing the signal, the absolute minimum sampling frequency required to characterize the continuous process must be at least twice the highest frequency component in the continuous system. This minimum frequency is termed the Nyquist frequency of the process (Jerri 1977). If one assumes exponential growth, then the highest frequency component in the process is the specific growth rate of the culture. Thus, one typically samples at a Nyquist frequency of twice the specific growth rate of the culture. For a CHO culture with a 16 hour doubling time, the Nyquist sampling interval is every 8 hours, which is greater than typical sampling frequencies found in literature (Abu-Absi and Srienc 2002 ; al-Rubeai and Singh 1998 ; Deshpande and Heinzle 2004 ; Wlaschin

and Hu 2006). However, if one samples at the Nyquist frequency, assuming exponential growth, one cannot make accurate statements or projections about processes occurring at frequencies higher than the sampling rate. Cell death, partial or fully synchronous growth, and cell cycle related events occur at frequencies that are higher than the specific growth rate of the culture. Important features such as the partial synchrony induced by the fed batch addition and the death phase of the process would not become readily apparent at a traditional sampling rate. Thus, one must sample from the bioreactor at a high enough frequency to accurately characterize cell death, synchrony, and cell cycle processes. Unless significant labor is expended, offline techniques like hemacytometer counts cannot reach a sufficient sampling rate to characterize high frequency processes. The higher sampling rates required to characterize these processes practically require an online technique.

Currently developed online biomass monitoring methods are either indirect or direct methods (Konstantinov, et al. 1994). Indirect methods typically measure a growth byproduct or a metabolic rate (i.e. lactate, glucose, OUR (Oxygen Uptake Rate), Glucose uptake rate, etc). However, these methods assume that the specific metabolic rates are constant, which is often not the case, especially during transient growth conditions or during death phase (Deshpande and Heinzle 2004 ; Grammatikos, et al. 1999 ; Konstantinov, et al. 1994 ; Locher, et al. 1992a ; Locher, et al. 1992b). Direct methods such as in-situ microscopy (Bittner, et al. 1998 ; Joeris, et al. 2002), dielectric spectroscopy (Cerckel, et al. 1993 ; Kell, et al. 1990), turbidity (Konstantinov, et al. 1994), or capacitance detection (Cannizzaro, et al. 2003) measure the cells or components within the cells directly. However, these methods tend to have low

sensitivity, are affected by medium debris, and usually are unable to measure cell concentrations below $5x10^5$ cells ml^{-1}. Furthermore, of the methods listed above, only dielectric spectroscopy is able to estimate the viable and non-viable fractions of the population although only qualitatively (Cannizzaro, et al. 2003). An additional direct online biomass monitoring method, the CEDEX cell counter, is able to detect viable and non-viable cells at low concentrations while measuring cell size. Thus, for the data acquired in this study, this online instrument would be able to acquire similar data. However, the full range of possible applications for automated flow cytometry has not been exhausted as automated flow cytometry can in principle provide online data relating to any single-cell property for which a flow cytometry stain exists.

Therefore, the described instrumentation provides an advantage over traditional biomass characterization techniques due to its capability to frequently sample from the bioreactor and accurately assess the heterogeneity of the cell population. As this study shows, this high accuracy, high frequency approach is important in uncovering new critical process parameters and implementing control strategies around these parameters. It is this type of approach that is central to the FDA's PAT initiative where process improvements stem from improved process supervision derived from knowledge-based data analysis (Gnoth, et al. 2007).

For example, as shown in this study, the traditional indicator of cell death, the viable fraction, is a poor indicator of the cell death kinetics. The viable fraction is calculated by dividing the viable cell concentration by the sum of the viable and non-viable cell concentrations. Since the viable and non-viable cell concentrations are typically separated by several orders of magnitude, changes in the non-viable cell

concentration are masked by changes in the viable cell concentration. This is illustrated in bioreactor A Figure 2A,C where from the onset of cell death to the fed-batch addition, the viable fraction decreased by only 0.6% while the non-viable cell concentration increased by a factor of four.

Furthermore, as this data shows, there is significant variation in the specific proliferation rate of the culture between batches as well as within individual batches despite control of bulk culture parameters. It is this type of behavior that cannot be explained by unstructured models of cell proliferation. Thus, it is likely that traditional unstructured modeling approaches, which have been successfully used in previous PAT initiatives to understand batch to batch variations in bacterial cultures (Gnoth, et al. 2007 ; Streefland, et al. 2007) would not adequately describe mammalian cell culture processes. Instead, structured models that can account for the inherent culture heterogeneity arising for instance from genetic differences, cell cycle position, or stochastic fluctuations, would be more applicable (Abu-Absi, et al. 2003 ; Europa, et al. 2000 ; Fredrickson, et al. 1970 ; Kacmar, et al. 2004b ; Kacmar, et al. 2006 ; Kacmar and Srienc 2005 ; Kromenaker and Srienc 1991 ; Kromenaker and Srienc 1994a ; Mantzaris, et al. 2002 ; Mantzaris, et al. 1999 ; Mantzaris, et al. 2001a ; Mantzaris, et al. 2001b ; Mantzaris, et al. 2001c ; Sandhu, et al. 2007).

6.5 Conclusion

The developed passaging and fed-batch addition strategy can be used to reproducibly control fed-batch additions to a culture and automate culture scale-up. This ensures exponential proliferation at all times thus minimizing the time required for culture scale-up. The strategy can also be used to ensure that fed-batch additions occur

during the appropriate proliferation phase, resulting in a significantly higher total integral cell counts in the reactor. Furthermore, the instrumentation utilized in this study provides a distinct advantage over traditional biomass characterization techniques due to its capability to frequently sample from the bioreactor and accurately assess the properties of each sample. This is important in uncovering new critical process parameters and implementing control strategies around these parameters. It is this type of approach that is central to the FDA's PAT initiative where process improvements stem from improved process supervision derived from knowledge-based data analysis.

7 Cell Population Laboratory for Engineers

7.1 Introduction

Bioengineering has gained a central role in chemical engineering, and its advances are expected to lead to future technological developments significantly impacting society in the new century. The increasing impact of biology within chemical engineering has been evident over the past several decades within the chemical engineering community. As a result, during the past several years, there have been several chemical engineering departments who have changed even their department name to reflect the increasing role of biology. The increased emphasis on biology within chemical engineering must be reflected also in the curriculum that forms the basis for educating undergraduate students with the fundamentals of the new fields. According to the new ABET accreditation criteria, successful programs with enhanced biology focus must demonstrate that future graduates have proficiency in mathematics through differential equations, a thorough grounding in chemistry and biology and a working knowledge of advanced biological sciences consistent with the program educational objectives. Competence must be demonstrated in the application of engineering to biological systems.

Outstanding instruction should draw upon strength in research. As recently pointed out in a planning report (Harvard University Planning Committee for Science and Engineering 2006) there is now ample evidence that lecture based instruction in science and engineering is less effective than many would like to think (DeHaan 2005 ; Handelsman 2004 ; Kenney 1998). To make biology and engineering come alive for

students, it is recommended to implement hands-on learning as a cornerstone in undergraduate science and engineering education. For the efficient introduction of the new biology focus into the chemical engineering curriculum it is, therefore, particularly important to enhance the existing curricula with increased hands-on learning for undergraduates in areas that bridge these disciplines and that demonstrate how chemical engineering principles are applied to biological problems.

Teaching and research in science and engineering require access to an evolving set of cutting edge tools and facilities. This requires steady renewal of teaching facilities for science and engineering, commensurate with the focus on hands-on learning. To enhance undergraduate education it is recognized that undergraduate laboratory experiences should move toward including project-based efforts in addition to training in basic laboratory skills. While it will still be necessary to train students in the basics of how to work in a laboratory, performing a series of experiments to ask a novel question will increase educational value and a student's excitement about a career in science or engineering. A set of project laboratory courses that integrate with the didactic curriculum to build both technical and investigational skills will fulfill this goal. In the Chemical Engineering curriculum the Unit Operations laboratory traditionally provides the hands-on environment in which the principles conveyed in lecture classes are applied in real-world, project-oriented experiments.

We have developed novel, cutting edge, biological laboratory experiments within the framework of the traditional Unit Operations laboratory course for chemical engineers. In contrast to most biological research interests, many chemical engineering problems revolve around the dynamics of systems. Therefore, it is less of concern what

the detailed structural components are of a biological system. The real chemical engineering interest relates to how this system changes in time as the dynamics determines the design of how the biological system can be used in specific applications and how it can be sized to production scale. The designed experiments focus on the interactions of cells with their environment which supports cell growth, the consumption of nutrients, and the formation of useful products. It was impossible to carry out the envisioned experiments in the past because they involved extended proficiency in sophisticated analytical laboratory techniques and cell biological methods. It would have required a prohibitive amount of time for a chemical engineering undergraduate to learn these techniques in order to get to the desired dynamic data.

This was accomplished through the application of automated flow cytometry that handles the cell preparation task in an automated, highly reproducible manner. Moreover, it can generate data on cell cultures over extended time periods without manual intervention. Thus, the proficiency in sophisticated cell biological laboratory techniques is not needed, and the students are still able to generate the data that are of the core concern and that are the true subject of study. Moreover, the obtained data are of the most detailed nature as the distributions of cellular properties in a developing and growing cell population are generated. Therefore, students are trained immediately to think about cell cultures in terms of populations of individual cells that are distributed in their properties and that need a description using statistical tools. This way of thinking is not very common, not even among biological scientists as it is standard practice to investigate cellular activities as the average obtained from populations of cells. This is

practiced also in traditional biochemical engineering approaches that typically lump the entire cell population into a single, unstructured biomass that is followed in time. The proposed experiments, described in this proposal, represent a major deviation from the traditional approaches. These experiments will enable the hands-on learning of concepts in population dynamics by chemical engineering undergraduates. Such experiments were accessible so far only to a small group of researchers proficient in rather sophisticated analytical and cell biological laboratory techniques. In view of the expectations we have in biological engineering in this century it seems only appropriate that future generations of biology oriented chemical engineers are trained and educated at a level of sophistication commensurate with the expectations.

7.2 Current Engineering Laboratory Methodologies

While many laboratory experiments have been developed to teach the concepts of cellular growth and bioreactor principles none have been developed to explore the population balance aspects of cellular growth. Furthermore, current laboratory experiments designed to teach the concepts of cellular growth and bioreactor principles have common themes that detract from the core concepts outlined above:

1. The relatively slow response time of biological systems limits what can be taught in an undergraduate course (Li, et al. 2004 ; Shuler, et al. 1994)
2. An assumption that students must be present to sample from the bioreactor (Anderson 1972 ; Badino, et al. 2004 ; Davis and Kompala 1989 ; Robinson, et al. 2002 ; Shuler, et al. 1994)
3. Having students perform analytical methods (i.e. glucose assays, HPLC, etc) occupies valuable laboratory time (Anderson 1972 ; Badino and Hokka 1999 ;

Badino, et al. 2004 ; Davis and Kompala 1989 ; Shonnard, et al. 2003 ; Shuler, et al. 1994) and leads to consistent errors in the analytical procedure (Anderson 1972).

4. Due to these limitations, undergraduate laboratory experiments in the field of cellular growth have been effectively stagnant since early descriptions of undergraduate batch growth experiments (Anderson 1972) and undergraduate oxygen transfer experiments (Davis and Kompala 1989).

Therefore, we incorporated a new instrument, automated flow cytometry, into an undergraduate laboratory course. This instrument can overcome the fundamental limitations of current undergraduate cellular growth and bioreactor experiments. First, because cytometry measures how cellular properties are distributed across a population of cells, the concepts of the population balance equation can be explored. Second, by having an instrument automatically sample a bioreactor, students can set up an experiment, leave the lab, and come back days later. This enables undergraduates to overcome the limitations of the slow response time of biological systems. Furthermore, the instrumentation enables a new type of continuous culture, called the cytostat, which eliminates the need to measure metabolites in continuous cultures and quantitative physiological parameters of engineering relevance can be readily determined.

7.3 Course Development

7.3.1 Current Course

In past semesters, a special section of the Chemical Engineering Unit Operations course at the University of Minnesota was offered to Chemical Engineering

undergraduate students. The course taught the concepts of viewing biological processes as a stoichiometric equation, bioreactor operation, oxygen transfer fundamentals, and batch growth dynamics. The course also implemented automated flow cytometry to monitor the batch growth of yeast cells. The half semester long laboratory course was comprised of three two-week long experiments.

7.3.2 Experiment #1: Media Design and Selection

The major theme of the first experiment was to use a statistical design of experiments to optimize a media composition for an auxotrophic yeast strain. During the two week long experiment, students were exposed to the concepts of the stoichiometric balance of cell growth, yield coefficients, statistical design of experiments, auxotrophy, and selection pressure. Students explored these concepts by varying the concentration of carbon and nitrogen in the medium according to a statistical design of experiments. The dependent variable the students measured was the total amount of cell growth assessed by traditional biomass characterization techniques i.e. optical density, cell dry weight, and cell counts using a Coulter counter. By measuring the biomass response as a function of nutrient concentration, students were able to calculate yield coefficients. During this lab, students became proficient with the technical skills of sterile technique and performing traditional biomass characterization techniques.

7.3.3 Experiment #2: Bioreactor Operation and Oxygen Transfer Kinetic

The major theme of the second experiment was to determine the effect of agitation and aeration on the oxygen transfer rate and measuring the oxygen uptake rate

of the cells. During the two week experiment, students were exposed to the concepts of oxygen transfer in a bioreactor, the oxygen uptake rate by the cells, and the overall oxygen mass balance in a bioreactor. During the first week of the experiment, students explored the concept of oxygen transfer using the sulfite degassing method at various agitation and aeration rates according to a statistical design of experiments (Hermann, et al. 2001). In the second week of the experiment, students explored the oxygen uptake rate of cells using off-gas mass spectroscopy to measure the amount of oxygen consumed by the cells. During these experiments, students became proficient with the technical skills of operating a bioreactor.

7.3.4 Experiment #3: Batch Growth Monitoring with Automated Flow Cytometry

The major theme of the third experiment is to expose students to the idea of batch growth kinetics and automated flow cytometry. During this lab, students learn about the different phases of batch growth, cytometry, the kinetics in each phase, and are exposed to the concept that cells are heterogeneous. The students work with a yeast cell line containing a plasmid encoding for green fluorescent protein (Gfp).

Over two weeks, students prepare and sterilize a bioreactor, prepare medium in accordance with their results from experiment #1, inoculate the bioreactor, operate the bioreactor at the ideal agitation and aeration rates determined in experiment #2, and monitor the process of cell growth with automated flow cytometry. In this experiment, the automated flow cytometry device samples from the inoculated bioreactor every 10 minutes, dilutes the sample a prescribed amount, and then injects the sample into the

cytometer where the absolute cell count, mean Gfp fluorescence, cell viability using propidium iodide staining, and cell size are determined. The automated device allows students to set-up the experiment, leave the lab, and then return days later to collect their results. As the example data from the existing lab shows in Figure 7-1, students can easily see the boundaries between lag, exponential, stationary. Furthermore, students can begin to see how the culture changes on a single cell basis. For example, students can track the mean of a cellular property (i.e. Gfp fluorescence as shown in Figure 7-1, cell size, etc).

7.4 Proposed Course

While the current course helps students learn important material about cell growth, the potential of automated flow cytometry in the undergraduate lab is not fully developed. In its present state, the course does not convey the concepts of continuous cultures and population balances to the students. Therefore, we developed three new experiments to convey this information. These proposed experiments will fit into two-week blocks and when combined with the existing set of experiments will expand the course to a full semester that will cover the complete theory of cell growth.

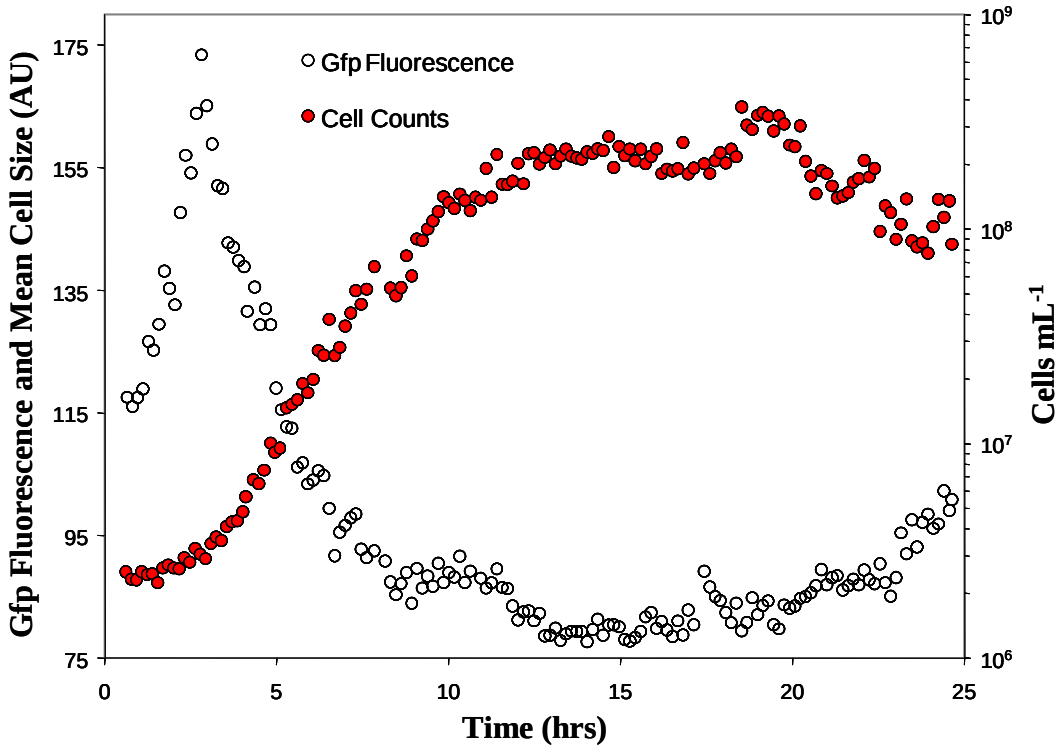

Figure 7-1: Student acquired data of yeast cells growing and expressing Gfp. Time course of the mean single cell Gfp fluorescence and absolute cell counts obtained by students using automated flow cytometry for yeast cell growth.

7.4.1 Proposed Experiment #1: Cytostat Operation

The batch growth experiment monitored by automated flow cytometry exposed students to the kinetics of cell growth and provided a glimpse at the population dynamics of the culture. However, the experiment did not expose students to the relation between the cell physiology and the environment and the specifics of the population dynamics. This is because the composition of culture medium will not reach a non-trivial steady-state in a batch experiment and thus the relation between the cells and the environment is always changing. Therefore, the cytostat (Gilbert and Srienc 2008 ; Gilbert, et al. submitted ; Kacmar, et al. 2006), a type of continuous culture described above is ideal because the composition of the culture medium is constant and identical to the composition of the feed medium. Thus, the major theme of the first new experiment will be for the students to operate a cytostat to determine the Monod parameters for yeast growth on glucose as shown in Figure 7-2. Thus, students will be able to precisely determine the relationship between the environment and cell physiology because the automated flow cytometry system provides a detailed time course of cell phenotype. Also, this experiment allows examination of the population dynamics of the culture. Specifically, the single cell growth rate function can be determined. Since immediately after the glucose concentration is upshifted from a 'low' to a 'high' amount the culture becomes partially synchronized. When the degree of synchronization is high, it is possible to approximate the net birth rate function as zero (i.e. the right hand side of (1.1)). Now, the one-dimensional population balance model simplifies to

$$\frac{\partial f(m,S,t)}{\partial t} + \frac{\partial [r(m,S,t) f(m,S,t)]}{\partial m} = 0 \tag{6.1}$$

Since the substrate concentration (*S*) is constant and the automated flow cytometer measures the distribution of cell sizes *f(m,S,t)* over time, this equation is readily solved (Gilbert 2008):

$$r(m,S,t) = \frac{1}{f(m,S,t)} \frac{\partial \left(\int_{m}^{\infty} f(m,S,t) dm \right)}{\partial t} \tag{6.2}$$

Thus, students can begin to experimentally determine the functions of the population balance models.

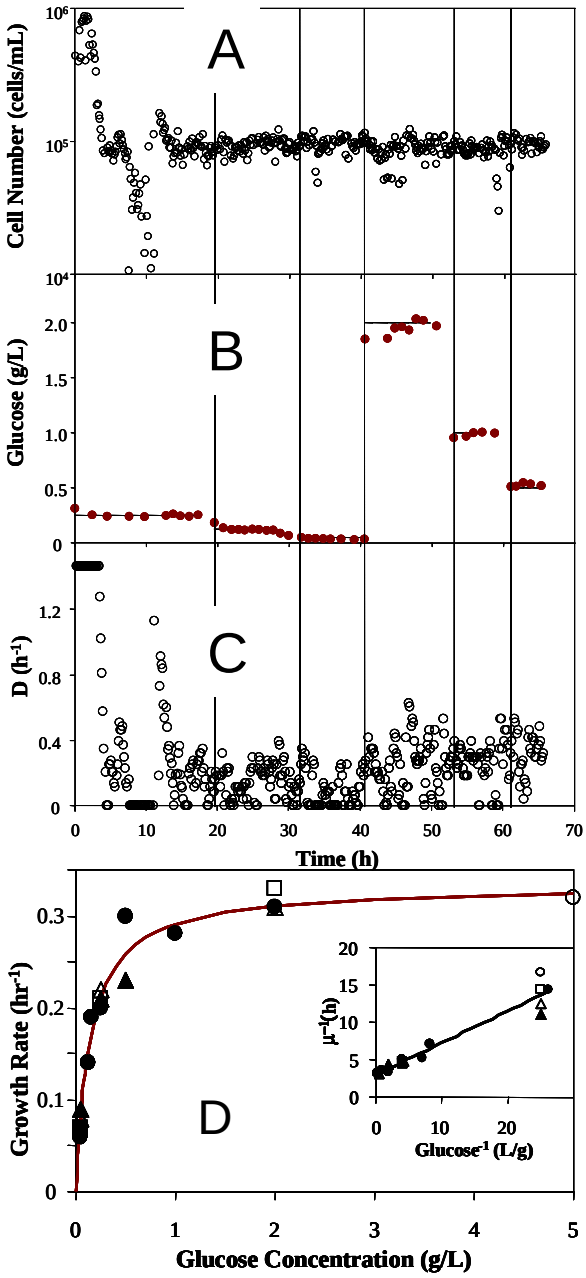

Figure 7-2: Example cytostat data for a proposed experiment. **(A)** Control of cell number at 10^5 cells mL^{-1}. **(B)** Glucose concentration in the feed is shifted to different levels and the glucose concentration is measured in the bioreactor. **(C)** Dilution rate at the different glucose concentrations **(D)** Monod curve of the cell growth rate versus the substrate concentration.

7.4.2 Proposed Experiment #2: Plasmid Stability and Induction

The major theme of the second proposed experiment is to have students study the processes of plasmid stability and induction using the cytostat and batch culture monitoring with automated flow cytometry. Combined, these two experiments will teach students the basic kinetics of protein expression from plasmids. In the plasmid stability experiment, the students will apply the concepts of continuous cultures to model how the culture will revert back to wild-type, and then extract the relevant parameters from their experiment. In the protein induction experiment, students will apply the concepts of a product mass-balance, as well as precisely observe the response kinetics of the system across the entire population of cells.

Genetic engineering of organisms in both commercial and laboratory scale settings typically involve transfection of cells with a plasmid. Cultures of plasmid containing cells are typically unstable and lose the plasmid over time due to unequal partitioning and genetic modification of the plasmid. Plasmid containing cells typically grow at a slower rate than wild-type cells due to the increased metabolic burden forced by the formation of the encoded protein. The larger growth rate of wild-type cells eventually leads to the reversion of the culture back to the wild-type phenotype (Bentley and Kompala 1990). The automated flow cytometry system is ideal for studying this process, because for a cell containing a plasmid constitutively expressing Gfp, the fraction of plasmid containing and wild-type cells can be readily determined over time as shown in Figure 7-3. Therefore, the major theme during the first week of the second

proposed experiment is to track how a transfected yeast culture reverts back to its wild-type state in a cytostat.

During the second week of the experiment, students will study the response of inducible promoters in a batch culture. An inducible promoter begins expressing the encoded protein only in the presence of an inducer molecule. Inducible protein expression is common in both the natural world and in industrial fermentations. Therefore, understanding the kinetics of this process is of significant relevance. For a cell containing a plasmid with inducible expression of Gfp, automated flow cytometry is ideal for studying protein induction due to the ability of the system to easily quantitate the amount of Gfp in single cells.

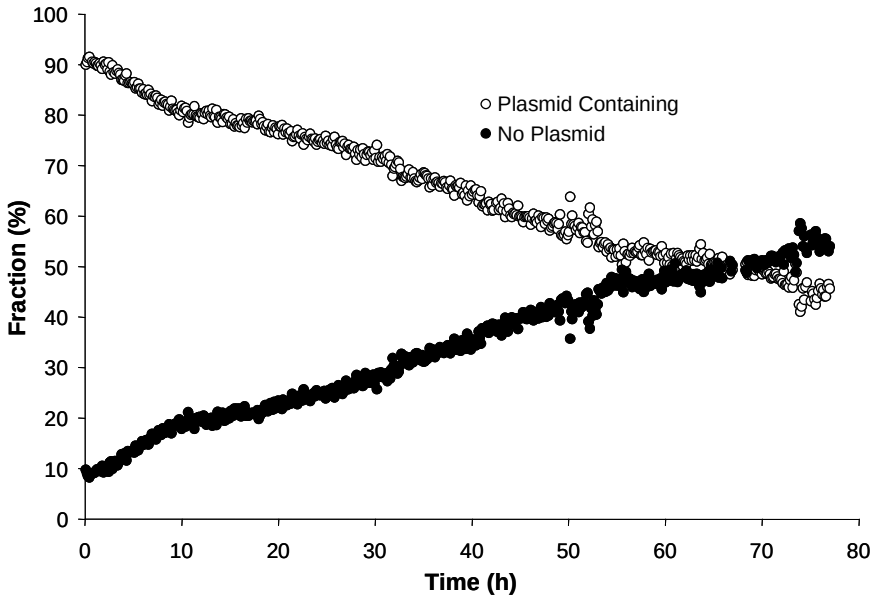

Figure 7-3: Plasmid free yeast cells overtake plasmid containing cells in non-selective media. The population dynamics of a yeast culture in a cytostat containing a plasmid expressing Gfp in nonselective medium. Over time, the population containing no plasmid grows faster, and overtakes the plasmid containing population.

7.4.3 Proposed Experiment #3: Transient Gene Expression in Mammalian Cell Culture

The major theme of the third proposed experiment is to study the population dynamics of transient gene expression in batched mammalian cell culture. During this experiment, undergraduate students will learn the technical skills unique to mammalian cell culture and bioreactor operation of mammalian cell culture. They will also apply the concepts of the population balance equation to interpret the response of the system. Transient gene expression is when plasmid encoding a protein of interest is introduced into cells and no effort is made to select or screen for positive transfectants. Transient gene expression is frequently used in industry to rapidly generate usable quantities of a protein from cultured cells. It is also used in gene therapy applications to express a therapeutic protein *in vivo*. Cell heterogeneity significantly affects the transient gene expression characteristics of a culture. Therefore, the population dynamics of this process are of significant interest. Specifically, once a parent cell is loaded with a non-replicating plasmid, subsequent divisions of the parent cell will partition plasmid and the expressed protein between the two daughter cells. Therefore, subsequent generations of cells will have discretely lower quantities of the expressed protein present in the cells. This is shown by the clearly visible discrete groups in Figure 7-4. Figure 7-4 is comprised of a series of histograms that are stacked to show the time evolution of the distribution of Gfp content. Cell frequency is coded by the color (Sitton, et al. 2006).

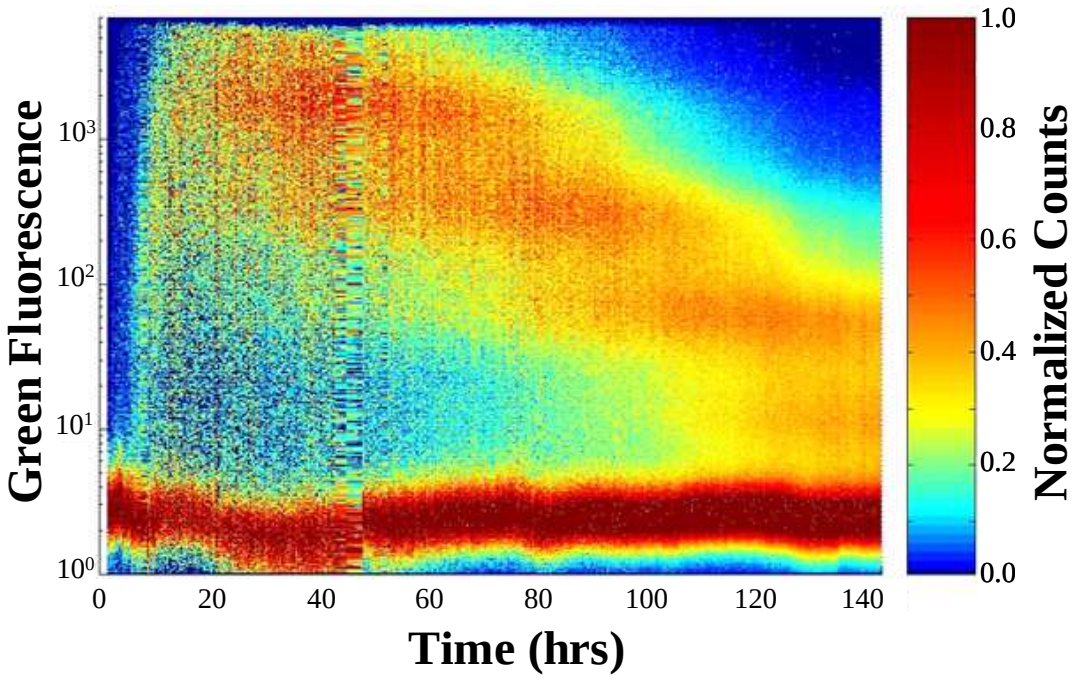

Figure 7-4: Time course histogram of Gfp fluorescence during transient gene expression. This graph is comprised of a series of histograms that are stacked to show the time evolution of the distribution of Gfp content. Cell frequency is coded by the color. Initially, cells are loaded with a high amount of plasmid and subsequently express a high amount of Gfp as seen by the highest discrete group. Subsequent generations have discretely less plasmid and thus less Gfp due to partitioning of plasmid and Gfp between daughter cells as seen by each discrete group at a lower Gfp content.

8 Single Cell Tracking Cytometer: Theory

8.1 Instrument Concept

The core idea of the single cell tracking cytometer is to take a plug of tens to hundreds of suspended cells in a capillary and pump this plug of cells past a measurement point in one direction. For each event when a cell crosses the laser, the time that this occurs, the fluorescent properties, and the light scattering properties of each cell in the plug is recorded. Next, by simply reversing the flow for an equivalent amount of volume, the same plug of cells will pass by the measurement point as shown in Figure 8-1. This oscillatory pumping cycle is then repeated hundreds of times over hours. By grouping all strokes in a respective direction together one can then associate events in adjacent strokes that have similar laser crossing times, fluorescent properties, and light scattering properties to an individual cell. Thus, an individual cell can be 'traced' through hundreds of cycles.

As a first approximation, one would assume that since cells are micron sized particles, diffusion of the particles would play a large role in the particles shifting radial positions between strokes. However, the core innovative concept enabling this cell detection scheme is a two-phase flow phenomenon termed the Segre Silberberg effect (Segre and Silberberg 1961 ; Segre and Silberberg 1962). The Segre Silberberg effect states that if dilute, neutrally buoyant, constant size particulates in a fluid are placed in a tube and subjected to Poiseuille flow, particulates of significant particulate to tube radius ratio will accumulate on an equilibrium radius. Therefore, all particulates of a given size and shape will self-organize on the same streamline and therefore have the same velocity independent of the direction of the flow. Since each particulate in the

plug has the same velocity and has been pumped for the same amount of time in opposing directions, each particle will move the same distance during each set of opposing movements and return to the same location. Therefore, the order that the particulates cross the measurement point can be preserved.

8.2 Segre Silberberg Effect – Theory

Since the observation of radial migrations of particles with a significant particle diameter to tube diameter ratio in Poiseuille flow by Segre and Siberberg in 1961, many attempts have been made to analytically examine this phenomenon (Auton 1987 ; Bretherton 1962 ; McLaughlin 1991 ; Rubinow and Keller 1961 ; Saffman 1965). These analyses assume Stokes flow is perturbed by inertia or vorticity. The results of these formulae showed that the lift force generated by the rigid particle in Poiseuille flow is a function of the slip translational and the slip angular velocity. However, the Stokes flow assumption used in these analyses to generate the explicit formulae prohibits their application to finite Reynolds number flows. Therefore, to attain useful formulae, Yang et al used direct numerical simulations of circular particles in Poiseuille flow to generate useful correlations between the system geometry and the lift force (Yang, et al. 2005). However, in both the explicit analyses and in Yang et al's analysis, particle size was assumed large enough so that Brownian forces could be neglected. For suspensions of particles with large void fractions where particle-particle interactions are significant, theory has been developed to account for the Brownian motion and the hydrodynamic forces (Nott and Brady 1994). However, for very dilute suspensions of Brownian particles in flow, insufficient theory exists to accurately predict how Brownian particles will be distributed across a flow over time. With the wide-spread

usage of micro-fluidic devices, this topic is increasingly important. Therefore, this section considers how the distribution of dilute, non-interacting Brownian particles across a flow will evolve in time.

Since the particles are assumed to be non-interacting, the behavior of the particles in the flow can be approximated by considering a single Brownian particle in a force field as shown in Figure 8-2.

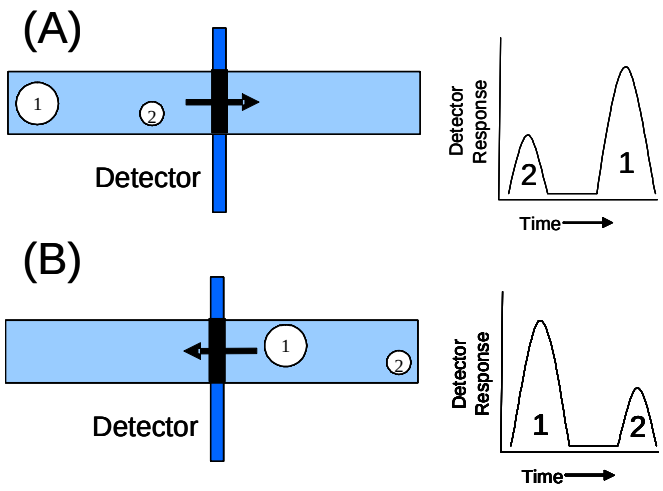

Figure 8-1: Cartoon depicting that the order of cells in a capillary can be preserved during the reversal of flow. **(A)** Scan #1: The two particles, with their respective locations are subjected to flow and travel past the detection point. Particle two is detected first, and then particle one is detected. **(B)** Scan #2: The two particles are then subjected to flow in the reverse direction and travel past the detection point. Particle one is detected first and then particle two is detected. Scan n: This process is then repeated for many iterations.

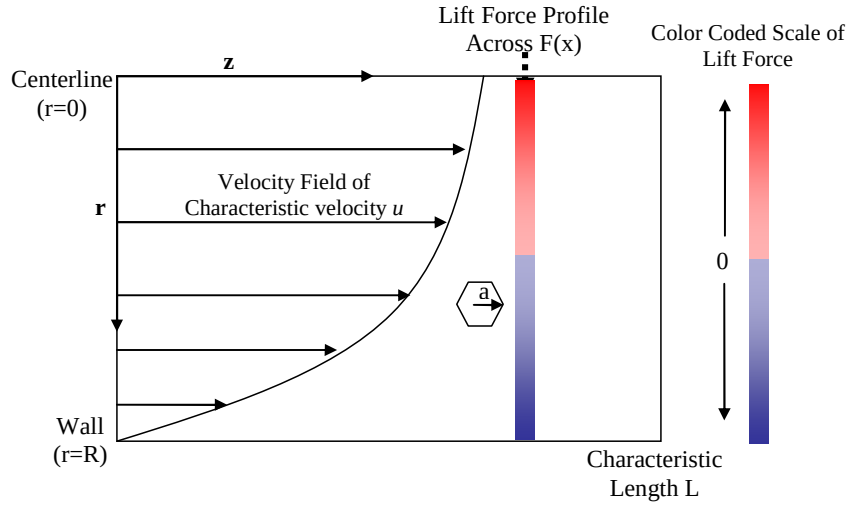

Figure 8-2: Cartoon depicting an arbitrary particle of length scale a in a flow field with characteristic velocity u exposed to a hydrodynamic force F dependent on its radial position r. In this case, an equilibrium position exists when the force on the particle equals 0. Therefore, particulates of a particular size will exist on the same streamline and have the same velocity. Thus, if the pumping time in each direction can be kept the same, the distance traveled by each particle will be identical, and the order of cells can be preserved.

This system can be described by the Langevin equation:

$$mx'' = -\gamma x' + F_{hydrodynamic}(x) + \sigma\xi(t) \tag{7.1}$$

where m is the mass of the particle, x is the position of the particle, γ is a scalar friction constant, $F_{hydrodynamic}(x)$ is a force field caused by hydrodynamic effects, and σ is the amplitude of the fluctuating force ξ. In the absence of an external force field $F_{hydrodynamic}(x)$, it can be shown that a particle will lose its memory of its initial velocity after a time $\tau \approx m/\gamma$. Therefore, if the ratio of the distance the particle traveled after being set into motion at the velocity v_0 to its radius is much less than one, then the particle is said to be in the Smoluchowski time-scale. For a spherical particle, with an initial velocity of $\sqrt{3k_BT/m}$ this ratio can be expressed as:

$$\frac{v_0\tau}{a} = \frac{1}{a}\frac{\sqrt{3k_BT/m}}{\gamma/m} = \frac{\sqrt{3mk_BT}}{6\pi\eta a^2} \tag{7.2}$$

Therefore, if this ratio is much less than 1, which holds for suspensions and some colloids, then it can be assumed that the case of strong friction exists where:

$$|mr''| << |\gamma r'| \tag{7.3}$$

And subsequently, the Langevin equation can be expressed as:

$$\gamma r' = F(r) + \sigma\xi(t) \tag{7.4}$$

The corresponding Fokker-Planck equation to this langevin equation describes the probability of a particle existing at a particular location and at a particular time:

$$\frac{\partial p\left(\bar{x}, t \mid \bar{x}_0, t_0\right)}{\partial t} = \left(\nabla^2 D - \nabla \bullet \frac{F_{hydrodynamic}(x)}{\gamma}\right) p\left(\bar{x}, t \mid \bar{x}_0, t_0\right) \tag{7.5}$$

where p is the probability distribution function of the particle given an initial position and time $\bar{x}_0$, t_0 and D is the diffusion coefficient of the particle equal to $\sigma^2/2\gamma^2$. The derivation of this equation can be found in many statistical mechanics textbooks. This equation is termed the Smoluchowski equation. In the one dimensional case of the Smoluchowski equation, where the diffusion coefficient is equal to $k_B T/\gamma$ and the force field due to hydrodynamic effects can be expressed as the derivative of a potential:

$$F_{hydrodynamic}(x) = \frac{d\phi_{hydrodynamic}}{dx} = \phi'_{hydrodynamic} \tag{7.6}$$

Equation (7.5) can be rewritten:

$$\frac{\partial p}{\partial t} = D\left(\frac{\partial^2 p}{\partial x^2} - \frac{1}{k_B T}\frac{\partial}{\partial x}\left(\phi'_{hydrodynamic}(x)\, p\right)\right) \tag{7.7}$$

Also, given a fully developed velocity field, the time variable t in equation (7.7) can be replaced by the z-location variable z given the relation $z=ut$ to yield :

$$u\frac{\partial p}{\partial z} = D\left(\frac{\partial^2 p}{\partial x^2} - \frac{1}{k_B T}\frac{\partial}{\partial x}\left(\phi'_{hydrodynamic}(x)\, p\right)\right) \tag{7.8}$$

This equation can be non-dimensionalized:

$$\begin{gathered}\frac{uR^2}{DL}\frac{\partial p}{\partial z^*} = \frac{\partial^2 p}{\partial \chi^2} - \frac{F_{char} R}{k_B T}\frac{\partial}{\partial \chi}\left(F^*(\chi)\, p\right) \\ z^* = z/L \\ \chi = x/R \\ F^* = \phi'/\phi'_{char} = F/F_{char}\end{gathered} \tag{7.9}$$

where R, L, $t_{char,}$ and F_{char} are characteristic x length, z length, time, and force scales respectively.

If the probability distribution of a particle at a fixed distance can be experimentally measured, then the hydrodynamic force field can be directly calculated from equation (7.8), at a given z location, temperature, and diffusion coefficient according to:

$$F_{hydrodynamic}(x) = \frac{k_B T}{p(x, z_{fixed})} \int \left(-\frac{u}{D} \frac{\partial p}{\partial z}|_{z_{fixed}} + \frac{\partial^2 p}{\partial x^2} \right) dx \tag{7.10}$$

Alternatively, one can simply examine the system at steady state, as determined by sufficiently small $\frac{uR^2}{DL}$. The steady-state solution to equation (7.8) is simply the Boltzmann formula:

$$p(x) = p_0 e^{-\frac{\phi_{hydrodynamic}(x)}{k_B T}} \tag{7.11}$$

and solving for $F_{hydrodyanmic}$:

$$F_{hydrodynamic}(x) = k_B T \frac{\partial}{\partial x} \left(\ln(p_0) - \ln(p) \right) \tag{7.12}$$

Both equations (7.10) and (7.12) have advantages and disadvantages to experimentally determine the hydrodynamic force. Use of equation (7.10) requires the calculation of $\frac{\partial p}{\partial z}|_{z_{fixed}}$. Therefore, the distribution must be known at two z locations that are sufficiently close for accurate calculation of $\frac{\partial p}{\partial z}|_{z_{fixed}}$. One z location can be the inlet of the tube. If the source of particles at the inlet is sufficiently agitated, this initial distribution can be approximated as uniform. Therefore, the distribution can then be

directly observed at a single point close to the inlet. Alternatively, use of equation (7.12) requires an observation at sufficiently large L such that $\frac{uR^2}{DL} \approx 0$. Furthermore, it requires that the distribution *p(x)* has sufficiently large probabilities across all values of x that it can be experimentally measured in a reasonable time frame. Use of either equation in a properly designed experimental system would be a unique and novel method to determine the lift force across the flow profile with many advantages over previous experimental techniques. Previous attempts to experimentally measure the lift force involves tethering a particle to some force measuring device or tracking a single particle's trajectory (Goldsmith and Mason 1962 ; Goldsmith and Mason 1967). Tethering the particle has the potential to disturb the flow, and thus influence the experimental results. Also, tracking a single particle's trajectory has the drawback of requiring specialized equipment.

The relationship between the imposed hydrodynamic force field and the thermal fluctuations of the system can be expressed by the dimensionless group, $\frac{F_{char}R}{k_BT}$ in equation (7.9). This group defines the balance between the imposed hydrodynamic force field and the thermal fluctuations of the system. This dimensionless group is a generic version of the Peclet number for mass transport. The more commonly defined Peclet number $\frac{uR}{D}$ can be arrived at by defining the characteristic force as γu , otherwise known as the Stokes drag force. However, the Stokes drag force is a very poor choice to scale the hydrodynamic force. Previous theoretical investigations into the

hydrodynamic force, otherwise known as the lift force, have shown that the lift on the particle is:

$$F_{lift} = k\Omega_s U_s \tag{7.13}$$

where k is a proportionality constant, Ω_s is the angular slip velocity defined as the difference between the angular velocity of the particle and the angular velocity of the particle at it equilibrium radius, and U_s is the translational slip velocity between the particle and the fluid (Yang, et al. 2005). It has been shown by direct numerical simulation that the lift force on a spherical particle in Poiseuille flow varies non-linearly with the ratio of the particle radius to tube radius and the Reynolds number of the flow (Yang, et al. 2005). This non-linear behavior is not captured by simply scaling the lift force by the Stokes drag force. Instead, a better method to determine the characteristic force is to find the maximum of the lift force across all x. The location that this will occur is when the product $\Omega_s U_s$ is at its maximum. This product would be maximized when the particle is held stationary relative to the flow. Without external intervention, the only possible location where this can occur is as the particle approaches the wall. Leighton and Acrivos determined that at this location in a shear flow the lift force on a spherical particle equals:

$$F_{lift} = 9.33G^2 a^4 \rho \tag{7.14}$$

where G is the gradient of the velocity and ρ is the density of the carrier liquid (Leighton and Acrivos 1985). In Poiseuille flow at the wall, the velocity gradient can be approximated as shear flow and equation (7.14) becomes:

$$F_{lift} = \frac{150u^2a^4\rho}{R^2} \tag{7.15}$$

Therefore, the Peclet number for a spherical particle in Poiseuille or shear flow:

$$N_{Pe} = \frac{150u^2a^4\rho}{k_BTR} \tag{7.16}$$

For a particle of arbitrary shape, Leighton and Acrivos' analysis would have to be repeated, and a corresponding characteristic force would be used in the generic Peclet number. Thus, for a particle's diffusion to be neglected the Peclet number must be kept high.

8.3 Segre Silberberg Effect – Experiment

For instance, the developed device described in Appendix 13.II.e) obtains a Peclet number of ~10^5 for 6 μm polystyrene particles. For this Peclet number, one would expect the Segre Silberberg effect to dominate, and diffusion of the particle could be neglected. To demonstrate if the theory outlined above holds true, a single 6 μm particle was loaded in the device and oscillated. As Figure 8-3 shows, where the x-axis are all strokes in the up direction and the y-axis is the time that a particle crossed the laser within a stroke a single particle follows a defined trajectory. This defined trajectory allows one to track a particle for hours.

To assess the magnitude of the difference in particle crossing times between neighboring strokes, the histogram of these distances is shown in red in Figure 8-4. This data is compared to a simple Monte Carlo simulation that neglects the Segre-Silberberg effect and allows an *in silico* 6 μm particle to diffuse randomly in an oscillating plug of fluid. In this figure the Segre-Silberberg effect becomes clearly

visible. The experimental distances are much narrowly distributed than the expected distribution due to random diffusion. It is interesting to note that the experimentally determined distribution is not centered on the origin but shifted to the right. If the density of the particles is higher than the fluid medium then the particles are expected to settle during the oscillatory movement of the fluid. If the density is less than the fluid then the particles will rise due to buoyancy effects. Thus, it is hypothesized that the slope to the particle traces are partially due to the particle settling velocity causing the trajectories.

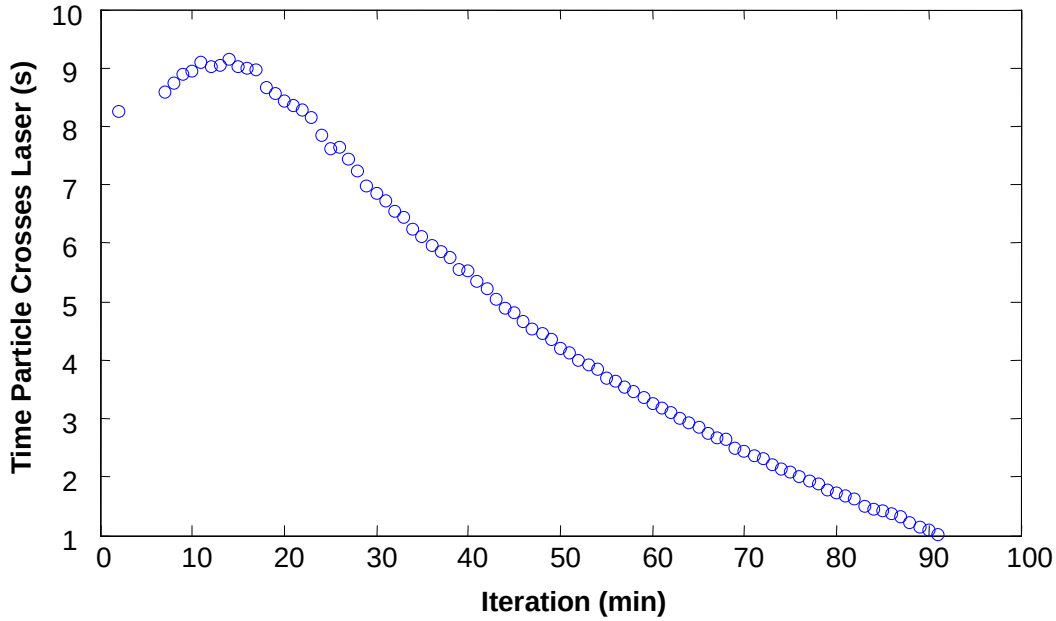

Figure 8-3: A trace of a single 6 μm particle in the developed cytometer described in Chapter 13-II-f). The x-axis are all strokes in the up direction and the y-axis is the time that a particle crossed the laser within a stroke. The particle is traced for over 2 hours.

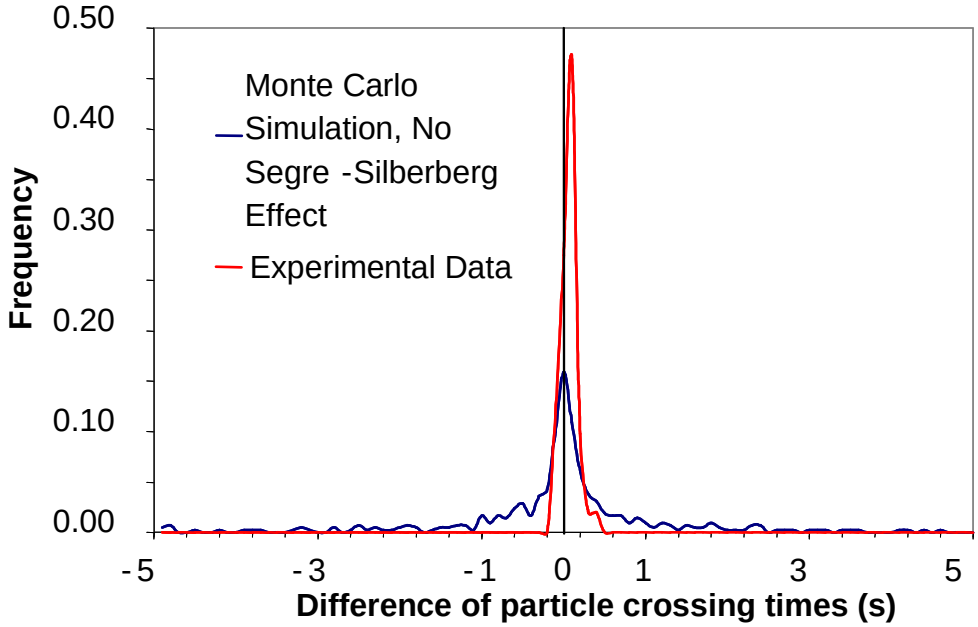

Figure 8-4: Monte Carlo simulation of a particle with and without the Segre Silberberg effect. Distribution of the relative distances that particles move between two strokes. Experimental data (red) and Monte Carlo simulation (blue) permitting particles to diffuse freely. Both simulations were performed with a 1.5 μL stroke length.

8.3.1 Particle Mixtures

As shown in Figure 8-3, a single, constant sized and shaped particle can be tracked in the device for many hours. However, to successfully apply the instrument concept to analyze a cell population, many particles must be measured in a single plug. To accomplish this, the concentration of 6 μm polystyrene particles in the plug was increased and oscillated in the device as shown in Figure 8-5. As this figure shows, multiple unique particles follow predictable traces during oscillating flow. However, it is apparent that some particles in the plug of cells (highlighted in the yellow box) do not cross the laser at predictable times. Instead, the change in the slope and the discontinuities in the traces are hypothesized to arise from particles shifting their streamlines due to potentially asymmetric particle shapes, or multiple particles that are near each other during oscillation and thus two particles are interacting. It is also possible that acceleration and density differences between cells play a role in this behavior.

Next, to more accurately simulate a distribution of cells, a mixture of different sized polystyrene particles: 10 and 20 micron were oscillated in the device. These particle sizes were chosen to represent the extreme ends of a distribution of a CHO cell size distribution. The mixture that was loaded into the experimental device and analyzed consisted of 17 particles 4 were 10 micron and 13 were 20 micron polystyrene particles. Similar to Figure 1, the plot of when each particle crosses the laser for each respective stroke allows analysis of the trajectory of each particle in the plug as shown in Figure 5A. While this Figure shows that this is an ordered system where most

particles follow predictable paths through the plug, even at this low cell density, tracking is less clear based on the timing information alone. However, the identification of individual particle tracks becomes possible again if the individual particle properties as reflected in the measured signals are taken into account. The FSC signals of 10 and 20 um particles are significantly different. If the tracking data are gated according to the signal intensity of 10 um particles then these particles can be clearly differentiated from the 20 um particles. The corresponding tracks are shown in Figure 8-6B.

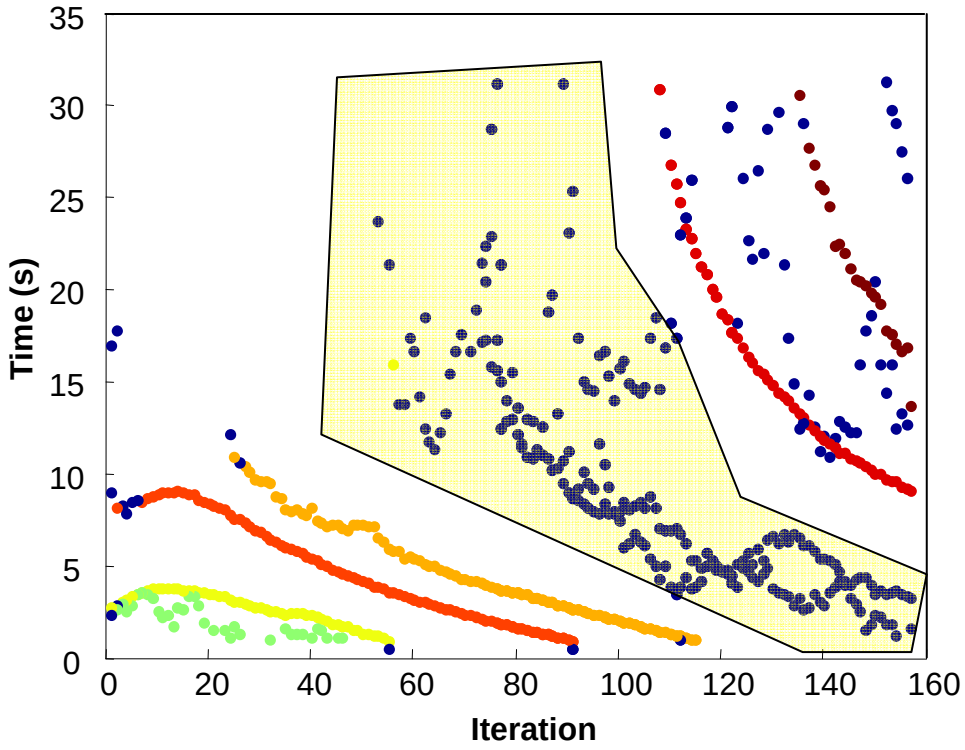

Figure 8-5: Traces of many 6 μm fluorescent particles. A plug with an increased concentration of 6 μm particles, relative to Figure 8-3 were oscillated in the device. Particles that are colored indicate unique individual particles traced through the device. The two particles highlighted in the yellow box do not follow predictable lines as the other particles do.

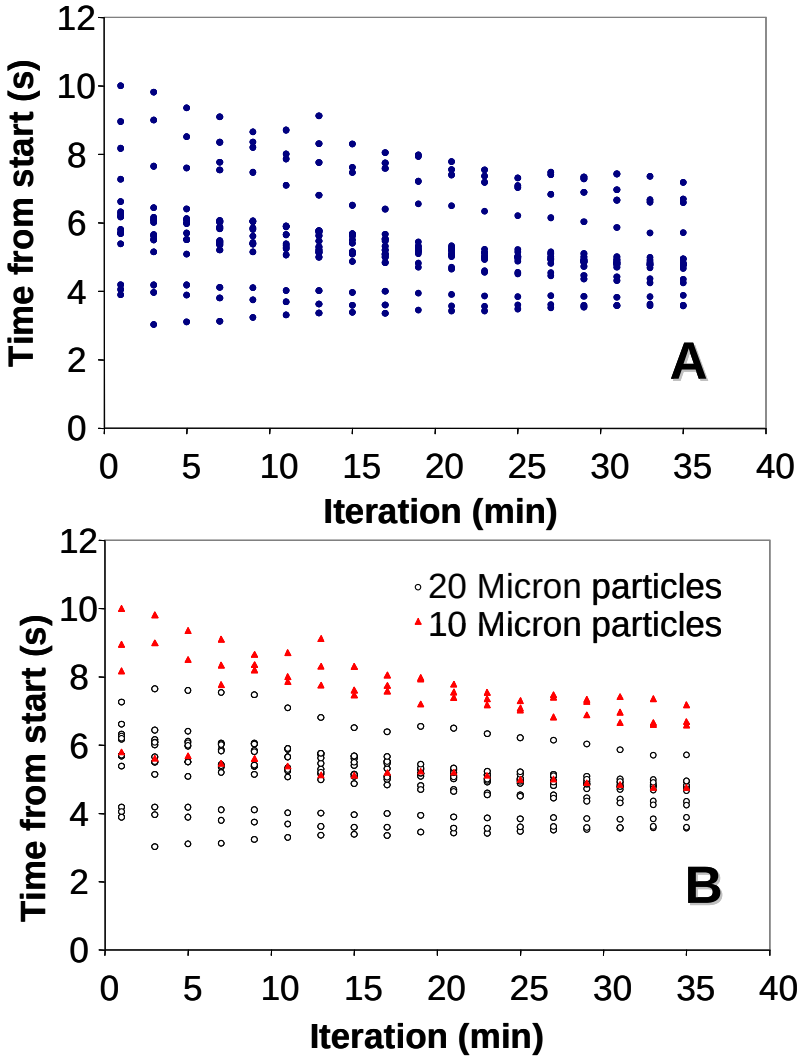

Figure 8-6: Tracks of a mixture of 10 and 20 μm particles. Tracking of mixture of 4 particles (10 μm) and 13 particles (20 μm). (A) Displays timing of all particles. (B) Displays timing gated on particle signals. Note, a 10 um particle is clearly tracked in a dense set of 20 um particles.

8.3.2 Scaling Up the Tracked Cell Number

To accurately describe the population dynamics of an entire population one would want to track as many cells as possible. What defines a sufficient number of cells from a population to measure is dependent on the heterogeneity of the physiological functions. For example, a common assumption for modeling single cell rates of growth is to assume that cells grow as a function of their cell mass (Mantzaris 2006 ; Mantzaris, et al. 1999). If all cells truly follow the same rate law, then ideally one would only need to measure a single cell through its entire growth cycle. However, if cells in a population follow different rate laws, than one must ideally measure a single cell from each sub-population through its growth cycle. Practically, to understand the dynamics of an entire population one would track hundreds of cells enabling quantification of the population to the ~1% level.

As indicated with the multiple particle experiment in Figure 8-6, the number of cells that can be uniquely identified in a plug of cells is a question of how many unique measurements can be obtained from each single particle. As a base case, the relative timing variable shown in the y-axis of Figure 8-6A can be used to differentiate cells from each other. However, from this figure, one can see that the particles do show some random variation from stroke to stroke, probably due to slight pumping errors, particle interference, or particle densities.

As illustrated in Figure 8-6, for each additional parameter that is obtained from each cell more unique information is added that can differentiate neighboring cells. Furthermore, in real cell populations the properties vary over a measurable range across

each unique piece of information obtained from the cell. The tracking should be possible as long as neighboring cells in the section of ordered cells are sufficiently different from each other. If one picks a narrow size group of cells consisting of 10 % of the entire cell population then the probability of encountering the same cell type as the neighboring cell in the plug of ordered cells is only 0.1. It is much more probable ($p=0.9$) that a different cell will be the neighbor in the tracking experiment. Therefore, the variability of cell populations should help the tracking process as long as the single cells do not change their properties at a rate faster than the data acquisition. This is a reasonable assumption since data from each cell is acquired once every 30 seconds, and cells change their properties over the course of hours. This example can be extended to additional pieces of information for instance fluorescence or right angle scattered light. With each additional parameter measured, the number of cells that can potentially be tracked increases dependent on the amount of variability a cell population has and the uniqueness of each parameter.

For example, 6 μm polystyrene beads with different fluorescence intensities were mixed into a single solution. As show in Figure 8-7A, beads were divided into four unique fluorescence groups indicated by different colors. Each of these unique groups were then used to identify unique traces of particles during fluid oscillation as indicated by different dcolored traces in Figure 8-7B. It is important to note that despite the beads coming from a different manufacturer, some beads (blue dots, Figure 8-7B) exhibited highly reproducible traces, while other beads had significant randomness in their traces as previously observed in Figure 8-5.

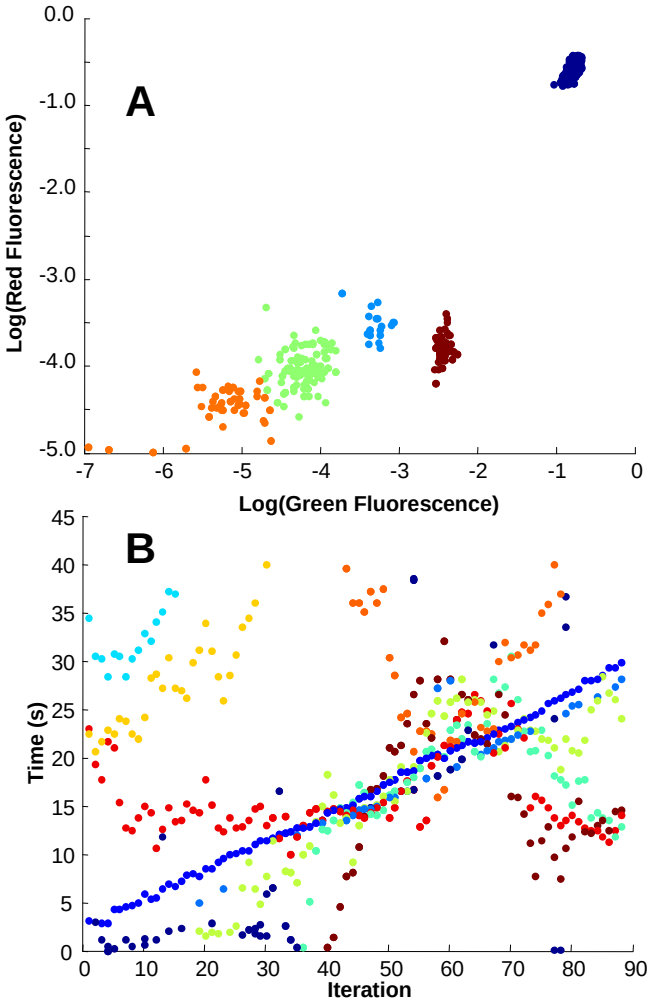

Figure 8-7: Traces of many 6 μm beads of different fluorescent intensities. **(A)** The log of Green and Red fluorescence for the mixture of polystyrene beads. Each color represents a unique fluorescence intensity. **(B)** The traces of a mixture of the fluorescent beads with each color representing a unique particle trace extracted using the laser crossing time and each particle's unique fluorescence and light scattering characteristics.

8.3.3 Particle Crossing Prediction

As seen in Figure 8-5 and Figure 8-7, some particles exhibit very predictable traces, while other particle exhibit more random traces. While the exact cause of this phenomenon is unknown, a model was created to qualitatively explain the changes in when each particle crosses the laser as a function of the particle's radial position and velocity. This model with additional equipment can be used to further increase the number of cells that can be traced, by making predictions when each cell will cross the laser on the next stroke. By predicting if the trace of a particle will change its slope, the effective maximum difference between particle crossing times can be reduced.

As shown in Figure 8-8, a single particle is at an initial location, d_0. The particle is moved to position d_1 (red arrow) and crossed the laser at time (τ_0). This is shown in Equation 1 where $v_1(t)$ is the velocity of the particle as a function of time, and t_{stroke} is the total time of the stroke. Equation 2 shows a simple model for the particle velocity where it is assumed that the particle behaves as a point particle in a parabolic velocity profile where $v_{max}(t)$ is the velocity at the centerline, r_1 is the radial location of the particle, and R is the radius of the capillary.

$$d_1 = d_0 - \int_0^{t_{stroke}} v_1(t)\,dt \tag{7.17}$$

$$d_2 = d_0 - \int_0^{t_{stroke}} v_{\max}(t)\left(1 - \frac{r_1(t)}{R}\right)^2 dt \tag{7.18}$$

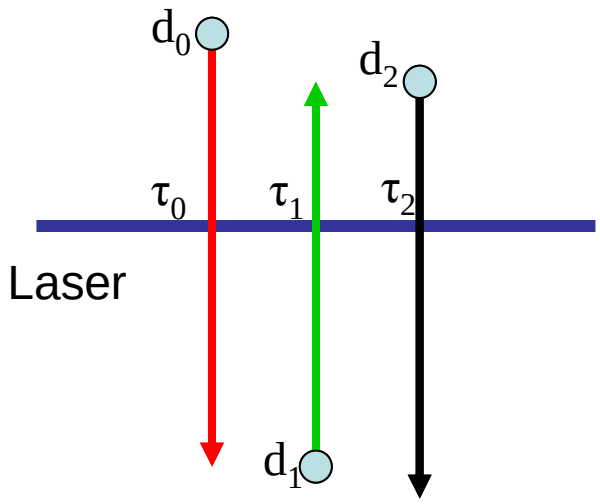

Figure 8-8: Cartoon depicting the movements of a single particle. An particle is inially located at d_0. The particle is moved to position d_1 (red arrow) and crossed the laser at time (τ_0). Next, the particle is pumped in the up direction (green arrow) to position d_2 and crosses the laser at time (τ_1). Position d_2 is measured by pumping in the down direction (black arrow). This cycle is repeated n times.

Thus, to predict the future location of a particle, one must measure v(t). Previously, a highly accurate flow sensor (Sensirion, West Lake Village, CA) was placed in the flow path. This sensor measured the flow rate of the fluid as a function of time. Knowing the cross-sectional area of the capillary allows us to compute the average or maximum velocity of the flow as a function of time as shown in Figure 8-9A. The different maximum flow rates in opposing directions are potentially due to differing amounts of small air bubbles in the lines preceding the capillary. The flow sensor verified that our oscillatory pumping moves the same quantity of fluid within +/- 1 nL. However, since there are discontinuities in the time that each particle crosses the laser, it is apparent that cells are changing their radial positions, potentially due to changes in a particle's radius, shape, mass, or particle-particle interference. Thus, the radial position must be estimated.

To accomplish this, the velocity of each particle at some instant in time during the stroke must be estimated. By measuring the bulk flow rate at this same instant using the flow sensor, the radial position at this instant in time can be estimated by:

$$K(\tau) = \frac{v(\tau)}{v_{\max}(\tau)} = \left(1 - \frac{r}{R}\right)^2 \tag{7.19}$$

Thus, assuming that the radial location r at the instant the velocity of the particle crosses is measured, Equation (7.18) simplifies to:

$$\begin{aligned} d_1 &= d_0 - F\left(t_{stroke}\right) K\left(\tau_0\right) \\ d_0 &= F\left(\tau_0\right) K\left(\tau_0\right) \end{aligned} \tag{7.20}$$

where the function F is:

$$F(t) = \int_0^t v_{\max}(t)\,dt \tag{7.21}$$

as shown in Figure 8-9B.

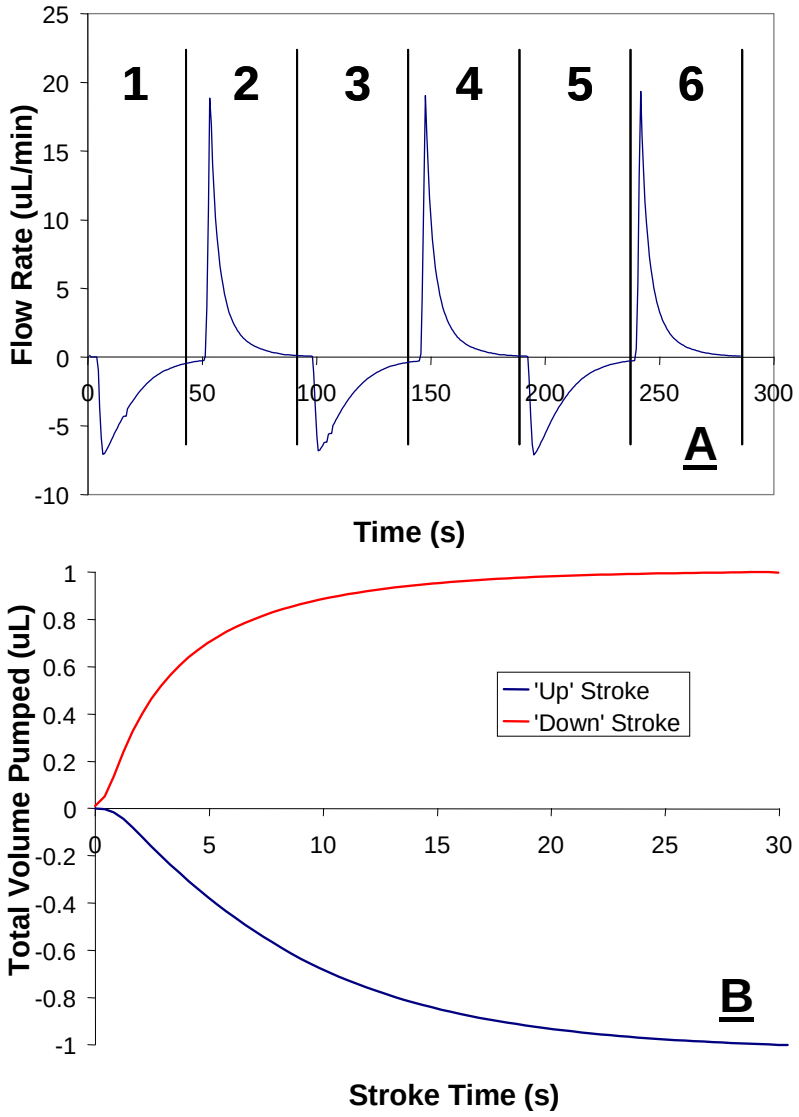

Figure 8-9: Flow rates during strokes. **(A)** Bulk volumetric flow rate for 6 strokes as measured by the flow meter. **(B)** The function F(t) for strokes in the up and down direction. The flow rate in (A) is multiplied by two, divided by the cross sectional area of the capillary, and integrated from zero to t as in Equation 5.

Thus, for each particle in a given stroke, the resulting location in the opposing stroke can be computed using Equation (7.20). The actual location can be estimated during the next opposing stroke where

$$d_1 = F(\tau_1) K(\tau_1) \tag{7.22}$$

This prediction algorithm forms the basis for scaling up the number of particles that can be tracked. By comparing the results from Equations (7.20) and (7.22), predictions can be made where each individual particle will rest at the end of a stroke, and then compared to the actual location measured during the next stroke.

8.3.4 Qualitative Model Verification

With the above model, hypotheses for why the traces are sloped can be made. For instance, the traces of 2 NCI-H929 cancer cells stained with Rhodamine 123 are shown in Figure 8-10A for all strokes in the up direction and Figure 8-10B for all strokes in the down direction. Each particle was isolated based on its differing fluorescent intensity. For each particle, between 'Up' and 'Down' strokes, their traces are mirror images of each other. If a particle has a positive slope in the up direction, than it has a negative slope in the down direction. These qualitative observations can be compared to the model for three potential cases: 1) a particle gradually moving toward the centerline over 30+ iterations 2) away from the centerline, or 3) maintaining its radial position (Figure 8-10C-D). Thus, for example, if the slope of the trace is positive in the up direction, it would imply that the particle is moving away from the centerline. Also, the mirror image behavior observed in the experiment is replicated in the model. With actual velocity measurements, these hypotheses can be tested. Novel data about

how a cell is changing its macroscopic shape and density could then be extracted and further analyzed.

8.4 Population Balance Function Extraction

Once individual cells' traces are identified from these experiments the waveforms of these cells can then be analyzed for the peak height, width, and area of the signal as used in standard flow cytometry. Also, since the individual waveforms are stored, additional parameters such as peak skewness, dip index, etc can be extracted depending on the data of interest. Whichever parameter is extracted from the individual waveforms, this parameter would then be analyzed within the context of the population balance equation. Specifically, the derivative of the property change with respect to time would be the rate change function of the cells. The division rate function can be calculated by recording the properties of the cell at the division time. If the cell can be tracked completely through division, then the properties of the daughter cell and the parent cell can be observed immediately after division, thus obtaining information on the partitioning function.

For example, from the experiment shown in Figure 8-7, the fluorescence of a single, example traced particle is highlighted in blue in Figure 8-11. From this trace, the rate of change as a function of fluorescence can be computed i.e.:

$$\frac{df}{dt} = r(f) = 0 \tag{7.23}$$

where t is time, f is the green fluorescence, and $r(f)$ is the rate function in the population balance equation. As expected, for a constant, stained, polystyrene bead the rate of change in fluorescence is zero. This process can be repeated for each successfully

traced particle in the plug of cells (n=7), and the rate function for each particle computed and plotted in Figure 8-11B.

8.5 Photobleaching in the single cell tracking cytometer

Fluorescein is a common dye used in many different staining protocols such as antibody staining. However, fluorescein is prone to photobleaching such that only 40% of the fluorescence remains after 1 minute of illumination under a fluorescent microscope (Haugland 2005). While many different fluorescent dyes have been developed to minimize photobleaching relative to Fluorescein, no dye is completely immune to photobleaching. Thus, it is important to note that over the course of the 1.5 hour experiment shown in Figure 8-11, the particles were illuminated by the laser for a total of only 90 ms. This is in contrast to both video microscopy and laser scanning cytometry where the sample would have been continually illuminated by the laser for over 90 minutes. Thus, photobleaching in the developed cytometer would be practically non-existent.

Photobleaching plays an important role in protein expression measurements using fluorescent microscopy. All fluorescent proteins photobleach at an exponential rate when exposed to illumination. Experiments using fluorescent microscopy to study fluorescent protein production rates must account for as much as of a 40% loss in signal due to photobleaching (Sigal, et al. 2006). Since the developed cytometer significantly reduces the total illumination time, photobleaching of fluorescent proteins is expected to be negligible.

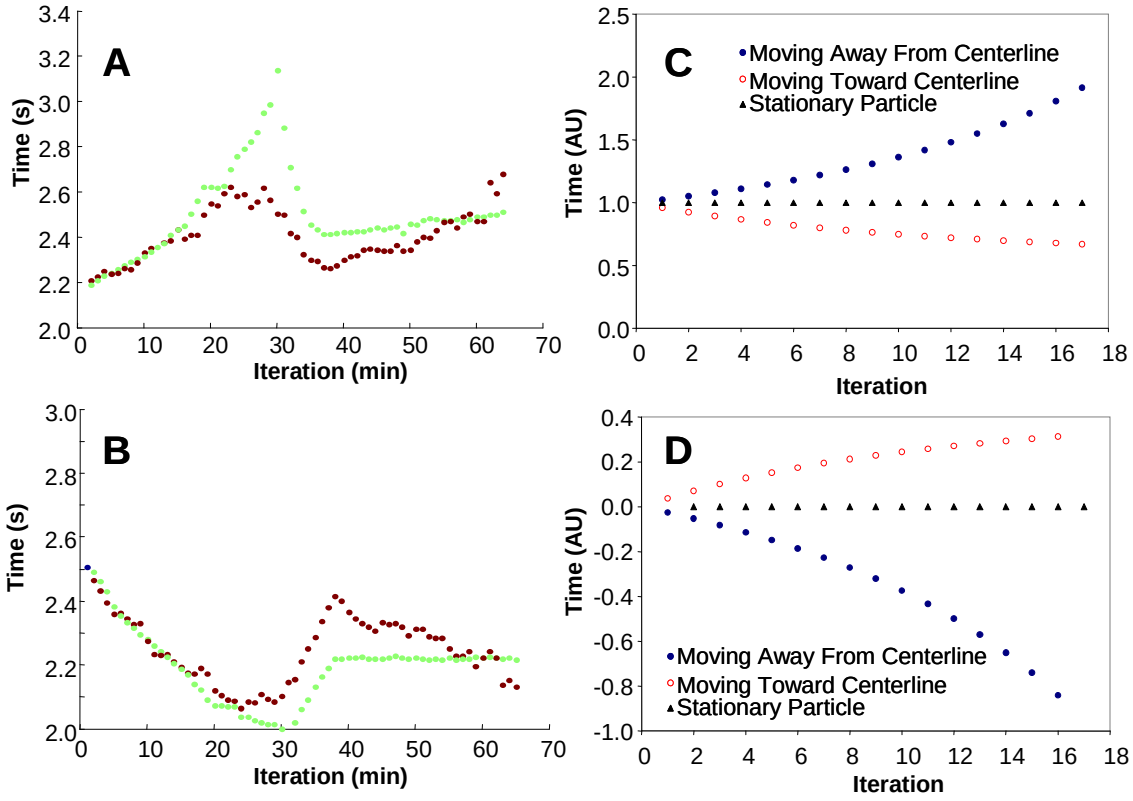

Figure 8-10: Qualitative model verification using two cells. Grouping of all strokes in the 'Up' **(A)** and 'Down' **(B)** Direction for two NCI-H929 cancer cells stained with Rhodamine 123. Colors indicate two unique cells identified by their different fluorescent intensities. The model described above was simulated for a square pulse of flow for a particle moving toward the centerline, away from the centerline, or maintaining its radial position for all strokes in the Up **(C)** and Down **(D)** directions**.**

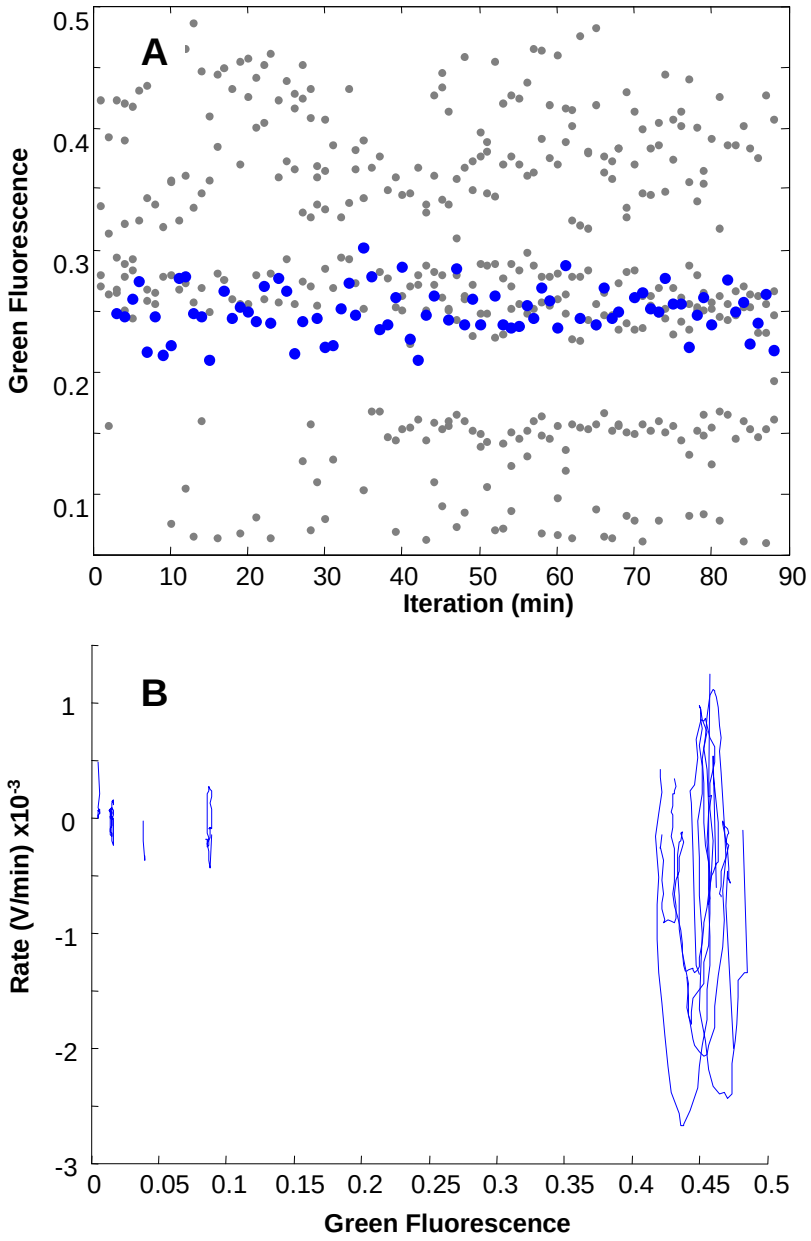

Figure 8-11: Time course of fluorescence from a single uniformly fluorescent bead. **(A)** Peak heights for all events during the course of the experiment shown in Figure 8-7B. Highlighted by blue dots is the peak height as a function of time for a single, example traced particle within this experiment. The noise in the peak height is due to variations in laser intensity across the capipllary. **(B)** The rate of change as a function of fluorescence for each successfully traced particle (n=7). The graph shows that the rate of change is essentially zero for all particles. The noise in the rate function is due to the systemic noise in the instrument caused by a variation in the laser beam intensity.

9 Mammalian Cell Single Cell Tracking Data

9.1 Multi-Drug Resistance Assay in Multiple Myeloma Cells

9.1.1 Introduction

During the progression of cancer, malignant cells can develop resistance to many chemotherapy drugs (Tan, et al. 2000 ; Tucci, et al. 2009). This is a major hurdle for cancer chemotherapy protocols to overcome. Previous studies have shown that many different active transporters play a role in developing the multidrug resistance (MDR) phenotype. For instance, the overexpression of the P-glycoproteins in cancer cells induces the MDR phenotype (Goda, et al. 2009). P-glycoproteins have been shown to act as a general transport pump that moves broad classes of compounds from the cytoplasm to the extracellular environment (Aouali, et al. 2005).

A common test for MDR is to initially load cells with Rhodamine 123 (R123) (Haugland 2005). R123 is a fluorescent substrate of Pgp and other active transporters. R123 is cell membrane permeable, and is accumulated in mitochondria (Chen 1988). To stain cells, R123 is introduced to the extracellular environment. R123 actively crosses the plasma membrane to the cytosol due to the membrane potential, and is then actively transported into mitchondria due to the mitochondrial membrane potential. Once cells have reached a steady state level of R123 in the mitochondria, cells are then washed. It has been previously shown using video microscopy (Altenberg, et al. 1994) that the subsequent efflux of R123 is mediated by the presence of P-glycoprotein.

9.1.2 Population Averaged Viewpoint

A typical assay used in hospitals to assess MDR of cancers uses traditional flow cytometry. First, a sample of tumor cells from a cancer patient is loaded with R123. MDR cells expressing high levels of Pgp rapidly extrude R123 from the cells, reducing R123 levels (Haugland 2005 ; Karaszi, et al. 2001). After treating a control sample with a drug that inhibits P-Glycoproteins, the fluorescence levels of the control can be compared to the sample. If the sample has a much lower mean fluorescence than the control, than the cancer from the patient who supplied the sample is deemed to be MDR. Treatment of the patient can then be modified accordingly (Karaszi, et al. 2001). These assays are typically performed using flow cytometry where after a given amount of time, the mean population fluorescence of the sample is compared to the control population fluorescence (Krishan, et al. 1997 ; Krishan 2001 ; Krishan 2002 ; Krishan and Hamelik 2005). Treatment decisions are then made based on the population averaged measurement. However, these approaches completely neglect the actual kinetics of the drug efflux.

9.1.3 Eulerian Viewpoint

The kinetics of drug efflux in terms of a rate law equation can yield important clues as to the underlying process. It was previously shown using the R123 staining protocol and video microscopy that the kinetics of R123 efflux are a first order process as a function of cell fluorescence (Altenberg, et al. 1994), i.e:

$$\frac{df}{dt} = r(f) = kf \tag{8.1}$$

where *t* is time, *f* is the green fluorescence, *k* is a constant, and *r(f)* is the rate function in the population balance equation. Knowledge of the kinetics of this process yields important clues towards understanding the underlying mechanism of R123 efflux from cells. For instance, if the rate is zeroth order, than one has an indication that passive diffusion through the cell membrane is dominating the process. However, as in this case, if the rate law is first order, or even a Monod curve, than some active process is governing the efflux.

One can use a simplified population balance equation with a flow cytometer to measure the R123 efflux over time to generate a measure of the rate law of the culture. Specifically, the single cell growth rate function from the population balance equation can be determined by assuming that cell proliferation over the course of the experiment is negligible. If this is true, then the net birth rate function as zero (i.e. the right hand side of (1.1)). Now, by assuming that the population balance model is one dimensional and only a function of the single cell fluorescence the equation simplifies to:

$$\frac{\partial g(f,t)}{\partial t}+\frac{\partial\left[r(f,t)g(f,t)\right]}{\partial f}=0 \tag{8.2}$$

The flow cytometer measures the distribution of fluorescence *g(f,t),* and thus this equation is readily solved for the rate function (Gilbert 2008):

$$r(f,t)=\frac{1}{g(f,t)}\frac{\partial\left(\int_f^\infty g(f^*,t)df^*\right)}{\partial t} \tag{8.3}$$

To compute the rate equation, NCI-H929 multiple myeloma cells known to be MDR (Gazdar, et al. 1986) were grown in RPMI-1640 medium supplemented with 10% fetal bovine serum. Cells were harvested in exponential phase and exposed to a 15

μM R123 solution in fresh medium, washed, and resuspended in medium without R123. One minute after the wash step, cells were loaded into a flow cytometer and continually acquired. As shown in Figure 9-1A, the function of single cell R123 fluorescence as a function of time, *g(f,t)*, is measured. For two histograms taken near in time, Equation (8.3) can be estimated as:

$$r(f) = \frac{1}{\langle g(f) \rangle} \frac{\left(\int_f^\infty g(f^*, t_2)\, df^* \right) - \left(\int_f^\infty g(f^*, t_1)\, df^* \right)}{\Delta t} \tag{8.4}$$

where $\langle g(f) \rangle$ is the average distribution between these time points. Using the data in this plot with Equation (8.3), the rate function *r(f)* for the histograms at t=0 and t=60 s is shown in Figure 9-1B.

Qualitatively, this function is a Monod model characterized by a zeroth order rate function at high fluorescence content and a first-order process at lower fluorescence content. This type of rate law is characteristic of enzymes and is a direct piece of evidence that an active process is used to transport R123 out of the cell.

Equation (8.3) is an example of an inverse solution to the population balance equation as it takes the Eulerian viewpoint of the system. However, it is important to note that when one attempts to apply an inverse method, one a priori chooses a subset of state variables that can be measured and then attempts to measure their effect on the rate function. In this case, we are assuming that the rate function is only dependent on the fluorescence. The method will reliably compute the dependence as an averaged rate per fluorescent unit similar to other approaches such as Collins-Richmond (see section 4.5)

(Collins and Richmond 1962 ; Koch 1999). The method assumes that all cells follow the same rate law.

9.1.4 Lagrangian Viewpoint

To truly measure the rate function of each individual cell, one must take the Lagrangian viewpoint and measure individual cells. To accomplish this, the experiment that generated Figure 9-1 was duplicated in the single cell tracking cytometer. As shown in Figure 9-2A, 20 cells were successfully traced through the system. Each cell's fluorescence was followed over the two hour experiment and shown in Figure 9-2B. As can be clearly seen in this Figure, each individual cell varied its rate of R123 efflux. Based on this data, the rate law of each individual cell can then be computed and is shown in Figure 9-3. The rate of loss is first order for a large majority of cells, with Monod characteristics for some cells. It is likely that the cells exhibiting first order behavior had already pumped sufficient levels of R123 from the cell, and thus, first order kinetics were observed. These single-cell kinetics qualitatively match the population averaged kinetics observed using the Eulerian viewpoint in Figure 9-1B.

Of particular interest is the variation in each single cell response. Since there is significant variation in the individual rate law as a function of fluorescence intensity there are more variables that may play a role in R123 efflux. Much of the variation can potentially be explained by varying amounts of P-glycoproteins on the cell surface. If multiple transporters are present in a cell, then the rate of R123 loss would be the sum of each transporters rate.

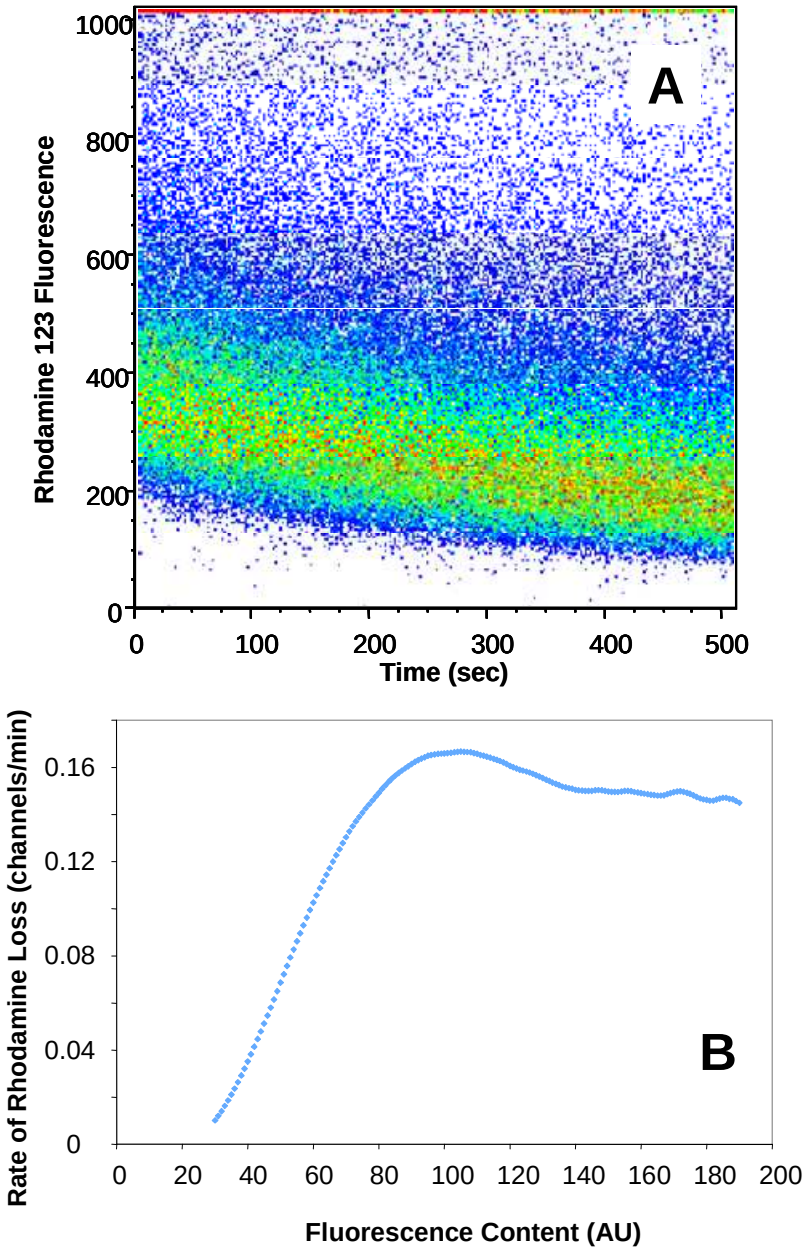

Figure 9-1: Eulerian viewpoint of dye loss in cancer cells **(A)** Distribution of single cell Rhodamine 123 fluoresensce as a function of time. Hotter colors indicate a higher probaility that a cell has a given fluorescence value at a given time. Cells were initially loaded in a 15 μM R123 solution, washed, and resuspended in medium without R123. Time zero in the plot is 1 minute after resuspension in fresh medium. **(B)** The rate equation computed using Equation (8.3) and the distributions in Figure 9-1A. The distribution was rebinned from a 1024 channels cale to a 256 channel scale

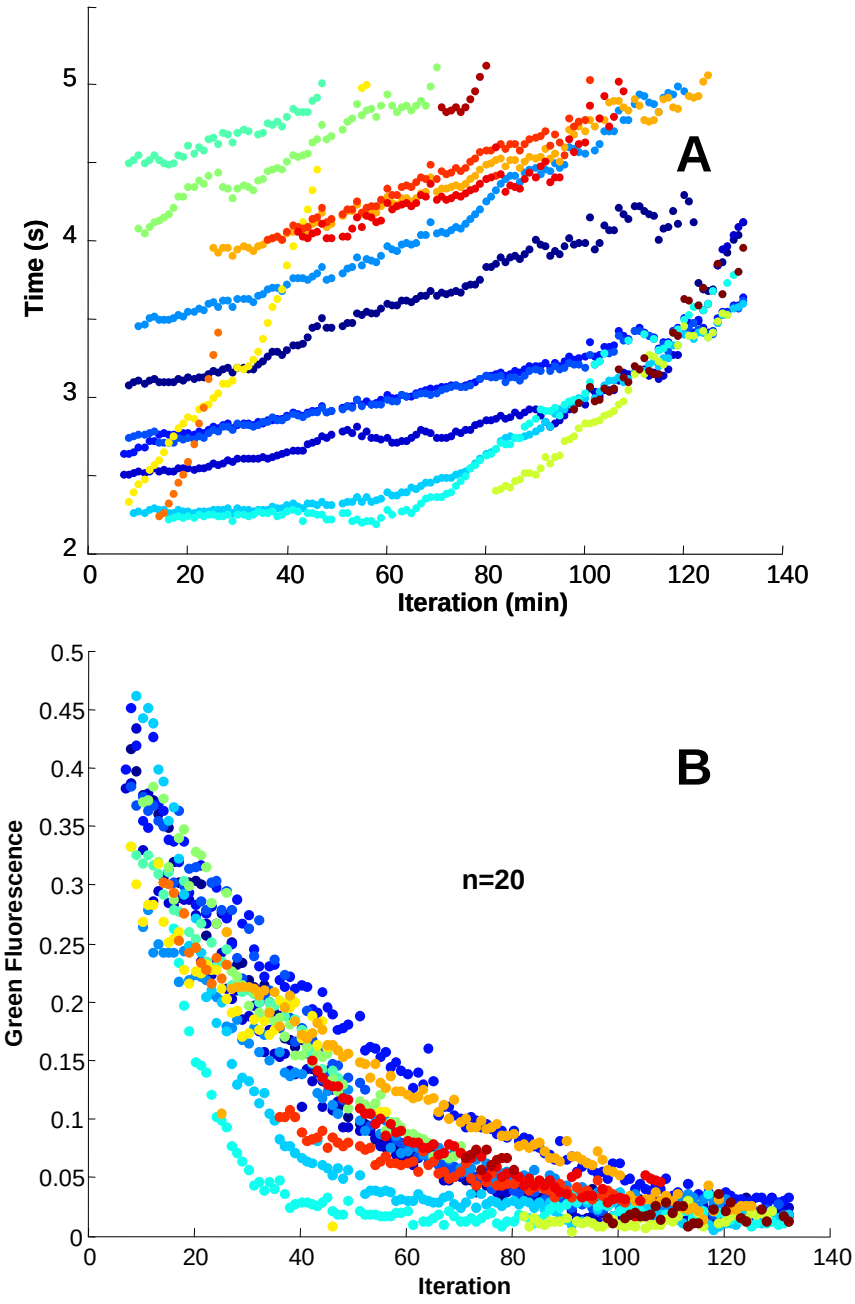

Figure 9-2: Lagrangian viewpoint of dye loss in cancer cells. **(A)** 20 NCI-H929 myeloma cells were stained with R123, washed and loaded in the single-cell tracking cytometer. These cells were traced over the course of an experiment according to the protocols defined in Chapter 8. Each color indicates a unique successful trace. **(B)** The change in R123 fluorescence in each traced cell defined in A. The loss of R123 is different for each cell.

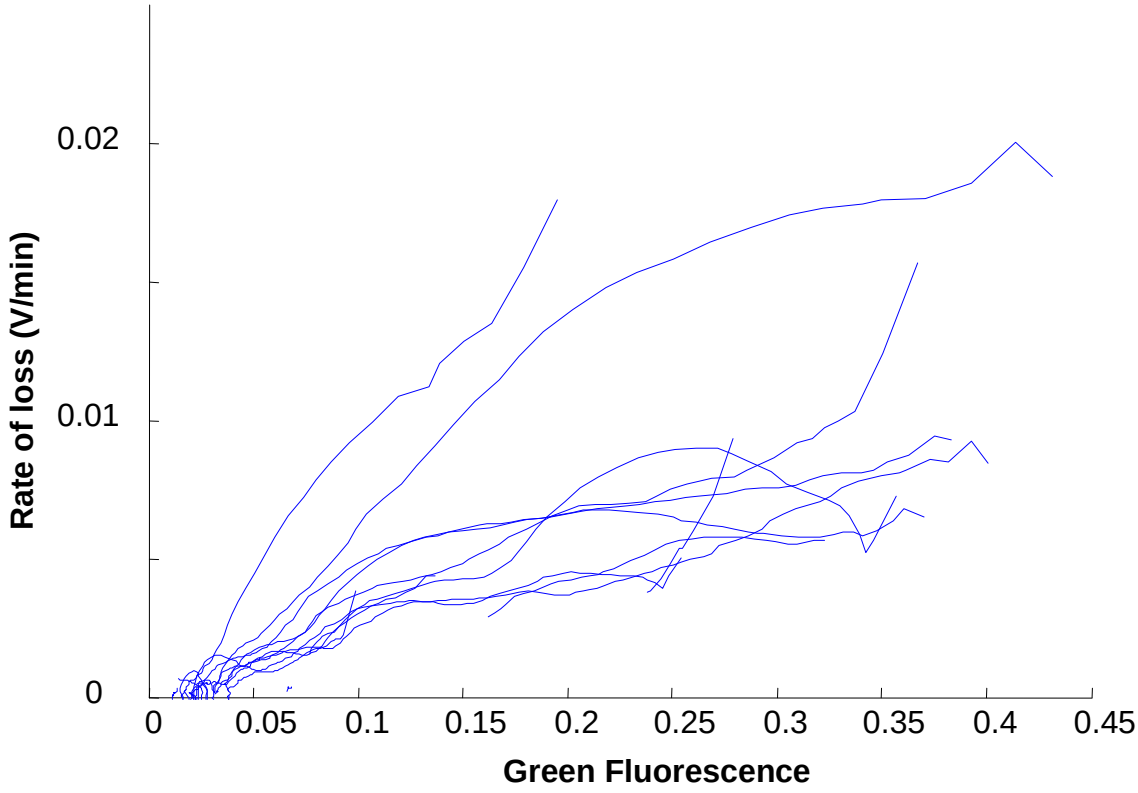

Figure 9-3: Rate of dye loss for individual cells. Each line represents the rate of loss of fluorescence for each individual cell in Figure 9-2. The rate law is first order for a large majority of cells, with Monod characteristics for other cells.

9.1.5 Conclusion

These experiments illustrate the difference between using a population averaged, an Eulerian reference frame, and a Lagrangian reference frame for assessing a cancer's state of MDR. This base experiment in the single cell tracking cytometer is intended to show the richness of the data provided by the Lagrangian viewpoint in contrast to the Eulerian and population averaged measurements. For instance, with the Lagrangian viewpoint, treatment decisions can then be made based on how sub-populations of a cancer are behaving.

The data also serves as a proof of concept of the device for use in measuring the response of mammalian cells. Additional experiments could be performed using the Lagrangian reference frame with additional drugs that inhibit different steps in R123 efflux through P-glycoproteins. For instance, vinblastine could be added to the culture, and the arrest of R123 efflux across the population observed (Altenberg, et al. 1994). One could then clearly determine if there is cell to cell variation in the R123 efflux in response to this drug. Recently, sigmaR(S) inhibitors have been shown to disrupt P-glycoprotein expression signals and restore apoptosis machinery in cancer cells (Tan, et al. 2000 ; Tucci, et al. 2009). Using the protocols and instrumentation outlined in this section, the individual cell response to this drug could be measured.

9.2 TGE in Single CHO cells

Transient gene expression is frequently used in industry to rapidly generate usable quantities of a protein from cultured cells, and in gene therapy applications to express a therapeutic protein *in vivo*. A quantitative assessment of the expression

kinetics is important because it enables optimization and control of culture conditions for higher productivity (Batard, et al. 2001 ; Derouazi, et al. 2004 ; Sitton, et al. 2006 ; Subramanian and Srienc 1996). At present, initial experiments to quantify green fluorescent protein (GFP) in CHO cells have been attempted in the single cell tracking cytometer. CHO cells expressing GFP 3 hours after transfection (see materials and methods Section 13.I.b) and Chapter 5) were diluted into RPMI medium without phenol red and tracked for 30 minutes as shown in Figure 9-4A. As previously determined (Figure 5-3A), a majority of cells have begun to express Gfp at 3-5 hours after transfection. Thus, no initial transient expression events were observed. Each cell was observed to have a constant level of fluorescence consistent with general theories of gene expression (Kaern, et al. 2005). This experiment is given as a proof of concept that protein expression in mammalian cells can be monitored over time. This is significant since a large body of scientific work uses fluorescent proteins for many applications including monitoring of gene noise (Kaern, et al. 2005) and cell fate determination (Spencer, et al. 2009). Thus, the cell to cell variability of many applications can be monitored.

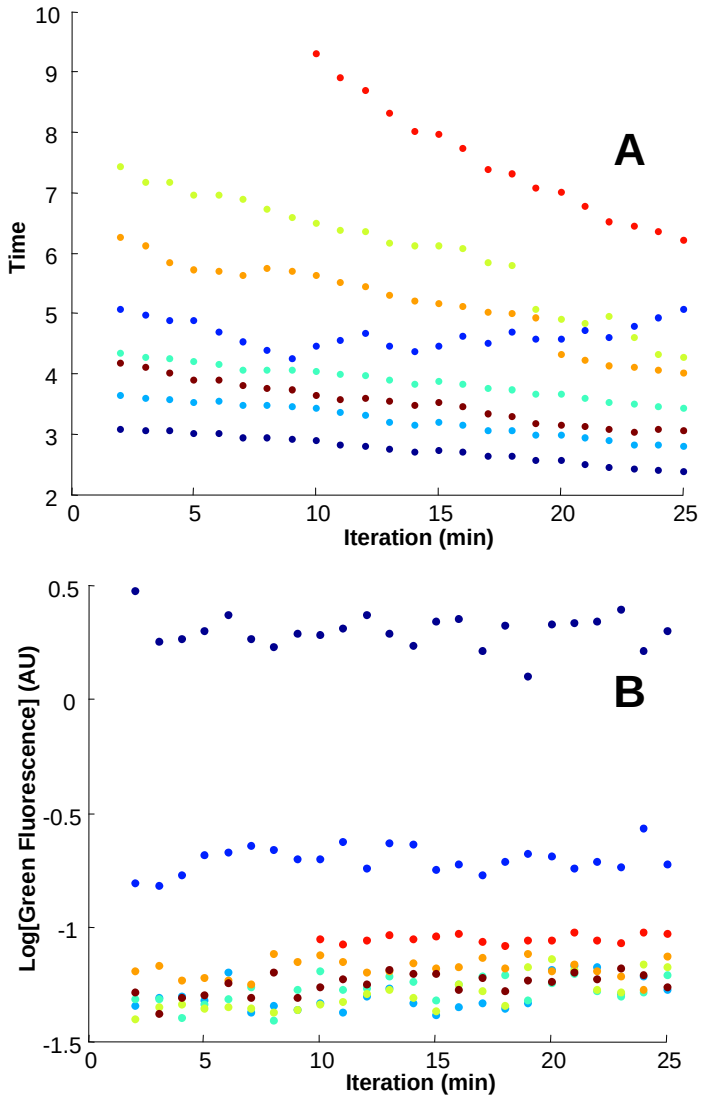

Figure 9-4: Lagrangian viewpoint of TGE in CHO cells. **(A)** Traces of 8 GFP producing CHO cells over the course of 30 minutes. **(B)** The peak height of GFP content as a function time for the 8 unique CHO cells. The constant fluorescence is due to either a steady-state or a lack of protein production.

10 Yeast Gfp Expression: Response to Temperature Fluctuations

10.1 Introduction

Due to its short doubling time and fast protein production rates relative to mammalian cells, yeast has been used extensively as a model eukaryotic organism. A famous example is the determination of the components of the cell cycle network in response to different external stimuli (Nurse 2002). A common feature of these studies is the use of fluorescent proteins conjugated to proteins of interest. This allows one to follow the expression pattern of the protein in response to external stimuli by measuring fluorescent signals. From the previous theoretical analysis, yeast cells present unique challenges to operation in the developed cytometer. Primarily, the smaller particle size (~2-10 μm) would result in lower Peclet numbers (Equation (7.16)) compared to the larger mammalian cells. Thus, diffusion of cells in the radial direction may be more significant. Also, at any given time, a significant fraction of yeast cells are budding, yielding non-spherical cells (Hatzis and Porro 2006). Furthermore, yeast cells become ovoid as the ploidy level of the cell increase. Thus, to demonstrate that the developed cytometer can be used with yeast cells, the individual cell response of Gfp producing yeast cells was monitored in response to a constant and a varying temperature.

10.2 Results

10.2.1 Constant Temperature

Haploid yeast cells of strain YPH399a (Natarajan A, et al. 1998) containing a centromeric plasmid constitutively expressing Gfp from a TEF2 promoter (Kacmar, et al. 2004a) were grown overnight at 30°C in a shake flask in SD minimal medium. The next morning, during late exponential phase, cells were diluted into room temperature RPMI-1640 medium adjusted to pH 5.4 with 2 M hydrochloric acid. Cells were diluted into clear RPMI-1640 medium since standard SD minimal medium has a small yet significant absorbance at visible wavelengths. This absorbance decreases the amount of fluorescence signal that reaches the fiber optic at the end of the capillary Figure II-9. Cells were loaded into the single cell tracking cytometer and analyzed at a constant 30°C for 1.5 hours. As shown in Figure 10-1, for the majority of cells, both the single cell green fluorescence and side scatter signals from each identifiable cell remained constant. The constant level of Gfp fluorescence is consistent with general theories of gene expression (Kaern, et al. 2005). One cell in the plug continually decreased its Gfp content (blue). A cause for this decrease is unknown.

SSC is expected to scale with both cell granularity and cell size (Shapiro 1985), and can be used as an indicator of cell growth. In this experiment, the SSC was constant for the majority of the signals. One cell (orange) began to double the SSC signal while there was as sustained decrease in Gfp content (Figure 10-1, arrow (a)). In a separate experiment performed under similar conditions (Figure 10-2) a similar trend of a constant SSC signal followed by a sharp increase was observed. It is hypothesized

that this trend is indicative of cell growth. To date, no division events have been observed where a separate daughter cell is observed to separate from the mother cell. It is hypothesized that the system lacks sufficient shear stress to completely separate mother and daughter cells. Further testing on this matter is intended.

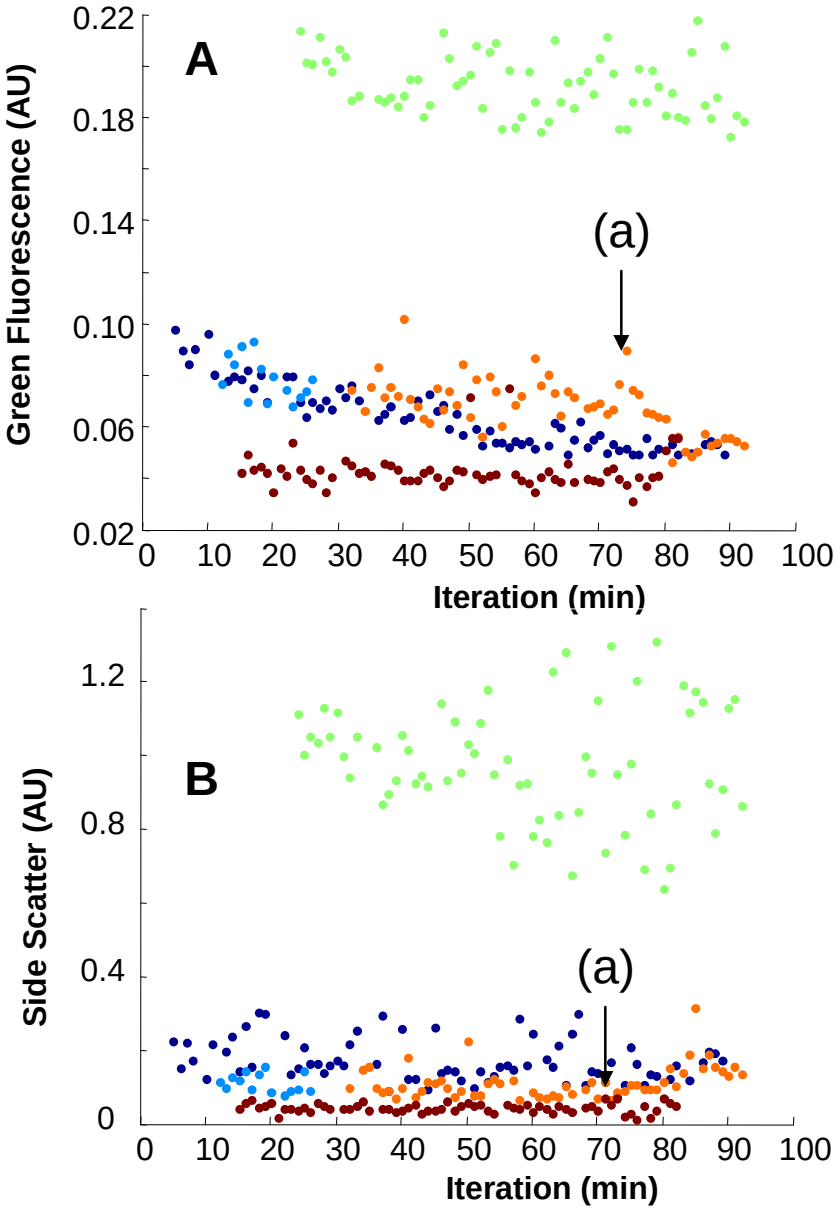

Figure 10-1: Lagrangian viewpoint of single yeast Gfp content. Each color in the figure represents a single, tracked yeast cell. **(A)** Gfp content and **(B)** SSC values as a function of time for cells are shown. The color of each cell correspond between A and B. Arrow (a) indicated a sharp, sustained rise in the SSC signal of an individual cell, during a sustained, sudden decrease in Gfp content. It is hypothesized that this corresponds to a cell growth event.

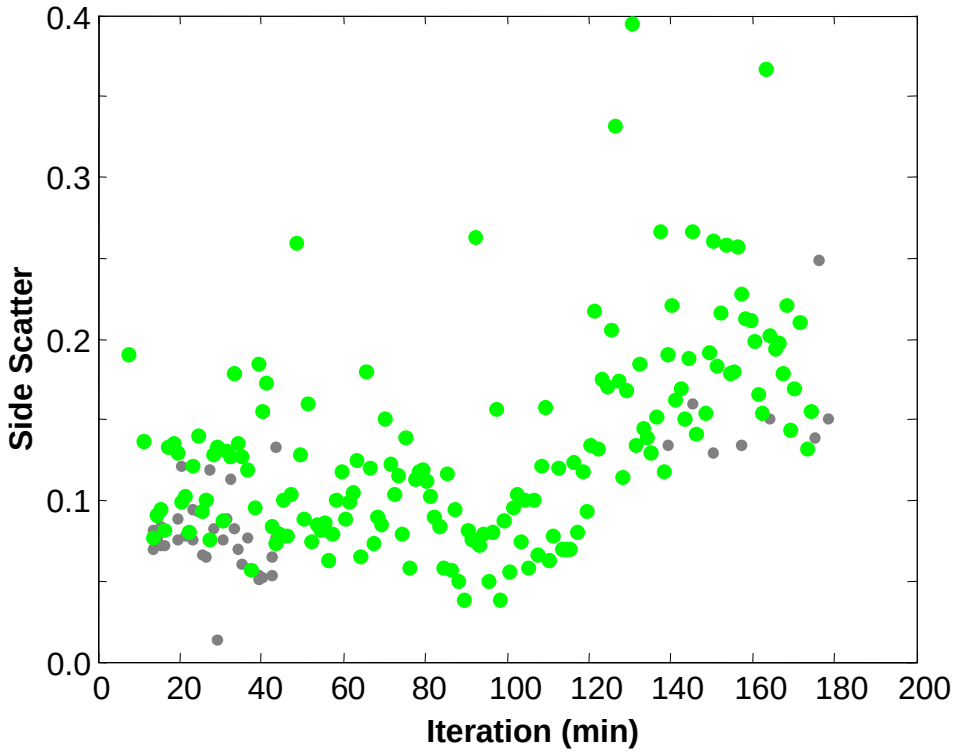

Figure 10-2: SSC signal from a growing yeast cell. Example SSC time course for a single cell tracked under growth conditions in the cytometer. At 100 minutes, the cell began a sharp increase in SSC peak height indicative of cell growth.

10.2.2 Expression Noise

Due to low gene copy numbers in cells, the kinetic parameters of gene expression, and low numbers of certain signaling proteins in cells, gene expression for most cell systems is typically regarded as probabilistic as opposed to deterministic (Kaern, et al. 2005). The resulting noise in gene expression has been indicated as the cause of certain diseases as well as one of the causes of cell heterogeneity (Bird 1995 ; Blake, et al. 2003 ; Elowitz, et al. 2002 ; Sigal, et al. 2006 ; Spencer, et al. 2009).

The noise in a cell's expression of a protein can potentially be measured by the single cell tracking cytometer. First, standard, fluorescent beads of known distribution are pumped through the system and the spread of the distribution is measured. The standard deviation divided by the mean (the coefficient of variation or CV) is then computed. For the experiments outlined in this thesis, this value was ~10% +/- 2%. During measurement of single cells, any CV in a signal greater than 10% can then be attributable to the noise of the signal from the cell. There are two different causes of signal noise from each cell. The first type of noise can be attributable to a non-spherical cell tumbling through the laser. As the cell tumbles, the cross-sectional area of illumination is different during each pass through the laser. Take for instance a dividing cell tumbling during flow. If the axis of the particle is aligned with flow (Figure 10-3E, 1), then the cross-sectional area of the cell is lower then if the particle crosses the laser perpendicular to the axis of flow (Figure 10-3E, 2). Since Gfp is a cytosolic protein, it can be assumed that the distribution of Gfp is homogeneous through the cell. Thus, the peak height of the fluorescent signal will be directly related to the cross-sectional area

of the cell as it passes through the laser. The second cause of signal noise is the actual noise generated by the gene expression.

These two cases were experimentally observed in the single cell tracking cytometer. Take for instance two single yeast cells expressing Gfp constitutively that were tracked through the device during two separate experiments as shown in Figure 10-3A, C. From Figure 10-3A, the waveforms of SSC and Gfp of two points are shown in Figure 10-3B. As the waveforms indicate, the particle is asymmetric and tumbling since the width of the signals double between the two points. This is in contrast to Figure 10-3D, where the waveforms of SSC and Gfp of two points from Figure 10-3C are plotted. Since the width of signals are nearly identical between these two points, then these waveforms indicate that the cross sectional area of the particle was similar, and there is more Gfp in the cytosol.

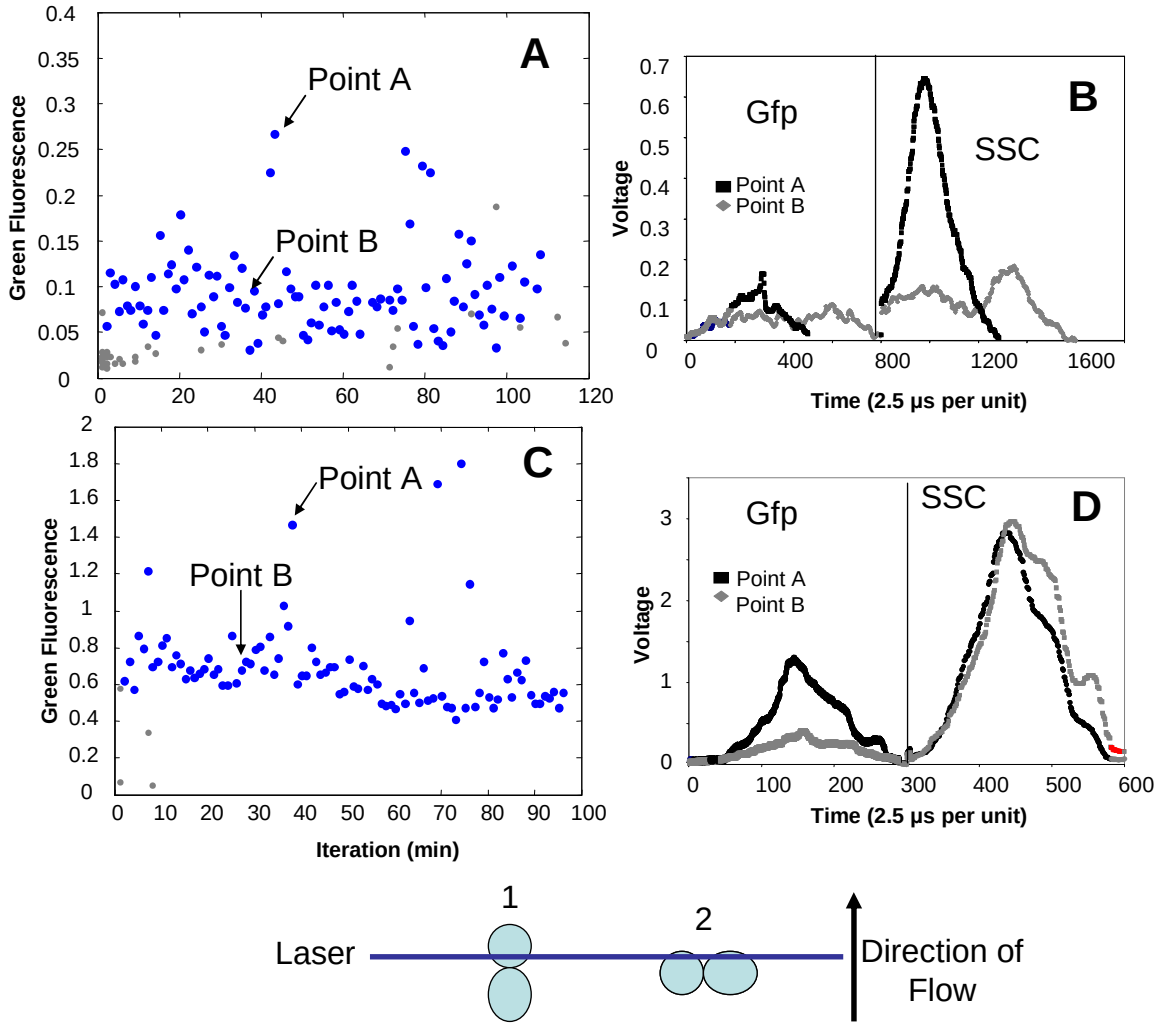

Figure 10-3: The effect of a tumbling asymmetric yeast cell on the peak height. Time course of Gfp peak height response for two single yeast cells highlighted in blue in **(A)** and **(C)**. **(B)** Illustrates the waveforms of two points in (A). Between these two points, the width of the signal changes; indicating a tumbling particle. **(D)** Illustrates the waveforms of two points in (D). In this case, the width of the particle does not change; indicating a real difference in the Gfp content of the cell between these two points. **(Bottom)** A cartoon depicting the consequences of an asymmetric particle tumbling in terms of its cross sectional area. In 1) the cross sectional area is small, and thus the peak height of the fluorescent signal will be lower than in 2) where the cross-sectional area will be higher.

10.2.3 Oscillating Temperature

To demonstrate that the developed cytometer can be used with yeast cells, the individual cell response of Gfp producing yeast cells was monitored in response to a varying temperature. The same strain of yeast cells and the same dilution protocol used in 10.2.1 was used in this experiment, with the temperature varying between 24°C and 33°C. After dilution, the yeast cells were left at room temperature for 6 hours, and then analyzed. As shown in Figure 10-4A, 11 yeast cells were tracked in the plug. As previously seen using constant polystyrene beads (Figure 8-5), some cells behave very predictably, and cross at times near the previous stroke while others behave relatively unpredictably. It is unknown what factors differentiates these responses.

The richness of single cell Gfp response as a function of temperature was surprising. As shown in Figure 10-4C, a fraction of cells oscillated their single cell Gfp content inversely with temperature while other cells were unaffected by the temperature oscillations. The Gfp responses of four individual cells are highlighted in Figure 10-5. Each cell in this figure underwent a unique response to the temperature oscillation Figure 10-5. Of note is the increased noise of the expression in particle (B) compared to the other particles. After analysis of the width of the individual waveforms, and as described in section 10.2.2 this noise is attributable to an asymmetric particle. Also, of note is the continual increase of Gfp content for particles (A) and (C) in this figure.

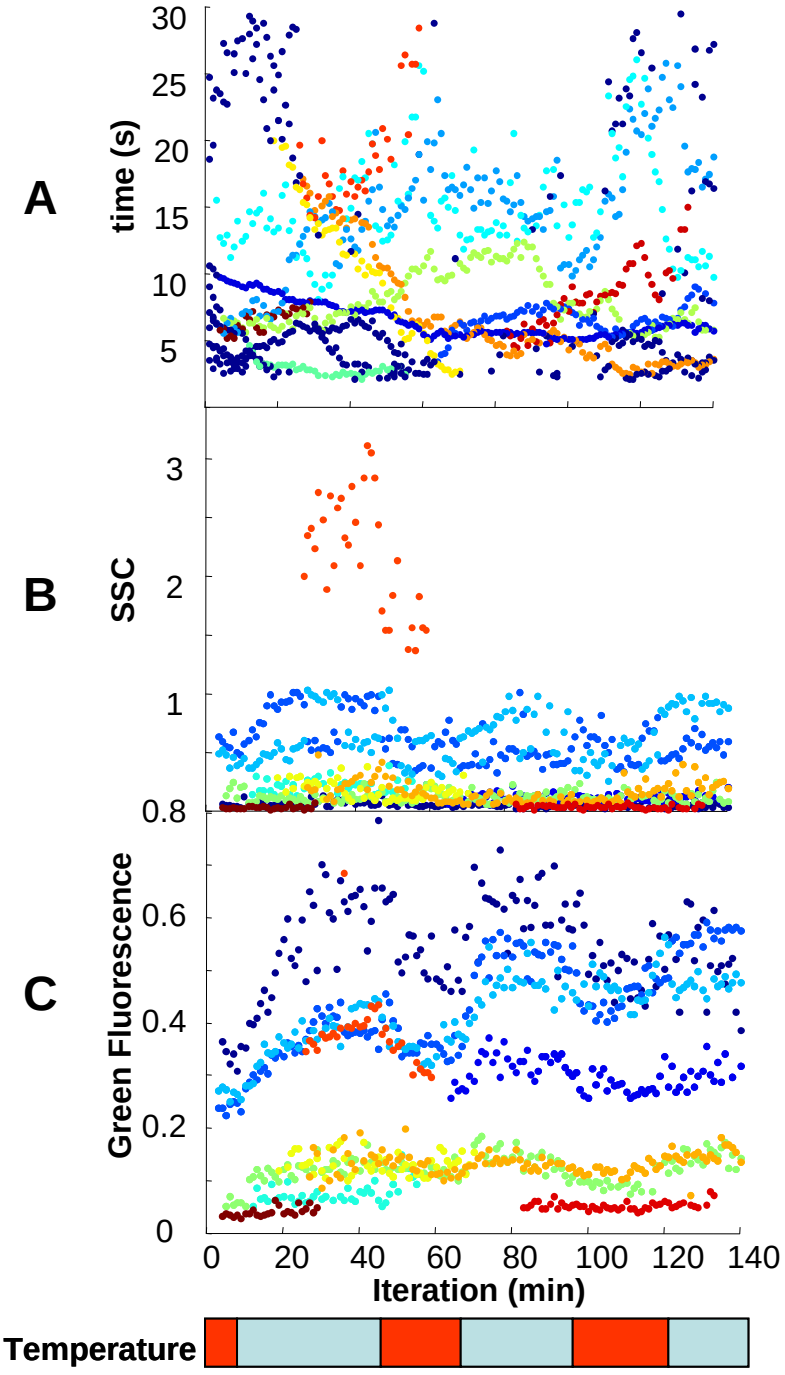

Figure 10-4: The effect of temperature on the Gfp content of individual yeast cells. Individual colors represent unique, tracked, individual cells across all figures. In **(A)** the time that each particle crosses the laser for all up strokes is recorded. In **(B)** the SSC and **(C)** the Gfp peak height response fro each individual cell is shown. The temperature was oscillated between 33°C ( ) and 24°C ( ) for the indicated periods of time.

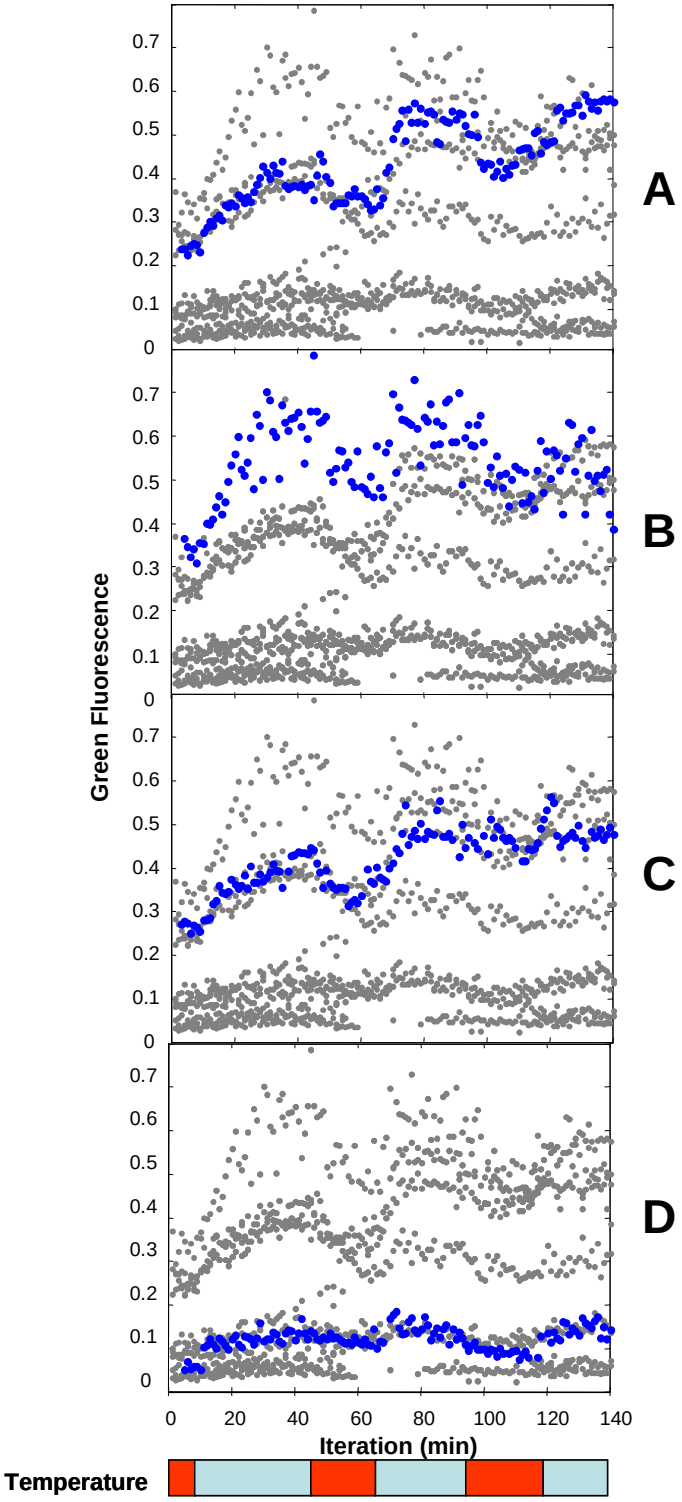

Figure 10-5: The Gfp response of four example cells. The unique cells **(A-D)** are from Figure 10-4 and are highlighted against the other 10 cells in the plug.

10.2.4 Oscillating Temperature II

After performing the experiment described in 10.2.3 it was attempted to duplicate the experiment without diluting cells into a different medium. This would eliminate potential nutrient shocks to the cells and maintain cells in exponential growth. Thus, a clear SD minimal medium was made by not adding two B-vitamins, riboflavin and folic acid. This medium had no detectable absorbance and yielded no detectable decrease in the growth rate of yeast cells. After performing the procedure in 10.2.1 with this clear SD minimal medium, cells were loaded into the cytometer. As shown in Figure 10-6A, the Gfp content of some of the cells oscillated with temperature consistent with Figure 10-4. However, in this experiment, the oscillation was directly as opposed to indirectly related to temperature.

It was then hypothesized that perhaps the RPMI medium as well as the temperature and duration the cells spent at room temperature in the diluting medium had a role in the cell response. Perhaps in section 10.2.3, the cells were adapted to room temperature in the RPMI and that led to the indirect relationship between temperature and Gfp content. To test this hypothesis, the procedure described in 10.2.3 was duplicated and two experiments were performed: 1) cells were grown overnight at room temperature and 2) overnight at 30°C. For both the cells grown at room temperature, Figure 10-6B, and the cells grown at 30°C, Figure 10-6C, the same trend of an individual cell's Gfp content varying directly with temperature was observed. This is in direct contrast to Figure 10-4 where the Gfp content was indirectly related to temperature.

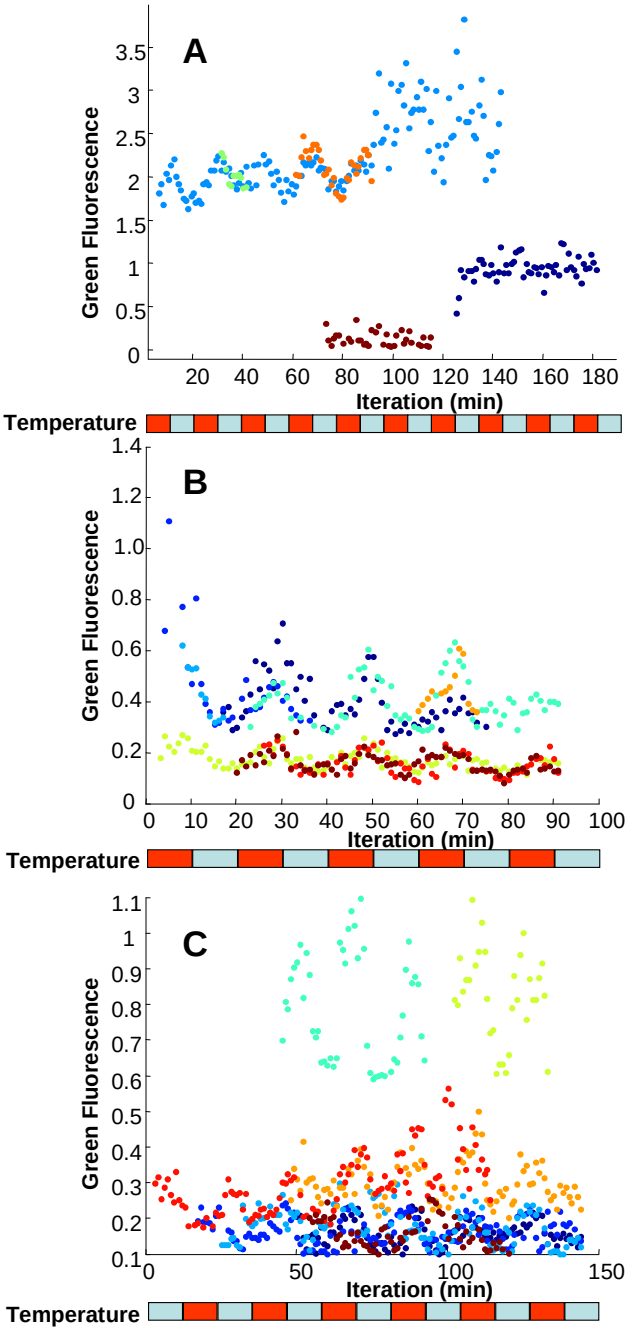

Figure 10-6: Gfp peak height response of individual cells during temperature oscillations. Cells **(A)** grown at 30°C in clear SD minimal and diluted into clear SD minimal medium at 30°C, **(B)** grown overnight in SD minimal at room temperature and diluted into RPMI medium and **(C)** grown at 30°C in SD minimal and diluted into RPMI medium. In direct contrast to Figure 10-4 the Gfp peak height changed directly with temperature for all experimental conditions.

10.2.5 Eulerian Viewpoint

During the course of the experiments displayed in Figure 10-6B,C, a sample of the diluted cells were placed in a shake flask and placed in a water bath at 33°C. The shake flask was then alternated between agitated water baths at 33°C and 24°C every 20 minutes. A sample was withdrawn before every temperature shift and 10,000 cells were scored for the fluorescence content with the Eulerian viewpoint on the cytometer. As shown in Figure 10-7, for both of these experiments, there are no discernable changes in the fluorescence distribution of the cells over the course of this experiment.

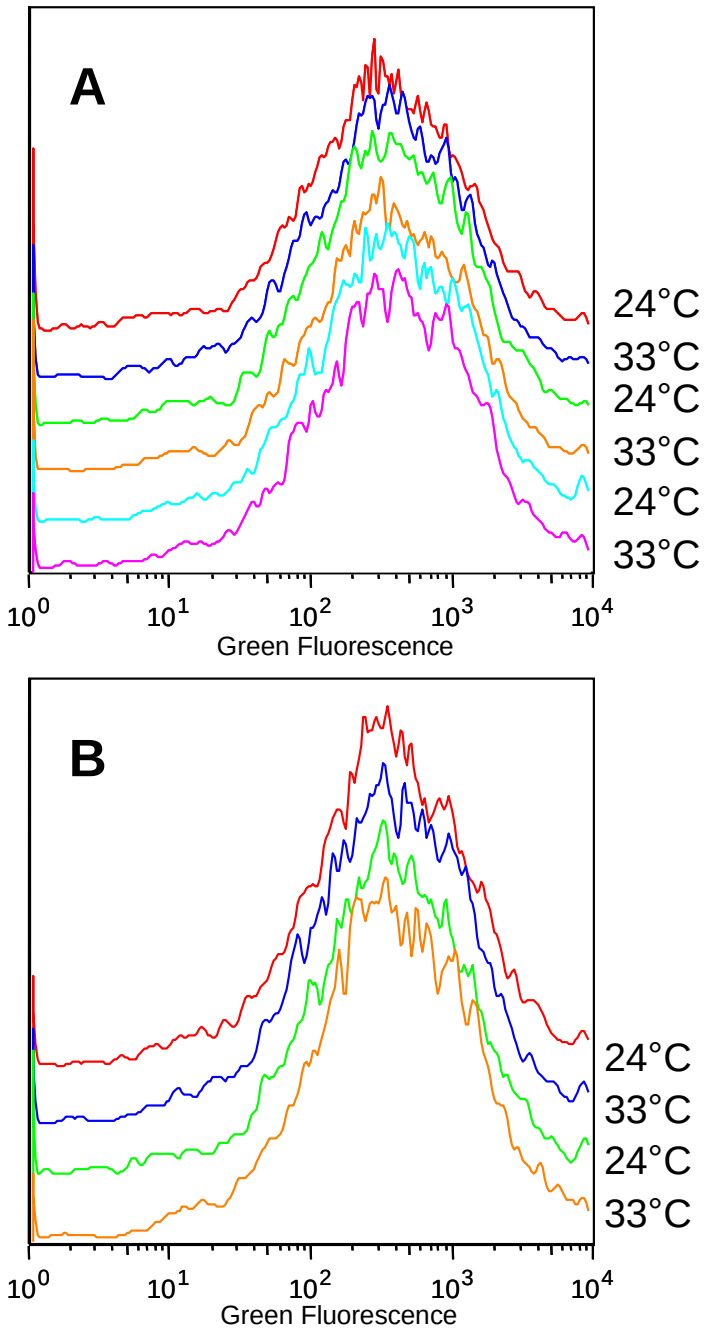

Figure 10-7: Eulerian viewpoint of temperature oscillations with yeast cells. **(A)** The diluted cells from Figure 10-6B and in graph **(B)** from Figure 10-6C were placed in a shake flask and placed in a water bath at 33°C. The shake flasks were then alternated between agitated water baths at 33°C and 24°C every 20 minutes. A sample was withdrawn before every temperature shift and 10,000 cells were scored for their fluorescence content with the Eulerian viewpoint on a FACS Calibur flow cytometer.

10.3 Discussion

It was surprising to see the Gfp peak height respond within 1 minute of a temperature shift. Since it takes on the order of hours for the Gfp protein to completely mature and become fluorescent (Greenbaum, et al. 2002 ; Heim, et al. 1995), these responses cannot be attributed to changes in the rate of mRNA production from the plasmid. Instead, it is hypothesized that the temperature dependence must originate within the existing pool of Gfp protein in the cell. Thus, it is either a function of a change in the protein degradation rate or a function of the change in the folding kinetics of the Gfp protein. The energy landscape of Gfp is complex with multiple local minima (Greenbaum, et al. 2002). Thus, it is hypothesized that the Gfp pool or a fraction of the pool is moving between two folded states at these temperatures. Since the Gfp content returns to nearly the same value after a temperature oscillation, Figure 10-6, this change appears reversible. The folding kinetics might also be affected by the state of the helper proteins inside a cell. These helper proteins are hypothesized to affect proper Gfp folding. Further testing of these hypotheses under different transient conditions is necessary to further elucidate these effects.

It was also surprising to see no change in the distribution of Gfp content during the temperature oscillations in Figure 10-7. It is likely that there are real changes in the shape of the total distribution, but the data processing in the flow cytometer is not accurate enough to record these changes. This is due to the use of a log scale to measure the Gfp content of the individual cells. Using a log scale to measure fluorescence is the most common setting on a flow cytometer. However, this comes at the cost that the 20-30% changes in the fluorescent signal only results in a net

movement of ~10 channels on the 1024 channel scale in the cytometer. This is only a 1% change in the measurement, and would be practically unobservable using these common settings.

Also, during the course of this experiment, the rate of cell division is significant compared to the time-scale of the experiment, and this would affect the distribution. Thus, these 1% changes that might be observed could be attributable to cell division and not the single cell response. These effects would also apply to using a linear digitization scale on the flow cytometer. Thus, the only way to observe affects like this is to approach the problem with a Lagrangian viewpoint.

11 Flow Cytometry without Alignment of Collection Optics

11.1 Introduction

The basic principles of a flow cytometer have been invented over 40 years ago (Kamentsky and Melamed 1967) and have since been refined into highly developed, sophisticated instruments. Over this time the basic principles have not been changed significantly. In traditional flow cytometry, the illuminating laser beam and the light collection optics are placed in the same plane perpendicular to the flow stream. In most current instrument configurations microscope objectives gather scattered or fluorescent light. In place of microscope objectives, optical waveguides butted against the flow cell wall have been proposed and shown to collect light similar to microscope objectives (Shapiro and Hercher 1986). The collected light is then passed through a series of dichroic mirrors and bandpass filters to measure light from fluorophores correlated with a specific aspect of cell physiology. For high accuracy and precision, this traditional arrangement requires a precise alignment between the illumination optics, the flow stream, the collection optics, and the dichroic mirrors and filters used. Properly aligning these elements is a sensitive task that requires considerable skill and experience.

Current research to expand this technology has taken two directions: (i) development of higher-end cytometers with increasing signal strength, numbers of illuminating lasers, and fluorescence parameters analyzed (Bigos, et al. 1999 ; De Rosa, et al. 2001 ; Roederer, et al. 1997) and (ii) development of instruments that are smaller, less expensive, and more accessible (Guava Technologies Inc, Accuri) (Ateya, et al. 2008 ; Bernini, et al. 2006 ; Shapiro 2004). This report describes an alternate

configuration that has the potential to make cytometers less expensive, more accessible, and more robust.

The described instrument configuration uses a Teflon AF® capillary as the flow cell (TFC). The TFC has the unique optical property that the refractive index of the polymer (n=1.290) is lower than water (n=1.333) (Hougham, et al. 2002). Thus, a water filled TFC behaves and functions as a liquid core waveguide (Hecht 2006). Furthermore, the material itself is transparent to both UV and visible light (Hougham, et al. 2002). Thus, a laser can be directed perpendicular to the axis of the TFC and illuminate the path of the cell stream. A sheath flow configuration permits individual hydrodynamically focused cells to flow through the TFC in single file and cross the illuminating laser beam one at a time as in conventional flow cytometry. Subsequently, orthogonally scattered or fluorescent light from each cell is collected by the TFC and directed along the axis of the waveguide to the terminus of the TFC. The light is then transferred to a solid core fiber optic connected to a PMT where light is measured, converted to an electronic signal, and recorded by a computer similar to the data acquisition process of traditional cytometry.

In such a configuration it is possible to completely replace the light collecting objectives and dichroic mirrors used in a traditional cytometer with fiber optic splitters to enable signal collection at different wavelengths. Multimode fiber optic splitters divide light of all wavelengths in one fiber into multiple fibers by fusing the fiber cores together. Thus, by simply attaching an appropriate optical filter on the end of each fiber, different fluorescent signals can be collected and analyzed. In contrast to optical lenses and mirrors fiber optic splitters are not sensitive to reasonable mechanical forces

and form the basis of robust cytometers insensitive to temperature fluctuations and capable of surviving mechanical jolts without losing alignment. Also, it significantly simplifies the changing of filter sets to any desired configuration.

11.2 Results

11.2.1 Comparison of Light Collection

The amount of light that can be collected by a TFC or any optic is expressed by the numerical aperture (NA). The NA defines the cone of light collected and for a lens is computed using the equation:

$$\mathrm{NA} = n_1 \sin(\theta_{\text{half angle}}) \tag{10.1}$$

where n_1 is the refractive index of the fluid surrounding the lens and $\theta_{\text{half angle}}$ is the half angle of the vertex of cone of light collected by the optic. For a fiber optic, the NA is defined by:

$$\mathrm{NA} = \sqrt{n_{core}^2 - n_{clad}^2} \tag{10.2}$$

where n_{core} is the refractive index of a water core and n_{clad} is the refractive index of the capillary wall (Hecht 2006). For the TFC, this results in a numerical aperture of 0.34. Table 11-1 shows the NA of the constructed TFC compared to several other flow cell configurations. These include a stream in air cytometer where light is collected along the axis of the fluid stream similar to the TFC (Mariella, et al. 1996), a microscope objective with a NA of 0.60 (Shapiro 1985), and a cytometer where fiber optics are butted against the flow cell in place of microscope objectives (Shapiro and Hercher 1986). In contrast to a waveguide cytometer where light does not leave the flow cell, in a traditional microscope based cytometer light must leave the flow cell and transit a

gap of air before reaching the microscope objective. Thus for a square flow cell, the divergence of the light leaving the flow cell is increased, and results in a lower effective NA as shown in Table 11-1.

By comparing the NA between systems, a measure of the relative light collection efficiencies in units of decibels (dB) and percent can be computed using the equation (Crisp and Elliott 2005):

$$\begin{aligned} Efficiency \ \ (dB) &= -10\log_{10}\left(\frac{NA_1}{NA_2}\right)^2 \\ Efficiency \ \ (\%) &= 100*\left(\frac{NA_1}{NA_2}\right)^2 \end{aligned} \tag{10.3}$$

As shown in Table 11-1, the relative efficiency in percent of each device is computed by using the effective NA of a microscope objective as the reference optic. The constructed TFC collects 56% of the light that a microscope system would collect.

11.2.2 Fiber Optic Splitter

With only one fiber optic leaving the capillary, only one fluorescence or scatter signal can be acquired. For generating additional fluorescence channels the potential exists to use a variety of dichroic mirrors and bandpass filters (Hammamatsu Corp) to split out the various wavelengths of light and input them into their respective PMTs (Mariella, et al. 1999). However, this option is still subject to the rigors of proper alignment of each of the mirrors in the filtering units.

As an alternative option, mirrors and filters with their associated alignment issues can be replaced with a fiber optic splitter. Commercially available splitters divide light of all wavelengths in one fiber into multiple fibers by fusing the fiber cores

together (Figure 11-1). The ratio of the split can be adjusted by varying the length of the fused segments (Hecht 2006). Then, filters can be placed at the end of each fiber to pass only select wavelengths of light to the PMT (Figure 11-1). It is important to note that while this option requires no alignment, it comes at the cost of both increased light loss due to the division of the total signal by the split ratio and an increased burden on the filters to eliminate scattered illumination light from fluorescent signals. Typically, due to imperfections in the fusing of the fiber cores 60-70% of the total light inputted into a splitter reaches the output fibers. Thus, when coupled to a TFC the overall system delivers approximately 10-15% of the light for a given fluorescence channel when compared to a traditional cytometer.

Table 11-1: Comparison of the numerical aperture (NA) and relative light collecting efficiencies of the TFC to existing cytometers. The effective NA accounts for increased divergence of light out of a flow cell due to the flow cell/air interface. The NA of the optic without correction is in parentheses. The relative efficiency of each device is computed by comparing the volumes of the cones of collected light using equation (2) and using the microscope objective as the base case.

Cytometer	Effective NA	Relative Efficiency (%)	Reference
Stream In Air	0.88	375	(Mariella, et al. 1996)
Microscope Objective	0.46 (0.60)	100	(Shapiro 1985)
TFC	0.34	56	
Fiber Optic Light Collection	0.27 (0.3)	35	(Shapiro and Hercher 1986)

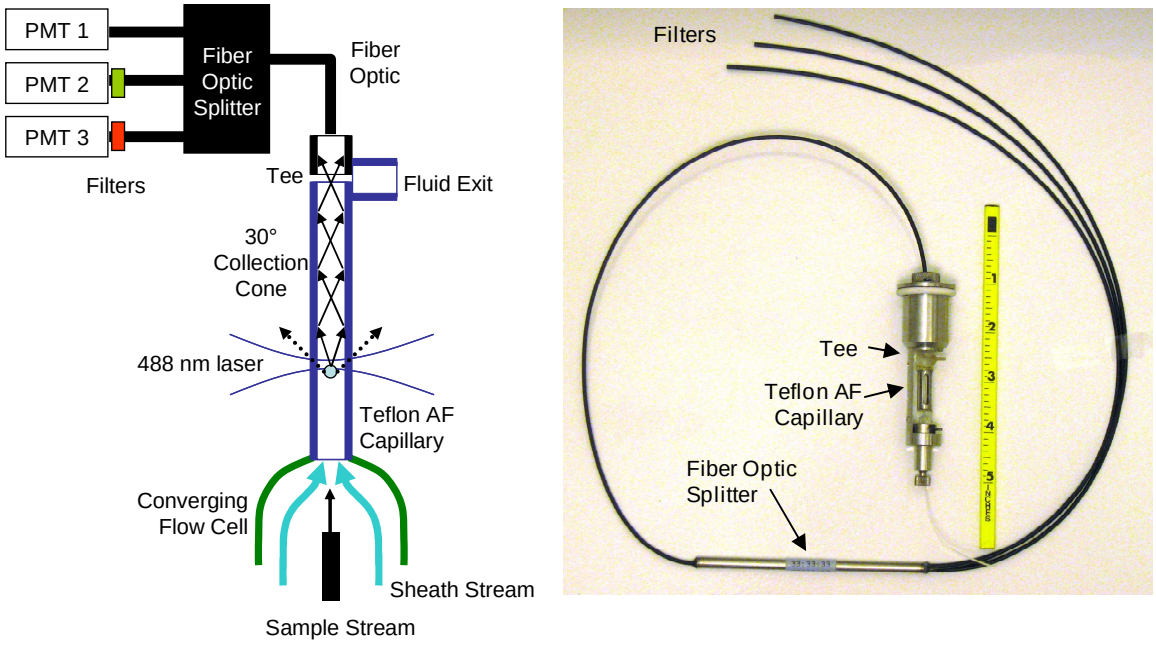

Figure 11-1: Cartoon and picture of the assembled flow cell. ***(Left)*** Schematic of the TFC attached to the fiber optic splitter. The tee holds the fiber optic close to the terminus of the TFC. Light entering the fiber optic splitter is divided into three different fibers. At the terminus of each fiber, different wavelengths of light are filtered out**.** ***(Right)*** Picture showing the actual system described in the schematic.

11.2.3 TFC alignment

The TFC was placed in the flow cell holder of the Ortho cytometer and illuminated with a 20 mW, 488nm laser beam focused through a set of crossed cylindrical lenses. Using air pressure, a suspension of 2 µm beads was passed through the TFC. The side scatter signals of the beads were collected by the fiber optic and measured by a PMT without any optical filters. Little light was lost between the TFC and the fiber optic since (i) the NA of the fiber is larger than the NA of the TFC and (ii) the 1 mm diameter of the fiber optic is much greater than the spot size projected onto the fiber from the 0.1 mm inner diameter of the TFC. After adjustment of the sheath flow rate, sample flow rate, and placement of the capillary in the illuminating beam the peak heights of the side scatter signal converged to a very narrow range as shown in Figure 11-2A. The CV of the side scatter from the TFC was 4.9%. This value compares very well to the 4.8% CV value of the side scatter signal obtained from the same set of beads acquired by a conventional BD Calibur cytometer, Figure 11-2C.

Fluorescent signals were measured by placing a 515 nm cutoff long pass filter at the terminus of the fiber optic. Using the same flow cell alignment used with the 2 µm beads the fluorescence peak height signals of 6 µm fluorescent beads converged to a narrow range as shown in Figure 11-2B. In this case, the CV of the fluorescent beads obtained with the TFC was 5.7% compared to the slightly higher 6.1% CV obtained with the BD Calibur cytometer, Figure 11-2D.

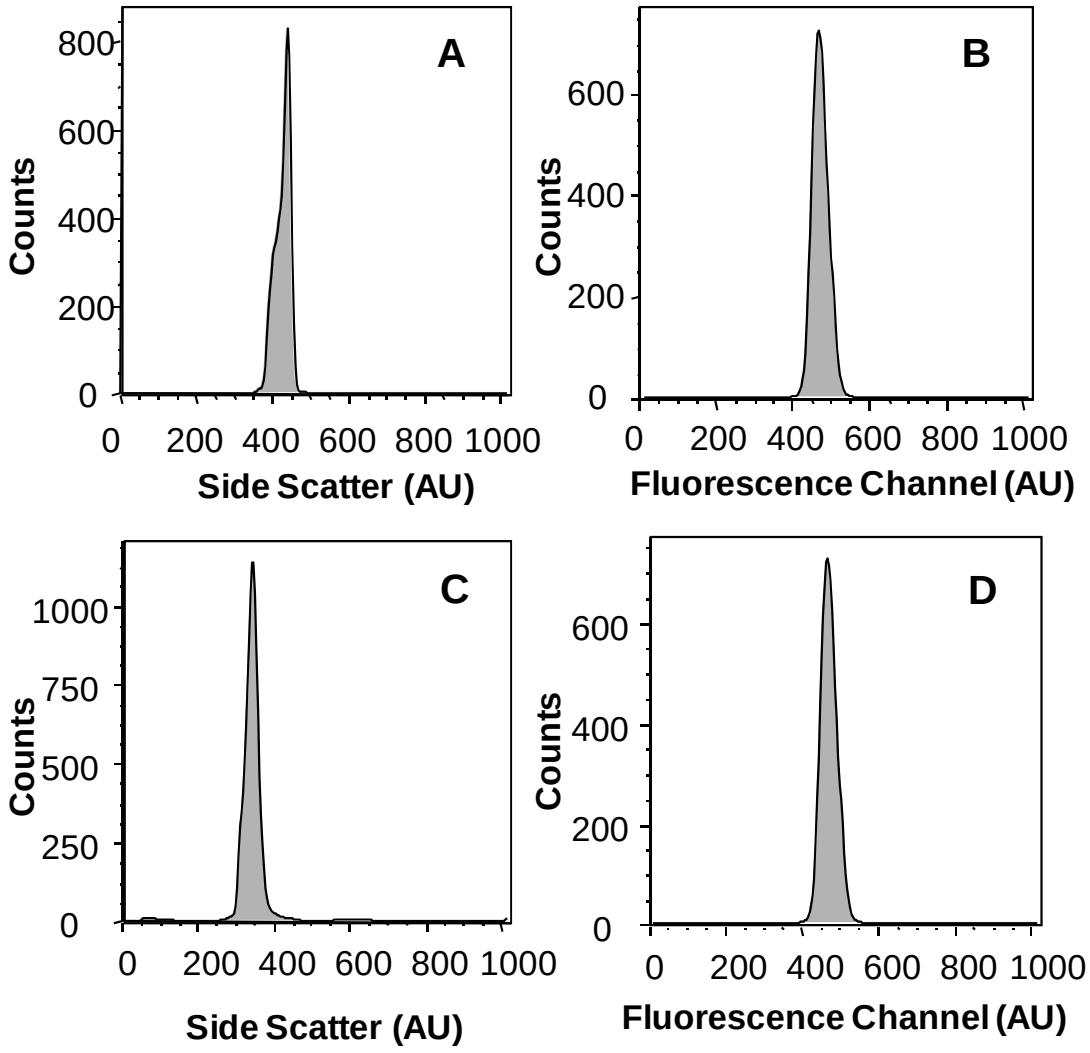

Figure 11-2: Comparison of the bead CVs using the TFC and the FACS Calibur. Histograms showing **(A)** the side scatter signal from 2 μm beads CV=4.9% and **(B)** the fluorescence signal from 6 μm AlignFlow plus reference beads CV=5.7% collected using the TFC. Histograms **(C)** and **(D)** illustrate corresponding data acquired using a BD Calibur cytometer.

11.2.4 Flow Cell and Splitter Performance

To test how much fluorescent light is reaching the PMT, a mixture of 6 μm beads with relative intensities of 100%, 10%, 2%, 0.4%, and 0.1% were passed through both the assembled flow cell with the fiber optic splitter and the BD Calibur. Using the side scatter signal as a trigger, fluorescence was acquired in log mode. As shown in Figure 11-3A, the TFC was able to resolve beads down to 2% of the fluorescence. Due to the large amount of noise measured by the PMT module due to leakage through the filters and electronic noise, there was only an effective 2.5 decade scale available from the flow cell. This is compared to the BD Calibur where all fluorescence intensities over 4 decades were resolved. It is probable that more sophisticated electronic and light filters could be used to further reduce the signal noise.

Cells stained for their DNA content were acquired using both the TFC and the BD Calibur. CHO cells were stained with PI. The resulting cell cycle distributions are shown in Figure 11-4A,C). The CV of the G1 peak for both the TFC and the BD Calibur was 8% and the fractions of cells in each cell cycle phase as calculated by MultiCycle agreed to within 3%. Yeast cells were stained with Sytox green (Haase and Reed 2002). The cell cycle distribution for the TFC is shown in Figure 11-4B and the BD Calibur is shown in Figure 11-4D. The CV of the G1 peak for both the TFC and the BD Calibur were approximately 12% and the fractions of cells in each cell cycle phase as calculated by MultiCycle agreed to within 4%. As this data shows, the TFC can be used for common and basic staining protocols for mammalian and yeast cells.

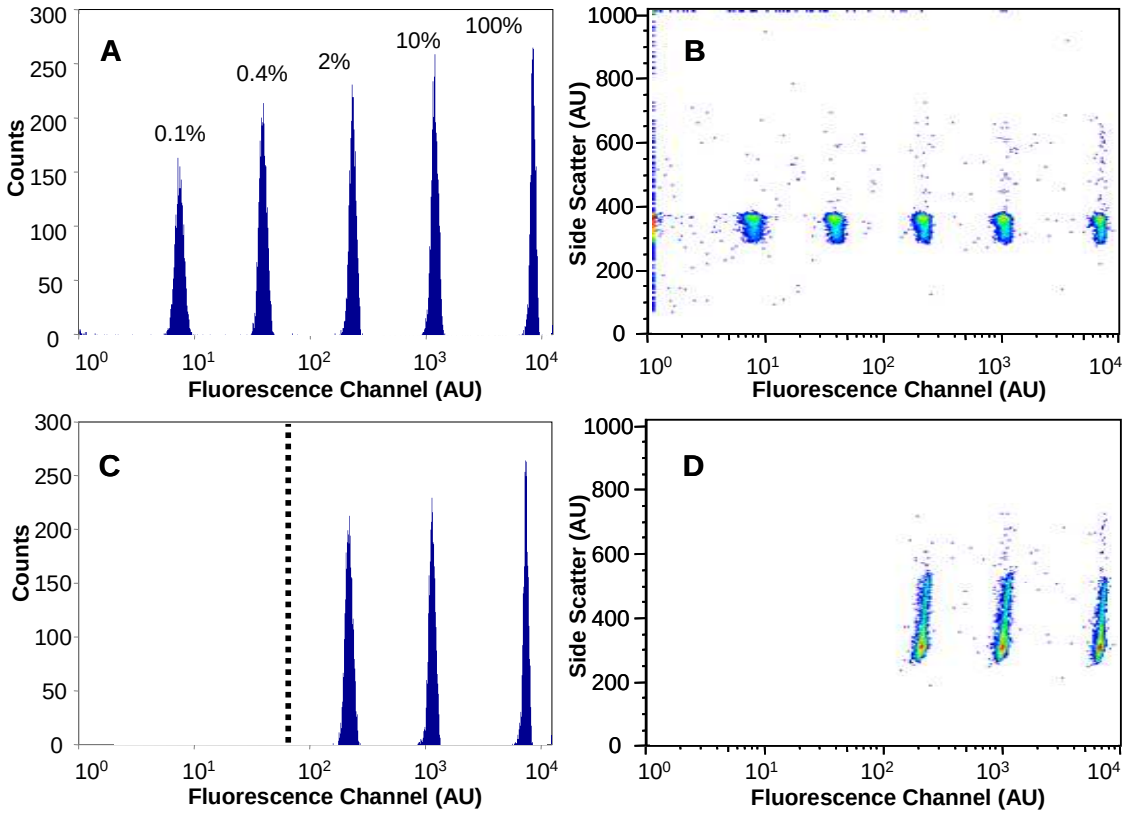

Figure 11-3: Comparison of instrument sensitivity between the FACS Calibur and the TFC **(A)** Histogram and **(B)** cytogram of a mixture of 6 µm fluorescent beads for the BD Calibur and the TFC **(C)** and **(D)**. The reference beads were a mixture of fluorescence intensities at 100%, 10%, 2%, 0.4%, and 0.1%. Due to noise in the TFC configuration a threshold was applied to the fluorescence signal in (C) and (D) where peaks were no longer able to be resolved from the noise as indicated by the dashed line in the figure.

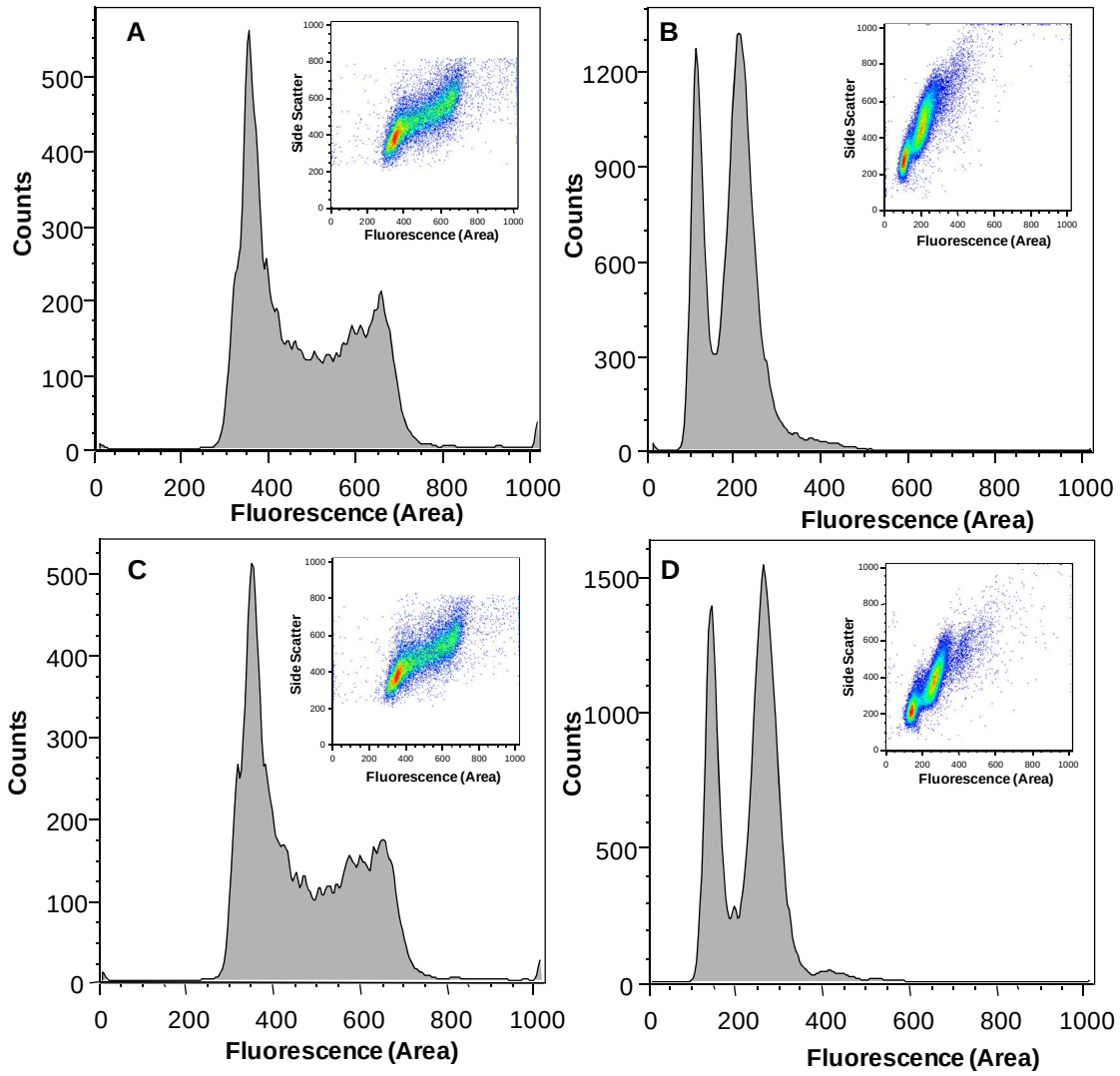

Figure 11-4: Cell cycle distributions obtained using the TFC for **(A)** CHO cells stained with PI and **(B)** diploid yeast cells stained with Sytox Green. The same stained cell sample were also acquired using a BD Calibur **(C)** and **(D)**. The CV values of the G1 and G2 peaks as well as the ratio of G2/G1 channels were statistically identical for the two cytometers.

11.2.5 Side Scatter Pulse Shape

During acquisition of the fluorescent 6 μm beads, a significant difference in the SSC signals was observed. While the fluorescence signal converged to a CV comparable to the value measured on the BD Calibur, the SSC signal was drastically different (Figure 11-3B,D). This was in contrast to the 2 μm bead SSC CV signal which was very comparable to the BD Calibur signal. To further test the SSC differences between the two optical layouts, different sizes of polystyrene beads were acquired using both the TFC and the BD Calibur. As shown in Figure 11-5, the difference between the SSC CVs increase with bead size until a plateau is reached at lager bead sizes as indicated by the difference between the two CV values.

While acquiring the larger beads it was observed that the SSC pulse shape of an individual particle became bimodal with the second peak having a smaller magnitude than the first peak (Figure 11-6A). This is illustrated in the histogram of Figure 11-6B where the ratio of the peak voltages of peak 1 divided by peak 2 as indicated in Figure 11-6A is generated for 5000 20 μm polystyrene beads. The histogram shows that peak 1 is larger than peak 2 for 99% of beads with a mode of 1.5. The bimodal behavior was observed for the 16 μm beads, however was not observed for smaller beads.

11.2.6 Side Scatter Pulse Shapes in Opposing Directions

Using the capillary configuration, 6 μm fluorescent beads were pumped through the capillary in opposite directions. Pulse shapes of both fluorescence and side scatter were obtained and a representative SSC and fluorescence pulse shape from a particle is shown in Figure 11-7A. Side scatter signals of these beads showed a bimodal peak

while the fluorescence signal was unimodal (Figure 11-7A). This data indicates that the bimodal behavior of the SSC pulse shape is not due to an asymmetric illumination beam since the fluorescence pulse shape is unimodal. Bimodal behavior was not observed in the sheath flow cell configuration for the 6 μm beads likely due to a 75 times larger particle velocity in the sheath flow configuration compared to the capillary configuration. A slower particle velocity allows more data points per pulse shape to be obtained, resulting in a higher resolution pulse shape. With this configuration, 4 representative pulse shapes from beads pumped towards the fiber optic (Figure 11-7B) and away from the fiber optic (Figure 11-7C) are shown. These pulse shapes are mirror images of each other.

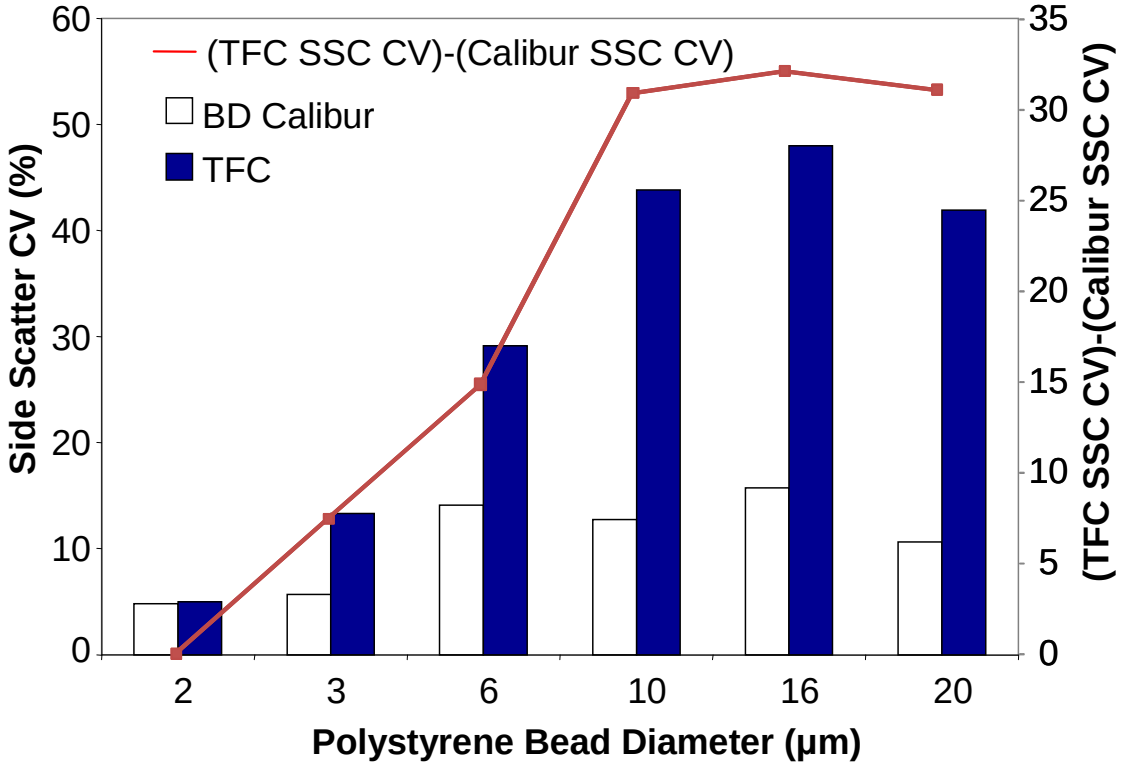

Figure 11-5: The SSC CV values for increasing diameter of polystyrene beads for the (■) TFC and the (□) BD Calibur. The line indicates the difference in the CV values between the two cytometers and is plotted on the right axis. CV values were generated from peak height signals.

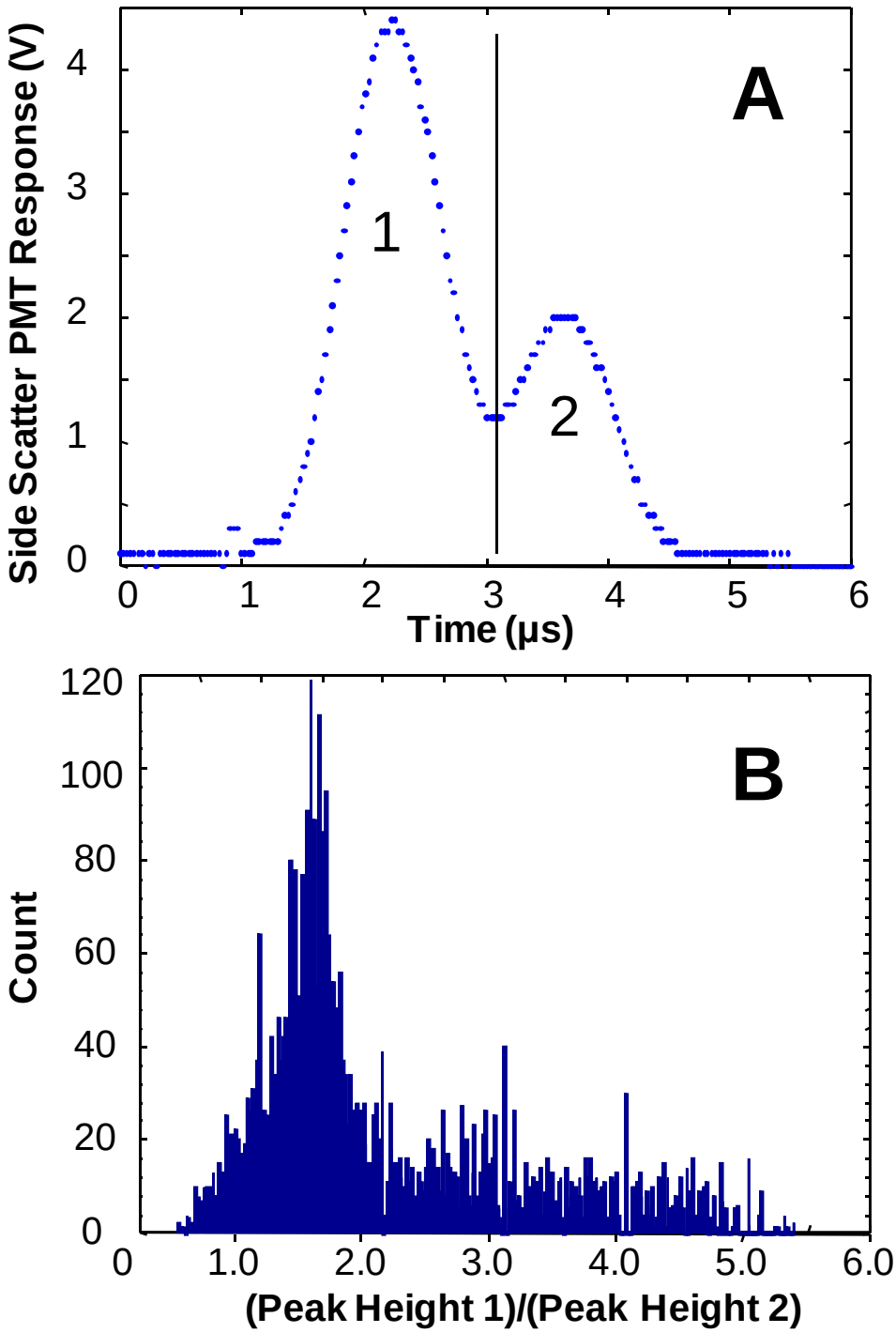

Figure 11-6: SSC waveforms showing two humps **(A)** A representative SSC pulse shape waveform from a single 20 micron particle illustrating the bimodal behavior of the SSC signal. **(B)** A histogram of 5000 beads of the ratio of the peak voltages of peak 1 divided by peak 2 as indicated in (A). The histogram shows that peak 1 is larger than peak 2 for 99% of beads with a mode of 1.5.

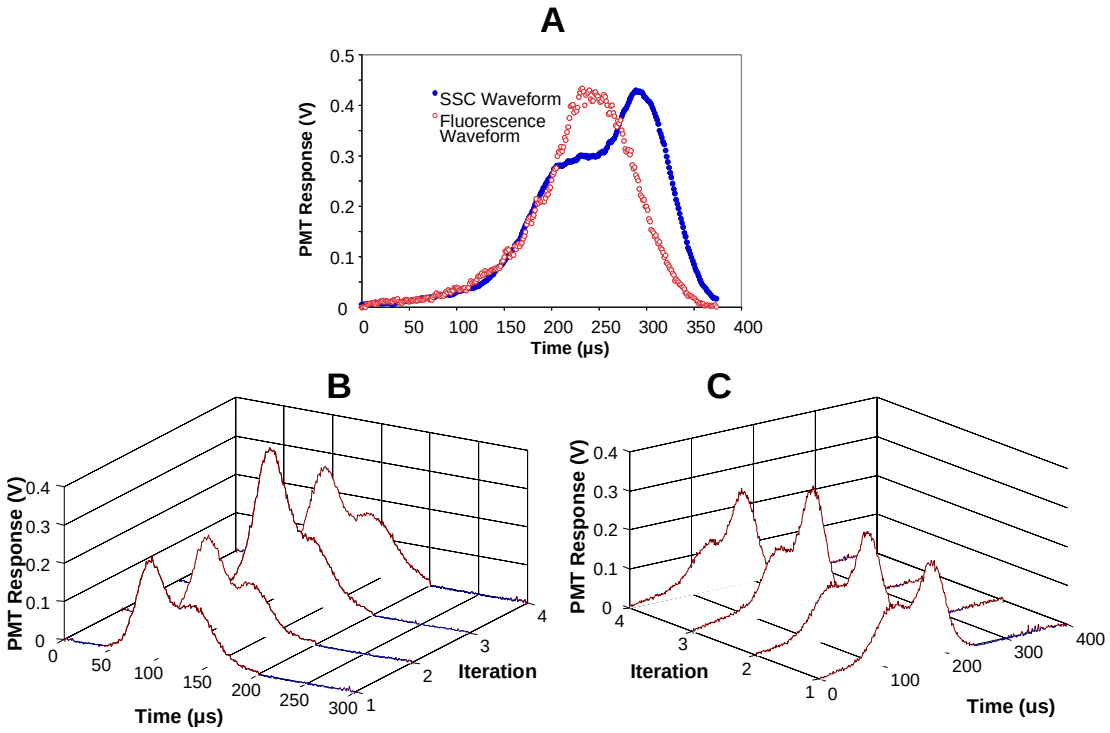

Figure 11-7: Mirror images of the two humped SSC peaks as a function of flow direction **(A)** Representative pulse shape of the fluorescence and SSC of 6 µm fluorescent beads. The SSC signal is bimodal while the fluorescence signal is unimodal. Representative SSC pulse shapes of fluorescent 6 µm beads when the particle flows towards the fiber optic **(B)** and away from the fiber optic **(C)**. The pulse shapes are mirror images of each other.

11.3 Discussion

Flow cytometers that integrate the fluidic components with the optical components are a relatively new addition to the field. The first reported instance was implemented in a stream in air cytometer. In this instrument, the water stream in air naturally forms a liquid core waveguide due to air having a lower refractive index than water (Mariella, et al. 1996) (Mariella, et al. 1999). Scattered light from cells was then conducted to a fiber optic placed in the fluid stream and measured by a PMT as in this study. However, the design described in this paper is unique in the fact that the flow cell is integrated with the light collection requiring only a single, robust component, and in contrast to the stream in air cytometer, the fluid is completely contained in a flow cell.

The second reported instance used a micro-channel cytometer with the fluid pathways coated with a series of materials that formed a reflective Fabry-Perot mirror (Bernini, et al. 2006). The reflective fluid channel was used to guide the illuminating laser collinearly with the fluid flow and scattered light from particles was collected orthogonal to the fluid stream, in essence the inverse arrangement reported in this study with the TFC. However, the Fabry-Perot mirror constructed is wavelength dependent with a bandpass of 200 nm centered around 633 nm (Bernini, et al. 2006). Thus, UV light could not be used. A channel using a coating of Teflon AF and relying on total internal reflection is only limited by the absorption of the water core. It is likely that Teflon AF coated micro-channels can be created in microchip cytometers as the methodology to coat micro-channels etched in silicon with Teflon AF has previously been developed (Datta, et al. 2003).

The TFC and fiber optic splitter flow cell could be used in the construction of a simple, robust cytometer resistant to perturbations by mechanical forces. If a fiber optic is used to deliver illuminating light (Shapiro and Hercher 1986), then one could construct a cytometer that would never need alignment despite reasonable mechanical stress. Also, it would enable a lay person to change filter sets at will by simply changing fiber optics. The TFC would also allow the use of many different illumination lasers at various wavelengths focused to different spots along the axis of the fiber. Since the light collection from scattered particles is not bound by the field of view of a microscope objective, this could be accomplished over the entire 2 centimeter length of the TFC.

Collecting scattered light along the axis of flow results in the bimodal behavior of the SSC pulse shapes for large polystyrene beads (Figure 11-7). A potential simplified explanation for this behavior is illustrated in Figure 11-8. When spherical beads enter the illuminating laser beam all illuminated regions of the sphere have a normal to the surface with a z-component that points toward the collecting fiber optic. Thus, light that is reflected and refracted from the particle that falls within the acceptance cone of the TFC will be guided to the collecting fiber optic and measured. However, once the particle is halfway through the laser beam (Figure 11-7B) the illuminated surface has a normal with a z-component that points away from the collecting fiber optic. Thus, light is reflected away from the collecting fiber optic and only light that is refracted through the particle can be scattered towards the collecting fiber optic. Thus, one would expect the first half of the SSC pulse shape to have a higher intensity due to both refracting and reflecting components being measured as

compared to the latter half of the SSC pulse shape which should only be comprised of light that is refracted through the particle. This is observed when the particle flow direction relative to the fiber optic is reversed as shown by the mirror image SSC pulse shape in Figure 11-7B, C.

One does not see this effect in traditional optical layouts, since at all times while the particle is transiting the laser beam there is a component of the normal that points toward the collector. Therefore, at all times some component of both reflected and refracted light is collected. Thus, SSC light collection is asymmetric when light is collected collinearly with the flow while light collection is symmetric in traditional cytometry when light is collected orthogonal to the flow direction. Therefore, when measuring the SSC collinearly with the direction of flow one must expand the traditional definition of SSC from simply particle granularity to include terms that account for the asymmetry of light collection. The asymmetry of light collection is hypothesized to cause the increased CV in larger beads compared to traditional cytometers as illustrated in Figure 11-5. It is important to note that the bimodal behavior of light scatter is not expected to influence fluorescence light measurement since fluorescent light from fluorophores is emitted randomly in all directions as consistent with the fluorescence data collected from the 6 µm fluorescent beads (Figure 11-7A).

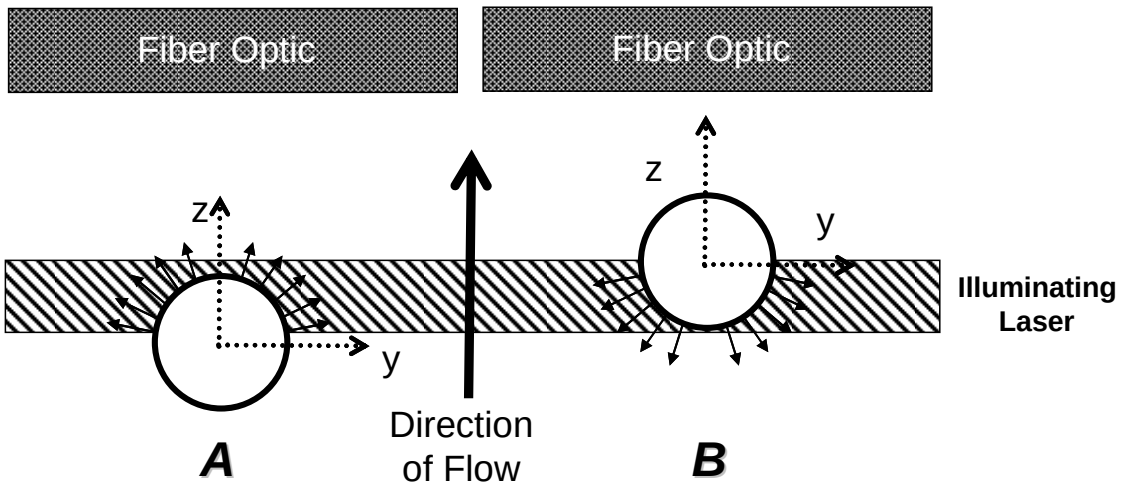

Figure 11-8: A simplified cartoon depicting the asymmetry of collecting light along the axis of flow. **(A)** As the particle initially enters the laser all illuminated regions of the sphere have a normal to the surface (dashed arrow) with a z-component directed toward the collecting fiber optic. Thus, reflected and refracted light falling within the acceptance cone of the TFC will be guided to the collecting fiber optic and measured. **(B)** Once the particle is halfway through the laser beam the normal has z-components that point away from the collecting fiber optic. Thus, reflected light is not collected by the fiber optic and only refracted light is collected.

12 Future Applications

12.1 Example Studies

Based on the preliminary experiments, it is envisioned that a wide variety of cell biologists will find a use for the instrumentation. Initially, the device would find application mainly in the biological research community for carrying out studies on cell population dynamics. However, this instrument will also be of interest in research and development for biotechnology for the characterization and isolation of desired strains. The information obtained will be useful for basic biological research providing information for instance on stem cell development, for medically related research by providing information on properties of cancer cells and how they respond to certain drugs, and for biotechnology related research and development. Two potential applications are further discussed.

12.1.1 Effects of chemicals on growth physiology:

A cell's physiology is dependent on both its genotype and its environment. Thus, the rate, division rate, and partitioning functions of the population balance equation are dependent on the environment of the cell. One example of the dependence of the cell physiology on the environment is the relation between ethanol concentration and the cell size of the budding yeast S. cerevisiae (Alberghina, et al. 1998 ; Aon and Cortassa 1998 ; Kubota, et al. 2004 ; Porro, et al. 2003). By combining the abilities to rapidly change the extracellular medium to new compositions, to maintain the extracellular medium at a constant composition over time, and track single cells in suspension over time, the proposed instrumentation will be ideally suited to rapidly

study the dependence of the cell physiology on the environment. For example, one will be able to begin growing and tracking a culture of cells under a standard set of growth-friendly conditions. Next, a toxin or drug can be rapidly introduced into the culture and its effect on the cell physiology assessed. Thus, the instrument would permit testing of the effects of specific chemicals on the growth dynamics of individual cells.

12.1.2 Cell aging

In budding yeast, the cell physiology is highly dependent on the genealogical and chronological age of the cells (Hughes 2002 ; Porro, et al. 2003). For example, the size distributions of budding yeast populations directly reflect the cell cycle progression and regulation due to the tight coupling between cell growth and cell division (Cipollina, et al. 2007 ; Hatzis and Porro 2006). Therefore, by fundamentally understanding the relation between cell growth and cell division as a function of cell age, new insight into how cells regulate the cell cycle can be obtained. The instrumentation will be able to rapidly and accurately address research questions like this. This is due to the proposed instrumentation's ability to track growing single cells in suspension in a well-controlled, constant environment throughout time.

12.2 Instrument Testing and Improvement

To expand the scope of potential experiments that could be performed on the device and improve the functionality a series of improvements are envisioned.

12.2.1 Extraction Algorithm

At present, a cell's trace is generated by assigning events across multiple strokes to a trace through a search algorithm. The assignment algorithm works by having the user choose two initial points in a trace. Then using up to a user specified number (typically 8) of past points in the trace, the algorithm does a linear extrapolation of each parameter to the next iteration that does not have a trace member. The extrapolated value is then searched for in the next iteration, by computing the weighted Euclidean distance from the extrapolated value to each event in the next iteration. Given a user specified threshold, a matching particle is assigned to the trace and the algorithm continues to the next stroke. The weighted Euclidean distance is more heavily weighted to favor fluorescence and timing than scattering.

While functional, there are many aspects to this algorithm that need addressing. First, it would be required that all user input is avoided. Second, the algorithm only considers a single trace at a time irregardless of other potential traces that may influence assignment of the next event to a trace. A superior algorithm would consider all possible traces at once. One possible approach to these shortcomings is to implement a Hough transform that will search for lines in the figures (Gonzalez, et al. 2004). Each line would be considered a trace, and particles would be assigned to it.

12.2.2 Bacteria Testing

While initial experiments have shown that the device works with yeast and mammalian cells, it is unknown if it will work with bacterial cells like E. Coli. The first issue with working with bacterial cells is the small size of the cells. This limits scatter

signals to near background levels. Typically, cells must be stained with a dye to make them detectable over background noise. Second, since bacteria can be rod, ovoid, circular, or spiral, the noise induced by a tumbling bacterium would have to be accounted for. It would be possible to examine other aspects of the waveform to account for this. For instance, the area under the waveform would be a measure of the total fluorescence content irregardless of the tumbling cell.

12.2.3 Aqueous Nutrient Shifts

With the Teflon AF capillary, gases can be supplied at sufficient rates to keep the cells growing as well as to induce transient shifts in aqueous gas concentrations. To induce transient shifts for aqueous nutrients we have devised a series of pumps and valves that enables a continuous supply of aqueous nutrients to be delivered to the cells. At each end of the capillary, a valve and pump will be connected as shown in Figure 12-1 left. While pumping in the down direction, the bottom valve is actuated to waste, while the top valve is actuated to the pump. The pump is then turned on, and the fluid moves in the down direction. Likewise, to pump in the up direction, the top valve is actuated to waste, while the bottom valve is actuated to the pump. In this way, a constant supply of fresh medium is continually introduced to the capillary during each stroke.

For a wide range of cell sizes the cells are confined to a range of potential radial positions 55-75% of the distance from the centerline to the wall (Patankar, et al. 2001 ; Yang, et al. 2005). Thus, the particles will move at a slower velocity than the tip of the parabolic velocity profile of the fluid and the cells will always lag behind the tip of the

fluid. Therefore, if the stroke volume is set to where the tip of the velocity profile of the fresh fluid reaches the end of the capillary, then the cells will be retained in the capillary. In this situation, the capillary behaves like a laminar flow reactor with dispersion, commonly referred to as Aris-Taylor dispersion. This can be simulated by continually introducing fresh medium at the inlet of each stroke during the oscillation. Thus, as shown in Figure 12-1 right, given a capillary initially devoid of a solute, the oscillatory flow scheme will completely replace 99% of the contents of the capillary within 10 strokes while confining the particles in the capillary.

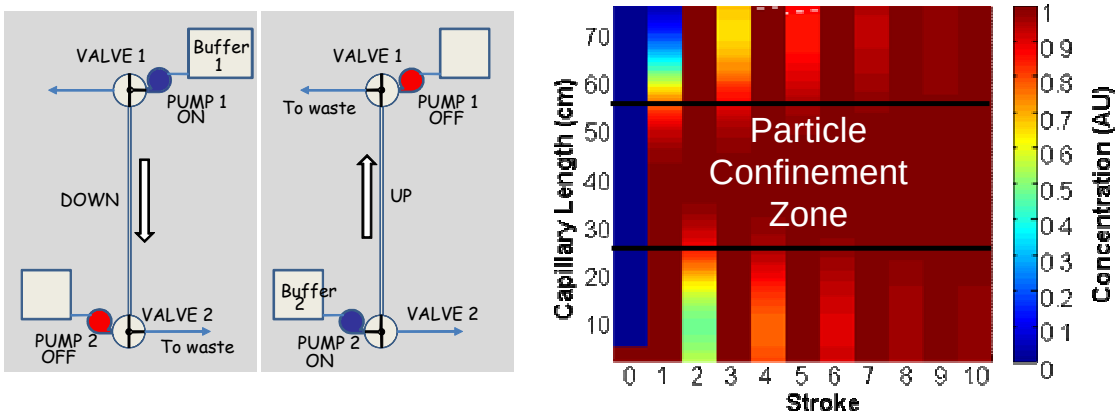

Figure 12-1: Replacing the extra-cellular environment with fresh media. **(Left)** Cartoon depicting the pumping strategy to introduce new fluid into the capillary while maintaining the cells in the capillary. **(Right)** Simulation showing the solute concentration at the end of each stroke. Stroke zero corresponds to the initial conditions. The cells are retained in the capillary while the fluid is replaced, due to the fact the cells move slower than the maximum velocity of the fluid. Thus, if the tip of the fresh fluid reaches the end of the capillary, then the cells are guarnteed to be retained in the capillary.

13 References

Abu-Absi NR, Zamamiri A, Kacmar JA, Balogh SJ, Srienc F. 2003. Automated Flow Cytometry for Acquisition of Time Dependent Population Data. Cytometry 51A:87-96.

Abu-Absi NR, Srienc F. 2002. Instantaneous evaluation of mammalian cell culture growth rates through analysis of the mitotic index. J Biotechnol 95:63-84.

Abu-Absi NR, Zamamiri A, Kacmar JA, Balogh SJ, Srienc F. 2003. Automated Flow Cytometry for Acquisition of Time Dependent Population Data. Cytometry 51A:87-96.

Albano CR, Randers-Eichhorn L, Bentley WE, Roa G. 1998. Green Fluorescence Protein as a Real Time Quantitative Reporter of Heterologous Protein Production. Biotechnol Prog 14:351-354.

Alberghina L, Smeraldi C, Ranzi BM, Porro D. 1998. Control by nutrients of growth and cell cycle progression in budding yeast, analyzed by double-tag flow cytometry. Journal of Bacteriology 180:3864-3872.

Al-Rubeai M, Emery AN. 1993. Flow Cytometry in Animal Cell Culture. Bio/Technology 11:572.

al-Rubeai M, Singh RP. 1998. Apoptosis in cell culture. Curr Opin Biotechnol 9:152-156.

Altenberg GA, Vanoye CG, Horton JK, Reuss L. 1994. Unidirectional fluxes of rhodamine 123 in multidrug-resistant cells: evidence against direct drug extrusion from the plasma membrane. Proc Natl Acad Sci U S A 91:4654-4657.

Anderson JB. 1972. *Biological Reactions: Kinetics of Yeast Growth*. Chemical Engineering Education 6:134-137.

Anderson MT, Tjioe IM, Lorincz MC, Parks DR, Herzenberg LA, Nolan GP, Herzenberg LA. 1996. Simultaneous fluorescence-activated cell sorter analysis of two distinct transcriptional elements within a single cell using engineered green fluorescent proteins. Proc Natl Acad Sci U S A 93:8508-8511.

Aon MA, Cortassa S. 1998. Catabolite repression mutants of *Saccharomyces cerevisiae* show altered fermentative metabolism as well as cell cycle behavior in gluocose-limited chemostat cultures. Biotechnology and Bioengineering 59:203-213.

Aouali N, Eddabra L, Macadre J, Morjani H. 2005. Immunosuppressors and reversion of multidrug-resistance. Crit Rev Oncol Hematol 56:61-70.

Ateya DA, Erickson JS, Howell PB,Jr, Hilliard LR, Golden JP, Ligler FS. 2008. The good, the bad, and the tiny: a review of microflow cytometry. Anal Bioanal Chem 391:1485-1498.

Auton TR. 1987. The Lift Force on a Spherical Body in a Rotational Flow. J Fluid Mech 183:199-218.

Badino AC, Almeida P, Cruz A. 2004. Agitation and Aeration: An Automated Didactic Experiment. Chemical Engineering Education 38:100-107.

Badino AC, Hokka CO. 1999. Laboratory Experiment in Biochemical Engineering: Ethanol Fermentation. Chemical Engineering Education 33:54-70.

Batard P, Jordan M, Wurm F. 2001. Transfer of high copy number plasmid into mammalian cells by calcium phosphate transfection. Gene 270:61-68.

Bentley WE, Kompala DS. 1990. Plasmid Instability in Batch Cultures of recombinant Bacteria. Chemical Engineering Education 24:168-172.
Bernini R, De Nuccio E, Brescia F, Minardo A, Zeni L, Sarro PM, Palumbo R, Scarfi MR. 2006. Development and characterization of an integrated silicon micro flow cytometer. Anal Bioanal Chem 386:1267-1272.
Bigos M, Baumgarth N, Jager GC, Herman OC, Nozaki T, Stovel RT, Parks DR, Herzenberg LA. 1999. Nine color eleven parameter immunophenotyping using three laser flow cytometry. Cytometry 36:36-45.
Bird AP. 1995. Gene number, noise reduction and biological complexity. Trends Genet 11:94-100.
Bittner C, Wehnert G, Scheper T. 1998. In situ microscopy for on-line determination of biomass. Biotechnol Bioeng 60:24-35.
Blake WJ, KAErn M, Cantor CR, Collins JJ. 2003. Noise in eukaryotic gene expression. Nature 422:633-637.
Block DE, Eitzman PE, Wangensteen JD, Srienc F. 1990. Slit scanning of Saccharomyces cerevisiae cells: Quantitation of asymmetric cell division and cell cycle progression in asynchronous culture. Biotechnol Prog
Boonstra J. 2007. Identification of a restriction point at the M/G1 transition during the ongoing cell cycle. Adv Enzyme Regul 47:208-221.
Boonstra J. 2003. Progression through the G1-phase of the on-going cell cycle. J Cell Biochem 90:244-252.
Boonstra J, Moes MJ. 2005. Signal transduction and actin in the regulation of G1-phase progression. Crit Rev Eukaryot Gene Expr 15:255-276.
Boschman GA, Rens W, van Oven CH, Manders EM, Aten JA. 1991. Bivariate flow karyotyping of human chromosomes: evaluation of variation in Hoechst 33258 fluorescence, chromomycin A3 fluorescence, and relative chromosomal DNA content. Cytometry 12:559-569.
Bretherton FP. 1962. Slow Viscous Motion Around a Cylinder in a Simple Shear. J Fluid Mech 12:591-613.
Cannizzaro C, Gugerli R, Marison I, von Stockar U. 2003. On-line biomass monitoring of CHO perfusion culture with scanning dielectric spectroscopy. Biotechnol Bioeng 84:597-610.
Cegovnik U, Novakovic S. 2004. Setting optimal parameters for in vitro electrotransfection of B16F1, SA1, LPB, SCK, L929 and CHO cells using predefined exponentially decaying electric pulses. Bioelectrochemistry 62:73-82.
Cerckel I, Garcia A, Degouys V, Dubois D, Fabry L, Miller AOA. 1993. Dielectric spectroscopy of mammalian cells. Cytotechnology 13:185-193.
Chen LB. 1988. Mitochondrial membrane potential in living cells. Annu Rev Cell Biol 4:155-181.
Chu L, Robinson DK. 2001. Industrial choices for protein production by large-scale cell culture. Curr Opin Biotechnol 12:180-187.
Cipollina C, Vai M, Porro D, Hatzis C. 2007. Towards understanding of the complex structure of growing yeast populations. J Biotechnol 2:393-402.
Clementschitsch F, Bayer K. 2006. Improvement of bioprocess monitoring: development of novel concepts. Microb Cell Fact 5:19.

Collins JF, Richmond MH. 1962. Rate of growth of Bacillus cereus between divisions. J Gen Microbiol 28:15-33.
Conlon I, Raff M. 2003. Differences in the way a mammalian cell and yeast cells coordinate cell growth and cell-cycle progression. J Biol 2:7.
Cormack BP, Valdivia RH, Falkow S. 1996. FACS-optimized mutants of the green fluorescent protein (GFP). Gene 173:33-38.
Crisp J, Elliott B. 2005. Introduction to Fiber Optics. Butterworth-Heinemann. 256 p.
Crissman HA, Oka MS, Steinkamp JA. 1976. Rapid staining methods for analysis of deoxyribonucleic acid and protein in mammalian cells. J Histochem Cytochem 24:64-71.
Crissman HA, Steinkamp JA. 1982. Rapid, one step staining procedures for analysis of cellular DNA and protein by single and dual laser flow cytometry. Cytometry 3:84-90.
Darzynkiewicz Z, Bedner E, Li X. 1999. Analysis of cell death by flow and laser scanning cytometry. In: Studzinski, GP .Apoptosis: A practical Approach. Oxford: Oxford University Press 61-63.
Darzynkiewicz Z, Bruno S, Del Bino G, Gorczyca W, Hotz MA, Lassota P, Traganos F. 1992. Features of apoptotic cells measured by flow cytometry. Cytometry 13:795-808.
Darzynkiewicz Z, Crissman H, Jacobberger JW. 2004. Cytometry of the cell cycle: cycling through history. Cytometry A 58:21-32.
Darzynkiewicz Z, Gong J, Juan G, Ardelt B, Traganos F. 1996. Cytometry of cyclin proteins. Cytometry 25:1-13.
Darzynkiewicz Z, Sharpless T, Staiano-Coico L, Melamed MR. 1980a. Subcompartments of the G1 phase of cell cycle detected by flow cytometry. Proc Natl Acad Sci U S A 77:6696-6699.
Darzynkiewicz Z, Traganos F, Melamed MR. 1980b. New cell cycle compartments identified by multiparameter flow cytometry. Cytometry 1:98-108.
Datta A, Eom I, Dhar A, Kuban P, Manor R, Ahmad I, Gangopadhyay S, Dallas T, Holtz MT, H., Dasgupta PK. 2003. Microfabrication and Characterization of Teflon AF-Coated Liquid Core Waveguide Channels in Silicon. IEEE SENSORS JOURNAL 3:788-795.
Davis RH, Kompala DS. 1989. Biotechnology Laboratory Methods. Chemical Engineering Education 23:182-187.
De Rosa SC, Herzenberg LA, Herzenberg LA, Roederer M. 2001. 11-color, 13-parameter flow cytometry: identification of human naive T cells by phenotype, function, and T-cell receptor diversity. Nat Med 7:245-248.
De Wulf P, Brambilla L, Vanoni M, Porro D, Alberghina L. 2000. Real-time flow cytometric quantification of GFP expression and Gfp-fluorescence generation in Saccharomyces cerevisiae. J Microbiol Methods 42:57-64.
DeHaan RL. 2005. *The Impending Revolution in Undergraduate Science Education*. Journal of Science Education and Technology 14:
DePalma A. 2004. PAT: Taking process monitoring to the next level. Gen Eng News 24:46-47.

Derouazi M, Girard P, Van Tilborgh F, Iglesias K, Muller N, Bertschinger M, Wurm FM. 2004. Serum-free large-scale transient transfection of CHO cells. Biotechnol Bioeng 87:537-545.
Deshpande RR, Heinzle E. 2004. On-line oxygen uptake rate and culture viability measurement of animal cell culture using microplates with integrated oxygen sensors. Biotechnol Lett 26:763-767.
DiStefano DJ, Mark DE, Robinson DK. 1996. Feeding of Nutrients Delays Apoptotic Death in Fed-Batch Cultures of REcombinant NS0 Myeloma Cells. Biotechnol Lett 18:1067-1072.
Doan LL, Tanner MK, Grimes HL. 2003. Intranuclear staining of proteins in heterogeneous cell populations and verification of nuclear localization by flow cytometric analysis. J Immunol Methods 279:193-198.
Elfwing A, LeMarc Y, Baranyi J, Ballagi A. 2004. Observing Growth and Division of Large Numbers of Individual Bacteria by Image Analysis. Appl Environ Microbiol 70:675-678.
Elowitz MB, Levine AJ, Siggia ED, Swain PS. 2002. Stochastic gene expression in a single cell. Science 297:1183-1186.
Europa AF, Gambhir A, Fu PC, Hu WS. 2000. Multiple steady states with distinct cellular metabolism in continuous culture of mammalian cells. Biotechnol Bioeng 67:25-34.
Fieder J, Wagner N, Grammatikos S, Hoffmann H, Kaufmann H, Otto RT. 2005. Use of flow-cytometric analysis to optimize cell banking strategies for production of biopharmaceuticals from mammalian cells. J Biotechnol 120:111-120.
Fraker J, King LE, Lill-Elghanian D, Telford WG. 1995. Quantification of apoptotic events in pure and hetereogeneous populations of cells using the flow cytometer. In: Schwartz LM, Osborne BA., editors. Cell death Methods Cell Biol. New York: Academic Press 46:62-65.
Franek F. 1995. Starvation Induced Programmed Death of Hybridoma Cells: Prevention by Amino Acid Mixtures. Biotech Bioeng 45:86-90.
Fredrickson AG, Megee RD,III, Tsuchiya HM. 1970. Mathematical models for fermentation processes. Adv Appl Microbiol 13:419-465.
Fredrickson AG, Ramkrishna D, Tsuchiya HM. 1967. Statistics and Dynamics of Procaryotic Cell Populations. Math Biosci 1:327-374.
Frykman S, Srienc F. 2001. Cell cycle-dependent protein secretion by *Saccharomyces cerevisiae*. Biotechnol Bioeng 76:259-268.
Gazdar AF, Oie HK, Kirsch IR, Hollis GF. 1986. Establishment and characterization of a human plasma cell myeloma culture having a rearranged cellular myc proto-oncogene. Blood 67:1542-1549.
Georges PC, Janmey PA. 2005. Cell Type Specific Response to Growth on Soft Materials. J Appl Physiol 98:1547-1553.
Gerdes J, Schwab U, Lemke H, Stein H. 1983. Production of a mouse monoclonal antibody reactive with a human nuclear antigen associated with cell proliferation. Int J Cancer 31:13-20.
Gilbert A. 2008. Improving Biotechnological Processes Through Automated Flow Cytometry.

Gilbert A, Sangurdekar DP, Srienc F. submitted. Rapid strain improvement through optimized evolution in the cytostat.
Gilbert A, Srienc F. 2008. Optimized evolution in the cytostat: a Monte Carlo simulation. Biotech Bioeng
Gnoth S, Jenzsch M, Simutis R, Lubbert A. 2007. Process Analytical Technology (PAT): Batch-to-batch reproducibility of fermentation processes by robust process operational design and control. J Biotechnol 132:180-186.
Goda K, Bacso Z, Szabo G. 2009. Multidrug resistance through the spectacle of P-glycoprotein. Curr Cancer Drug Targets 9:281-297.
Goldsmith HL, Mason SG. 1967. The Microrheology of Dispersions. Rheology 4:85.
Goldsmith HL, Mason SG. 1962. The Flow of Suspensions Through Tubes Part 1. Single Spheres, Rods and Discs. Colloid Sci 17:448.
Golzio M, Teissie J, Rols MP. 2002. Cell synchronization effect on mammalian cell permeabilization and gene delivery by electric field. Biochim Biophys Acta 1563:23-28.
Gonzalez RC, Woods RE, Eddins SL. 2004. Digital Image processing using MATLAB. Upper Saddle River, NJ:Pearson/Prentice Hall. 609 p.
Grammatikos SI, Tobien K, No W, Werner RG. 1999. Monitoring of intracellular ribonucleotide pools is a powerful tool in the development and characterization of mammalian cell culture processes. Biotechnol Bioeng 64:357-367.
Greenbaum L, Schwartz D, Malik Z. 2002. Spectrally resolved microscopy of GFP trafficking. J Histochem Cytochem 50:1205-1212.
Haase SB, Reed SI. 2002. Improved Flow Cytometric Analysis of the Budding Yeast Cell Cycle. Cell Cycle 1:132-132-136.
Handelsman J. 2004. *Scientific Teaching* . Science 304.
Harvard University Planning Committee for Science and Engineering. 2006. Enhancing Science and Engineering Education at Harvard.
Hatzis C, Porro D. 2006. Morphologically-structured models of growing budding yeast populations. J Biotechnol 2:420-438.
Hatzis C, Srienc F, Fredrickson AG. 1995. Multistaged corpuscular models of microbial growth: Monte Carlo simulations. BioSystems 36:19-35.
Haugland RP. 2005. The Handbook: A Guide to Fluorescent Probes and Labeling Technologies. USA:Invitrogen. 1126 p.
Hecht J. 2006. Understanding fiber optics. Upper Saddle River, N.J.:Pearson/Prentice Hall. 790 p.
Heim R, Cubitt AB, Tsien RY. 1995. Improved green fluorescence. Nature 373:663-664.
Heim R, Tsien RY. 1996. Engineering green fluorescent protein for improved brightness, longer wavelengths and fluorescence resonance energy transfer. Current Biology. 6:178-82.
Hermann R, Walther N, Maier U, Buchs J. 2001. Optical Method for the Determination of the Oxygen-Transfer Capacity of Small Bioreactors Based on Sulfite Oxidation. Biotechnology & Bioengineering 74:355-363.
Hiemenz PC, Rajagopalan R. 1997. Principles of Colloid and Surface Chemistry. New York:Marcel Dekker.

Hougham G, Cassidy P, Johns K, Davidson J. 2002. Fluoropolymers 2: Properties. New York:Kluwer Academic/Plenum.
Hughes TR. 2002. Yeast and drug discovery. Funct Integr Genomics 2:199-211.
Jerri AJ. 1977. The Shannon sampling theorem—Its various extensions and applications: A tutorial review. Proceedings of the IEEE 65:1565.
Joeris K, Frerichs JG, Konstantinov K, Scheper T. 2002. In-situ microscopy: Online process monitoring of mammalian cell cultures. Cytotechnology 38:129-134.
Johanson K, Allen PL, Gonzalez-Villalobos RA, Baker CB, D'Elia R, Hammond TG. 2006. Gene expression and survival changes in Saccharomyces cerevisiae during suspension culture. Biotechnol Bioeng 93:1050-1059.
Jorgensen P, Tyers M. 2004. How cells coordinate growth and division. Curr Biol 14:R1014-27.
Kacmar J, Gilbert A, Cockrell J, Srienc F. 2006. The cytostat: A new way to study cell physiology in a precisely defined environment. J Biotechnol 126:163-172.
Kacmar J, Zamamiri A, Carlson R, Abu-Absi NR, Srienc F. 2004a. Single-cell variability in growing Saccharomyces cerevisiae cell populations measured with automated flow cytometry. J Biotechnol 109:239-254.
Kacmar J, Zamamiri A, Carlson R, Abu-Absi NR, Srienc F. 2004b. Single-cell variability in growing Saccharomyces cerevisiae cell populations measured with automated flow cytometry. J Biotechnol 109:239-254.
Kacmar J, Carlson R, Balogh SJ, Srienc F. 2006. Staining and quantification of poly-3-hydroxybutyrate in *Saccharomyces cerevisiae* and *Cupriavidus necator* cell populations using automated flow cytometry. Cytometry Part A 69A:27-35.
Kacmar J, Gilbert A, Cockrell J, Srienc F. The cytostat: A new way to study cell physiology in a precisely defined environment. Journal of Biotechnology In Press, Corrected Proof:
Kacmar J, Srienc F. 2005. Dynamics of single cell property distributions in Chinese hamster ovary cell cultures monitored and controlled with automated flow cytometry. J Biotechnol 120:410-420.
Kaern M, Elston T, Blake WJ, Collins JJ. 2005. Stochasticity in Gene Expression: From Theories to Phenotypes. Nat Rev Gen 6:451.
Kamentsky L, Melamed MR. 1967. Spectrophotmetric cell sorter. Science 156:1364.
Karaszi E, Jakab K, Homolya L, Szakacs G, Hollo Z, Telek B, Kiss A, Rejto L, Nahajevszky S, Sarkadi B, Kappelmayer J. 2001. Calcein assay for multidrug resistance reliably predicts therapy response and survival rate in acute myeloid leukaemia. Br J Haematol 112:308-314.
Keith MB, Farrell PJ, Iatrou K, Behie LA. 2000. Use of flow cytometry to rapidly optimize the transfection of animal cells. BioTechniques 28:148-154.
Kell DB, Markx GH, Davey CL, Todd RW. 1990. "Real-time" monitoring of cellular biomass: methods and applications. Trends Anal Chem 190-194.
Kenney S. 1998. *Reinventing Undergraduate Education: A Blueprint for America's Research Universities.* .
Koch AL. 1999. The re-incarnation, re-interpretation and re-demise of the transition probability model. J Biotechnol 71:143-156.

Konstantinov K, Chuppa S, Sajan E, Tsai Y, Yoon S, Golini F. 1994. Real-time biomass-concentration monitoring in animal-cell cultures. Trends Biotechnol 12:324-333.
Kourti T. 2006. The Process Analytical Technology initiative and multivariate process analysis, monitoring and control. Anal Bioanal Chem 384:1043-1048.
Krishan A. 2002. Flow cytometric monitoring of drug resistance in human tumor cells. Methods Cell Sci 24:55-60.
Krishan A. 2001. Monitoring of cellular resistance to cancer chemotherapy: drug retention and efflux. Methods Cell Biol 64:193-209.
Krishan A, Fitz CM, Andritsch I. 1997. Drug retention, efflux, and resistance in tumor cells. Cytometry 29:279-285.
Krishan A, Hamelik RM. 2005. Flow cytometric monitoring of fluorescent drug retention and efflux. Methods Mol Med 111:149-166.
Kromenaker SJ, Srienc F. 1991. Cell-cycle dependent protein accumulation by producer and non-producer murine hybridoma cell lines: a population analysis. Biotechnol Bioeng 38:665-677.
Kromenaker S, Srienc F. 1994a. Cell cycle kinetics of the accumulation of heavy and light chanin immunoglobulin proteins in a mouse hybridoma cell line. Cytotechnology 14:205-218.
Kromenaker SJ, Srienc F. 1994b. Effect of Lactic Acid on the Kinetic of Growth and Antibody Production in a Murine Hybridoma: Secretion Patterns During the Cell Cycle. J Biotechnol 34:13-34.
Kubota S, Takeo I, Kume K, Kanai M, Shitamukai A, Mizunuma M, Miyakawa T, Shimoi H, Iefuji H, Hirata D. 2004. Effect of ethanol on cell growth of budding yeast: Genes that are important for cell growth in the presence of ethanol. Biosci Biotechnol Biochem 68:968-972.
Lazarus AH, Ellis J, Blanchette V, Freedman J, Sheng-Tanner X. 1998. Permeabilization and fixation conditions for intracellular flow cytometric detection of the T-cell receptor zeta chain and other intracellular proteins in lymphocyte subpopulations. Cytometry 32:206-213.
Leighton, Acrivos. 1985. The Lift on a Small Sphere Touching a Plane in the Presence of a Simple Shear Flow. Z Agnew Math Phys 36:174-178.
Li X, Chen XD, Hardin MT. 2004. Investigation into the Propagation of Baker's Yeast. Chemical Engineering Education 38:196-199.
Li J, Wang S, VanDusen W, Schultz L, George H, Herber W, Chae H, Bentley WE, Rao G. 2000. Green Fluorescence Protein in *Saccharomyces cerevisiae*: Real-time Studies of the *GAL1* Promoter. Biotechnol Bioeng 70:187-196.
Locher G, Sonnleitner B, Fiechter A. 1992a. On-line measurement in biotechnology: exploitation, objectives and benefits. J Biotechnol 25:55-73.
Locher G, Sonnleitner B, Fiechter A. 1992b. On-line measurement in biotechnology: techniques. J Biotechnol 25:23-53.
Mantzaris NV. 2006. Stochastic and deterministic simulations of heterogeneous cell population dynamics. J Theor Biol 241:690-706.

Mantzaris NV, Srienc F, Daoutidis P. 2002. Nonlinear productivity control using a multi-staged cell population balance model. CHEMICAL ENGINEERING SCIENCE 57:1-14.
Mantzaris NV, Daoutidis P, Srienc F. 2001a. Numerical solution of multi-variable cell population balance models. II. Spectral methods. Comput Chem Eng 25:1441-1462.
Mantzaris NV, Daoutidis P, Srienc F. 2001b. Numerical solution of multi-variable cell population balance models. III. Finite element methods. Comput Chem Eng 25:1463-1481.
Mantzaris NV, Daoutidis P, Srienc F. 2001c. Numerical solution of multi-variable cell population balance models: I. Finite difference methods. Comput Chem Eng 25:1411-1440.
Mantzaris NV, Liou J, Daoutidis P, Srienc F. 1999. Numerical solution of a mass structured cell population balance model in an environment of changing substrate concentration. J Biotechnol 71:157-174.
Mariella R,Jr, van den Engh G, Masquelier D, Eveleth G. 1996. Flow-stream waveguide for collection of perpendicular light scatter in flow cytometry. Cytometry 24:27-31.
Mariella RP,Jr, Huang Z, Langlois RG. 1999. Characterization of the sensitivity of side scatter in a flow-stream waveguide flow cytometer. Cytometry 37:160-163.
McLaughlin JB. 1991. Inertial Migration of a Small Sphere in Linear Sphere Flows. J Fluid Mech 224:261-274.
Mitchell SA, Poulsson ANH, Davidson MR, Bradley RH. 2005. Orientation and Confinement of Cells on Chemically Patternerd Polystyrene Surfaces. Colloids and Surfaces B 46:108-116.
Mullaney PF, Van Dilla MA, Coulter JR, Dean PN. 1969. Cell Sizing: A Light Scattering Photometer for Rapid Volume Determination. The Review of Scientific Instruments 40:1029.
Murray AW, Hunt T. 1993. The cell cycle : an introduction. New York:Oxford University Press. 251 p.
Natarajan A, Subramanian S, Srienc F. 1998. Comparison of mutant forms of the green fluorescence protein as expression markers in Chinese hamster ovary (CHO) and *Saccharomyces cerevisiae* cells. J Biotechnol 62:29-45.
Nott PR, Brady JF. 1994. Pressure driven flow of suspensions: simulation and theory. Journal of Fluid Mechanics 275:157-199.
Nurse PM. 2002. Nobel Lecture. Cyclin dependent kinases and cell cycle control. Biosci Rep 22:487-499.
Nusse M, Beisker W, Hoffmann C, Tarnok A. 1990. Flow cytometric analysis of G1- and G2/M-phase subpopulations in mammalian cell nuclei using side scatter and DNA content measurements. Cytometry 11:813-821.
Patankar NA, Huang PYlK, T., Joseph DD. 2001. Lift-off of a single particle in Newtonian and viscoelastic fluids by direct numerical simulation. J Fluid Mech 438:67-100.
Pestov DG, Polonskaia M, Lau LF. 1999. Flow cytometric analysis of the cell cycle in transfected cells without cell fixation. BioTechniques 26:102-106.

Poppenborg L, Friehs K, Flaschel E. 1997. The green fluorescent protein is a versatile reporter for bioprocess monitoring. J Biotechnol 58:79-88.
Porro D, Brambilla L, Alberghina L. 2003. Glucose metabolism and cell size in continuous cultures of Saccharomyces cerevisiae. FEMS Microbiology Letters 229:165-171.
Ramkrishna D. 2000. Population Balances: Theory and Applications to Particulate Systems in Engineering. San Diego:Academic Press.
Resnick PR, Buck WH. 2006. Teflon AF: A Family of Amorphous Fluoropolymers with Extraordinary Properties. Topics in Applied Chemistry: Book Fluoropolymers 2
Robinson KK, Dranoff JS, Tomas C, Tummala S. 2002. Mass Transfer and Cell Growth Kinetics in a Bioreactor. Chemical Engineering Education 36:216-221.
Roederer M, De Rosa S, Gerstein R, Anderson M, Bigos M, Stovel R, Nozaki T, Parks D, Herzenberg L, Herzenberg L. 1997. 8 Color, 10-Parameter Flow Cytometry to Elucidate Complex Leukocyte Heterogeneity. Cytometry 29:328-339.
Rubinow, Keller. 1961. The Transverse Force on a Spinning Sphere Moving in a Viscous Fluid. J Fluid Mech 11:447-459.
Saffman PG. 1965. The Lift on a Small Sphere in a Slow Shear FLow. J Fluid Mech 22:385-400.
Sandhu KS, Naciri M, Al-Rubeai M. 2007. Prediction of recombinant protein production in an insect cell-baculovirus system using a flow cytometric technique. J Immunol Methods 325:104-113.
Schmid I, Cole SW, Korin YD, Zack JA, Giorgi JV. 2000a. Detection of cell cycle subcompartments by flow cytometric estimation of DNA-RNA content in combination with dual-color immunofluorescence. Cytometry 39:108-116.
Schmid I, Cole SW, Zack JA, Giorgi JV. 2000b. Measurement of lymphocyte subset proliferation by three-color immunofluorescence and DNA flow cytometry. J Immunol Methods 235:121-131.
Schoenherr I, Stapp T, Ryll T. 2000. A comparison of different methods to determine the end of exponential growth in CHO cell cultures for optimization of scale-up. Biotechnol Prog 16:815-821.
Segre G, Silberberg A. 1962. Behaviour of Macroscopic Rigid Spheres in Poiseuille Flow: Part I. J Fluid Mech 14:136-157.
Segre G, Silberberg A. 1961. Radial Poiseuille Flow of Suspensions. Nature 189:209.
Shapiro HM, Perlmutter NG. 2006. Personal Cytometers: Slow Flow or No Flow. Cytometry A 69A:620-630.
Shapiro HM. 1985. Practical Flow Cytometry. New York:Alan R. Liss, Inc. 295 p.
Shapiro HM. 2004. The evolution of cytometers. Cytometry A 58:13-20.
Shapiro HM, Hercher M. 1986. Flow cytometers using optical waveguides in place of lenses for specimen illumination and light collection. Cytometry 7:221-223.
Shonnard DR, Fisher ER, Caspary DW. 2003. A Batch Fermentation Experiment for L-lysine Production. Chemical Engineering Education 37:262-267.
Shuler ML, Mufti N, Donaldson M, Taticek R. 1994. A Bioreactor Experiment for the Senior Laboratory. Chemical Engineering Education 28:24-28.

Sigal A, Milo R, Cohen A, Geva-Zatorsky N, Klein Y, Alaluf I, Swerdlin N, Perzov N, Danon T, Liron Y, Raveh T, Carpenter AE, Lahav G, Alon U. 2006. Dynamic proteomics in individual human cells uncovers widespread cell-cycle dependence of nuclear proteins. Nat Methods 3:525-531.

Sitton G, Hansgate A, Srienc F. 2006. Transient gene expression in CHO cells monitored with automated flow cytometry. Cytotechnology 52:13-24.

Sitton G, Srienc F. 2008a. Growth dynamics of mammalian cells monitored with automated cell cycle staining and flow cytometry. Cytometry A 73:538-545.

Sitton G, Srienc F. 2008b. Mammalian cell culture scale-up and fed-batch control using automated flow cytometry. Journal of Biotechnology 135:174-180.

Smith PJ, Wiltshire M, Davies S, Patterson LH, Hoy T. 1999. A novel cell permeant and far red-fluorescing DNA probe, DRAQ5, for blood cell discrimination by flow cytometry. J Immunol Methods 229:131-139.

Spencer SL, Gaudet S, Albeck JG, Burke JM, Sorger PK. 2009. Non-genetic origins of cell-to-cell variability in TRAIL-induced apoptosis. Nature 459:428-432.

Srienc F, Campbell JL, Bailey JE. 1986. Flow cytometry analysis of recombinant *Saccharomyces cerevisiae* populations. Cytometry 7:132-141.

Srienc F. 1999. Cytometric data as the basis for rigorous models of cell population dynamics. J Biotechnol 71:233-238.

Streefland M, van de Waterbeemd B, Happe H, van der Pol LA, Beuvery EC, Tramper J, Martens DE. 2007. PAT for vaccines: the first stage of PAT implementation for development of a well-defined whole-cell vaccine against whooping cough disease. Vaccine 25:2994-3000.

Subramanian S, Srienc F. 1996. Quantitative analysis of transient gene expression in mammalian cells using the green fluorescent protein. Journal of Biotechnology 49:137-137-151.

Tan B, Piwnica-Worms D, Ratner L. 2000. Multidrug resistance transporters and modulation. Curr Opin Oncol 12:450-458.

Tao D, Wu J, Feng Y, Qin J, Hu J, Gong J. 2004. New method for the analysis of cell cycle-specific apoptosis. Cytometry A 57:70-74.

Tarnok A. 2006. Slide-Based Cytometry for Cytomics - A Minireview. Cytometry A 69A:555-562.

Tucci M, Quatraro C, Dammacco F, Silvestris F. 2009. Role of active drug transporters in refractory multiple myeloma. Curr Top Med Chem 9:218-224.

Valic B, Golzio M, Pavlin M, Schatz A, Faurie C, Gabriel B, Teissie J, Rols MP, Miklavcic D. 2003. Effect of electric field induced transmembrane potential on spheroidal cells: theory and experiment. Eur Biophys J 32:519-528.

Vermes I, Haanen C, Reutelingsperger C. 2000. Flow cytometry of apoptotic cell death. J Immunol Methods 243:167-190.

Watson JV. 1991. Introduction to Flow Cytometry. Cambridge:Cambridge University Press.

Wlaschin KF, Hu WS. 2006. Fedbatch culture and dynamic nutrient feeding. Adv Biochem Eng Biotechnol 101:43-74.

Yang BH, Wang J, Joseph DD, Hu HH, Pan TW, Glowinski R. 2005. Lift Force on a Sphere in Tube Flow. J Fluid Mech 540:109-131.

Zanghi JA, Fussenegger M, Bailey JE. 1999. Serum protects protein-free competent Chinese hamster ovary cells against apoptosis induced by nutrient deprivation in batch culture. Biotechnol Bioeng 64:108-119.
Zhao R, Natarajan A, Srienc F. 1999a. A Flow Injection Flow Cytometry System for On-Line Monitoring of Bioreactors. Biotechnol Bioeng 62:609-617.
Zhao R, Natarajan A, Srienc F. 1999b. A Flow Injection Flow Cytometry System for On-Line Monitoring of Bioreactors. Biotechnol Bioeng 62:609-617.
Zilmer NA, Godavarti M, Rodriguez JJ, Yopp TA, Lambert GM, Galbraith DW. 1995. Flow cytometric analysis using digital signal processing. Cytometry 20:102-117.

14 Appendices

I. Materials and Methods

a) Cell line and growth medium

a. CHO

Serum free CHO cells of the strain CHO-S (Invitrogen, Carlsbad, CA) were used. Cells from a working cell bank, stored in liquid nitrogen, were thawed at 37º C and placed in a T-flask (75 cm^2, Corning, Inc., Corning, NY) containing 25 ml of CHO-S-SFM II medium (Invitrogen) at a concentration of $1x10^5$ cells ml^{-1}. The cells were incubated at 37º C in air containing 7.5% carbon dioxide. After being passed once into 50 ml of medium in the same size T-flask, the cells were passed a third time into a total volume of 300 ml in a 500 mL spinner flask, Corning, Inc., Corning, NY).

b. NCI-H929

NCI-H929 cells from a working cell bank, stored in liquid nitrogen, were thawed at 37º C and placed in a T-flask at a concentration of $1x10^5$ cells ml^{-1}. (75 cm^2, Corning, Inc., Corning, NY). The T-flask contained 25 ml of RPMI-1640 medium, without phenol red, with L-glutamine, and supplemented with 10% fetal bovine serum. The cells were incubated at 37º C in air containing 7.5% carbon dioxide. Dilutions to $1x10^5$ cells ml^{-1} were performed every 3 days.

c. Yeast YPH399a

S. cerevisiae YPH399 (MATa, ade2-101,leu2D1, lys2-80, his3D200, trp1D63, ura3-52) were grown at 30°C on SD minimal medium supplemented with adenine sulfate (100 mg/L), histidine (80 mg/L), lysine (150 mg/L), leucine (50 mg/L), and

uracil (100 mg/L). Tryptophan (20 mg/L). was used to select for the centromeric plasmid.

Clear SD minimal medium was made as above except with no riboflavin or folic acid.

d. Yeast D603

Diploid saccharomyces cerevisiae cells (strain D603) (Srienc, et al. 1986) were grown in YPD medium at 30°C in a 50 mL shake flask.

b) CHO Transfection procedure

Transfections were performed by dividing an inoculum into aliquots containing $2x10^7$ cells and then centrifuging each aliquot. The resulting cell pellets were resuspended in CHO-S SFM II medium with 100 μg plasmid peGfp-N1 (Clontech) for a final electroporation volume of 800 μL. Plasmid peGfp-N1 was extracted from E. coli using Qiagen's Maxiprep column. Each 800 μL aliquot was transferred to an electroporation cuvette with a gap of 0.4 mm (Fisher, Pittsburgh, PA) and incubated on ice for 10 minutes. The aliquots were then electroporated with an exponentially decaying pulse at a voltage of 330 V, and an average time constant of 18 ± 0.5 ms. The electroporated aliquots were then incubated on ice for 10 minutes, recombined into 20 mL of CHO-S medium, and used to inoculate bioreactors.

c) Bioreactor operation

Mammalian bioreactors (LH Fermentation) with a working volume of 1-L were operated at 37 °C. The bioreactors were agitated at a rate of 100 rpm using a six blade disk impeller with a 5 cm diameter. Air and CO_2 were sparged to control DO and pH respectively. The DO remained above 80% during the duration of the experiments and

the pH remained at 7.2±0.05. Initial culture volume and the fed-batch additions were CHO-S SFM-II medium supplemented with sodium penicillin G 0.17 mM (Sigma, St. Louis, MO) and streptomycin sulfate 68.6 µM (Sigma, St. Louis, MO).

d) Reactor sampling and analysis

Samples were automatically withdrawn from the bioreactor every 20 min and processed by the previously described automated cell preparation system (Abu-Absi et al., 2003; Zhao et al., 1999). A commercial version of such sample preparation system has been recently developed by MSP Corp, Shoreview, MN (http://www.mspcorp.com/). Briefly, the automated cell preparation system loaded a sample directly from the bioreactor into a 46 µL sample loop. The content of the sample loop was then injected into a flow cytometer for analysis at an average flow rate of 13 µL min^{-1}. A second cell sample was loaded into a continually stirred microchamber and subsequently stained with propidium iodide. The stained cells were then washed with phosphate buffered saline. The stained cells in the microchamber were then loaded into the sample loop and the content of the sample loop was injected into the cytometer for analysis.

e) Cell Cycle Sampling and Cell Staining

The staining microchamber previously described (Abu-Absi, et al. 2003), was modified to create separate pathways through the microchamber for loading and eluting cells. Also, a syringe pump was directly connected to the microchamber to inject stain. Prior to loading cells into the microchamber, the exit pathway from the microchamber and the sample loop of the device were filled with a 30 µg/mL PI solution. After a cell sample from the bioreactor was loaded into the microchamber with the peristaltic pump

through the waste pathway of the microchamber, the stain syringe pump added 30 µL of staining solution to the 180 uL microchamber filled with cells using the loading pathway. The microchamber was agitated at 100 rpm and kept at room temperature. The staining solution was prepared by first placing 30 mg of crude digitonin extract in 10 mL of a PBS solution. After vortexing and waiting 5 minutes at room temperature, 2 mL of a 1 mg/mL PI solution and 50 mg of RNase A was added to the staining solution. The remaining undissolved crude digitonin extract was removed by filtering through a 0.2 µm syringe filter. Thus, the resulting staining solution was comprised of saturated digitonin, 170 µg/mL PI, and 0.5 mg/mL RNase. After addition to the microchamber, the concentrations of PI and RNase in the microchamber were 30 µg/mL and 80 µg/mL respectively. Once the staining solution was added, the cells were allowed to incubate for 15 minutes. Then, the stained cells were eluted from the microchamber into the sample loop by the saline syringe pump containing 30 µg/mL of PI, and the contents of the sample loop were injected into the cytometer for analysis. Cell cycle distributions were analyzed using MultiCycle analysis software.

To analyze live cells, the automated cell preparation system loaded a sample directly from the bioreactor into a sample loop. The content of the sample loop was then injected into a flow cytometer for live cell analysis of the cell concentration, cell size, cell granularity, and non-viable concentration.

f) Flow cytometry

A FACS Calibur (Becton-Dickinson Immunocytometry System, San Jose, CA) flow cytometer was used for the analysis of cells. A 15mW laser (Spectra-Physics, Mountain View, CA) with a wavelength of 488 nm was used for excitation. Data from

the forward scatter diode was digitized with a linear scale. Data from the side scatter photomultiplier tube was digitized on a linear scale. Finally, data from the photomultiplier tube collecting the green fluorescence (530 nm) of the cells was digitized on a logarithmic scale.

g) Dispersion Testing

To examine the dispersion characteristics, fixed yeast cells were drawn into the FCP. The dispersion caused by each unique pathway through the FCP was then tested by collecting fractions of the discharge and measuring the particulate concentration. Two methods were used to collect the fractions. One method pumped continuously and samples were manually collected using a stopwatch to determine fractions. The second method started and stopped the flow as determined by the amount of liquid in a fraction. Particle counts of each fraction collected were obtained using a coulter counter (Elzone XY).

h) Teflon AF Flow Cell Construction

To construct the TFC, a 2.1 cm length of 250 µm ID, 500 µm OD Teflon AF® capillary (courtesy of Systec Corporation, New Brighton, MN) was attached to a converging flow cell original to the Ortho Cytofluorograph using an acrylic adapter piece, Figure 1. The acrylic adapter piece fits into the top of the Ortho's converging flow cell and had a 0.5 mm hole in the center. The capillary was then secured using epoxy such that the end was flush with the top of the converging flow cell. The other end of the capillary was then placed into a custom tee connector and secured using epoxy. The space between the converging flow cell and the custom tee was maintained using a stainless steel spacer. The custom tee allowed a 2.3 mm OD jacketed acrylic

core fiber optic (ESKA, Mitsubishi International Corp.) with a core diameter of 1 mm to be butted 1 mm from the terminus of the capillary (figure 1). A 1/16" hole was drilled perpendicular to the fiber optic, and a piece of PEEK tubing was glued into this hole to allow an exit for fluid.

i) Fiber Optic Splitter

All light transferred to the fiber optic from the TFC was equally split into three 1 mm ESKA fiber optics using a fiber optic splitter (Industrial Fiber Optics, Cat# IF543, Phoenix, AZ) (Figure 1). All ends of the fiber optics were flat polished using the procedure outlined by Thor Labs, Inc (Catalog# FN96A). At the terminus of one of the fibers a 3 mm diameter disc of a 515 nm long pass filter was glued into place and inserted into a PMT (Figure 1). All light from a second, unfiltered fiber was measured by a second PMT (Figure 1) that detected the light scattering signal. The third fiber was left unmonitored and left open for future fluorescence filters.

j) Flow cytometry—Teflon Flow Cell

The constructed TFC was placed in the optical box of an Ortho flow cytometer and illuminated with a 488 nm, 20 mW Cyan® solid state laser (Spectra Physics, Mountain View, CA). The laser beam was focused through the original Ortho crossed cylindrical lenses. Scattered light was acquired by an original Ortho PMT (9828B, Electron Tubes, Uxbridge, UK) and fluorescent light was acquired with a PMT module (H9306-03, Hamamatsu, Bridgewater, NJ). The signals from each PMT were processed with the Ortho electronics and acquired with a Cicero interface and the Cyclops data acquisition software. Sheath fluid flowed through the assembly at 15 mL

min^{-1}. The pulse shapes of individual particles were acquired at 2 MHz using a digital oscilloscope (Rapid Systems, Seattle, WA).

k) Offline DNA staining

To stain CHO cells for their DNA content, 10^6 cells were centrifuged, and resuspended at room temperature in 1 mL of a saturated digitonin, 30 μg/mL PI, and 80 μg/mL RNase solution (Sitton and Srienc 2008a). This preparation was then incubated at room temperature for 15 minutes.

Yeast cells were stained with Sytox Green using a standard protocol (Haase and Reed 2002).

l) Polystyrene Beads

All beads used in this study were made of polystyrene. For alignment of the system, both 2 μm non-fluorescent beads (Ortho Diagnostic systems, Raritan, NJ) and 6 μm unimodal BODIPY labeled calibration beads (AlignFlow Plus, Invitrogen, Eugene, OR) were used. A set of 6 μm fluorescein labeled beads at 100%, 10%, 2%, 0.4%, and 0.1% relative fluorescence (LinearFlow, Invitrogen, Eugene, OR) were used for assessing the sensitivity of the fluorescence detection. Non-fluorescent beads of various sizes 3 μm, 16 μm (Polysciences, Warrington, PA), 10 μm, and 20 μm (Fluka, Germany) were used to assess the side-scatter pulse shape dependence.

m) Flow direction during measurement

To examine the relationship between flow direction and detector orientation, a 98 μm inner diameter, 307 μm outer diameter, 75 cm long Teflon AF® capillary (Random Technologies, San Francisco, CA) was placed in a holder in the Ortho optical box. The capillary was illuminated with a 488 nm laser passed through a single

cylindrical lens to reduce the beam height to a diffraction limited height. The beam width was 700 μm. Each end of the capillary was attached to a 'tee' connector (P-713, Upchurch Scientific, Oak Harbor, WA) where a fiber optic was brought within 1 mm of the capillary terminus. A bidirectional, continuous syringe pump (Milli-GAT, Global FIA, Fox Island, WA) was connected to the fluid port of the tee on each end of the capillary in a closed loop. For each particle crossing the laser, the pulse shapes of the scattering and fluorescent events were recorded with a data acquisition card (PCI-6120, National Instruments, Austin, TX) and custom LABVIEW based acquisition software.

II.Single Cell Tracking Experimental Platforms

a) Introduction

Over the course of three years, a series of experimental platforms to implement the single cell tracking cytometer were constructed. This appendix traces the evolution of the experimental platform from a microscope and syringe pump based instrument to the current instrument using a Teflon AF capillary and a Milli-GATT pump. The Teflon capillary instrument was used to obtain the experimental results described in Chapters 8, 9, and 10.

b) Imaging Cytometer: Reverse Plug Monitoring

As an initial proof of concept, a 7 cm length of 100 μm inner diameter fused silica capillary tubing was attached using 300 μm diameter silicon tubing to a 0.5 μL syringe in a syringe pump. The capillary tubing/syringe pump were mounted vertically. A microscope at objective magnification 40x was focused onto the capillary as shown in Figure II-1. A 340x280 pixel microscope camera was connected to a computer running a custom image processing MATLAB program and pump control algorithm. Next, a suspension of YPH-399a yeast cells in SD minimal medium at a cell concentration of 10^4 cells mL^{-1} was loaded into the capillary. Then, a simple control algorithm where the syringe pump pushed in one direction until a cell transited the image window. Next, the pump was reversed until the cell transited the image window in the opposite direction. This cycle was repeated at room temperature and an image of the cell was recorded every 5 minutes. An example image is shown in the inset of

Figure II-2. The single cell growth rate **r**(**x**, t) was extracted from the images by calculating the cell size in discrete μm^2 by thresholding the image (inset Figure II-2).

However, since the camera had a finite exposure time, the velocity of the particle must be kept sufficiently small such that a non-blurred image could be acquired. For the system described, the Peclet number was 0.5. Therefore, diffusion was significant and the cell was able to consistently reach the capillary wall and adhere to it, preventing further measurements. Despite this limitation, the experiment showed that the same cell in suspension can be analyzed multiple times by reversing the flow direction, a simple control algorithm will be sufficient to control the movement of the cell, and nutrient transfer in the capillary is sufficient to maintain cell growth, for small numbers of cells.

Figure II-1: Picture showing the experimental microscope based imaging system. The flow was controlled by a 0.5 μL syringe mounted in a syringe pump. The glass capillary was attached to the syringe pump, and the microscope was focused onto the capillary.

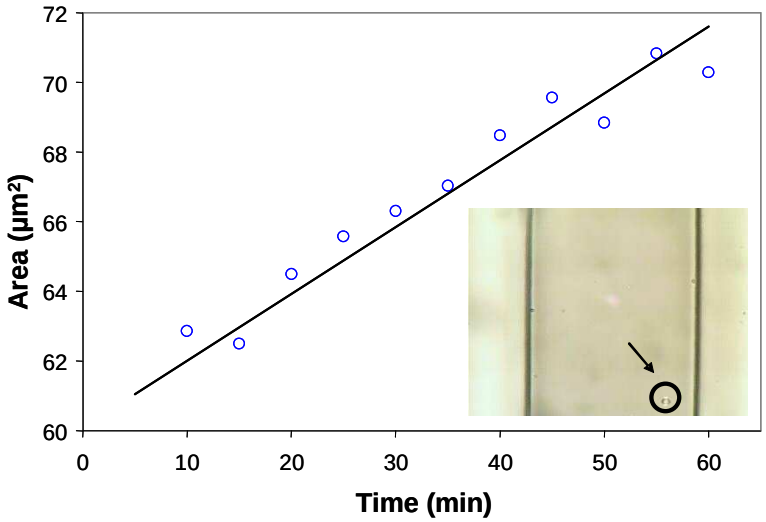

Figure II-2: Cell growth assessed by the imaging system. The yeast cell circled in the inset was placed in an oscillating flow that passed the cell through the imaging window on average once every 20 seconds. Images were recorded every 5 minutes, and the area of the growing yeast cell in the capillary is plotted as a function of time. The data shows that a single cell can be tracked over extended time periods by simply reversing the flow.

c) Imaging Cytometer: Batch Growth Monitoring

By a flowing a suspension of cells in a single direction at a constant flow rate through the device described in Figure II-1; a simple, effective cell counting device was created. With custom written software that automatically samples from a vessel, and counts the number of cells per mL in the capillary, this device was turned into an online cell counter. This device was coupled to a small 10 mL bioreactor growing haploid YPH399a yeast cells in SD minimal medium. As shown in Figure II-3, the growth curve of this culture was measured. It is important to note that Microscope cell counter is accurate at low cell densities. Periodic samples were taken from the culture and the cell number was assessed using a Coulter counter. As shown in Figure II-3, the correlation of the cell counts between the constructed microscope counter and a Coulter counter is high, and the slope is approximately one indicating that the constructed device yields similar measurements of a Coulter counter. While more points will obviously be needed to confirm the correlation, the initial results look promising. Such a simple cell counter accurate at low cell densities could be implemented to control the cell number in a small bioreactor, as in a cytostat (Kacmar, et al. 2006 ; Kacmar, et al.)

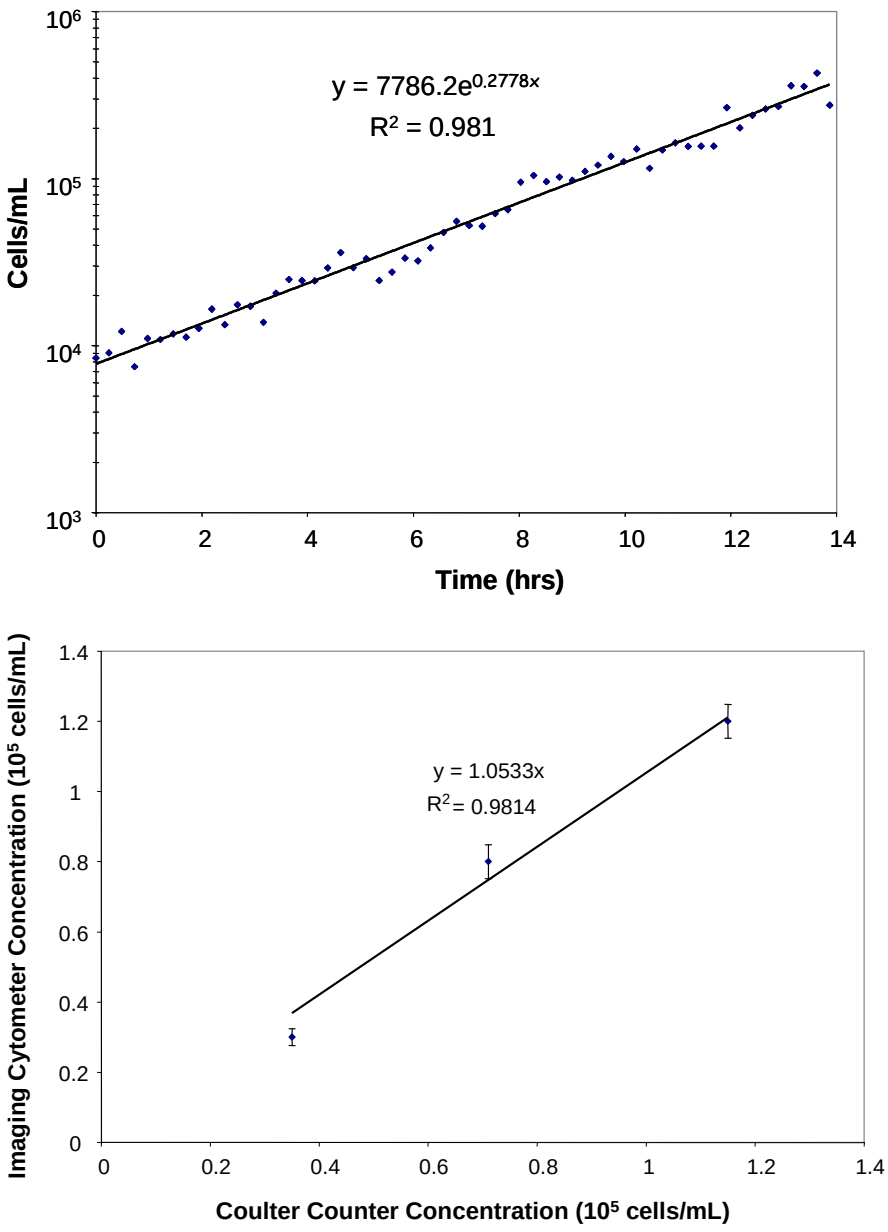

Figure II-3: Batch growth of yeast assessed by the imaging cytometer. **(Top)** Growth curve of YPH399a yeast cells in SD minimal mediumat 28°C acquired using the constructed online cell counter. **(Bottom)** Correlation of the cell counts between the constructed microscope counter and a Coulter counter. The slope is approximately one indicating that the constructed device yields similar measurements of a Coulter counter.

d) Air Pressure Switching

While the microscope based instrument described in the previous section showed that a single cell can be tracked over extended time periods, the measurement will become more significant if many cells can be observed at the same time. This can be experimentally feasible if the order of cells can be maintained over extended periods of time. To experimentally show that the order of a suspension of cells can be maintained during forward and reverse flow, a system was designed where the velocity of the flow was increased such that the Peclet number was on the order of 10^6. Therefore, diffusion in the radial direction is expected to be minimal and each particulate is expected to exist only along its equilibrium radius. To flow in both directions at the required high flow rate (~20 uL/min) a set of two three-way valves were devised such that either end of the capillary could be exposed to 5 psig air or vented to atmospheric pressure as shown in Figure II-4. When flow from the top was required, the 'top' valve would be actuated to the pressurized air and the 'bottom' valve would be vented to the atmosphere, and vice versa if flow from the bottom was required.

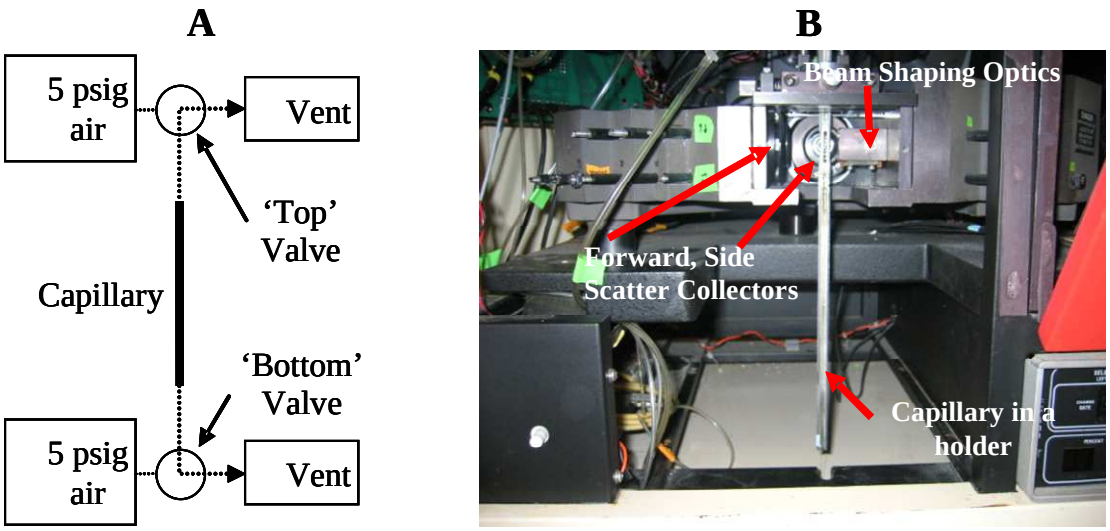

Figure II-4: (A) Schematic of the air pressure pumping scheme. When flow from the top to the bottom of the capillary was needed, the top valve actuated to 5 psig air while the bottom valve opened the bottom of the capillary to the atmosphere (vice-versa for flow from the bottom) **(B)** Image of the modified Ortho Cytofluorograph showing the capillary held in the path of the elliptical laser beam.

Since the velocity of the particle has been drastically increased, the video camera-microscope system could not be used. So, an Ortho Cytoflurograph 50H flow cytometer was modified to include a 75 cm long 100 µm inner diameter capillary as shown in Figure II-4B. A capillary of this length can hold 5.9 uL of solution. Briefly, a laser beam at a wavelength of 488 nm was focused at the midpoint of the capillary. Next, a suspension of particulates flows through the capillary. As each particle transits the laser beam, light is scattered and collected with photomultiplier tubes at two locations: at a small angle <8° from the laser beam axis termed forward scatter, which is proportional to particulate size and orthogonal to the laser beam axis termed side scatter which is proportional to particulate granularity. Different wavelengths of light can be split out of the side scatter signal and particulate fluorescence can be measured. The photomultiplier tube signals of both side and forward scatter are amplified and converted to a voltage signal. The shape of the signal is the convolution of the laser beam intensity and the particle cross sectional area. Subsequently, the voltage signal is digitized by a Data Acquisition PCI card at a frequency of 250 KHz, and analyzed by a custom LABVIEW data analysis program in real time.

A key variable in consistently measuring the light scattering properties of a particulate is the homogeneity of the laser beam. In the experimental apparatus, the laser beam is shaped into an ellipse 120 µm wide by 5 µm tall. Within the ellipse, the laser beam intensity is Gaussian in shape with a peak intensity occurring at the center of the ellipse. When the laser beam intersects the capillary, the curvature of the capillary compresses the ellipse to a smaller ellipse 90 µm wide by 5 µm tall. The inhomogeneous shape of the laser beam intensity in the theta direction of the capillary

impacts the accuracy of the particulate measurements. For example, if two particles with identical quantities of fluorophores intersect the laser beam at the same location at the same laser intensity, the signal they emit should be identical. On the other hand, if the two particulates intersect at two different locations with two different laser intensities the resulting signals will differ. This effect is illustrated when an equilibrium radius of particles intersect a Gaussian laser beam as illustrated in Figure II-5. As Figure II-5 shows as the equilibrium radius decreases, the variation in laser beam intensity across the equilibrium radius also decreases. This effect can be experimentally measured by running suspensions of uniform polystyrene microspheres through the device. For the same flow Reynolds number, larger particles will have a smaller equilibrium radius than smaller particles. Therefore, the standard deviation of forward scatter signal peak heights will be smaller for larger particles as shown in figure 8 for 3, 6, and 10 um particles.

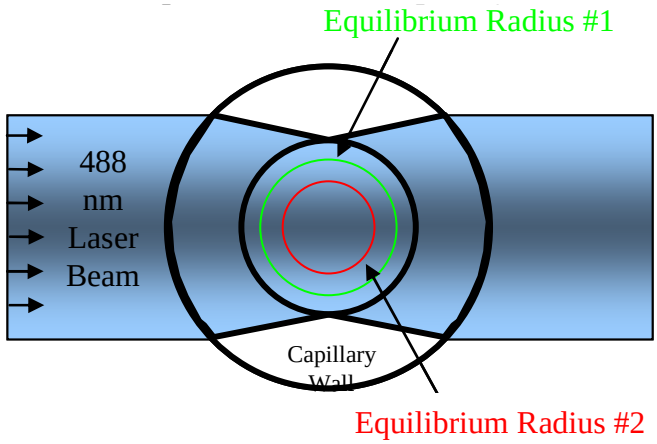

Figure II-5 A cartoon of the top view of the capillary intersecting the Gaussian laser beam. Darker blue colors denote a higher intensity section of the laser beam. The capillary focuses the laser beam to 90 μm wide. Two different equilibrium radii are shown. The larger the equilibrium radius, the more variation in laser beam intensity the particles experience.

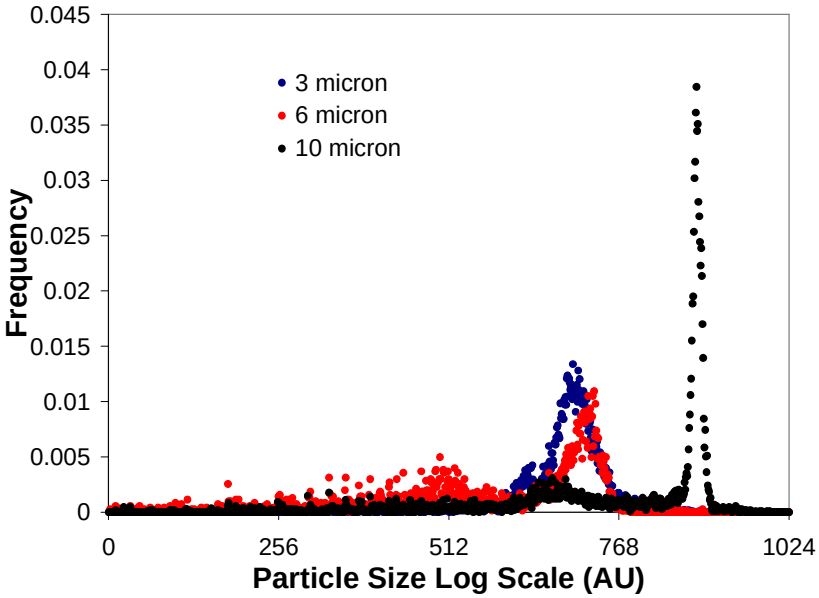

Figure II-6: Histogram of forward scatter peak height intensities for 3, 6, and 10 μm particles. The peak heights, which correlate to the particle size are plotted on a logarithmic scale. Samples were acquired at an event rate of approximately 600 particles per second. The pulses were analyzed with a custom LABVIEW program.

As Figure II-6 shows, despite variation in laser beam intensity, there is sufficient difference in the detected particle sizes to differentiate between 3 and 10 µm particles. So, to experimentally test that the order of cells in the capillary can be maintained a mixture of 3 and 10 µm particles were loaded into the capillary shown in Figure II-4B. The mixture of particles in the capillary generates a unique 'barcode' of alternating particle sizes. Next, using the pumping apparatus described in Figure II-4A, flow was begun in the forward direction for 3 seconds at 5 psig, and then reversed for 3 seconds at 5 psig. This process was continued for many scans. As shown in Figure II-7, a unique barcode of 59 particulates was preserved for three scans. As expected, the order is reversed for a scan occurring in the opposite direction. Due to systemic inaccuracies and random fluctuations in the pumping apparatus, the pattern was not able to be maintained for longer than three scans. It is expected that a more accurate pumping apparatus as described in the management plan will enable the device to maintain the order of cells for extended periods of time.

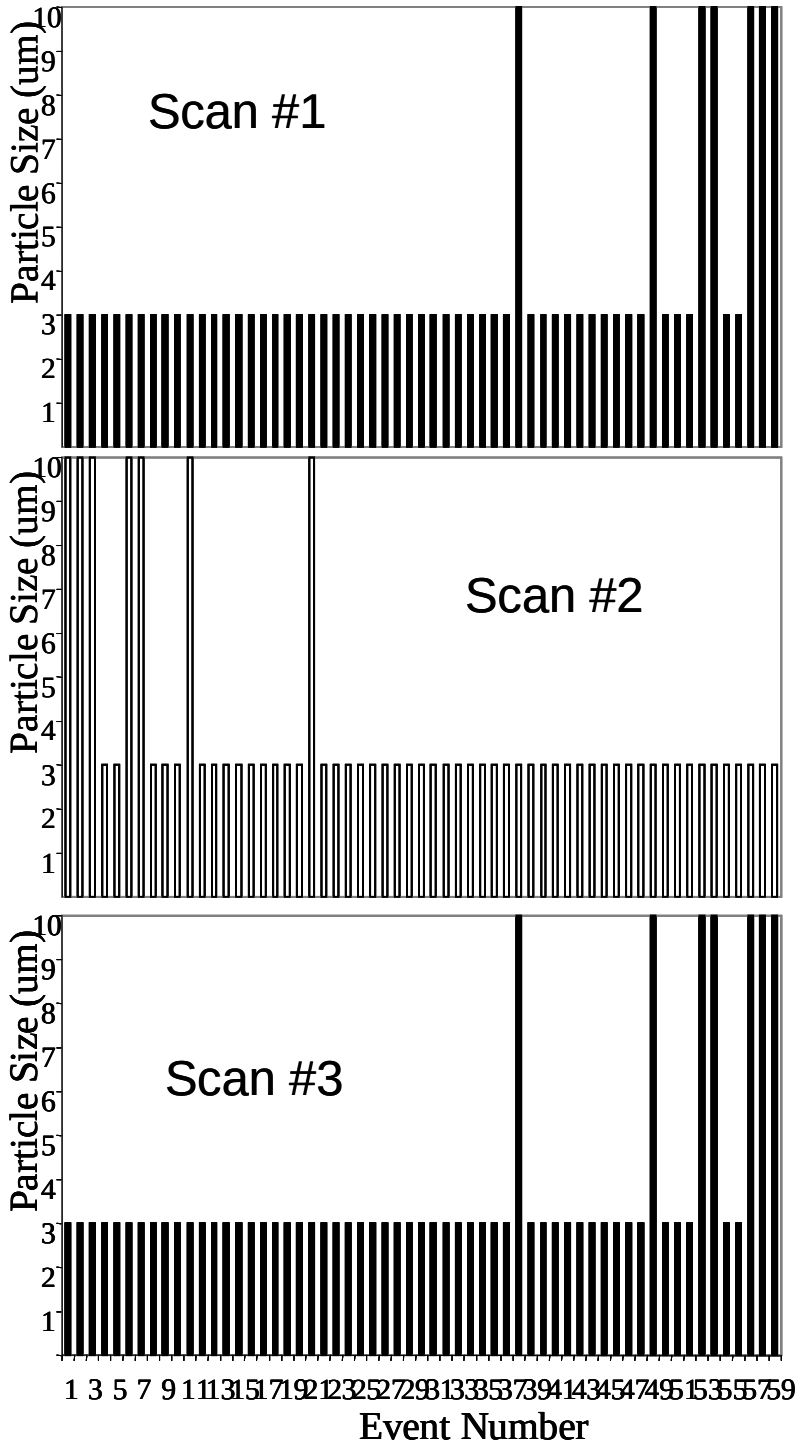

Figure II-7: Bar code of cells crossing the laser based on particle size. Three consecutive scans denoting a unique barcode of 3 and 10 μm particles as detected by the modified flow cytometer. Due to the inaccuracies in the pumping apparatus, the pattern was not able to be maintained for longer than three scans.

e) Precise Pumping: Milli-GAT Pump

A precise, repeatable pumping of the fluid is the most critical aspect of the device. To ensure a precise, repeatable pumping of microliter scale volumes of fluid we used a commercially available 'Milli-GAT' pump made by GlobalFIA. The 'Milli-GAT' positive displacement continuous syringe pump is capable of bi-directional flow accurate to 10 nL across a wide range of flow rates. The inlet and the outlet port of the pump were connected to either end of the capillary in a closed loop as shown in Figure II-9A. To monitor the flow, we have added in the flow stream a sensitive flow sensor (Sensirion, Westlake Village, CA) that measures the fluid velocity as a function of time which provides the basis for a much more accurate handling of the fluid and of particles in the stream compared to the air pressure switching scheme described in the previous section. The highly reproducible oscillatory velocity pattern in the up and down direction is shown in Figure II-8. Figure II-8B illustrates the reproducibility of the pumping where 40 strokes were overlaid on top of each other. No discernible differences in the velocity of the stroke are apparent. The shape of the pulse is likely due to air bubbles lodged in the system..

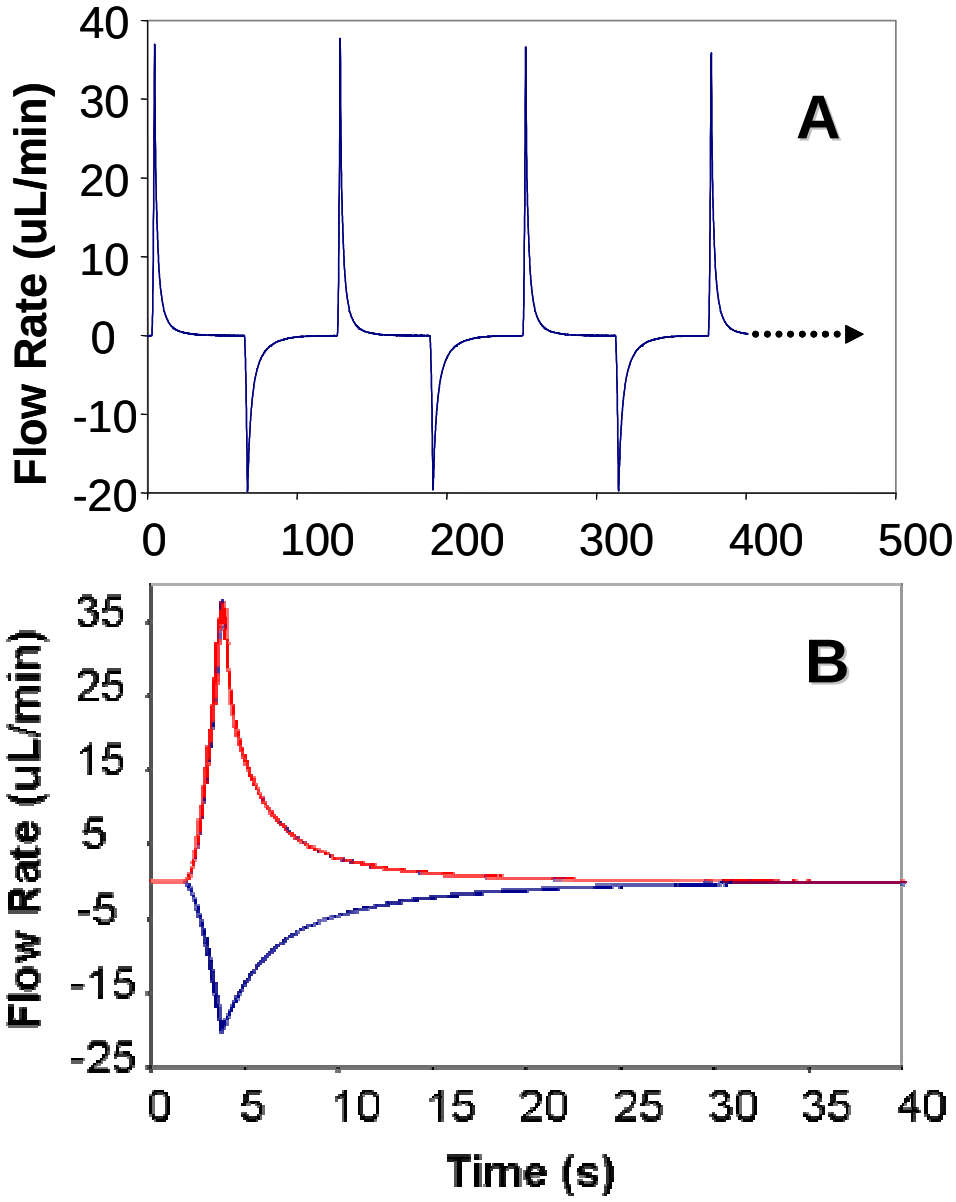

Figure II-8: (A) Fluid velocity as a function of time. The flow sensor monitors the fluid motion during pumping. **(B)** Fluid velocity changes during 40 pumping pulses of 1.5 μL of volume. Upstrokes (red), downstrokes (blue).

f) Teflon AF Capillary

As described in Chapter 0, a Teflon AF flow cell can conduct scattered or fluorescent light from an individual cell to the terminus of its capillary due to Teflon AF's lower refractive index than water. To construct aTeflon AF capillary, a 98 μm inner diameter, 307 μm outer diameter, 75 cm long Teflon AF® capillary (Random Technologies, San Francisco, CA) was placed in a holder in the Ortho optical box. The capillary was illuminated with a 488 nm laser passed through a single cylindrical lens to reduce the beam height to a diffraction limited height. The beam width was 700 μm. Each end of the capillary was attached to a 'tee' connector (P-713, Upchurch Scientific, Oak Harbor, WA) where a fiber optic was brought within 1 mm of the capillary terminus. A bidirectional, continuous syringe pump (Milli-GAT, Global FIA, Fox Island, WA) was connected to the fluid port of the tee on each end of the capillary in a closed loop as shown in Figure II-9.

To test if the alignment of the Teflon AF capillary is adequate, the histogram of fluorescent intensity from uniformly stained 6 micron BODIPY labeled beads were obtained with a Teflon AF capillary as shown in Figure II-9 and from a commercially available Guava cytometer equipped with a silica capillary. As Figure II-10 shows, the distribution obtained with the Teflon AF capillary matches the distribution obtained with the commercially available Guava cytometer. Thus, the alignment of the Teflon AF capillary is sufficient.

During a stroke, the velocity of the fluid varies (Figure II-8). To test if the particle's velocity has an effect on the peak height of fluorescent beads, the flow rate

during acquisition was varied and the average peak height of fluorescence from 1000 6 μm fluorescent beads were recorded and shown in Figure II-11. As the figure shows, there is no dependence of the average peak height on the velocity of flow.

A key aspect of the device will be to watch how growing cells change their properties over time. To maintain cell growth in a constant environment, cells need fresh nutrients supplied at a rate greater than the rate of nutrient consumption. Since relatively small amounts of oxygen can be dissolved in water relative to the oxygen uptake rate of cells, oxygen must be continually supplied to a culture. A Teflon AF capillary is ideal for adjusting the gas concentrations of the fluid inside the capillary. In contrast to a virtually impermeable silica capillary, Teflon AF has a large gas permeability (Resnick and Buck 2006). Thus, gas concentrations within the fluid can be controlled by adjusting the gas mix flowed over a Teflon AF capillary. For instance, anaerobic conditions could be obtained by flowing only nitrogen over the capillary, aerobic conditions can be maintained by adjusting the oxygen concentration in the gas mixture, or alternatively the concentration of CO_2 in the air stream can be varied to adjust the pH of the fluid in the capillary.

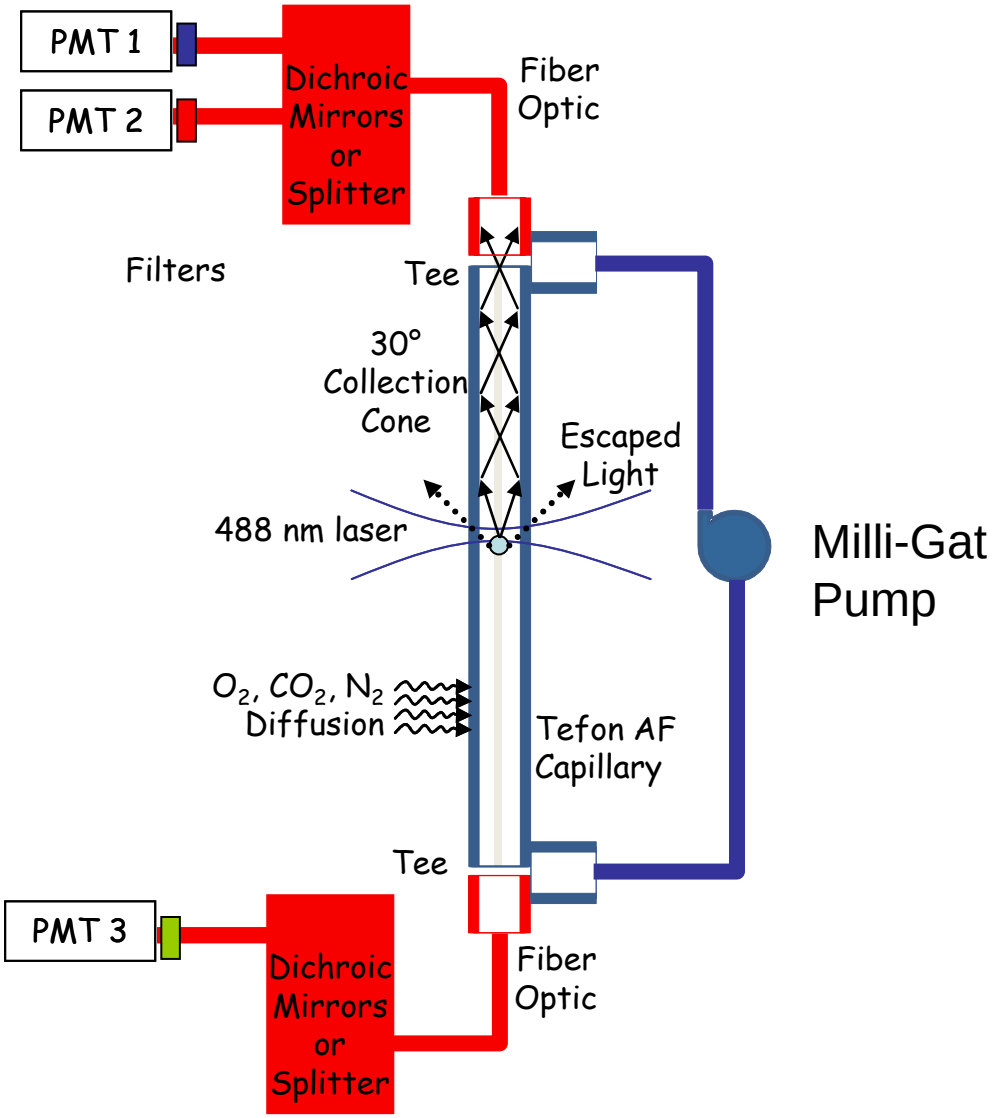

Figure II-9: Cartoon depicting the optical layout of the device with the Teflon AF capillary and associated fiber optics. Each PMT has an associated filter to collect light from a narrow range of wavelengths.

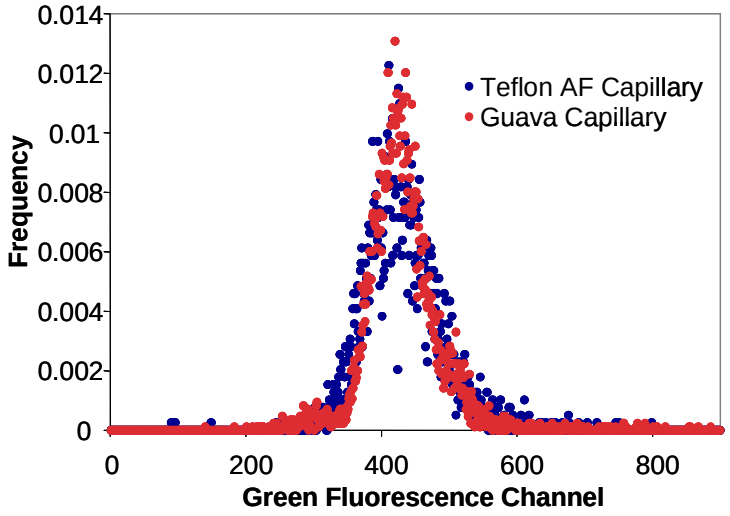

Figure II-10: Assessing instrument error**.** Histograms of green fluorescent intensity from 6 micron BODIPY labeled beads obtained with a Teflon AF capillary as in figure 7 and from a commercially available Guava cytometer equipped with a silica capillary.

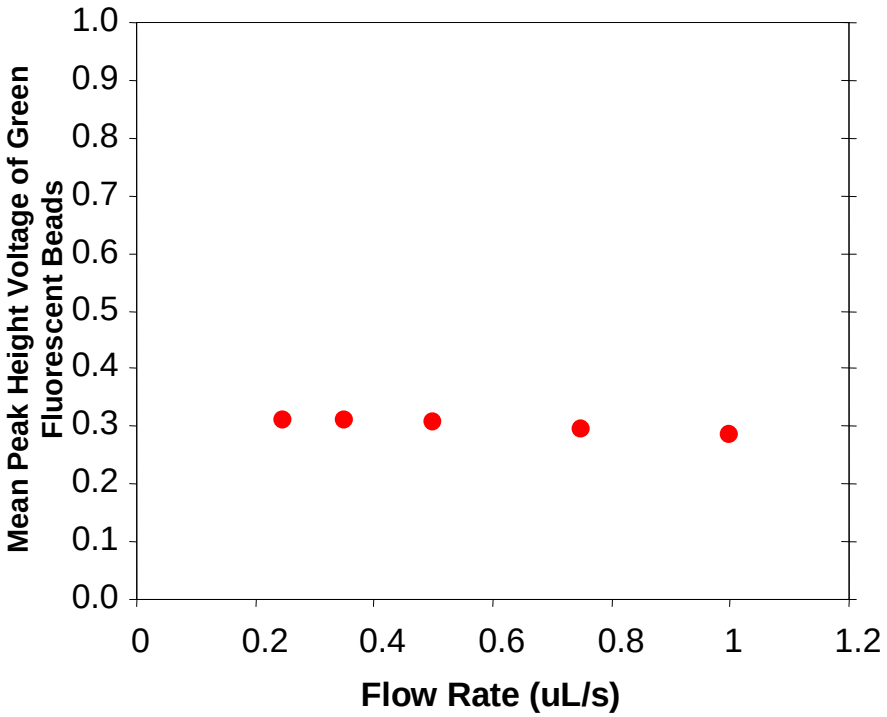

Figure II-11: Peak height as a function of flow rate. Six micron calibration bead average fluorescent peak height (n=1000) as a function of the flow rate through the device. There is no apparent dependence on the flow rate and the peak height response.

g) Data Acquisition

For each particle crossing the laser, the pulse shapes of the scattering and fluorescent events were recorded with a data acquisition card (PCI-6120, National Instruments, Austin, TX) and custom written LABVIEW based acquisition software. The software continuously digitized signals from each PMT in the device at up to 800 kHz. For each event resulting in a peak, the software recognized the peak based on a user inputted threshold for a given trigger channel, and then extracted that peak across all PMT signals. These waveforms along with the iteration, the time the event occurred within a stroke, and the peak heights were then recorded to disk in ASCII format. Each event occupied one line in this file. The software also controlled the Milli-GAT pump and recorded the flow rate of the fluid during each individual stroke given by a flow sensor (Sensirion, Corp, Switzerland). A screen shot of the software is provided in Figure II-12.

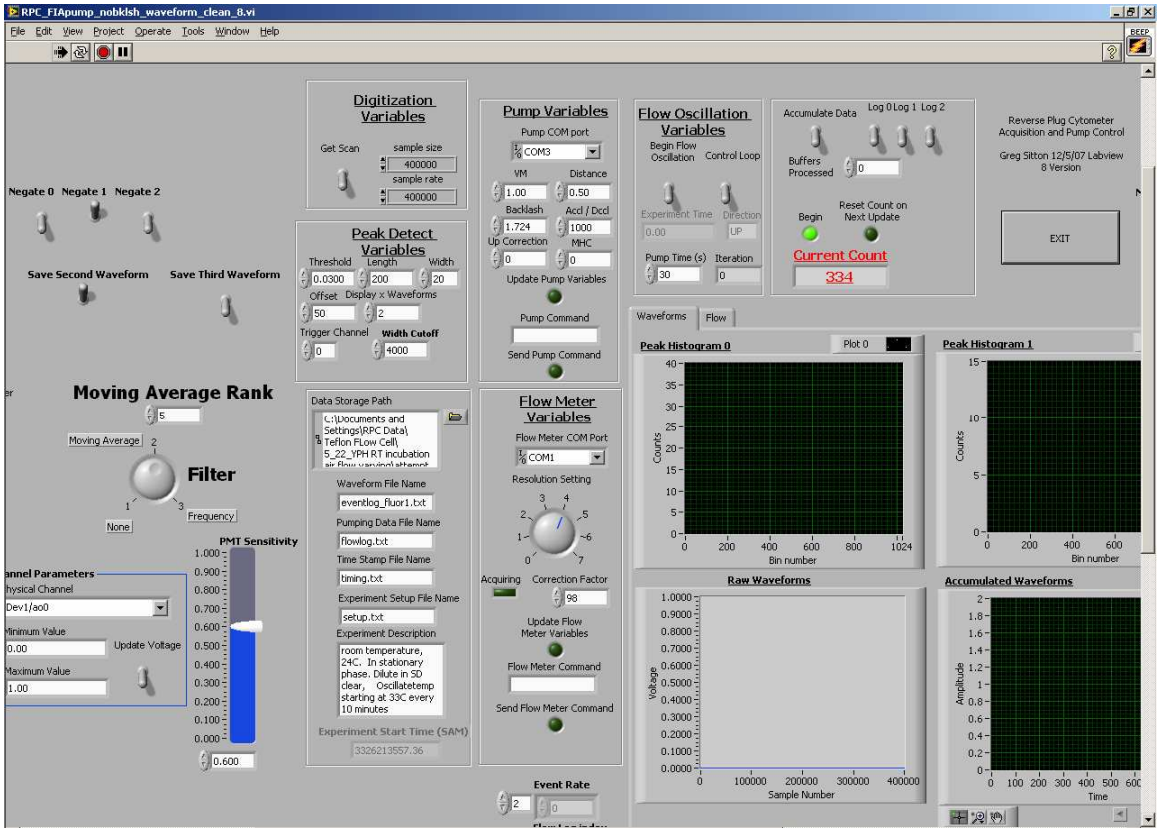

Figure II-12: Screen shot showing the front end interface of the data acquisition software written in LABVIEW.

h) Data Extraction Algorithm

Once the data is acquired in table format, events across multiple strokes must be assigned to individual particles. To accomplish this, a graphical user interface (GUI) was created in MATLAB. A screen shot is provided in Figure II-13. The assignment algorithm works by having the user choose two initial points in a trace. Then using up to a user specified number (typically 8) of past points in the trace, the algorithm does a linear extrapolation of each parameter to the next iteration that does not have a trace member. The extrapolated value is then searched for in the next iteration, by computing the weighted Euclidean distance from the extrapolated value to each event in the next iteration. Given a user specified threshold, a matching particle is assigned to the trace and the algorithm continues to the next stroke. The weighted Euclidean distance is more heavily weighted to favor fluorescence and timing.

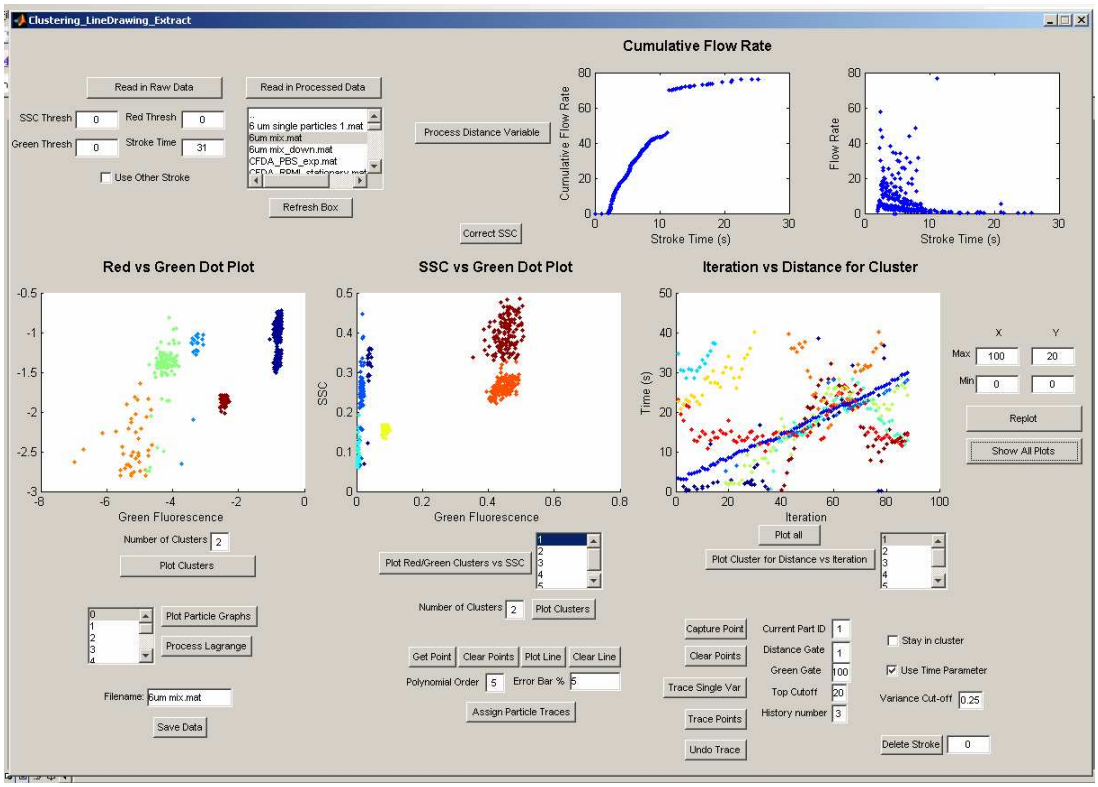

Figure II-13: A screen shot of the MATLAB GUI used to assign events from the acquired data to a given trace that defines a unique particle.